Biomechanical analysis of the human cornea

Nicolas Falgayrettes

Submitted in partial fulfillment for the degree of PhD

University of Lorraine

C2MP: Mechanics of material

directed by

GeorgiaTech Lorraine

IRL GT-CNRS 2958

Submitted by

Nicolas Falgayrettes

the 17th november 2023

Biomechanical analysis of the human cornea

Director : **Jean-Paul Salvestrini**
Co-director : **Franck Cleymand**

Jury

Mrs. Emmanuelle Jacquet,	Professor,	Reporter
Mr. Sebastien Laporte,	Professor,	Reporter
Mrs. Claire Morin,	Associate,	Reviewer
Mr. Tarak Ben Zineb,	Professor,	Reviewer, President

GeorgiaTech Lorraine
IRL GT-CNRS 2958, Lorraine, France

THESIS

Acknowledgements

I first thank my parents for their love and supports, which laid the foundation for extensive future graduate education and allowed me to be where I am today. I thank very much my advisor, Professor Etienne Patoor, for his guidance and encouragement throughout this doctoral degree. Earning this PhD turned out to be very difficult and it would not have been possible without his and Dr. Franck Cleymand support.

I was very fortunate to pursue this research thanks to the doctor Jean-Marc Perone, head of the department of ophthalmology at Mercy's hospital (Metz, France), who initiated this corneal project. I would like to thank him for his trust and his very active and motivating involvement in this work.

I would like to thank Jean-Paul Salvestrini, director of the IRL GT-CNRS 2958, for welcoming me to his laboratory and for agreeing to become my thesis supervisor following the retirement of Etienne Patoor. I would like to thank Abdallah Ougazzaden, president of GeorgiaTech Lorraine, for welcoming me to the laboratory and co-funding this project, and I would like to thank the CNRS for recruiting me as a doctoral student.

Finally, I am grateful to all my friends in GeorgiaTech Lorraine who made this stay a very special moment beyond just work. Many thanks to them.

I thank the program DREAM set up by the Université de Lorraine within the framework of the Lorraine University of Excellence Initiative (LUE) to finance an international mobility to Università Campus Bio-Medico, Roma, Italy during this PhD. In that regard, I thank Alessio Gizzi of Università Campus Bio-Medico, Roma, Italy, for the welcoming stay and his great help when developing the simulation.

This work is supported by grant n°17CP-1391-C63 from Region Grand Est, France.

Résumé en français

Cette thèse de doctorat résulte d'un travail collaboratif entre le service d'ophtalmologie de l'hôpital de Mercy (Metz, France) et l'expertise en mécanique des matériaux et modélisation numérique de GeorgiaTech Lorraine (Metz, France). Elle a porté sur la modélisation du comportement biomécanique de la cornée humaine et de son altération dans les cas pathologiques.

Comparée à l'étude de la biomécanique vasculaire ou osseuse, la biomécanique cornéenne fait l'objet de moins de recherches et de nombreux défis sont à relever pour mieux comprendre la physiologie de la cornée et ses pathologies. Le but de ce travail a été de répondre aux besoins du milieu médical quant à l'étude de deux maladies de cornée : le kératocône et la dystrophie de Fuchs. Pour ce faire, deux modèles numériques ont été développés.

Un premier modèle qui décrit l'architecture de collagène dans le stroma cornéen a été utilisé pour étudier la biomécanique d'une déformation conique comme observée dans le Kératocône, ainsi que pour observer les contraintes imposées par le frottement des yeux. Un second modèle qui décrit les propriétés multiphasiques de la cornée, la pression du fluide et le contrôle de l'hydratation a été utilisé pour étudier les phénomènes physiques impliqués dans un œdème cornéen comme observé dans la dystrophie de Fuchs et différencier l'influence des actions de la barrière et de la pompe endothéliale dans le contrôle de l'hydratation du tissu.

Comme la plupart des tissus biologiques, la cornée est largement composée de collagène, la principale protéine structurelle de la matrice extracellulaire de l'organisme. Dans la cornée, les molécules de collagène s'organisent en fibres microscopiques dont la direction et la rigidité définissent les propriétés mécaniques du tissu. Il a été démontré qu'une désorganisation des fibres pouvait provoquer des pathologies et une faillite du tissu cornéen, comme celle observée dans la maladie du kératocône dont les symptômes sont une déformation conique et un amincissement localisé sur le centre de la cornée.

Une analyse de la littérature a été faite pour déterminer l'organisation des fibres dans la cornée et les inclure dans le modèle numérique. Elle a montré que la direction préférentielle des fibres de collagène varie considérablement en fonction de l'épaisseur et des régions de la cornée, résultant en une architecture tridimensionnelle complexe. Pour décrire cette architecture, les fibres incorporées dans le modèle ont été réparties en un quadrillage orthogonal le long des méridiens inférieur-supérieur et nasal-temporal dans la zone centrale de la cornée, avec l'ajout d'un renforcement annulaire en périphérie. Il a aussi été observé que les fibres antérieures sont préférentiellement entremêlées et les fibres postérieures stratifiées et organisées, une répartition isotrope antérieure et une répartition anisotrope postérieure ont donc été introduites dans le modèle pour reproduire cette caractéristique. Au final, cette architecture de collagène a conféré des propriétés mécaniques anisotropes au modèle de cornée.

La cornée est également un tissu très hydraté qui contient de l'eau à hauteur de 78% de sa masse totale et qui obtient ses nutriments par des échanges de fluides et des interactions osmotiques avec l'humeur aqueuse en contact avec sa surface postérieure. Il est donc important de décrire les aspects d'hydratation et de pression de fluide du tissu dans son comportement mécanique. En effet, prédire la pression de gonflement de la cornée est utile en clinique car un œdème stromal excessif provoque un épaississement et une opacification du tissu et modifie les courbures des surfaces limitrophes, ce qui nuit à sa fonction de lentille optique.

Dans cet objectif, le modèle fibreux a été étendu en un modèle fibreux et poreux en incluant une phase fluide dans la description de son comportement mécanique. En se plaçant dans le cadre de la théorie des mélanges, le matériau a été considéré comme un mélange d'une phase

fluide composée d'un solvant neutre et de solutés chargés et d'une phase solide comprenant des charges fixes attachées. L'incorporation de charges fixes a donné lieu à une différence de pression osmotique entre intérieur/extérieur et à l'apparition de phénomènes de transport électrocinétique comme la diffusion, l'osmose et l'électro-osmose.

En outre, la cornée représente un cas intéressant car le tissu dépend de processus de transports actifs se produisant au niveau des cellules endothéliales pour réguler son niveau d'hydratation. En effet, l'endothélium agit comme une membrane sélectivement perméable qui utilise des pompes métaboliques pour maintenir une pression de fluide stable dans le stroma cornéen et empêcher son gonflement. Le mécanisme d'équilibre pompe-barrière de l'endothélium a donc été inclus dans le modèle et appliqué à l'étude de la dystrophie de Fuchs.

Une fois cet état de l'art accompli, la première étape de la modélisation fut de reconstruire une géométrie de la cornée humaine à partir de données topographiques et tomographiques prises à l'hôpital de Metz-Thionville. Sachant que la surface postérieure de la cornée est constamment soumise à la pression intra-oculaire d'environ 20mmHg, les données récoltés correspondaient à celles de la cornée in vivo déformée par la pression intra-oculaire, et une procédure inverse a dû être développée pour obtenir une géométrie de référence (non déformée par la pression intra-oculaire) sur laquelle l'application des conditions aux limites retrouverait la configuration de la cornée in vivo. Cette procédure inverse a ensuite été étendue au second modèle de matériau multiphasique avec comme paramètres la géométrie de la cornée (coordonnées des nœuds), la densité de charge fixe et la fraction de volume de fluide. Les problèmes mathématiques furent ensuite posés sur cette géométrie de référence et résolus avec la méthode éléments finis en 3D, en utilisant les logiciels Abaqus et FEBio.

La première analyse numérique s'est concentrée sur les aspects fibreux du stroma cornéen avec l'objectif d'identifier les conditions nécessaires à une déformation conique du tissu telle qu'observée dans la maladie du kératocône. Sachant que l'étiologie et les mécanismes de cette maladie restent inexpliqués après plus de deux siècles de recherches et de nombreuses études en biologie, l'objectif de ce travail a été d'apporter de nouvelles informations en se plaçant d'un point de vue nouveau qui est celui de la mécanique des matériaux.

Une vision largement répandue de la physiopathologie du kératocône propose que la maladie soit initiée par la dégradation des couches antérieures de la cornée, cependant, une constatation clinique récurrente dans le kératocône précoce est une élévation postérieure à la vidéokératoscopie sans signes de dégradation des couches antérieures ou de courbure antérieure anormale. Une incohérence existe donc entre la perception de l'origine de la maladie et la chronologie des symptômes. Ce travail de modélisation a tenté d'apporter plus d'informations à ce sujet.

La loi de comportement de matériau H.G.O. a été utilisée pour décrire le comportement mécanique du stroma cornéen dans le modèle numérique. Cette loi de comportement macroscopique structurelle inclut les contributions d'une matrice néo-hookéenne non collagénique isotrope et de deux familles anisotropes de fibres de collagène avec une orientation et une dispersion définies. Elle permet de décrire le comportement hyperélastique anisotrope et de rigidification à la déformation des matériaux renforcés par des fibres.

En créant des zones pathologiques sur la géométrie de cornée et en variant les paramètres de rigidité de la matrice et des fibres, la simulation a pu recréer le bombement local prononcé caractéristique de la maladie du kératocône. Plusieurs analyses paramétriques ont ensuite démontré que tant que les couches postérieures du stroma gardaient leur rigidité, la cornée ne se déformait pas de manière conique et conservait une forme sphérique antérieure adéquate, nécessaire à la réfraction des rayons lumineux sur la rétine.

Si, en raison d'une maladie, les fibres de collagène du stroma postérieur perdaient leur rigidité ou devenaient désorganisées, le soutien mécanique du tissu à cet endroit s'affaiblissait, entraînant une déformation conique transmise aux couches supérieures. La simulation numérique a donc mis en évidence certaines incohérences dans la vision traditionnelle selon laquelle les couches antérieures de la cornée seraient les premières touchées et à l'origine du kératocône.

Il a aussi été démontré que la perte de rigidité devait être localisée et appliquée graduellement sur une petite partie du tissu pour obtenir une déformation conique de la cornée. Une perte de rigidité sur l'ensemble de la cornée n'a pas entrainé de déformation conique. Ces deux points peuvent indiquer une origine de l'ectasie cornéenne due à des dommages localisés dans le stroma postérieur qui se propage ensuite aux tissus sains antérieurs.

A noter qu'une perte de rigidité des couches antérieures n'a pas entrainé de déformation conique, ce qui est rassurant quant à l'utilisation de la chirurgie réfractive, massivement pratiquée tous les jours, et qui consiste en une ablation des couches antérieures de la cornée.

En outre, comme les frottements des yeux sont souvent soupçonnés d'être à l'origine du kératocône, le développement d'un modèle de contact a permis de visualiser la répartition et l'intensité des contraintes mécaniques induites par le frottement d'un indenteur sur la cornée. Les résultats de cette simulation ont montré que cette pratique sollicitait fortement le stroma postérieur en tension et en cisaillement mais épargnait les couches antérieures qui étaient soumises à une faible compression au point d'indentation.

L'ensemble de ces études suggère que le stroma postérieur joue un rôle initial important dans la pathogenèse du kératocône. Sous réserve de validations supplémentaires, ces résultats suggèrent que la caractérisation du stroma postérieur pourrait aider à diagnostiquer le kératocône à un stade très précoce, facilitant les interventions rapides pour bloquer la progression de la maladie.

Dans la seconde analyse numérique, la cornée a été modélisée comme un matériau multiphasique avec une phase solide fibreuse et une phase fluide en utilisant la théorie des mélanges. La contribution volumique du fluide est composée d'une composante hydraulique et d'une composante osmotique provenant de la présence de solutés. Ce modèle multiphasique a permis de comprendre les phénomènes physiques impliqués dans l'œdème de la cornée, notamment le fait que les charges négatives fixes des protéoglycanes sur la matrice solide induisent un gradient de concentration ioniques entre le tissu et le fluide extérieur, créant un appel d'eau de l'humeur aqueuse vers le stroma par osmose et électro-osmose. Pour contrebalancer cette tendance, la membrane endothéliale in vivo utilise une action de pompes métaboliques pour abaisser la concentration osmotique dans le tissu.

Une description de la fonction de barrière et de pompe active de la membrane endothéliale a donc été incorporée sur la base d'un modèle bicarbonate simplifié pour modéliser les flux ion-

iques entrants et sortants et recréer le mécanisme de régulation de l'hydratation et de pression de fluide d'une cornée in vivo. Le modèle global a été validé contre la pression du fluide stromal mesurée expérimentalement in vivo à 60 mmHg, avec une valeur numérique moyenne obtenue à l'équilibre mesurée à 61 mmHg.

La simulation a reproduit la perte progressive du contrôle de l'hydratation et le gonflement stromal comme observé dans la dystrophie de Fuchs. Elle a permis de différencier l'influence des actions de la barrière et de la pompe endothéliale et tester l'hypothèse suggérant que la perte de densité cellulaire endothéliale est responsable d'une augmentation de la perméabilité de la membrane.

Des analyses paramétriques sur la diffusivité et le flux actif de bicarbonate ont montré qu'une fonction de barrière contre certains ions chargés négativement était nécessaire pour maintenir une bonne pression de fluide, même avec une pompe fonctionnant parfaitement. Lorsque la fonction de barrière était trop altérée et la perméabilité ionique trop élevée, il n'était plus possible de compenser la fuite et la cornée finissait par se sur hydrater et gonfler. La perte de cellules endothéliales dans la dystrophie de Fuchs résulte donc en une augmentation de la perméabilité de la membrane et une augmentation du volume d'eau dans la cornée.

Dans la même logique, une pompe endothéliale qui abaisse les charges négatives dans le stroma était nécessaire pour maintenir une bonne pression de fluide. En effet, même avec une fonction de barrière intacte, une diffusion lente opérait toujours et un flux actif fut nécessaire pour contrer la fuite passive d'ions dans la cornée et maintenir un niveau d'hydratation correct. Un équilibre entre les deux mécanismes de régulation est donc nécessaire.

La simulation a également montré que la perte initiale de la fonction barrière peut être compensée par une augmentation du flux actif, jusqu'à une certaine perte de densité cellulaire à partir de laquelle l'augmentation de la perméabilité ne peut plus être compensé par une augmentation du flux actif. Cette observation est en accord avec l'une des hypothèses médicales actuelle sur la progression de la dystrophie de Fuchs, selon laquelle, dans ses phases précliniques, le mécanisme de pompe peut être suractivé pour compenser la perte de cellules, jusqu'à un degré où l'endothélium ne peut pas s'adapter et où les symptômes de la maladie apparaissent progressivement.

Comme dernière validation, le modèle en état d'œdème a prédit un gonflement maximal de l'épaisseur centrale de la cornée (CCT) d'environ 660 µm, ce qui correspond aux observations cliniques de la dystrophie de Fuch, allant de 580 µm au stade précoce à 690 µm au stade avancé, alors que l'épaisseur normale est de 530 µm. Il a été observé que ce gonflement se produisait principalement dans la région stromale postérieure et dans le sens de l'épaisseur, comme vu cliniquement.

En adoptant cette approche de modélisation décrivant la microstructure et le comportement mécanique de la cornée, la simulation numérique a apporté de nouvelles connaissances sur deux maladies de cornée : le kératocône et la dystrophie de Fuchs. Elle a offert un cadre flexible et peu coûteux pour réaliser des analyses paramétriques et de sensibilité étudiant le rôle des paramètres microstructuraux de chaque couche cornéenne afin d'évaluer leur influence sur la biomécanique de la cornée et déterminer les conditions nécessaires à ses états pathologiques.

Les résultats obtenus dans cette thèse ont été jugés intéressants par les partenaires cliniques grâce à l'analyse numérique qui a fourni de nouvelles perspectives sur les deux maladies étudiées. Pour la maladie du kératocône, les simulations ont mis en évidence certaines incohérences dans la vision traditionnelle selon laquelle les couches antérieures de la cornée seraient les premières touchées et donc à l'origine de la maladie. En conséquence, un article combinant les résultats mécaniques et les observations cliniques a été publié, proposant une hypothèse modifiée sur l'étiologie de la maladie et indiquant qu'une déformation conique n'est pas possible si les couches postérieures de la cornée ne sont pas affectées.

Dans le cas de la dystrophie de Fuchs, les simulations numériques étaient en accord avec les connaissances médicales selon lesquelles la perte de la fonction de barrière endothéliale est due à la perte cellulaire et est initialement compensée par une suractivation du mécanisme de pompe des cellules restantes. Cette suractivation est efficace jusqu'à ce que la compensation ne soit plus suffisante et que la pression du fluide augmente, ce qui entraîne un gonflement de la cornée.

Au final, cette recherche doctorale a pu montrer l'intérêt d'appliquer les techniques de modélisation de la mécanique des matériaux à des problématiques médicales. La combinaison de différentes expertises a été prolifique pour l'étude des deux maladies de cornée et a démontré les bénéfices d'une approche multidisciplinaire.

Contents

Acknowledgements **2**

I Introduction 11

1 Thesis motivation **11**

2 Description of the human cornea **12**
2.1 Cornea microstructure . . . 13
2.1.1 Details of the stroma micro structure . . . 14
2.1.2 Details of the stroma nano structure . . . 16
2.2 Biomechanics of the cornea . . . 18
2.2.1 Intra-ocular pressure (IOP) of the eye . . . 20
2.2.2 Specific mechanical behavior of the different corneal layers . . . 22
2.3 Corneal hydration and the endothelial function . . . 23
2.4 Geometry of the cornea . . . 28
2.4.1 Corneal diameter . . . 29
2.4.2 Corneal curvature . . . 29
2.4.3 In vivo dimensions of the author's cornea . . . 30

3 State of the art in corneal modeling **31**
3.1 Continuum mechanics and large deformation framework . . . 32
3.2 Phenomenological modeling . . . 34
3.3 The Holzapfel-Gasser-Ogden model . . . 35
3.4 Structurally based model . . . 37
3.5 Micro-structurally based model . . . 42
3.6 Swelling behavior . . . 44
3.7 Conclusion . . . 48

4 Summary of the introduction **48**

II The cornea as a fiber-reinforced tissue 49

5 Objective **49**

6 Modeling methods **52**
6.1 Modeling the collagen fiber architecture in the stroma . . . 53
6.1.1 Material parameters of the model . . . 54
6.1.2 Geometry and boundary conditions . . . 55
6.2 Inverse procedure to recover the cornea initial/reference configuration . . . 56
6.3 Mesh convergence study . . . 59

7 Results **59**
7.1 Identification of the corneal tissue zones whose softening yielded keratoconus . . . 60
7.1.1 Analysis 1: Effect of local and global softening on corneal shape and thickness . . . 61

7.1.2 Analysis 2: effect of softening specific collagen-based layers on corneal shape and thickness . . . 63
7.1.3 Analysis 3: effect of disrupting the anisotropic orientation of posterior lamellae on corneal shape . . . 64
7.2 Effect of eye rubbing on corneal layers . . . 64

8 Discussion **68**

9 Fiber-reinforced cornea summary **72**

III The cornea as an hydrated tissue **73**

10 Objective **73**

11 Mixture theory for biological tissue **74**
11.1 Linear Momentum balance expressed in nodal variables . . . 75
11.2 Physics of solutes in mixture . . . 76
11.2.1 Osmotic pressure definition . . . 77
11.2.2 Electroneutrality condition in mixture . . . 79
11.2.3 Donnan equilibrium of a polyelectrolyte in salt solution . . . 80
11.3 Modelling flux of solutes . . . 82
11.3.1 Non-equilibrium thermodynamics prerequisite . . . 83
11.3.2 Link with Mixture Theory . . . 83

12 Hydrated corneal model development **85**
12.1 Material properties for the multiphasic cornea . . . 85
12.2 Introduction to biphasic material: consolidated undrained triaxial test . . . 91
12.2.1 Undrained triaxial test model description . . . 92
12.2.2 Results . . . 92
12.2.3 Interpretation . . . 94
12.3 Model verification: analytical calculation and comparison . . . 94
12.3.1 Model description . . . 95
12.3.2 Analytical verification . . . 97
12.3.3 Further testing and comparison . . . 98
12.4 Inverse procedure for multiphasic material . . . 101
12.4.1 Procedure description . . . 101
12.4.2 Fixed charge density and residual stresses in the cornea . . . 103
12.5 Model validation from in vivo corneal data . . . 105
12.5.1 Swelling pressure and intra ocular pressure in a multiphasic framework . 105
12.5.2 The active ionic flux in a multiphasic framework . . . 106
12.5.3 Numerical experiments for model validation . . . 107
12.5.4 Validation interpretation . . . 112

13 Model application: study of Fuch's dystrophy and Glaucoma **113**
13.1 Description of Fuch's endothelial dystrophy . . . 113
13.2 Modeling of Fuch's dystrophy disease . . . 115
13.2.1 Link between endothelial permeability and corneal swelling pressure . . . 115
13.2.2 Link between endothelial active flux and corneal swelling pressure . . . 117

13.3 Fuch's dystrophy edema presentation in the 3D cornea 120
13.4 Glaucoma presentation in the 3D cornea 122

14 What's next ?: molecular mechanisms underlying the corneal endothelial pump 123
14.1 Description of the corneal molecular endothelial pump-leak exchanger 123
14.2 Numerical application with a simple model of reactive membrane 124

15 Hydrated cornea summary 127

IV Conclusion 128

Bibliography 130

Appendix 131

A Mixture theory 131
A.1 Mass balance 131
A.2 Linear Momentum balance 132
A.3 Angular Momentum balance 136
A.4 Balance of internal energy 136
A.5 Entropy inequality 136

Part I
Introduction

1 Thesis motivation

Compared to vascular or bone biomechanics, less research are being conducted on corneal biomechanics and a lot of challenges need to be addressed to better understand corneal physiology and its alteration in pathological cases such as Keratoconus disease [1] [2] and Fuch's dystrophy [3] [4].

By adopting a modeling approach considering the mechanical behavior of the cornea and its microstructure, numerical simulation could provide new understandings on corneal diseases as it allows a low cost and flexible framework to explore the influence of various parameters on corneal biomechanics and to determine the necessary conditions leading to a pathological state.

Usually, medical problematic involves more readily epidemiological, cellular and biochemical studies. However, some corneal diseases like keratoconus have been unexplained for a long time and many of the possible "biological" explanations are still inconclusive [5]. For example, a widely held view of keratoconus physiopathology proposes that the disease is initiated by anterior layer degradation [6]. However, one recurrent clinical finding in early keratoconus is posterior elevation on videokeratoscopy without signs of anterior layers degradation and a normal anterior curvature.

Therefore in Part(II) of this thesis, we will develop a numerical model describing the mechanical behavior of the cornea and investigate if the posterior cornea plays an important early role in Keratoconus pathogenesis. Based on simulation results, it could suggest that characterizing the posterior stroma may help to diagnose keratoconus at a very early stage, thereby facilitating interventions and prevents disease progression. Of note to date, while numerical models have been very useful to understand the biomechanics of the cornea, none have successfully achieved the pronounced local bulging that characterizes keratoconus [7] [8] [9] [10].

Additionally, because eye rubbing is often suspected as the cause of Keratoconus, especially in young individuals, a contact model will be developed to assess the effect of rubbing on the cornea by displaying the mechanical stress induced by this practice.

Once the fiber-reinforced solid mechanics of the cornea is described, the model could be further advanced to include multiphasic constituents and describe the tissue hydration and swelling pressure. Indeed, most of current finite-element-based models for structural analysis of the cornea treat the interfibrillar fluid as an incompressible or nearly incompressible elastic solid [10] [11] [12] [13] and do not describe the swelling behavior and bulk compressibility of the tissue.

Therefore, the goal of Part(III) of this thesis will be to develop a porous corneal tissue model that describes the features of charge effects and swelling missed by purely hyperelastic approaches. As the corneal tissue depends on active transport processes occurring at the endothelial cellular layer to maintain its hydration level and prevent swelling, the model will also have to incorporate this feature.

A modeling capability to predict the tissue swelling pressure would be clinically interesting as excessive swelling modifies the curvatures of the cornea's surfaces and defeats its optical focusing function. For example, such a model could be used to investigate diseases whose symptoms are

related to corneal edema such as Fuch's dystrophy, and used to better understand the role of the endothelium in the corneal tissue hydration homeostasis.

In this thesis, the model will be used to test the hypotheses on Fuch's dystrophy suggesting that the imbalance in hydration and consequent swelling of the tissue comes from a loss of endothelial cells barrier and pumping functions, which creates an excessive osmotic pressure in the tissue [4] [14]. Moreover, the simulation will try to differentiate the influence of the barrier and the pump actions in the endothelial function and reproduce the progressive loss of hydration control and the consequent stromal swelling occurring in Fuch's dystrophy.

In the end, two models will be developed to describe the important features related to the diseases studied which are collagen fibers architecture and its disruption in Keratoconus in Part(II), and fluid swelling pressure and membrane hydration control and its disruption in Fuch's dystrophy in Part(III). Before that, some fundamentals on corneal physiology and a state of the art on corneal modeling will be presented in this Introduction.

2 Description of the human cornea

The cornea is the outermost transparent structure of the eye. It provides a tough, protective envelope for the ocular contents and accounts for two thirds of the eye's refractive power. As the primary refractive component, the human cornea demands precise curvature, being almost spherical near the visual axis but flattening toward the limbus as shown in Fig(1).

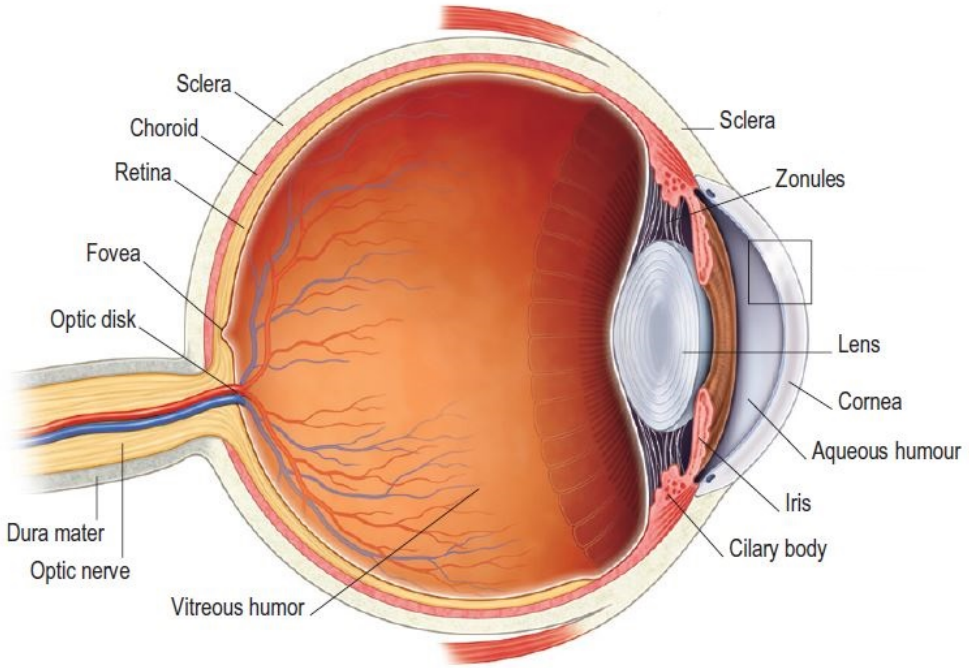

Figure 1: The human eye structure in section view. The cornea is the first transparent optical and protective layer in front of the eye acting as a lens for light refraction into the retina. [14]

The cornea can be viewed as a fiber-reinforced electrolyte gel that resists the intraocular pressure (IOP) applied on its internal boundary. Its mechanical strength derives from the three-dimensional organization of collagen fibers and its bulk properties derive from the interfibrillar fluid pressure. The cornea is the only tissue in the body requiring considerable mechanical

strength coupled with a perfectly defined shape and optical clarity. Its transparency is achieved through the small, uniform diameter of fibrils and their high level of lateral order.

Like most biological tissues, the cornea is largely composed of collagen, the main structural protein in the extracellular space in the body. It is an highly hydrated tissue containing water up to 78% of its total mass. Unlike most tissues in the body, the cornea contains no blood vessels to nourish or protect it against infection. Instead, the cornea receives its nourishment from tears and the aqueous humour, the inner fluid of the eye. To ensure this, fluid exchange and osmotic interaction happens between the cornea and the surrounding layers [14].

2.1 Cornea microstructure

The cornea is composed of 5 distinct layers, all with different functions and compositions. The mechanical strength and shape of the cornea are largely dependent on the corneal stroma, the most thick and mechanically influent layer which makes up over 90% of corneal thickness and 80% of the tissue stiffness [10] [15] .

In this section, a microstructural description of the cornea is provided, showing the specificities of each layer and the organizational particularity of the stroma with its three-dimensional lamellae architecture as shown in Fig(2). This is an important aspect of the modelling process as it is the tissue microstructure that determines its mechanical properties.

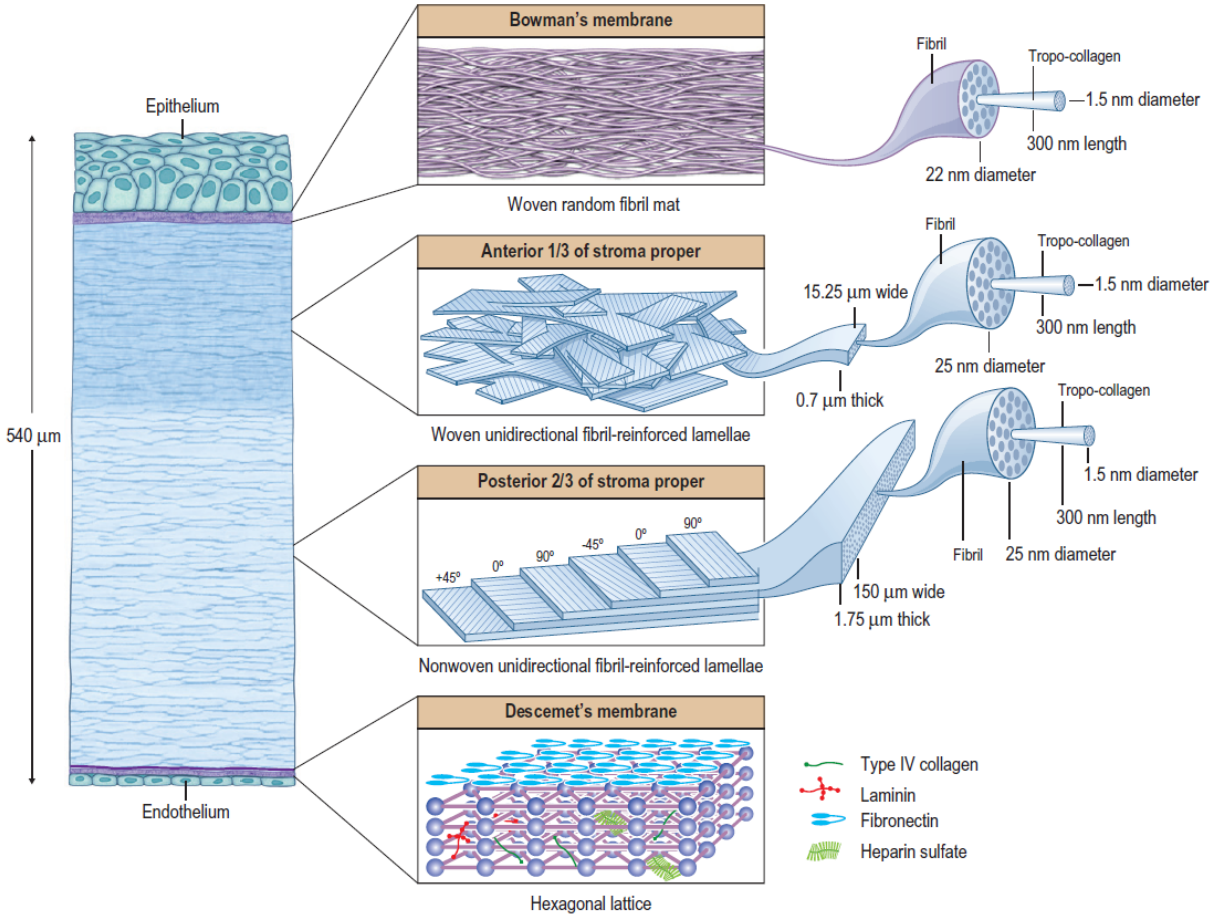

Figure 2: Layered structure and dimensions of the cornea in sectional view. The right part details the microstructure of the different mechanical layers and the lamellae preferential organisation of the stroma in blue. Dimensions are representative of the central cornea [14]

The epithelium This cellular membrane consists of 5 or 6 layers of cells stacked tightly. Its function is to provide a smooth surface to absorb oxygen and nutrients from tears, which are then distributed to the other layers of the cornea. It also blocks the passage into the eye of foreign material. The part of the epithelium in contact with Bowman's membrane that epithelial cells anchor and organize themselves to is called the basement membrane, which is around 60 to 65 nm thick [16].

The Bowman's membrane This membrane is approximately 12 µm thick, acellular and composed of densely packed, interweaved and randomly organized collagen fibrils of 20-25 nm in diameter. This membrane is a mechanical structural layer, highly resistant to penetration or damage. However, it cannot regenerate after injury, leading to its replacement by an outgrowth of epithelial tissue or stromal scar tissue [14].

The stroma Of the five anatomical layers of the normal cornea, the stroma accounts for 90% of total corneal thickness and dictates corneal strength and shape [10] [15] .

At the microscopic level, the collagen in the stroma is laid down within fibers referred to as lamellae that lies approximately parallel to the tissue surface. Collagen fibers/lamellae are approximately 1-2 µm thick and 10-200 µm wide and are distributed differently based on their localization in the stroma with a specific organization in the three-dimensional space. Overall, this stromal architecture endows the cornea with anisotropic mechanical properties.

The Descemet membrane The Descemet's membrane is around 5-20 µm thick and is synthesized by endothelial cells as the basement membrane of the corneal endothelium. It is a thin acellular layer that serves as protective barrier and is composed of less rigid collagen fibrils. Descemet's membrane repairs itself easily after injury [14].

The endothelium The endothelium is the corneal posterior-most layer of 5 µm thick consisting of cells that controls the cornea's hydration and maintain a transparent cornea. Normally, fluid leaks slowly from inside the eye into the stroma for uptake of nutrients from the aqueous humor [14]. The endothelium's primary task is to pump the excess of fluid out of the stroma by an active cellular mechanism. Without this pumping action, the stroma would swell with water and become thick and opaque [17]. Endothelial cells cannot divide or replicate, so if a loss occurs, the remaining cells have to change in shape or size to fill the corneal posterior surface.

2.1.1 Details of the stroma micro structure

Since the mechanical properties of the cornea are strongly related to the stromal layer, a detailed description of stromal microstructure has to be introduced in order to develop an accurate mechanical model of the cornea.

In the cornea, the stroma accounts for 90% of corneal volume and dictates corneal strength and shape [10] [15]. Its keratocytes generate a complex architecture composed of ground substance (non-fibrillar collagen and proteoglycans) and fibrillar collagen type I fibrils that are packed into lamellae. The lamellae are held in place by cross-links created by the ground substance molecules.

The anterior and posterior stroma differ markedly in terms of lamellar architecture: the anterior lamellae are randomly interwoven, thin, and anchored in Bowman's layer whereas towards the posterior two-thirds of the stroma, the lamellae adopt a stacked plywood-like

organization [18]. Compared to anterior lamellae, posterior lamellae are wider, thicker, less densely packed, and highly organized [19] [20] [21] as shown in Fig(3).

A transition exists from an isotropic anterior stroma to a more orthotropic microstructure going through the posterior stroma. These architectural differences have biomechanical consequences: the anterior stroma has greater cohesive tensile strength and swells less readily, while the posterior stroma allows the cornea to resist intraocular pressure (IOP) and maintain adequate corneal curvature. Indeed, the posterior orthogonal architecture is believed to have a directional rigid behavior against IOP loading due to the locking behaviour of the grid of fibers and allows the tissue to keep its optimal curved shape on the optical axis [10]. Overall, this stromal architecture endows the cornea with anisotropic mechanical properties.

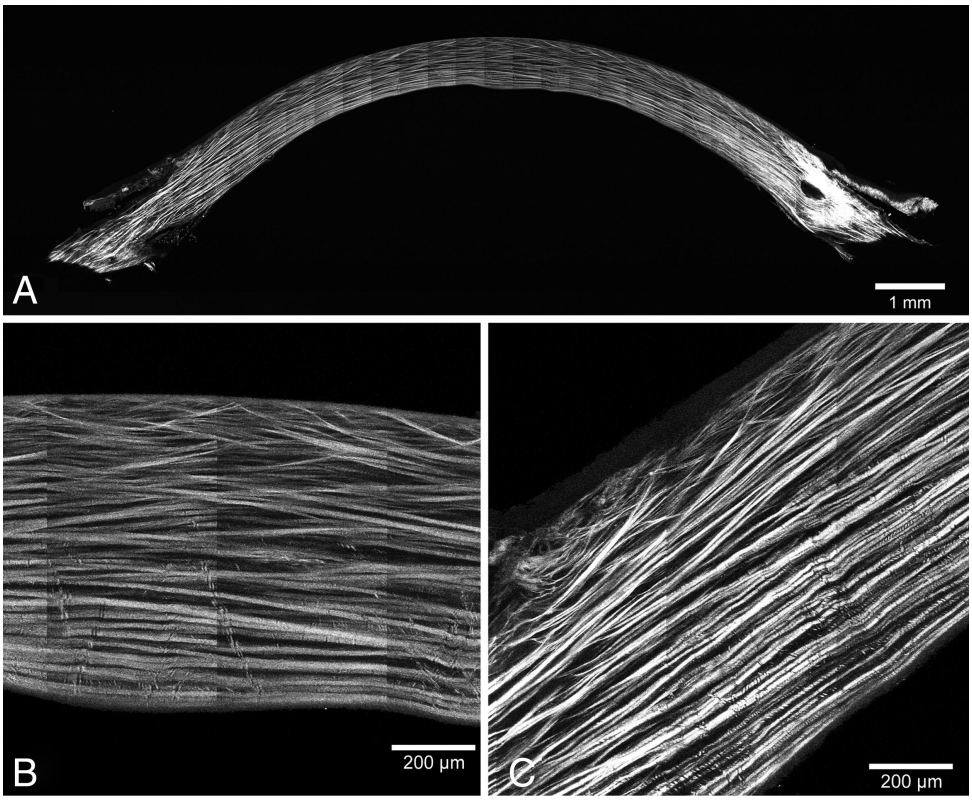

Figure 3: Second Harmonic Generation (SHG) microscopy imaging the collagen lamellae organization throughout the cornea orientation in section view [21]

The preferential alignment of lamellae vary considerably between stromal depths and regions so studies are proposing three dimensional models of corneal microstructure [22] [23]. When observed in front view, X-ray scattering studies can quantitatively determine the orientation of corneal fibers and has indicated that in the anterior stroma, lamellae are randomly organized in front view. On the other hand, a preferential orientation of collagen in the middle and posterior central human cornea has been quantified, in which fibers are orthogonally distributed around the inferior-superior (i-s) and nasal-temporal (n-t) meridians as shown in Fig(4).

Additionally, an important number of theoretical and experimental studies have indicated that the collagen microstructure of the peripheral cornea (called limbus) plays an important role in stabilizing corneal curvature. X-ray data are consistent with a scheme in which fibers change direction near the corneal periphery to run circumferentially, either by a discrete population of circular fibers or fibers from scleral origins inserting into the peripheral cornea without

entering the optical center [18] [22] .

To summarize, a simplified model of corneal and limbal lamellae orientations was proposed [14] where the central lamellae are predominantly oriented in the inferior-superior and nasal-temporal directions and curve near the limbus to form a pseudo-annulus, with puntual inserting fibers from the sclera.

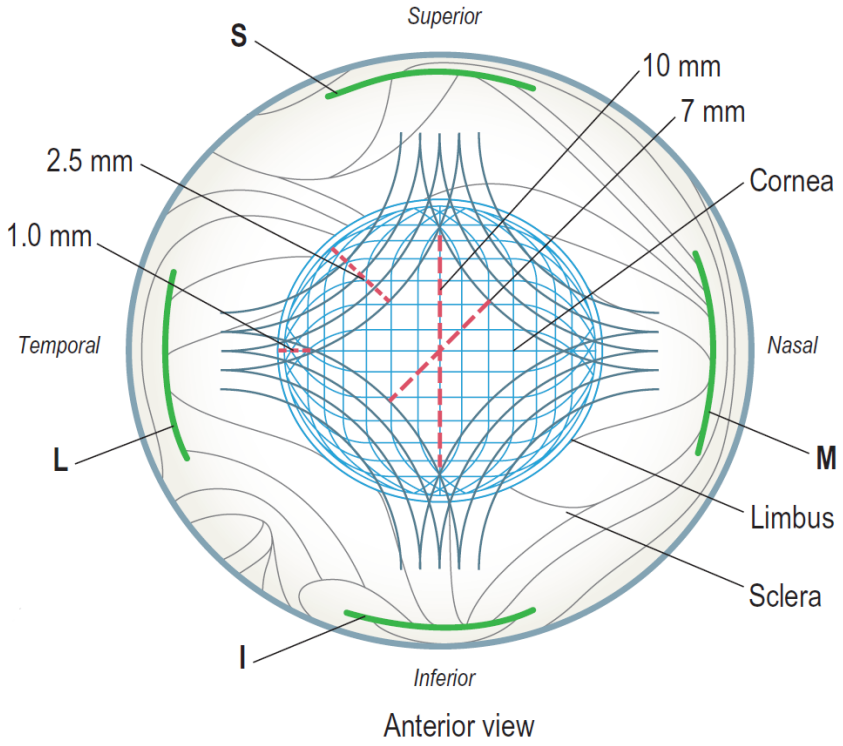

Figure 4: Ideal representation of collagen fibers organization in the human cornea. A central orthotropic population in the center, a preferential tangential fibers direction at the circumference and presence of sclera originated reinforcement fibers forming a diamond like shape out of the optical axis [14]

2.1.2 Details of the stroma nano structure

At nanoscopic level under the electron microscope, stromal lamellae are seen to be composed of uniform, small diameter collagen fibrils. The fibrils are spaced with a degree of lateral order and run parallel to the direction of the lamellae. This precise organization of collagen fibrils is imperative to maintain corneal clarity. In the central cornea, a fibril is 25 to 35 nm in diameter and maintained at an interfibrillar distance of around 50nm by proteoglycans (PGs) [14] as shown in Fig(5).

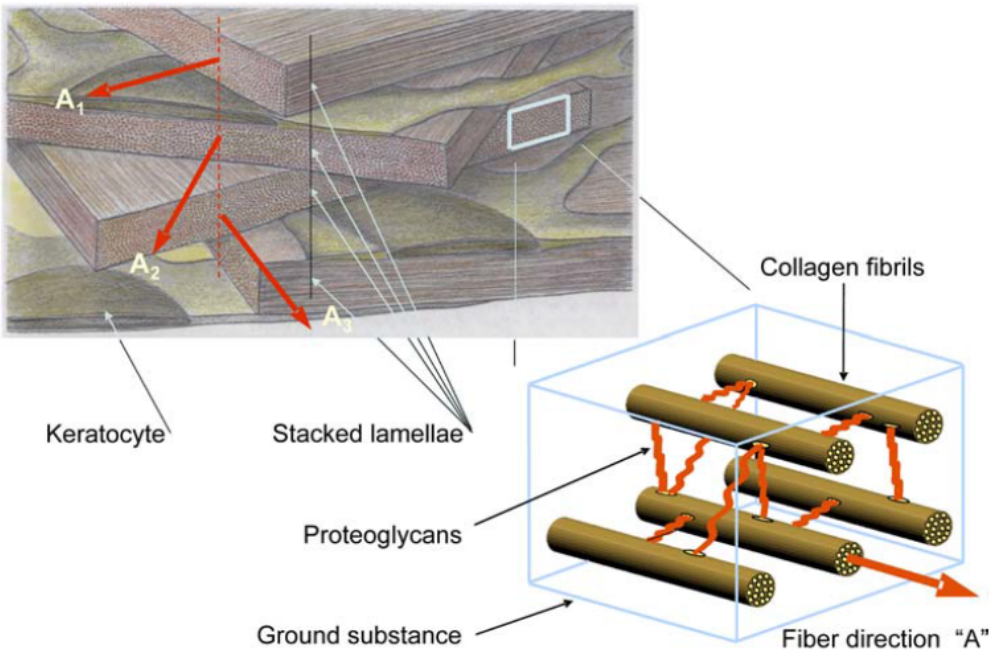

Figure 5: A collagen lamellae is composed or regularly spaced collagen fibrils maintained in lateral order by proteoglycans. At the nanoscale, fibrils follow the lamellae direction [18]

Proteoglycans are specialised glycoproteins trapped in the collagen fibrils. They are presents everywhere in the extracellular space and composed the interfibrillar matrix that maintain the adequate distance between fibrils. Proteoglycans are made of a protein backbone linked to a network of GAG chains as shown in Fig(6).

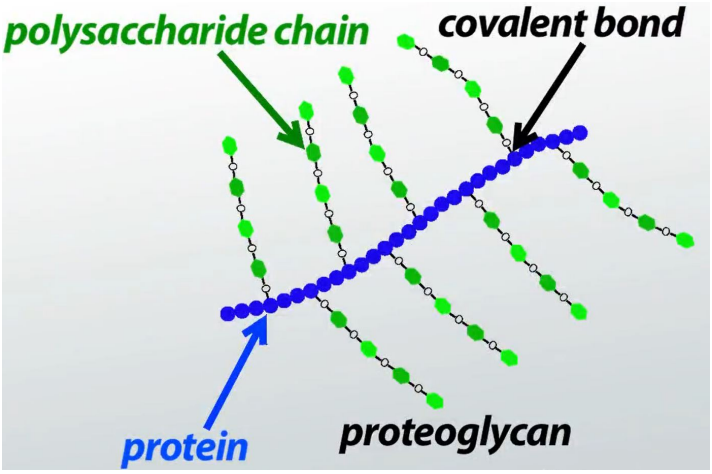

Figure 6: Proteoglycans are extracellular matrix proteins that are heavily glycosylated. A proteoglycan unit consists of a core protein (in blue) with one or more covalently attached glycosaminoglycan (GAG) chains (in green) [14]

Proteoglycan core protein attach to the surface of the collagen fibrils with the GAG chains projecting outwards. Because GAGs are negatively charged due to the occurence of sulfate and uronic acid groups, they are highly hydrophilic and therefore implicated in the maintenance of corneal structure and function. Indeed, by attracting and binding water, they produce a gel that renders the tissue resistant to compression.

Cheng and Pinsky 2013 [19] have proposed a model subdividing the PGs into two populations, one coating the collagen fibrils and a second forming bridges between adjacent fibrils. They concluded that electrostatic forces due to the PGs coating play little part in fibril spacing except when fibrils get very close, at which point these PGs serve to prevent fibril fusion.

However, in the interfibrillar fluid, the negatively charged GAG chains interact electrostatically with ions to produce osmotic pressure and lead to swelling forces that push the fibrils apart. The physic behind the osmotic phenomenon is explained in more detail in the Part(III) of the thesis.

It is generally accepted that the fibrils are regularly spaced in equilibrium position, and so an hexagonal lattice structure of fibrils is often assumed as shown in Fig(7). When any fibril undergoes an excursion from its lattice position, the electrostatic forces act to restore the fibril position.

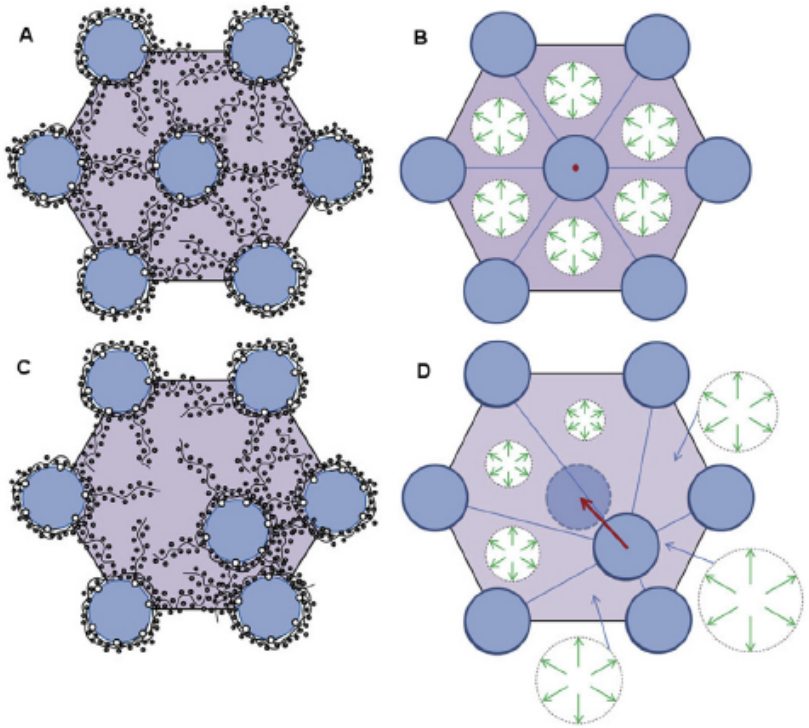

Figure 7: Figure explaining the electrostatic restoring force mechanism maintaining the fibril lattice organization. (c) shows a fibril displaced from its lattice position inducing a surconcentration of negatively charged GAG chains (d) indicates the resulting osmotic pressure in each of the subcells, which is higher where GAG fixed charge density has increased and lower where it has reduced, explaining the restoring force mechanism [19]

The GAG generated osmotic pressure is dependent on the degree of tissue hydration and ionic concentration and gives an important contribution to the bulk stiffness of a lamellae and the stroma at equilibrium [19]. The interfibrillar water is not strongly bound by the PGs and can flow in the highly porous environment so that local changes of water volume can occur as the water redistributes under pressure.

2.2 Biomechanics of the cornea

With this knowledge on corneal microstructure, we can now address the specificity of corneal mechanical behavior, which falls into the category of soft tissue biomechanics.

The features of living tissues differ considerably from materials employed in engineering applications. Soft living tissues are generally characterized by large strains since their microstructure does not allow them to sustain load at low strains. Because they are made of collagen fibers, they usually shows a strain-hardening or locking behavior, meaning that the material stiffness increases with the strain [24]. Since collagen fibers are strongest axially, tissue anisotropy may be expected, with fibers that work only in tension and do not resist compression [25].

Additionally, as a consequence of their high water content, soft biological tissues are almost incompressible, i.e., the volume of the material does not change under loading [26]. Experiments pointed out a dependence of mechanical properties on the hydration level with an increase in hydration causing a decrease in tissue stiffness [16].

Finally, age-related changes in the microstructure of corneal tissue have been observed, including an increase in stromal fibril diameter and interfibrillar cross-linking that lead to the stiffening of corneal tissue with age [27]. To give an order of magnitude, cornea's Young modulus found in the litterature varies between 0.01 and 10 MPa [28], with differences arising between testing methods, age, sex, and stromal thickness of the measured corneas.

Experimental tests on excised strips of corneal tissue provided sets of uniaxial stress-strains curves that show the typical mechanical behavior of the cornea. The stress-strain curve starts with a very low stiffness region, then as the crimped structure straightens and the collagen fibers stretch, the tissue stiffens, displaying a strain-hardening behavior. The stress-strain curve then becomes linear until it begins to fail as rupture occurs as shown in Fig(8).

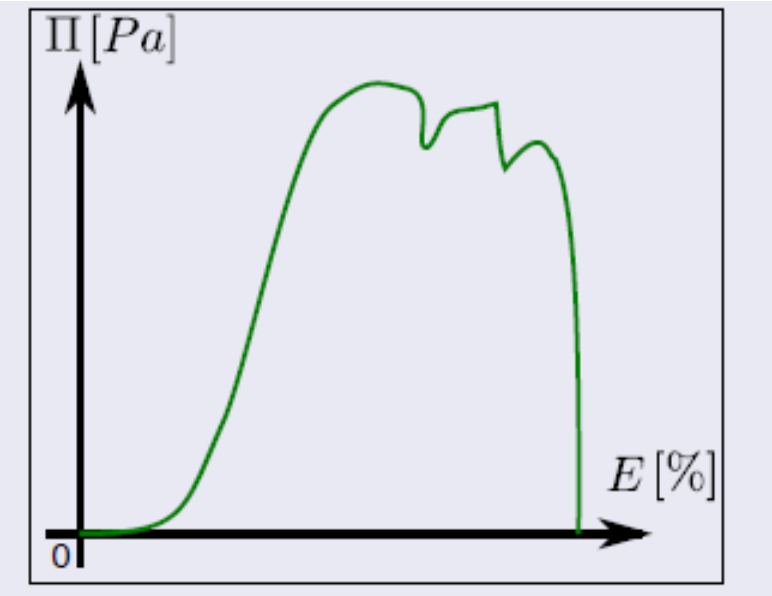

Figure 8: Typical strain-stress curve of biological tissue under quasi-static loading. Once the fibers are in tension, a strain-hardening behavior is observed until the tissue failure. Stress in the vertical axis, Strain in the horizontal axis [29]

Additionally, time-dependency or viscous behavior is observed in soft biological tissue, resulting in a change of stress level under constant strain. This viscosity is commonly associated to the shear interaction of collagen with the matrix of proteoglycans that provides a viscous lubrication between adjacent collagen fibrils. Therefore, under cyclic loading, biological materials may exhibit hysteretic loops, with a residual strain, called slack strain, stabilizing after a few cycles as shown in Fig(9).

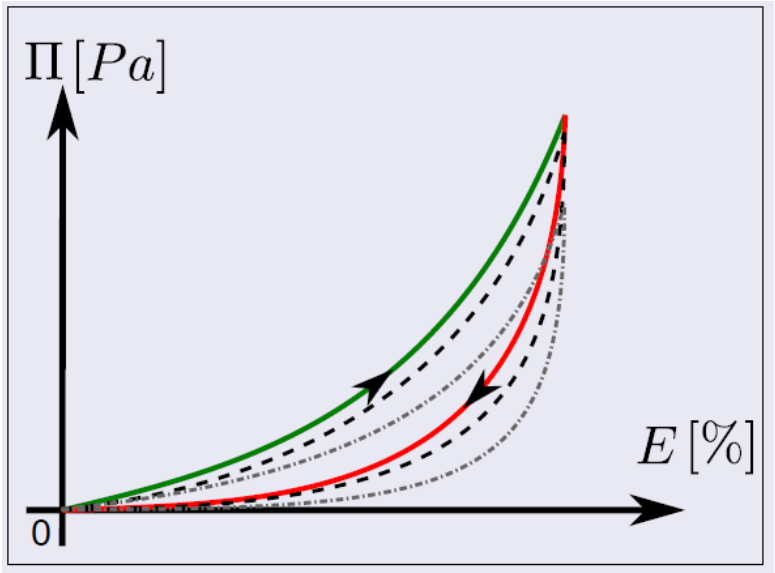

Figure 9: At physiological frequency, the viscous behaviour of the tissue is highlighted by an hysteresis that accomodates through loading cycles. Stress in the vertical axis, Strain in the horizontal axis [29]

After some cycles of loading and unloading, the mechanical response becomes independent of strain rate as expressed by the equation: $\Pi = \Pi(E, \dot{E}) \rightarrow \Pi = \Pi(E)$.

However, preconditioned soft tissues, despite their independence of strain rate, still present hysteresis. Their mechanical response can be modeled as hyperelastic with different behavior at loading and unloading. Fung [30] has called this behavior pseudoelastic.

2.2.1 Intra-ocular pressure (IOP) of the eye

In physiological condition, the internal fluid pressure (Intra Ocular Pressure) of the eye is constantly applied on the corneal inner surface and maintains the tissue in a deformed shape ideal for its optical refraction. This pressure is pushing on the cornea posterior surface with an intensity of 15 to 20 mmHg, corresponding to 2000-2650 Pa, which also creates a pressure gradient useful for nutrients supply from the external fluid into the cornea.

As the specific architecture of collagen fibers in the stroma endows the cornea with orthotropic mechanical properties, the posterior stroma is able to resist the intraocular pressure (IOP) and maintain an adequate corneal curvature as shown in Fig(10). The anterior stroma with its isotropic fiber distribution provides strength in multiple directions, but is less resistant against the loading induced by the intraocular pressure.

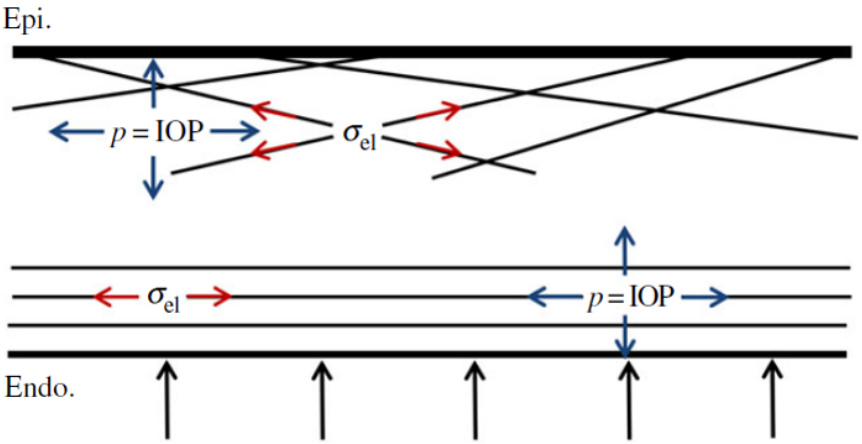

Figure 10: Collagen fibers orientation allows for mechanical strength in several directions depending on their position in the stroma. Black arrows represents the IOP load constantly applied into the cornea in physiological condition [31]

The cornea also demonstrated a nonlinear hyperelastic behavior during inflation experiments [27]. It showed that the inflation pressure vs deformation curve is characterized by an initial low stiffness stage and a final high stiffness stage as shown in Fig(11). During the first pressure increments and up to approximately 15 to 20 mmHg (close to physiological IOP), large deformations were observed in which the tissue stiffness was low. Beyond this pressure level, corneas demonstrated a gradual increase in stiffness that continued up to approximately 60 mmHg, followed by a zone of constant stiffness.

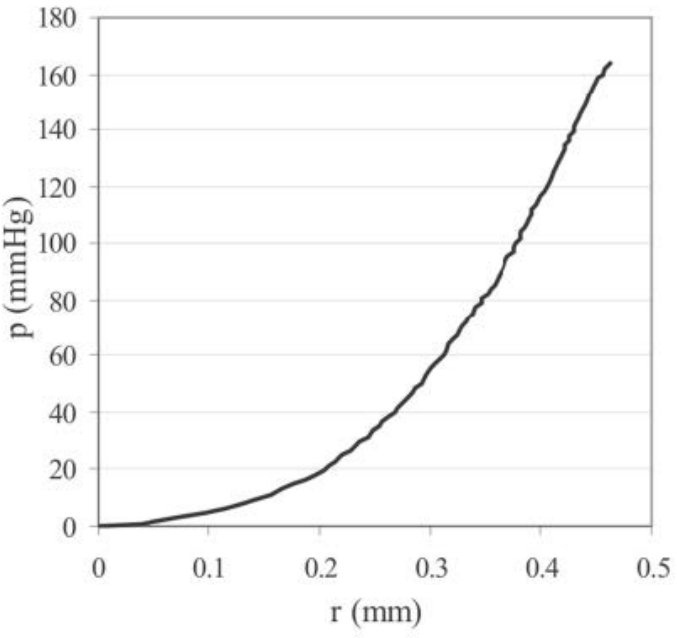

Figure 11: Experimental results of a 53-year-old cornea subjected to inflation pressure at constant rate showing a strain-hardening behavior. Inflation pressure in the vertical axis in mmHg, Vertical displacement in the horizontal axis in mm [27]

The non-linearity of the pressure-deformation curve is similarly due to the presence of reinforcing fibers in the tissue getting progressively stretched through the experiment. The initial

stage corresponds to fibers still crimped and not resisting the pressure, while their progressive stretching causes a progressive increase in tissue stiffness.

2.2.2 Specific mechanical behavior of the different corneal layers

Each corneal layer have a different mechanical behavior and a specific influence on the overall corneal biomechanics. Going into this detail is essential for the study of corneal diseases where each layer of the cornea can be altered and play a distinct role in their physiopathology.

Epithelium biomechanics The epithelium is principally made of cells impermeable to ionic species which gives semipermeable membrane properties to this layer. The direct contribution of the epithelium to corneal mechanics is estimated to be really minor but its semipermeable membrane properties are indirectly related to the control of stromal hydration and swelling and thus participate to the corneal biomechanics. Indeed, specimens with the epithelium intact demonstrated lower average stiffness by 5 to 11% compared to a cornea without epithelium for the same amount of stress [16].

Bowman's membrane biomechanics The Bowman membrane is a 12-µm-thick acellular structure composed of densely packed collagen fibrils that are randomly arranged. The fibrils are continuous with those in the stroma through so called anchoring fibers, explaining why the stiffness of Bowman's membrane is similar as the anterior stroma. The influence of this membrane on the mechanics of the cornea has often been estimated as primordial, however its small thickness and its absence in many other species possibly show that its role may not be as important as considered [32].

Stroma biomechanics The stroma is a laminated fiber composite whose collagen network, rather than the other four corneal layers, largely shapes the solid mechanics behavior of the cornea [10]. Its mechanics display the habitual nonlinear strain-hardening behavior, which is particularly pronounced outside the physiological IOP range of 15-18 mmHg, and maintains the adequate curvature against excessive IOP [15]. Towards the posterior two-thirds of the stroma, lamellae start taking orthogonal orientations, which gives the tissue anisotropic mechanical properties. Of note, it is important to perform material characterization that takes into account the complexity of the stroma mechanical behavior to develop a faithful mechanical model.

Descemet's membrane biomechanics The Descemet's membrane is a mechanical layer which serves as a basement membrane for the endothelium. Although stromal collagen fibers are not continuous with those in Descemet membrane, the membrane adheres tightly to the posterior surface of the corneal stroma. A volume-strain procedure and creep tests conducted by Danielsen [17] found an elastic modulus of 2.57±0.37 kPa for Descemet membrane, while AFM determined an elastic modulus of 50±17.8 kPa.

Endothelium biomechanics The corneal endothelium is a pure cellular layer of 5µm that indirectly and importantly affects the corneal stiffness by regulating its hydration level and fluid pressure. Its primary function is to maintain corneal transparency by maintaining a constant water volume fraction (78%) in the stroma through a leaky barrier and a metabolic pump [14]. Therefore, it is permeable to water, metabolic species and other salt ions. Its impairment can lead to corneal edema such as in Fuch's dystrophy [4].

2.3 Corneal hydration and the endothelial function

The corneal stroma consists of a mixture of solid, fluid and ionic phases. Water is the principal component in the stroma which saturates the collagen solid phase, solvates the ionic phase and accounts for about 78% of the cornea by weight. A small portion of the water is cellular or bound to the stromal collagen, but much of the water is free to flow within the stroma in response to gradients in fluid pressure or by osmosis effects. The most abundant ionic species found in the stroma includes dissolved salts, primarily Na^+ and Cl^-, and metabolites such as K^+ (potassium), $C_3H_5O_3^-$ (lactate ion) and HCO_3^- (bicarbonate ion) [33].

As described in Section(2.1.1), the solid phase comprises a collagen network organized in fibrils of 25 nm in diameter and their associated proteoglycans (PGs), densely packed together to compose lamellae of about 2 µm thick at the upper scale. Stromal proteoglycans have sulfated linear side chains of negatively charged disaccharide units called glycosaminoglycans (GAGs) that are covalently bound to the PG core protein. The negative stromal charge concentration is therefore almost entirely due to GAG ionization [14].

Due to this negative charge concentration from GAGs fixed charges, a positive osmotic pressure difference exists between the stroma and the external aqueous humor so that the stroma will swell by inflow of water from the anterior chamber until the charge concentrations are equalized or the expansion is restrained. Consequently, the greater the concentration of stromal GAGs charges, the higher the osmotic pressure.

In vivo, the cornea fluid swelling pressure (SP) at equilibrium is measured to be on the order of 60 mmHg, a value depending on both the hydraulic pressure, mostly dictated by the intra ocular pressure (IOP), and the osmotic pressure. The hydration level of a cornea is therefore dependent on having a normal endothelial function, but also on having a normal IOP [14] [34] as represented by the equation :

$$Swelling\ Pressure = Hydraulic\ Pressure + Osmotic\ Pressure \tag{1}$$

Therefore, a loss of corneal endothelial function, an IOP much greater than 20 mmHg, or a combination of the two typically results in the clinical appearance of corneal edema (Fig. 16). If the stroma is compressed as occurs with increasing IOP, the swelling pressure will correspondingly increase.

The osmotic pressure of the stroma is modulated by the endothelial active transport processes that pump excess of ions out of the stroma and into the aqueous humour, which can be represented by the equation $Osmotic\ Pressure = P_{free}^{osmo} - P_{active}^{osmo}$ where P_{free}^{osmo} represents the osmotic pressure induced by the presence of negative fixed charges and P_{active}^{osmo} represents the reduction in osmotic pressure from the endothelium active pumping. This active mechanism can be maintained only if the endothelial barrier and the metabolic pump are intact.

Fig(12) presents a schematic of the boundary conditions of the in vivo cornea. The aqueous humour filling the anterior chamber acts as an ionic bath that provides water and solutes to the stroma. By contrast, the anterior stroma is sealed by the epithelial cellular layer, which is nearly impermeable to water and ions but permeable to O_2 and CO_2 [35].

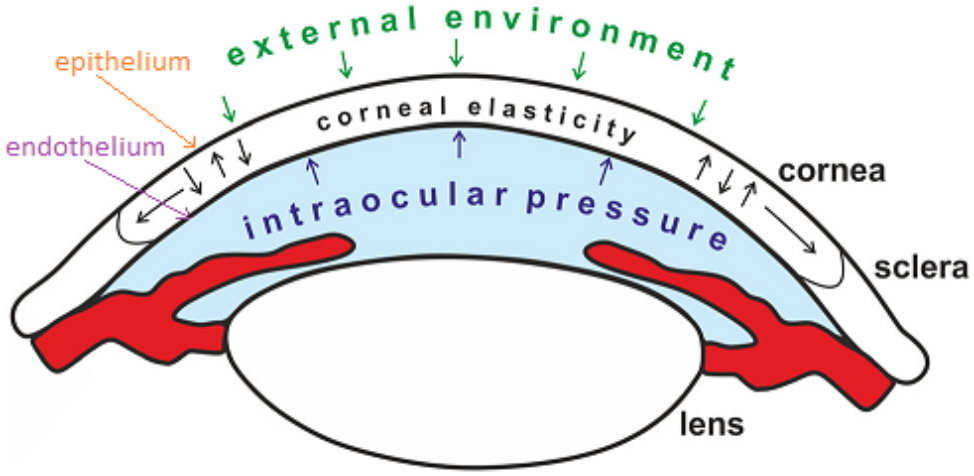

Figure 12: Schematic of the cornea boundary conditions in physiological environment. In blue: the aqueous humor (internal fluid in the eye), applying the intra-ocular pressure and acting as a ionic and nutrient bath that diffuses into the cornea [36]

Corneal endothelium function and impairment

The corneal endothelium is a 4 µm thin cellular monolayer located on the posterior surface of the cornea, with a high metabolic activity. It is composed of approximately 500 000 cells covering a surface area of 250 μm^2 (Fig. 13A) that form a polygonal mosaic [14].

The primary function of the corneal endothelium is to maintain corneal transparency and hydration through a leaky barrier and metabolic pump function. In that objective, it is permeable to water, metabolic species, including glucose and lactate ion, and other salt ions. The pump-leak hypothesis suggests that an equilibrium is required between the amount of passive fluid flow into the cornea and the active flux used to pump out excess for maintenance of relative dehydration of the corneal stroma. For a normal cornea, hydration is maintained at 78% water by weight.

The barrier function of the corneal endothelium is dependent upon a sufficient number of endothelial cells to cover the posterior surface of the cornea (Fig. 13A) but also of the intact tight and gap junctions between the endothelial cells (Fig. 13B,C), resulting in a barrier to the aqueous humor flow. In healthy human corneas, the tight junctions prevent most of the fluid flow from the aqueous humor but it does still allow moderate diffusion of small nutrients, water, and other metabolites to cross into the stroma through the 10 nm wide intercellular spaces. Leakiness of the endothelium is essential as most nutrients for all layers of the cornea come from the aqueous humor.

Additionally, several studies demonstrated that active transporters, located primarily in the basolateral cell membrane, transport ions, principally sodium (Na^+) and bicarbonate (HCO_3^-), out of the stroma and into the aqueous humor (Fig. 13C). An osmotic gradient is thus created by the endothelium and water is osmotically drawn from the stroma into the aqueous humor. This osmotic gradient can be maintained only if the endothelial barrier and the metabolic pump are intact.

Because the negative charges on corneal proteoglycan GAG side-chains are just over one-quarter saturated or bound with Na^+, the remaining unbound proportion is still available to bind more Na^+ and absorb more water if given the opportunity. Thus the important role of

the endothelial barrier and pump function to maintain the water volume at a healthy level.

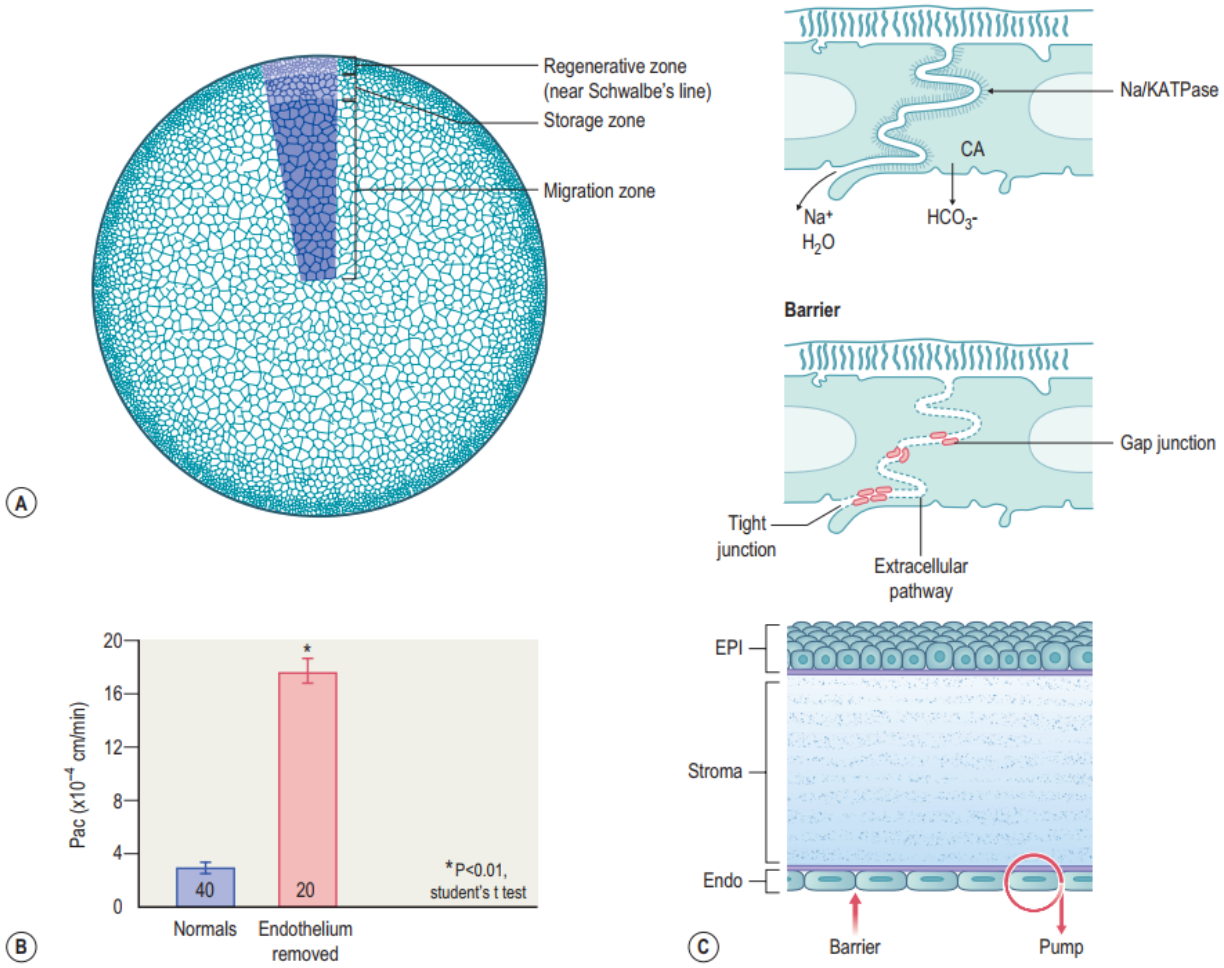

Figure 13: (A) The barrier function of corneal endothelium depends on endothelial cells covering the posterior corneal surface without gaps (B) the corneal permeability to carboxyfluorescein (2.26×10^{-4} cm/min) compared to that without endothelium (12.85×10^{-4} cm/min), which resulted in a six-fold increase in permeability (C) Gap and tight junctions are shown. When the leak rate equals the metabolic pump rate, the corneal stroma is 78 percent hydrated and the corneal thickness and transparency are steady [14]

At birth, the central endothelial cell density (ECD) of the cornea is around 5000 cells/mm^2, then a decline in central ECD with age occurs that typically involves two phases: a fast and a slow component. During the fast component, the central ECD decreases exponentially to about 3500 cells/mm^2 by age 5 and 3000 cells/mm^2 by age 14–20 (Fig. 14). Thereafter, a slow component occurs where central ECD decreases to a linear steady rate of 0.3–0.6 percent per year, resulting in a 50% decrease central ECDs around 2500 cells/mm^2 in late adulthood [4] [14] [37] as shown in (Fig. 14).

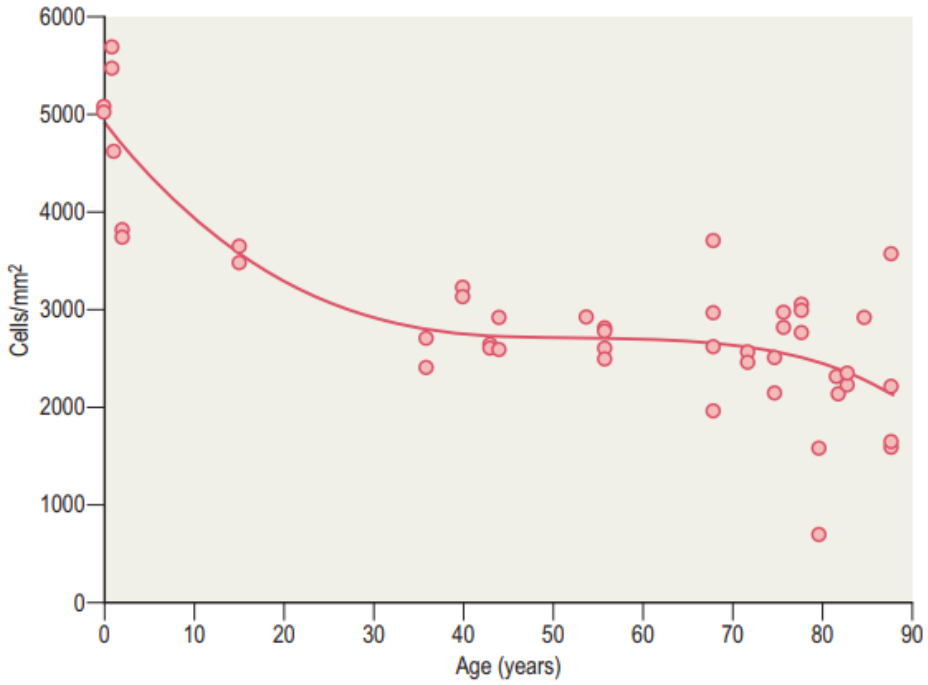

Figure 14: Scatterplot with best fit curve showing the average central corneal endothelial cell density (ECD) for healthy eyes of different ages [14]

Because the corneal endothelium maintains its continuity by migration and expansion of surviving cells to cover a larger surface area, it appears that the 50% decrease from birth to death in normal subjects does not cause corneal disease or pathology. Corneal over-hydration typically doesn't occur until central ECDs reach 500 cells/mm^2 (Fig. 15), which is a 90 percent decrease in central ECD from birth or an 80 percent decrease from healthy adulthood levels [14].

When central ECDs are between 2000 and 750 cells/mm^2, endothelial permeability does gradually increase but it seems that compensatory metabolic pump mechanisms prevent corneal edema from occurring up to a certain degree. This happens either by increasing the metabolic activity of pump sites, or by increasing the total number and density of pump sites on the lateral membranes of endothelial cells. A similar phenomenon occurs in the proximal tubule of the human kidney to adjust for an increased salt load [14].

The point at which compensatory mechanisms fail is when the central ECD reaches approximately 500 cells/mm^2 or less. At this point, the permeability has increased to a point where the metabolic pump fails to balance the leak and corneal edema results. This is because endothelial cells are spread so thin that they do not have enough room on their cell membranes for more pump sites, with all the existing pump sites maximally active [4] [14] .

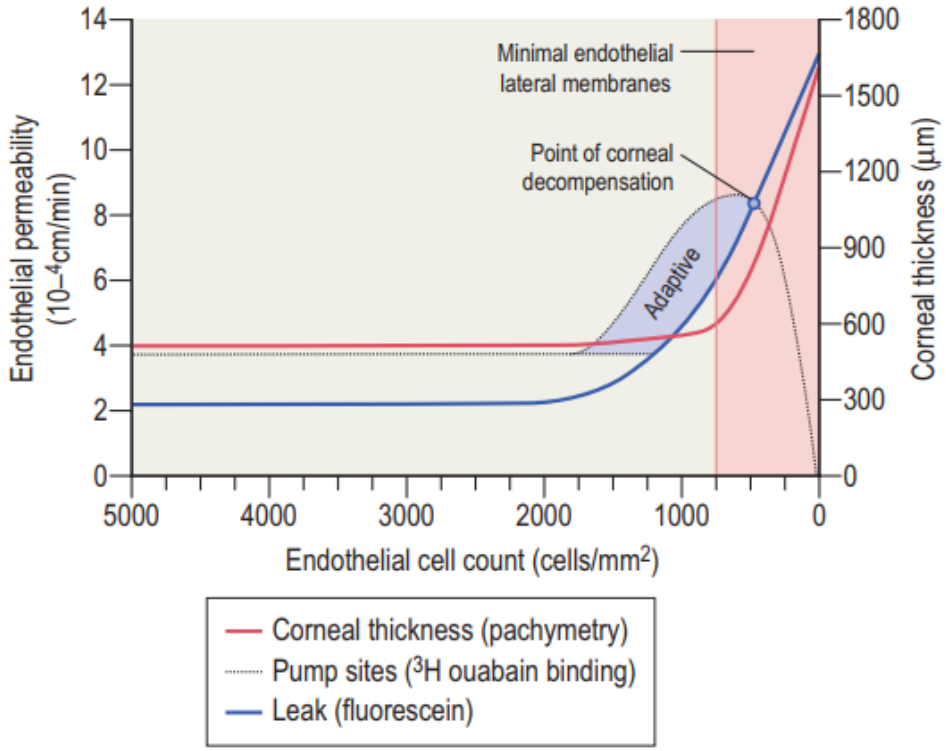

Figure 15: This figure shows the relationship between central Endothelial Cell Density, barrier function, metabolic pump sites and tissue thickness. In the normal healthy state (5000–2000 cells/mm^2), cellular pump sites are not maximally used. With increased permeability (2000–750 cells/mm^2), an adaptive phase happens in which the endothelial cells can maximally use all their pump sites or can make more pump sites to compensate the leak. When endothelial cell pump site adaptations intersect with permeability (500 cells/mm^2) is typically when corneal over-hydration occurs [14]

Corneal edema types Corneal edema refers to a cornea that is more hydrated than its normal physiological state of 78% water. Edema is important for clinicians because it affects the function of the corneal stroma and the epithelium. With minor ($< 5\%$) hydration changes, the corneal thickness changes with almost no effect on the refractive, transparency, and mechanical functions of the cornea. With more than 5% over-hydration, the cornea begins to scatter significant amounts of light and loses its transparency due to an increase in the interfibrillar distance between collagen fibrils. Some loss of refractive function may also occur if the epithelial surface becomes too irregular.

While epithelial and stromal edema commonly co-exist together, there are two notable exceptions. Because the epithelium has much weaker cohesive and tensile strengths than the corneal stroma, its state of hydration is mainly dictated by the IOP levels. This results in the transmission of stromal edema to the epithelial surface in cases of high IOP. Therefore, if IOP is $\geq$ 60 mmHg with normal endothelial barrier and metabolic pump function, epithelial edema usually occurs by itself. In comparison, if endothelial cell dysfunction and hypotony (IOP $\approx$0 mmHg) occur together, then stromal edema occurs alone [14] as shown in (Fig. 16).

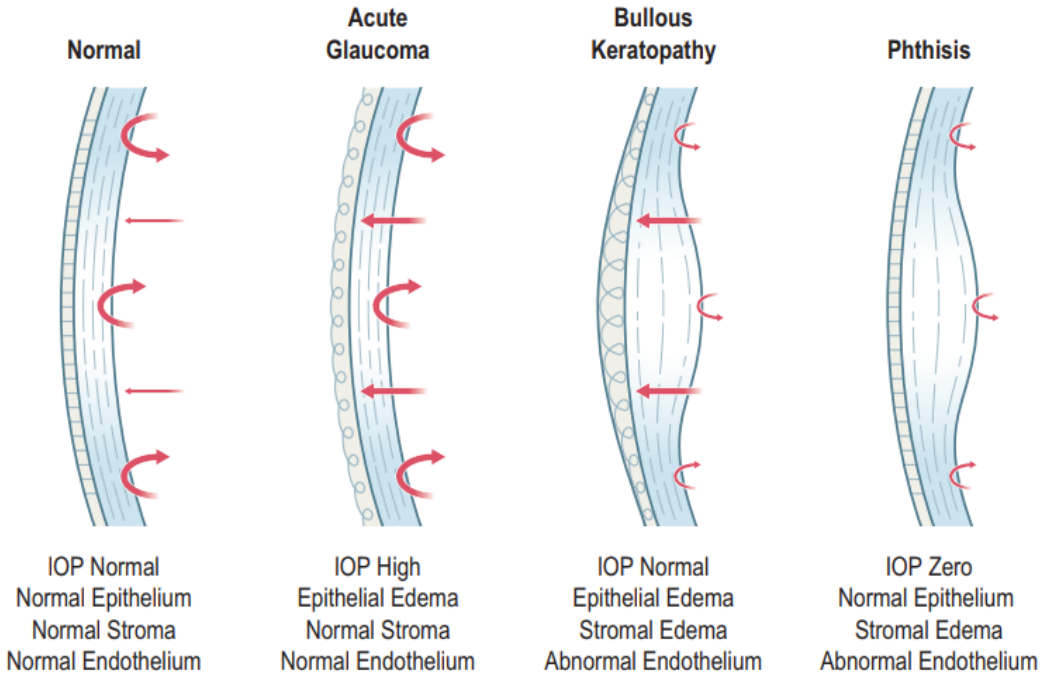

Figure 16: Figure showing the balance between stromal swelling pressure, endothelial function and intraocular pressure. If endothelial cell pump function fails and IOP remains at normal level, both stromal and epithelial edema occur (bullous keratopathy). If the IOP increases above the swelling pressure of the stroma with a normal endothelium, epithelial edema can occur by itself (acute glaucoma); only when IOP is around zero and the endothelium functions abnormally, does stromal edema occur alone (phthisis) [14]

2.4 Geometry of the cornea

To develop an accurate model of the cornea, it is essential to describe its precise geometry. Typically, the human cornea is regarded as a spherical cap with variable thickness as shown in Fig(17). The thickness of the in vivo cornea is roughly 0.52 mm at its center and 0.65 mm in its periphery, but varies between persons. Its radius, corresponding to the distance from the center to the cornea periphery, is over 6 mm.

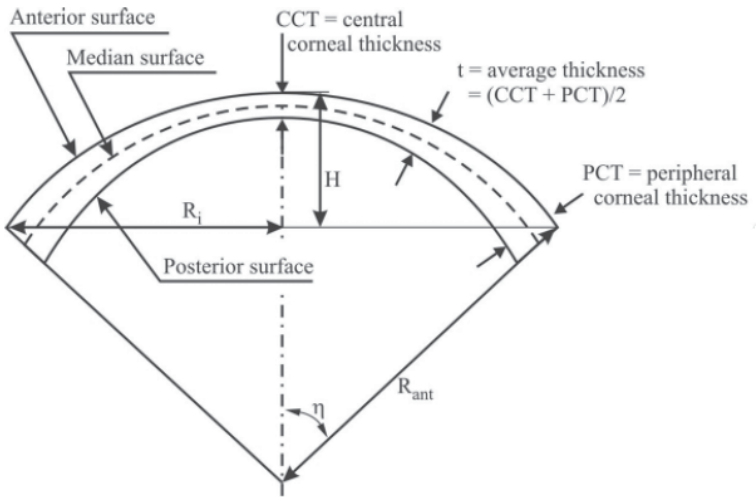

Figure 17: Cross-section of the corneal geometry with its main metrics. Dimensions are patient-specific [27]

Due to the fast variation of the corneal curvature in proximity of its periphery, an exact definition of the shape of the internal and external surfaces of the cornea is complicated. It is usually convenient to distinguish two regions: the optical zone, which is the central circular part of 3 mm radius, and the peripheral annular zone called limbus.

Then, several parameters can be determined to accurately describe its shape. It comprises the horizontal and vertical diameters, anterior and posterior curvature, and central and peripheral thicknesses. These parameters are patient specific and thus could vary with age, gender, ethnicity, refractive status and anthropometric factors [38].

2.4.1 Corneal diameter

The corneal diameter is the border-to-border distance. It is described by two distances: the horizontal corneal diameter with HVID (horizontal visible iris diameter) and vertical corneal diameter with VVID (vertical visible iris diameter). In adults the average horizontal diameter of the cornea is 12mm and the vertical diameter is 11mm as shown in Fig(18).

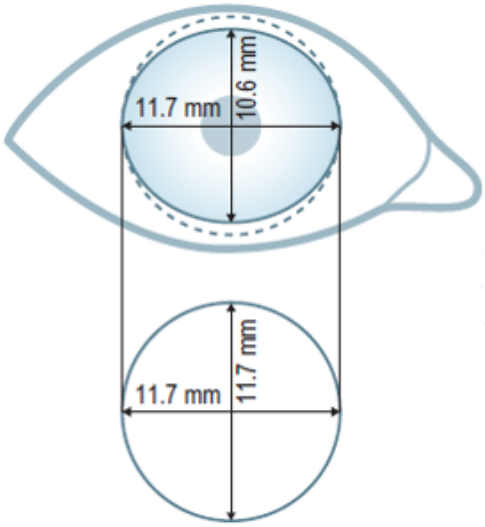

Figure 18: Average dimension of corneal horizontal and vertical diameters, showing that the cornea is slightly elliptical [14]

2.4.2 Corneal curvature

Because cross sections of the internal and external corneal surfaces are characterized by asphericity, the external surface is well described by an ellipsoid with horizontal maximum axis, while the internal surface is more spherical [10].

Anterior surface The anterior corneal curvature is an important measurements used to characterize optical properties of the cornea and for keratoconus diagnosis and management. Measurement of anterior curvature can be made with a variety of instruments, such as a keratometer and topographer. The average radius of the anterior corneal surface is 7.79 ± 0.27 mm.

Posterior surface The posterior surface curvature is not completely related to the anterior surface shape, with an asphericity that varies more significantly between meridians. The average radius of the posterior corneal surface is 6.53 ± 0.25 mm [39].

2.4.3 In vivo dimensions of the author's cornea

To construct the model geometry, we need to collect dimensions of a cornea in physiological configuration (in vivo). For that, we used the dimension of the author's cornea measured in vivo with pachymetry, tomography and topography examinations performed at the Regional Hospital Center of Metz-Thionville. The author provided written informed consent to undergo the ophthalmological measurements and this study was approved by the Ethics Committee of the French Society of Ophthalmology.

The in vivo dimensions measured corresponding to the author's cornea deformed by the intra-ocular pressure were: central corneal thickness=500 µm, peripheral corneal thickness=620µm, corneal height=3.4 mm, horizontal diameter=11.8 mm, and vertical diameter=10.7 mm as shown in Fig(19).

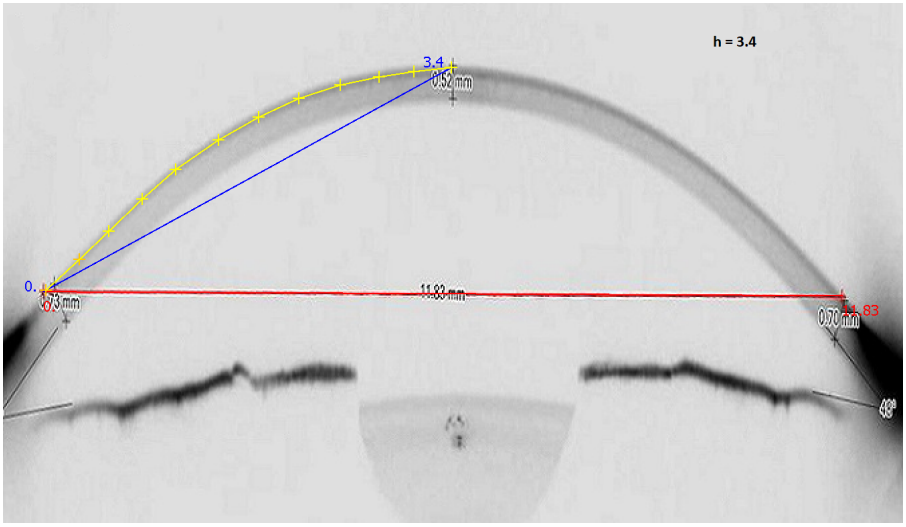

(a) Keratoscopy

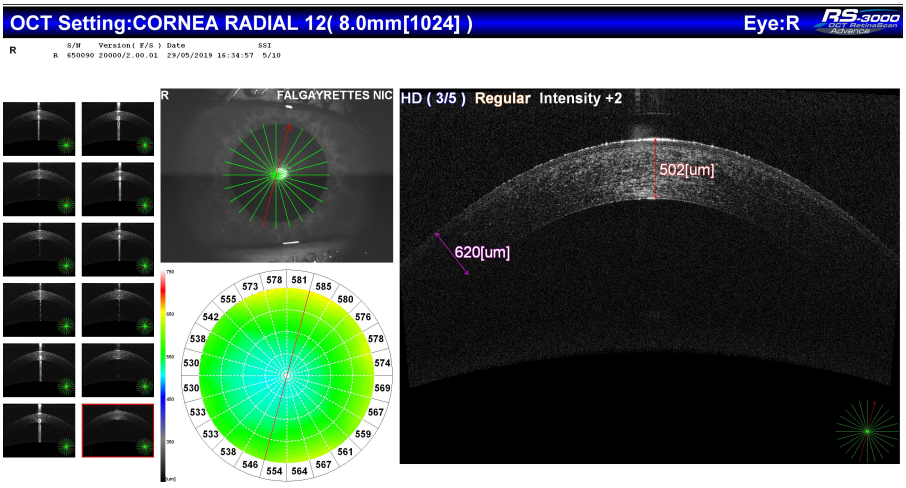

(b) Tomography

Figure 19: Corneal mensuration from videokeratoscopy and tomography examinations performed at Mercy's hospital in Metz, showing corneal diameters, curvature and thicknesses. Dimensions are the one of the author's cornea

The epithelial thickness was measured at 45µm on the tomography. The dimensions of the Bowman's membrane, Descemet's membrane and endothelium layers were defined based on anatomical dimensions found in litterature [14] because they were too small to be accurately measured from these experiments.

The central corneal thickness was measured at 500 µm and three zones corresponding to the anterior, middle and posterior stroma were distinguished as explained in Part(II) of the thesis. The dimension of the 3 stromal parts were based on SHG imaging and analysis performed in previous articles [31] [40]. Dimensions for each layers are given in Table(1). These dimensions corresponds to the center of the author's cornea in vivo.

Corneal layer	Thickness
Epithelium	45 µm
Bowman's membrane	10 µm
Anterior stroma	105 µm
Middle stroma	150 µm
Posterior stroma	173 µm
Descemet and Endothelium	17 µm

Table 1: Thickness of the corneal layers measured in vivo on the author's cornea. Values are subjected to measurement variability related to medical devices precision

3 State of the art in corneal modeling

An important characteristic of soft biological tissue is the presence of microstructural collagen reinforcements that call for the development of advanced material models. A faithful material model should therefore describe the fiber structure of the tissue and how it affects its macro mechanical properties, especially with the need to study diseases involving compromised tissue microstructure.

Modeling the cornea represents a challenge due to its multiscale and multiphasic properties. Indeed, fibrils are packed together to form large collagen fibers (lamellae) that are several micrometers thick. These lamellae are distributed throughout the tissue and contribute to its macroscopic mechanical behavior in their specific direction, which need to be defined. Additionally, like other soft tissues, the cornea is a multiphasic mixture made of interacting fluid, solid and ionic phases [20], which results in a complex volumetric behavior.

Thus, a choice must often be made between the development of a multiscale model that directly describes the fibers and other constituents at a lower scale, or a macroscopic model with specific contributions that accounts for the strain hardening behavior of fibers and a volumetric contribution that account for the presence of solvent and solutes. The challenge is to choose a method that is both sufficiently advanced to describe the corneal microstructure and control the mechanical parameters at this scale, but also sufficiently accessible to address the medical problematic in the time given.

3.1 Continuum mechanics and large deformation framework

We start by introducing the mathematical theory of finite elasticity. This theory represents a development of non-linear continuum mechanics and is necessary to model the mechanics of soft tissue undergoing large strain. It introduces the different tensors and quantities needed in our study, starting with the kinematic of a continuum.

Kinematic The different configurations and their coordinate systems are linked by the transformation gradient $\boldsymbol{F} = \frac{\partial \boldsymbol{x}}{\partial \boldsymbol{X}}$ which represents the transition from the reference coordinate system denoted by $\boldsymbol{X}$ to the current one denoted by $\boldsymbol{x}$, with $\boldsymbol{u}$ is the displacement vector defined as $\boldsymbol{u} = \boldsymbol{x} - \boldsymbol{X}$.

The transformation gradient tensor allows defining the deformation or strain tensors such as:

- the right Cauchy-Green tensor giving the dilatations in the reference configuration:

$$\boldsymbol{C} = \boldsymbol{F}^T.\boldsymbol{F} \tag{2}$$

- the Green-Lagrange tensor is defined in the reference configuration by:

$$\boldsymbol{E} = \frac{1}{2}(\boldsymbol{C} - \boldsymbol{I}) \tag{3}$$

As the strain tensor components values depend on the basis in which they are written, some use the strain invariants to express them. These invariants are defined for isotropic media as:

$$I_1 = tr(\boldsymbol{C}) \tag{4}$$

$$I_2 = \frac{1}{2}[tr(\boldsymbol{C})^2 - tr(\boldsymbol{C}^2)] \tag{5}$$

$$I_3 = det(\boldsymbol{C}) \tag{6}$$

For anisotropic media, it is necessary to define material direction with the use of an orientation tensor (or structural tensor). An unit vector $\boldsymbol{a}^{(0i)}$ is introduced to describe the initial orientation of the i^{th} fiber. An initial orientation tensor is defined as $\boldsymbol{A}^{(i)} = \boldsymbol{a}^{(0i)} \otimes \boldsymbol{a}^{(0i)}$. During deformation process, each material direction is transformed into $\boldsymbol{a}^{(i)} = \boldsymbol{F}\boldsymbol{a}^{(0i)}$ which it represents the orientation of the fiber in the current state.

The invariants for anisotropic media are defined as:

$$I_4^{(i)} = tr(\boldsymbol{C}\boldsymbol{A}^{(i)}) = \boldsymbol{a}^{(0i)} \cdot \boldsymbol{C}\boldsymbol{a}^{(0i)} \tag{7}$$

$$I_5^{(i)} = tr(\boldsymbol{C}^2\boldsymbol{A}^{(i)}) = \boldsymbol{a}^{(0i)} \cdot \boldsymbol{C}^2\boldsymbol{a}^{(0i)} \tag{8}$$

In the literature, in the case of two fiber directions (1) and (2), a notation I_4 and I_6 is often used instead of $I_4^{(1)}$ and $I_4^{(2)}$ (or I_5 and I_7 instead of $I_5^{(1)}$ and $I_5^{(2)}$).

These invariants depend only on one direction but it is possible to take into account the interaction between the different directions, by introducing a coupling between (i) and (j) by means of two other invariants:

$$I_8^{(i,j)} = (\boldsymbol{a}^{(0i)} \cdot \boldsymbol{a}^{(0j)})(\boldsymbol{a}^{(0i)} \cdot \boldsymbol{C}\boldsymbol{a}^{(0j)}) \tag{9}$$

$$I_9^{(i,j)} = (\boldsymbol{a}^{(0i)} \cdot \boldsymbol{a}^{(0j)})^2 \tag{10}$$

Thermodynamic potentials In the framework of elasticity, the thermodynamic function of entropy s, internal energy u and Helmholtz free energy ψ as well as the second Piola Kirchhoff stress tensor $\boldsymbol{S}$ are only function of the temperature Θ and the Green Lagrange strain tensor $\boldsymbol{E}$.

$$\boldsymbol{S} = \boldsymbol{S}(\boldsymbol{E}, \Theta) \quad , \quad \psi = \psi(\boldsymbol{E}, \Theta) \quad , \quad s = s(\boldsymbol{E}, \Theta) \tag{11}$$

As the Helmholtz free energy ψ is only function of Θ and $\boldsymbol{E}$, its derivative can be written:

$$\dot{\psi}(\boldsymbol{E}, \Theta) = \frac{d\psi(\boldsymbol{E}, \Theta)}{dt} = \frac{\partial \psi}{\partial \boldsymbol{E}} : \frac{\partial \boldsymbol{E}}{\partial t} + \frac{\partial \psi}{\partial \Theta}\frac{\partial \Theta}{\partial t} = \frac{\partial \psi}{\partial \boldsymbol{E}} : \dot{\boldsymbol{E}} + \frac{\partial \psi}{\partial \Theta}\dot{\Theta} \tag{12}$$

In the case of a reversible transformation such as an elastic loading, the Clausius Duhem equation has to be equal to zero as the intrinsic volume dissipation is null. Taking into account the previous development it gives:

$$(\boldsymbol{S} - \frac{\partial \psi}{\partial \boldsymbol{E}}) : \dot{\boldsymbol{E}} - (\frac{\partial \psi}{\partial \Theta} + \rho_0 s)\dot{\Theta} - \frac{\boldsymbol{Q}}{\Theta} \cdot \boldsymbol{grad}(\Theta) = 0 \tag{13}$$

This equality has to remain true independently of the temperature variation $\dot{\Theta}$ and of the strain rate $\dot{\boldsymbol{E}}$, therefore it comes:

$$\boldsymbol{S} = \frac{\partial \psi}{\partial \boldsymbol{E}} \quad and \quad s = -\frac{1}{\rho_0}\frac{\partial \psi}{\partial \Theta} \tag{14}$$

Those two equations define the laws of thermoelasticity. The expression of the second Piola Kirchhoff tensor $\boldsymbol{S}$ leads to define a constitutive law based on expressions of the Helmholtz free energy ψ also known as the strain energy density potential W.

Constitutive behaviour As constitutive laws have an intrinsic tensor expression, they have to be invariant regarding changes of basis. Those laws are therefore often defined as function of strain tensors' invariants from strain energy density function like:

$$W = f(I_1, I_2, I_3) \tag{15}$$

With the invariants given in terms of principal stretches:

$$I_1 = \lambda_1^2 + \lambda_2^2 + \lambda_3^2 \tag{16}$$
$$I_2 = \lambda_1^2\lambda_2^2 + \lambda_2^2\lambda_3^2 + \lambda_3^2\lambda_1^2 \tag{17}$$
$$I_3 = \lambda_1^2\lambda_2^2\lambda_3^2 \tag{18}$$

With $J = det(\boldsymbol{F}) = \lambda_1\lambda_2\lambda_3 = 1$ for an incompressible material meaning that its volume does not change under any applied deformation.

Hyperelastic constitutive models used for biological tissue materials often split the local deformation into volume-changing (volumetric) and volume-preserving (isochoric or deviatoric) parts to overcome numerical issues connected to incompressibility. Accordingly, the deformation gradient $\boldsymbol{F}$ is decomposed as follows:

$$\boldsymbol{F} = (J^{\frac{1}{3}}\boldsymbol{I})\overline{\boldsymbol{F}} \tag{19}$$

The term in parenthesis represents the volumetric portion of the deformation gradient and $\overline{\boldsymbol{F}}$ represents its isochoric portion, such that $det(\overline{\boldsymbol{F}}) = 1$ at all times.

The reduced invariants of $\overline{\boldsymbol{C}}$ are used for the isochoric counterparts of I_i, with the relationship $J = I_3^{1/2}$:

$$\overline{I}_1 = J^{-2/3} I_1 = I_1 I_3^{-1/3} \tag{20}$$

$$\overline{I}_2 = I_2 I_3^{-2/3} \tag{21}$$

$$\overline{I}_4 = J^{-2/3} I_4 \tag{22}$$

$$\overline{I}_6 = J^{-2/3} I_6 \tag{23}$$

Which leads to the expression for the hydrostatic work term $W_H = D_1(J-1)^2$ where $D_1 = K/2$, with K the bulk modulus of the material.

Stress measures For a general hyperelastic material with free energy ψ the stress tensors are given by:

- The second Piola Kirchhoff tensor, symmetric and Lagrangian, has been defined by:

$$\boldsymbol{S} = \frac{\partial W}{\boldsymbol{E}} \tag{24}$$

- The Cauchy stress tensor, symmetric and Eulerian, has been defined by:

$$\boldsymbol{\sigma} = \frac{1}{J} \boldsymbol{F} \frac{\partial W}{\partial \boldsymbol{E}} \boldsymbol{F}^T \tag{25}$$

Relations between the two stress formulation can be expressed as:

$$\boldsymbol{\sigma} = \frac{1}{J} \boldsymbol{F} \boldsymbol{S} \boldsymbol{F}^T \tag{26}$$

$$\boldsymbol{S} = J \boldsymbol{F}^{-1} \boldsymbol{\sigma} \boldsymbol{F}^{-T} \tag{27}$$

3.2 Phenomenological modeling

The history of finite elasticity can be traced back to the works of Cauchy, Green, Piola and others but the modern development of the subject starts with the seminal works of R.S. Rivlin, which have been compiled by Barenblatt and Joseph (1997) [41]. The contributions to the theory of elastic materials exhibiting large strain phenomena are too numerous to be cited individually, but exhaustive reviews of these developments are given in survey articles, with the most recent surveys being [42] [43] [44] [45] .

Most of the constitutive equation used to model soft tissue biomechanics before the year 2000 were phenomenological in nature [30][46][47]. As such, they considered average properties and could not predict the microscopic response of fibers since their parameters were not linked to the tissue microstructure. These earlier modeling studies simplified the mechanical behavior as a linear-elastic pattern, justified by the assumption that common loads on biological tissue create low stress levels. However, the influence of fibers at large deformations should be described in our study on the cornea.

Roy et al. [9] modeled the cornea as an isotropic and hyperelastic material using the Mooney-Rivlin model as shown in Eq(28) where W is the strain energy density function and C_{10} and C_{20} are material parameters. They fitted stress vs. strain data derived from ex vivo testing of corneas to a reduced polynomial material model. Therefore, their model was composed only of the isotropic contribution, leaving the fiber contribution not addressed, which does not allow to describe the meridional differences in geometry or in material properties.

$$W = C_{10}(I_1 - 3) + C_{20}(I_1 - 3)^2 \tag{28}$$

To account for the presence of fiber, Elsheikh [15] developed a simple fitted material model from the experimental data reported by [48] with an exponential term that describes the strain hardening behavior of fibers. They showed that the behavior of corneas of 50 years old could be described with the equations $\sigma_{MPa} = 0.0070(e^{59\times\epsilon} - 1)$ under inflation loading and $\sigma_{MPa} = 0.00004(e^{359.2\times\epsilon} - 1)$ under unloading, where σ and ϵ were stress and strain, respectively. Obviously, this behavior law was limited to the particular loading studied and could not be used in a versatile analysis.

To account for a load-independent contribution of fibers, they used another method with a linear-elastic model having a direction dependent Young's modulus E. They considered fibril direction to have 10 times the stiffness of the extracellular matrix in the perpendicular direction, wich did not describe the strain hardening behavior of fibers. Therefore, E_{fibril} and E_{matrix} were given the values of 1.018 and 0.102 MPa, respectively. Next we shall see how to account for both non-linear strain hardening and fiber contribution into a single model.

3.3 The Holzapfel-Gasser-Ogden model

With the introduction in the 2000s of the Holzapfel-Gasser-Ogden (HGO) model [49] describing anisotropic hyperelastic behavior of fiber reinforced materials, the modeling of biological soft tissues made a great leap forward. This structure motivated mechanistic model, as opposed to phenomenological ones, employs an invariant based approach which includes the contribution of two anisotropic 2D families of collagen fibers.

Parameters of such structure motivated macroscopic models find an interpretation at the lower scale through experimental validation but do not describe directly the mechanical properties of fibrils as in a multiscale framework. However through extensive testing and validation over a variety of soft biological tissues, the use of this approach may be equivalent to a multiscale model whose homogenization constraints also carries approximations.

An advancement of the HGO model was later made by Gasser et al. [50] to include a fiber dispersion parameter and allows a more realistic description of fibers distribution. Multiple studies show that finite element models based on the Holzapfel-Gasser-Ogden (HGO) law accurately replicate in vivo corneal biomechanical behavior in response to high IOP, excessive fluid influx [20], uniaxial tension, torsional shear [51], indentation, dynamic air-puff loading [52], LASIK surgery for high myopia, corneal transplantation, and refractive surgery [53] [54].

In this model, the overall tissue response is described by the total strain energy density $W(\boldsymbol{E})$ as a function of the Lagrangian strain tensor $\boldsymbol{E}$. Each fiber is assumed hyperelastic, with its response described by the strain energy function $\Psi(E_n)$, where E_n is the normal strain along the fiber direction.

The local deformation is split into volume-changing (volumetric) and volume-preserving (isochoric) parts and the total strain energy density $W(\boldsymbol{E})$ relates to the strain invariants I as:

$$W(\bar{I}_1, \bar{I}_2, I_3, \bar{I}_4, \bar{I}_6) = W_{vol}(I_3) + \bar{W}_{iso}(\bar{I}_1, \bar{I}_2) + \bar{W}_{aniso}(\bar{I}_1, \bar{I}_4, \bar{I}_6) \tag{29}$$

$W_{vol}(I_3)$ accounts for the volumetric response of the material. The isochoric strain-energy function $\bar{W}_{iso}$ describes the isotropic ground substance and $\bar{W}_{aniso}$ the isochoric anisotropic contribution describes two embedded orthogonal collagen fiber families with the same mechanical properties and dispersion; specifically, it addresses the strengthening caused by their stretching at high deformations. The arguments of the two isochoric contributions are the invariants $\bar{I}_1$, $\bar{I}_2$, $\bar{I}_4$, $\bar{I}_6$ of $\bar{C}$ and the argument of the volumetric contribution is $I_3 = det(C)$.

Volumetric contribution: This accounts for the volumetric response of the material. Due to high water content, soft biological tissues are assumed to be largely incompressible ($I_3 = 1$) and W_{vol} is treated as a penalty function enforcing the incompressibility in the form:

$$W_{vol}(I_3) = \frac{1}{D}(\frac{I_3^2 - 1}{2} - ln(I_3)) \tag{30}$$

where $\frac{1}{D}$ is a positive parameter independent of the deformation. This formulation allows relaxation of the incompressibility condition, which inserts slight unphysical compressibility into the model so that a stable solution is achieved. With the parameter $D = 0.5$, the equivalent Poisson's ratio of the material in linear elasticity is $\nu = 0.497$ that is close to a completely incompressible material.

Isotropic contribution: The isotropic term $\bar{W}_{iso}$ describes the behavior of the isotropic stromal components, namely, the ground substance and the 60% of total collagen fibers that are isotropically dispersed. It is modelled according to the incompressible isochoric Neo-Hookean strain energy function:

$$\bar{W}_{iso}(\bar{I}_1) = \mu(\bar{I}_1 - 3) \tag{31}$$

where $\mu > 0$ is the shear modulus of the material and describes its mechanical behavior under small deformation.

Anisotropic contribution: The anisotropic term $\bar{W}_{aniso}$ addresses the contribution of the two orthogonal collagen fiber families (40% of total collagen), which make the material anisotropy. The exponential function describes fiber strengthening under large stress.

$$\bar{W}_{aniso}(\bar{I}_1, \bar{I}_4, \bar{I}_6) = \frac{k_1}{2k_2} \sum_{i=4,6} e^{[k_2 < \bar{E}_i >^2] - 1} \tag{32}$$

The arguments are the first invariant $\bar{I}_1$ and the two modified invariants $\bar{I}_4$ and $\bar{I}_6$ of $\bar{C}$, which are expressed as: $\bar{I}_1 = \bar{C}_{II}$, $\bar{I}_4 = a_K^{(04)} \bar{C}_{KJ} a_J^{(04)}$, and $\bar{I}_6 = a_K^{(06)} \bar{C}_{KJ} a_J^{(06)}$. The material constant k_1 is a positive fiber stiffness coefficient (MPa) that describes the slope of fiber-stretching behavior. The k_2 constant is a dimensionless number used to adjust the stretching level required to engage the fibers.

The strain-like quantity $\bar{E}_i = \kappa(\bar{I}_1 - 3) + (1 - 3\kappa)(\bar{I}_i - 1)$ characterizes fiber family deformation by introducing the anisotropic pseudo-invariants $\bar{I}_1$, which are the squared stretch in the mean direction $a_K^{(0i)}$ for the i-th family of fibers: $\bar{I}_i = a_K^{(0i)} \otimes a_K^{(0i)} : \bar{C}$. In the $\bar{E}_i$ equation, the parameter $\kappa \in (0 \leq \kappa \leq \frac{1}{3})$ describes the dispersion of fibers around a mean direction. When $\kappa = 0$, the fibers are perfectly aligned (no dispersion). When $\kappa = 1/3$, the fibers are randomly distributed and the material becomes isotropic. The model assumes that fibers are dispersed

with rotational symmetry around a mean preferred direction $a_K^{(0i)}$ with $\rho(\theta)$ being the orientation density function that characterizes this distribution. Therefore,

$$\kappa = \frac{1}{4}\int_0^{\pi} \rho(\theta) sin^3\theta d\theta \tag{33}$$

describes the degree of anisotropy and represents fiber distribution in an integral sense. For perfectly aligned fibers (i.e. $\kappa = 0$), $\bar{E}_i = \bar{I}_i - 1$ with $i = 4, 6$. For randomly distributed fibers (i.e. $\kappa = 1/3$), $\bar{E}_i = \frac{1}{3}(\bar{I}_1 - 3)$.

A fundamental hypothesis of the model is that the collagen fibers cannot support any compression and would buckle under compressive loads. Thus, the anisotropic contribution in the strain energy function appears only when the strain of the fibers is positive or, equivalently, when $\bar{E}_i > 0$. This condition is enforced by the term $< \bar{E}_i >$, where the operator $< \cdot >$ stands for the Macauley bracket and is defined as $< x >= \frac{1}{2}(|x| + x)$. This modelling assumption is not only based on physical reasons but is also essential for reasons of stability [55].

Although initially designed to model cardiac tissue, we will see how this model has been repeatedly and successfully applied to the cornea.

Holzapfel 2020: Later in 2020, Holzapfel and Ogden [24] presented an extension of the previously developed HGO model to include the contribution of cross-links within a continuum model of collagenous soft tissues. They presented a new material strain-energy function as:

$$\Psi = \frac{1}{2}\mu(I_1 - 3) + \frac{k_1}{2k_2}(exp[k_2(I_4 - 1)^2] - 1) + \frac{1}{2}\nu(I - 1)^2 + \frac{1}{2}k(I_8 - c_0)^2 \tag{34}$$

with the introduction of the cross-links quadratic reinforcing form $\Psi_c = \frac{1}{2}\nu(I - 1)^2$ where ν is a positive parameter with the dimension of stress that measures the strength of the cross-links, and is referred to as the cross-link parameter and I is an invariant which is the square of the stretch in each of the cross-link directions.

They also defined the coupling between the collagen fiber and cross-link directions by a strain energy of a similar form $\Psi_{fc} = \frac{1}{2}k(I_8 - c_0)^2$ where they introduced new invariants I_8^+ and I_8^- to account for the coupling, with k a positive stress-like parameter measuring the strength of the interaction between the fibers and the cross-links.

3.4 Structurally based model

An exhaustive list of the constitutive equations that have been developed through time to model mechanical properties of soft incompressible biological tissues based on nonlinear continuum mechanics theory is presented in [56]. Starting from isotropic, to strain-hardening isotropic, to transversely isotropic, to orthotropic, to the development of fully anisotropic model, this paper compiles a piece of the history of material evolution in soft tissue modeling.

The provided list of hyperelastic strain energy density functions interestingly does not display a single application to the cornea, showing the lack of research in this particular field of biomechanics until recently. Indeed, the biomechanics of the cornea is a subject of study that has made great progress in the last two decades under the guidance of some major research groups.

Pandolfi et al. Pandolfi and Manganiello [57] presented the first application of HGO law to describe the anisotropic, hyperelastic and strain-hardening mechanical behavior of the cornea. Based on this model, they described two sets of reinforcing collagen fibers embedded in an isotropic matrix of proteoglycans. The tissue was assumed nearly-incompressible due to its large water content.

To overcome numerical issues connected to incompressibility they decomposed the strain-energy function into the sum of a volumetric part Ψ_{vol} and an isochoric part Ψ_{dev}, with:

$$\Psi = \Psi_{vol} + \Psi_{iso} + \Psi_{aniso} \tag{35}$$

For the volumetric strain-energy they adopted an expression in the form of

$$\Psi_{vol}(J) = K\frac{1}{4}(J^2 - 1 - 2log(J)) \tag{36}$$

where K is the bulk modulus, showing that if $J = 1$ the contribution is null. For the isochoric-isotropic strain-energy, they chose the two-constant Mooney–Rivlin model

$$\Psi_{iso}(\overline{I}_1, \overline{I}_2) = \frac{\mu_1}{2}(\overline{I}_1 - 3) + \frac{\mu_2}{2}(\overline{I}_2 - 3) \tag{37}$$

with $\mu = \mu_1 + \mu_2$ being the shear modulus. This model describes the isotropic extrafibrillar matrix made of water and proteoglycan that do not exhibit preferential directions.

Because models that use only the first 3 invariants I_1, I_2 and I_3 can only describe isotropic materials [56], they associated a fiber strain energy with the fourth and sixth invariant I_4 and I_6, which describes the stretch of the fibers and is dependent on their direction. For that, they used the expression from Holzapfel et al. (2000) [49] that describes the anisotropic part of the strain energy with:

$$\Psi_{aniso}(\overline{I}_4, \overline{I}_6) = \frac{1}{2k_2}\sum_{i=4,6} k_{1i} exp[k_2(\overline{I}_i - 1)^2] - 1 \tag{38}$$

with k_2 a dimensionless constant and k_{1i} (i=4,6) the stiffness moduli related to the collagen fiber sets. Similarly to the original model, they assumed that no contribution derives from the anisotropic part of the energy in the case of compressive loading.

For the model geometry, they disregarded the thinner layers and concentrated exclusively on the mechanical behavior of the stroma. They conducted an inverse analysis to obtain the reference geometrical dimensions from the mensuration of an in vivo cornea. Their code was designed to describe the distribution of the collagen lamellae across the cornea with an orientation of fibers orthogonal in the central part that gradually adopts a circumferential direction at the periphery as shown in Fig(20).

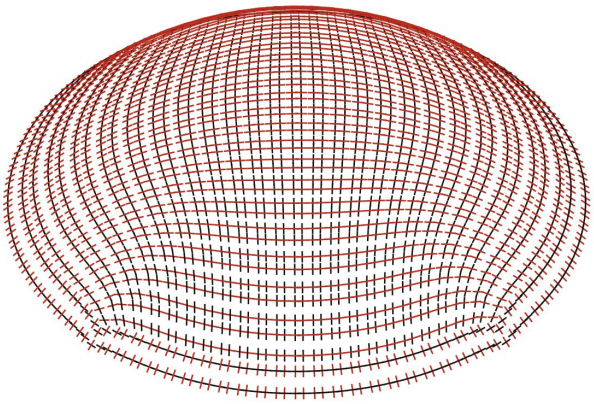

Figure 20: Local orientation of the two sets of fibers in the model developed by Pandolfi [57]

Later in 2008, they improved the model based on the work of Gasser et al. [50], which now considered the dispersion of the distributed collagen fibril around their mean directions to describe a smooth transition from a strong fiber organization in the posterior central cornea to a an isotropic structure anteriorly.

The energy stored in the two families of collagen fibers was now described with the same equation as shown in Eq(32), with the inclusion of a new term adjusting the model to various dispersion $\bar{E}_i = \kappa(\bar{I}_1 - 3) + (1 - 3\kappa)(\bar{I}_i - 1)$ where $\kappa \in [0, 1/3]$ is a dispersion parameter ($\kappa = 0$, the fibers are perfectly aligned, $\kappa = 1/3$, the fibers are randomly distributed and the material becomes isotropic).

Later in 2015 [53], they introduced an analytical description of this fiber dispersion by introducing a π-periodic normalized von Mises distribution with a concentration parameter b that describes the spatial dispersion of the fibrils around their main orientation according to Fig(21). Doing so, they rendered a complete 3D description of fibers dispersion.

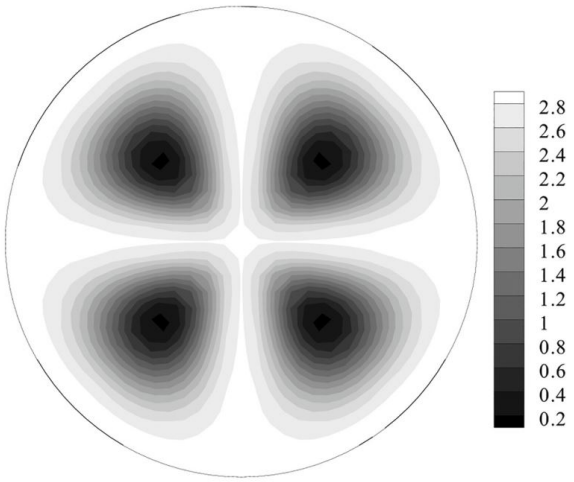

Figure 21: Map of the von Mises coefficient b for the statistical distribution of the orientation. High values of b define highly oriented set of fibers. Low values of b define nearly isotropic orientations [53]

In 2018 [11], they introduced a second order approximation of the strain energy function leading to the introduction of additional integral coefficients. This incorporation of higher-order statistics was later judged unnecessary in a review paper by Holzapfel et al. (2019) [58].

They tested their model with data from uni-axial extensiometry of excised corneal strips which showed that the model corresponded well. This was not the case when they used an isotropic material model (Mooney-Rivlin) without the anisotropic contribution. They also tested the model with data from inflation tests on whole eyes with all fibers having similar stiffness and the model corresponded very well.

They applied their model to recreate a keratoconus cornea by reducing fiber stiffness in a degenerated 1.5 mm radius inferocentral zone surrounded by a 3 mm radius annular transition zone [10]. They showed that keratoconus associates with different stress distributions. At normal IOP, a Keratoconus cornea displayed the maximum stress at the border of the degenerated zone. Maximum Cauchy stress showed strong gradient across the thickness in the conical zone. Minor deformation and elevation was observed at the center, which was not representative of a keratoconus in middle/late stage of the disease.

In the papers by Ariza-Gracia et al. [13] [52], they used a similar HGO model as in Pandolfi 2008 [59] and performed an interesting sensitivity analysis of the HGO material and geometrical parameters involved in the biomechanical response of the cornea. It showed that the most influential features on corneal displacements are the intra ocular pressure (19%), central corneal thickness (50%), and fiber stiffness k1 (18%). The isotropic matrix parameter μ also contributes a little, and the non dimensional fiber parameter k2 not significantly. They modeled the sclera with the isotropic hyperelastic Yeoh's constitutive model.

They also developed a medical application of the model to reproduce the mechanical response of the cornea subjected to a non-contact air-jet tonometry test. The total model was a three-dimensional finite element model of the anterior half ocular globe geometry, which accounts for three different parts: the cornea, the limbus and the sclera. They considered the classical orthogonal fiber distribution in the center with an annulus at the periphery.

Pinsky et al. Based at Stanford University, Pinsky & Datye (1991) [60] created the first structurally based model of the cornea. Their model, and all subsequent structural models, assumed that all lamellae have orientations that follow the cornea's curvature with no inclination. In a model developed in 2005 [61], they incorporated experimental data on lamellar orientation in the plane perpendicular to the optical axis obtained from X-ray diffraction experiments, which was latter used by others (Pandolfi & Holzapfel 2008 [59]; Grytz & Meschke 2010 [62]; Studer et al. 2010 [54]).

In their 2005 paper [61], they constructed a model that explicitly accounts for the strain energy of the collagen fibrils, extrafibrillar matrix, and proteoglycan cross-linking. They introduced the strain energy of a stromal lamella described as $W_{lamella} = W_{fibril} + W_{matrix}$ where $W_{lamella}$ is the strain energy per unit volume in a lamella, W_{fibril} is the strain energy density due to the fibrils, and W_{matrix} is the strain energy density due to the extrafibrillar matrix, which represents the proteoglycan crosslinking between fibrils.

The extrafibrillar matrix was characterized as a nearly incompressible material with low viscosity. They used a standard formulation for materials that displays this behavior which involves invariants I_1 and I_3 in the form:

$$W_{matrix} = \frac{1}{2}[\mu(I_1 - 3) - \mu log_e(I_3) + \lambda(log_e\sqrt{I_3})^2] \tag{39}$$

The λ parameter was associated with the near incompressibility of the extrafibrillar matrix (bulk modulus), μ was associated with the collagen crosslinking (shear modulus).

They associated the strain energy in the fibrils with the fourth invariant I_4, which measures the stretch of the fibrils and is dependent on their direction. They postulated a J-curve for the stress–stretch behavior representing the strain-hardening of fiber reinforced tissue. This behavior was approximated by an exponential function where α is an elastic parameter that can be interpreted as a generalized tensile modulus of a fibril similarly as in Holzapfel (2000) [49]. The strain energy density for the fibril contribution was:

$$W_f = \frac{1}{2}\alpha[e^{(I_4-1)} - I_4] \tag{40}$$

Finally, they used an angular integration approach rather than the generalized structural tensor approach of the HGO model, to provide an expression for the strain energy density of the stroma W_{stroma} that represents the preferred directions in the collagen architecture. An angular probability density function $\Phi(R, \psi, \theta)$ was introduced to give the probability of fibril orientations with variations in the angle θ through the thickness of the stroma. It gave the stromal strain energy density W_{stroma} in the form: $W_{stroma} = W_{matrix}(R, \psi, \theta) + \frac{1}{\pi}\int_0^{\pi} \Phi(R, \psi, \theta) W_{fibril}(R, \psi, \theta) d\theta$

The probability density function $\Phi(R, \psi, \theta)$ was constructed to directly match the experimental x-ray scattering data, which for the central part of the cornea was defined as: $\Phi(R, \psi; \theta) = cos^{2n}(\theta) + sin^{2n}(\theta) + c_1$ for $0 \leq R \leq 4$ and $\Phi(R, \psi; \theta) = sin^{2n}(\theta - \psi) + c_2$ for $5.5 \leq R \leq 6.5$. For the annuli with $6.5mm < R < 8.0mm$, they defined a linear combination of the 2 functions to smoothly transition from a primarily orthogonal to a tangential fibril arrangement and vice versa as shown in Fig(22).

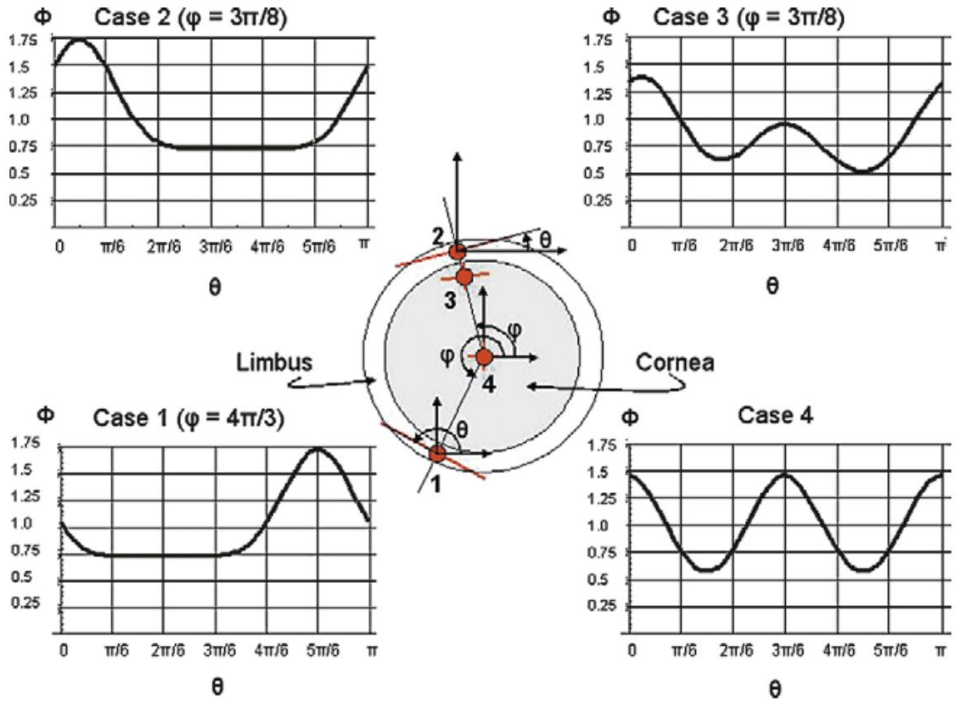

Figure 22: Distribution function Φ and its associated local coordinate system. The fluctuating portion under the function represents the population of fibrils in a particular direction. Orthognal population in the center (case 4), circumferential population in the periphery (case 1&2) [61]

In a later paper [31], Petsche and Pinsky also added a continuous description of fiber dispersion through the tissue thickness, giving the model better realism by accounting for the various inclination of lamellae. The lamellae inclination ψ was maximum at the anterior surface and decreased monotonically through the depth as shown in Fig(23).

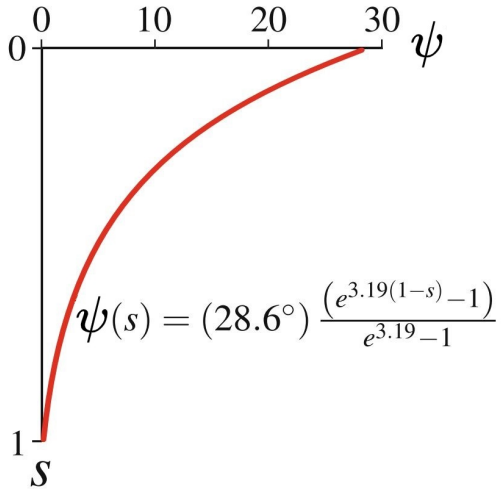

Figure 23: The variation of lamellae inclination ψ through the depth was a result of calibrating the model to experiments. Plotting ψ in degrees with depth S on the ordinate axis: 0=anterior surface, 1=posterior surface [31]

Additionally, Studer et al. [54] also applied the same model with a constitutive mechanical law that includes collagen fiber distribution based on X-ray scattering analysis, collagen cross-linking, and fiber strain-hardening, and made the distinction between each fiber family. They tested not only the response to inflation but also to uniaxial strip extensiometry tests, which assess anisotropy and the model responded well to both tests. They also examined the model using geometry from patients with different age groups. They observed that increasing age associates with changes in three parameters that represent tissue elasticity and collagen cross-linking, demonstrating an increase in collagen cross-linking for older specimens. In a later paper [63], they further developed their model, accounting for a more precise regional variation of fibril arrangement with multiple directions, with a resulting model that introduces collagen fibril density with regional variation, interlamellar cohesion and stiffening from aging.

3.5 Micro-structurally based model

Fueled by the increase in computer resources, there has been a recent push to understand how the structure of biological tissue at smaller scales leads to mechanical properties at the macroscale [64] [65]. Tang et al. [66] developed a multiscale continuum model for a non-specific collagenous soft tissue that was based on properties at both the molecular and fibril scale calculated from molecular dynamics simulation. The fibril properties were based on the work of Buehler [67] which modeled a collagen fibril as a 2-D collection of collagen molecules that interact by an area of adhesion at their ends.

Maceri et al. [68] also developed a multiscale model for the heart that started with a tropocollagen molecule modeled as a worm-like chain rather than directly with molecular dynamics. Their model includes the mechanics of collagen molecules, their crosslinks, fiber crimping, and the whole tissue. Grytz & Meschke [62] created the first multiscale model of the cornea, where the smallest scale included was the fibril, which was represented as a helical spring.

In the thesis by Petsche in 2014 [69], a multiscale model specifically dedicated to the cornea was developed starting from the collagen fibril modeled as a 2D collection of collagen molecules with cross-links between them, to the lamellae strain energy density function to finally the macroscopic stromal model. Their cornea model uses a multiscale approach at three different scales as shown in Fig(24). The high tensile stiffness of collagen fibrils relative to the properties of the surrounding matrix leads to strongly anisotropic mechanical properties of a single lamella.

Their process starts by describing the mechanics of a fibril from which properties calculated for a single fibril are used to define a hyperelastic strain energy density for a single lamella. The stroma is built by using an angular integration approach with spatially varying fiber distributions taken directly from imaging. This creates a macroscale model of the human corneal stroma that has highly heterogeneous and anisotropic mechanical properties.

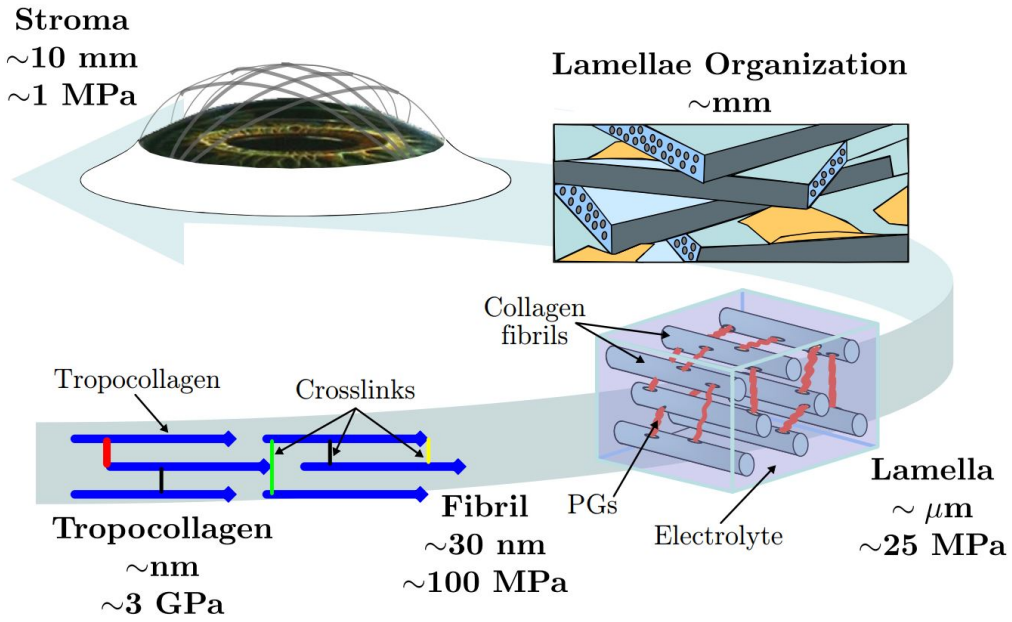

Figure 24: This illustration shows all of the length scales that are incorporated into a corneal multiscale model. Approximate elastic modulus values are included for each level of the hierarchy [69]

A similar approach by Marino and Vairo [70] [71] provided a multiscale method to model stress and strain localization in stretched collagenous tissue. They developed models of collagen molecules, fibrils, and fibers that could be later integrated by means of inter-scale relationships and homogenization methods. Their modeling framework allows a direct control of microstructural parameters on the macroscopic mechanical behavior of soft collagenous tissues and accounts for mechanics at lower scales without introducing phenomenological descriptions. Comparisons between numerical results obtained and the available experimental data in the case of tendons and aortic walls proved their multiscale approach to be effective in capturing the link between histology and mechanics.

A different micromechanical approach based on Eshelby's Equivalent inclusion theory is also an option to predict the effective mechanical properties of collagenous tissue. This multiscale method is notoriously used to model reinforced polymer matrix composites and is less computational demanding than a full finite element based simulation of a representative volume element (RVE). This paper from Raju et al. [72] reviews micromechanics based models for fiber reinforced polymer composites, starting from Voigt, Reuss and Hashin-Shtrikman bounds/models,

to well known micromechanics based models like Mori-Tanaka, Self-consistent and Differential scheme based models.

From this paper, it seems Mori-Tanaka scheme with Eshelby's equivalent inclusion model could predict values accurately for lower fiber volume fraction. They extended the Eshelby concept to higher volume fractions by combining the differential scheme with Eshelby's model to take into account the non-dilute dispersion effect which provided a revised Mori-Tanaka model for all volume fraction. They compared the theoretical results with experimental measurements, however not to hyperelastic materials.

Pandolfi 2019: Using a completely different approach, this paper developed by Pandolfi, Gizzi and Vasta in 2019 [73] uses a unique approach with the objective of addressing the keratoconus problematic. This model, not based on continuum mechanics, propose a discrete simplified micromechanical model of the fibrous reinforcement of the corneal tissue with two sets of parallel fibrils, connected by transversal bonds within fibril family (inter-crosslink) and across families (intra-cross-link) as shown in Fig(25).

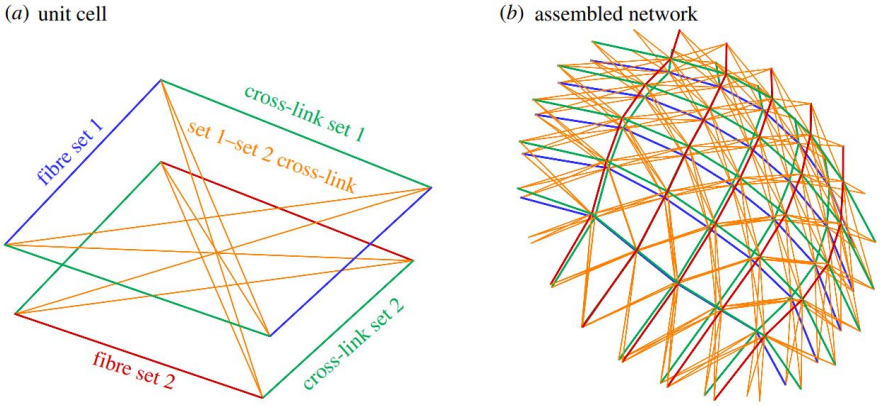

Figure 25: (a) Detail of the cross-links between the fibrils of the same set (inter-link, green) and of two different sets (intra-link orange). (b) Coarse model of the assembled trusswork including all fibril and cross-link trusses [73]

This particular design chosen for their structure relies on the fact that the stiffness of the corneal stroma and its ability to sustain loads is dependent on the degree of the cross-link and, therefore, on the density of the bonds. They showed that weakening transversal bonds between collagen fibers greatly increases the deformability of the system. In the case of keratoconus, mechanical, chemical or enzymatic reasons can justify the loss of stiffness of the stromal tissue from loss of transversal bonds resulting in localized thinning and bulging described in their paper.

3.6 Swelling behavior

Most biological tissues are highly hydrated, porous and permeable, such that their interstitial fluid flow and pressurization may contribute significantly to their mechanics. These porous tissues can be modeled as a mixture of a fluid and a solid, where the fluid itself may consist of a mixture of a solvent and multiple solutes [26] [74] [75].

Unlike in rubber materials, the inner fluid in the porous skeleton of biological tissue plays an important role in the maintenance of its large strain capability [74]. To account for this

effect, several phenomenological models were developed in the framework of poro-hyperelasticity theory that accounts for hyperelastic effects and fluid flow through the porous skeleton.

The classical theory of poroelasticity proposed by Biot (1941) [76] is a complete theory that accounts for three-dimensional elasticity and fluid transport effects in its formulation. The developments in the classical theory of Biot poroelasticity are quite extensive and are well documented in these review articles and volumes [74] [77] [78]. Early applications of porohyperelasticity to the study of soft tissue biomaterials are given in Simon et al. (1996) [79] who take into consideration the influence of large elastic deformations of the porous skeleton, fluid flow through the pore space and an effective stress relationship between the porous skeletal stresses and the pressure of the fluid.

The total Cauchy stress σ_{ij} in a fluid-saturated poro-hyperelastic material is composed of the Cauchy stress in the porous hyperelastic fabric denoted by $\sigma_{ij}^{'}$ and the isotropic stress in the interstitial fluids denoted by p, such that

$$\sigma_{ij} = \sigma_{ij}^{'} - p\delta_{ij} \tag{41}$$

where δ_{ij} is the Kronecker delta. The effective stress is further represented in terms of its deviatoric component $s_{ij}^{'}$ and an isotropic stress (effective pressure) $p^{'}$ such that

$$\sigma_{ij}^{'} = s_{ij}^{'} - p^{'}\delta_{ij} \tag{42}$$

with $p^{'} = -\sigma_{ij}^{'}/3$. In the paper by Selvadurai [80], they took the Mooney-Rivlin strain energy function U to model the isotropic hyperelastic material: $U(\overline{I}_1, \overline{I}_2, J) = C_{10}(\overline{I}_1 - 3) + C_{20}(\overline{I}_1 - 3)^2 + \frac{1}{D_1}(J-1)^2 + \frac{1}{D_2}(J-1)^4$ where C_{10}, C_{20}, D_1 and D_2 are material constants.

The constitutive developments are done to account for the flow of fluid through a porohyperelastic material. Assuming that the entire pore space of the hyperelastic skeleton is saturated with a fluid and that the flow takes place as a result of a gradient potential, in the case of slow flows the fluid velocity can be neglected in comparison with the other contributions [81].

Given the principle of conservation of mass, we have

$$-\nabla.\varphi(\boldsymbol{v}_f - \boldsymbol{v}_s) = \nabla.\frac{\partial \boldsymbol{u}}{\partial t} \tag{43}$$

where φ is the porosity, $\boldsymbol{v}_f$ is the velocity of the fluid in the pore space and $\boldsymbol{v}_s$ is the velocity of the solid skeleton of the porous material, ∇ is the gradient operator referred to the coordinates of a particle of fluid in the deformed configuration, and $\boldsymbol{u}$ is the displacement vector defined as $\boldsymbol{u} = \boldsymbol{x} - \boldsymbol{X}$. Derivation of the Eq.(43) is done from the mass balance equation presented in Appendix Section(A.1) and can be found in [80].

We assume that flow of the fluid through the isotropic hyperelastic skeleton can be described by an isotropic form of Darcy's law, which takes the form

$$\varphi(\boldsymbol{v}_f - \boldsymbol{v}_s) = -\frac{k}{\eta}\nabla p \tag{44}$$

where k is the permeability, which is assumed to be constant, and η is the dynamic fluid viscosity. Darcy's law, as used in the present context, is a phenomenological law that can be derived from a more generalized theory under simplifying assumptions as shown later.

The modelling can be made more complex if permeability heterogeneity is considered, for example when the porosity changes with the tissue deformation and stress [82] [83]. Indeed, tissue deformation results in pore closure and a concomitant reduction in permeability [84] [85] [86].

In the paper [87] and the book [74], they introduced two important features of porous biological materials which are their osmotic pressure and residual stresses. Applied to cardiovascular tissues, they introduced a mathematical formulation of osmotic pressure from thermodynamics principle, as well as the electroneutrality condition that regulates it. These two phenomena are presented in details in Part(III) of the thesis. It showed that if the thermodynamic balance between hydrostatic and osmotic pressure differences is not satisfied, water imbibes into the tissue, causing it to swell and becomes softer.

Pinsky and Cheng: Applied specifically to the cornea, the only known model describing swelling mechanisms and membrane active pumping of the cornea is the work of Pinsky and Cheng [20] [88] [89].

Using a thermodynamic free energy approach, they presented a simplified mathematical description of the corneal stroma as an electrolyte gel (solid, solvent, charged solutes) in equilibrium. Doing so, they were able to provide an analytical approximation of the stromal osmotic pressure to account for its swelling behavior [20], along with a three-dimensional organization of stromal fibers.

For the fibers contribution, they used a similar description as in Petsche 2013 [31], with a stromal collagen network based on three-dimensional distribution obtained from X-ray diffraction and second harmonic generated imaging.

Later, they expanded the model to account for active endothelial ionic transport in the in vivo cornea, which modulates the osmotic pressure and stromal hydration [89]. They modeled the endothelium as a simple bounding layer with ions that are transported both passively, with a driving force from the gradient of the electrochemical potential, and actively [88].

They used a set of enhanced Kedem-Katchalsky (KK) equations [90] that provides the theoretical foundations for analyzing fluid flow and solute fluxes of various membrane systems. This study [88] is of crucial importance as an equivalence of parameters can be used between their approach and others multiphasic approaches, such as mixture theory [26].

Their model has been implemented in a standard finite element code and was shown to be capable of reproducing fundamental in vitro swelling experiments, including massive swelling, and typical in vivo swelling observed in disease states such as Fuch's dystophy. Their analysis also suggested the need of active ionic fluxes to balance the fluid osmotic pressure arising from ionic concentration gradients. Indeed, this active transport mechanisms propel substances against their concentration gradients and is crucial in maintaining the hydration and transparency of the cornea [35].

Their study will act as a reference where several of their results, such as the stromal free swelling experiment or Fuch's dystrophy swelling, will be compared to our own study presented in Part(III) of this thesis.

However, in their approach, conditions of thermodynamic equilibrium were assumed to hold, rendering water and ionic fluxes time-independent. This limits the model to long-time solutions

and does not allow the time-course of the solution to be obtained, but avoids the high complexity of non-equilibrium theory.

Based on our need to describe the time course of swelling, we will resort to another approach for describing the multiphasic aspects of the cornea, an approach called mixture theory [26]. Indeed, in their paper, they showed that a broad equivalence exists between their proposed free energy approach and the mixture theory approach [89].

Mixture theory An alternative formulation of poromechanics have been developed in the framework of the theory of mixtures [91] [92] [93]. Mixture theory provides a continuum framework that accounts for interactions among all mixture constituents. The theory requires the formulation of mass, momentum, and energy balance equations for each of the mixture constituents, which may then be summed together to produce equivalent formulations for the mixture as a whole. This allows to model various phenomena such as problems of diffusion, osmosis, electro-osmosis ... [26]

One advantage of the mixture theory approach is its possibility to account for non-linearity laws governing flow in porous media. Indeed, through consideration of momentum transfer between the solid and the fluid phases, terms neglected in earlier phenomenological formulations like Darcy's law and Fick's law are rediscovered [26]. This is because in mixture theory, frictional drag tensors $f^{\alpha\beta}$ between every pair of constituents are defined, resulting in interaction not described by phenomenological relations [94] [34]. The linearization of such generalized relationships then leads to Darcy's result as shown in [26].

The application of mixture theory to a ground water flow problem and a comparison with predictions based on Darcy's law is given in [95]. The article by Pence (2012) [96] contains a systematic treatment of the application of the mixture theory approach to fluid saturated media and a comprehensive exposition of the current status. Also of particular interest to our problematic are the articles [97][98][99] who examine the application of coupled theories in the context of polymer swelling.

The mixture theory-based formulations are particularly relevant when a number of species saturating the porous space are encountered. When the tissue is described as a triphasic material consisting of a charged porous solid matrix, an interstitial fluid composed of a neutral solvent (water) and two monovalent counterions such as Na^+ and Cl^-, an analytical solution exists for the osmotic pressure called Donnan's pressure [89] [100]. This formulation can be recovered in a triphasic mixture and extended with as many constituents as needed.

Compared to the approaches presented earlier from empirical developments in soil mechanics [80] and the free energy of Pinsky and Cheng [89], mixture theory proposes a more generalized framework and allows to describe a multitude of physical phenomena within a single method.

Thanks to Pr. Ateshian and Dr. Weiss of the University of Utah, an implementation of mixture theory have been developed in an open-source software called FEBio. With this software, it is much more practical for us to use this approach to describe the swelling pressure of the cornea. All the mathematical details regarding the theory are introduced in Part(III) and Section(11) of the thesis, along with our application in studying hydration control mechanism of the cornea and investigation of Fuch's dystrophy.

3.7 Conclusion

Based on this litterature review, a choice will be made for a method that is both sufficiently advanced to describe the corneal microstructure and to control the mechanical parameters at this scale, but also sufficiently accessible to address the medical problematic of Keratoconus and Fuch's dystrophy in the time given.

In view of the recent advancements in the modeling of soft tissue, the structure motivated HGO model seems to be an adequate option for the modeling of fiber reinforced hyperelastic material. This macroscopic model, whose parameters find an interpretation at the microscale, accounts for the presence of oriented fibers dispersed around their mean direction. Through the use of strain tensors' invariants, it allows to control the matrix and fiber stiffness, fiber distribution and fiber dispersion. This ability makes it more simple than a multiscale model, yet rendering a much more complex behavior than a phenomenological model.

The HGO model already proved to be versatile and accurate in the modeling of soft tissue, notably with the studies of Pandolfi et al. which provided a number of developments and applications of this model to the cornea. The solid mechanics of our model will therefore be described by the HGO model.

Because the collagen fiber lies within a matrix of polyelectrolytes and water, modeling the multiphasic structure and swelling pressure of the corneal stroma is necessary for the study of disease related to corneal hydration. We will keep the same solid mechanics behavior and add a multiphasic porous aspect to the tissue.

Since multiscale models are highly complex and Eshelby's inclusion problem lack application in hyperelastic soft tissue, we opted for the use of mixture theory and its implementation in the FEBio software. In this framework, the tissue may be modeled as a mixture of a fluid and a solid, where the fluid itself may consist of a solvent and multiple solutes. This add the capability of describing tissue swelling pressure and the biomechanical response to possible variations in pressure, which will be important for the study of corneal edema.

This option fulfills both our needs to describe the multiphasic structure of the cornea with a flexible number of constituents and the possibility to describe the transient evolution of phenomena in a single framework.

4 Summary of the introduction

This introductive part allowed us to gather knowledge on the structure and biomechanical properties of the cornea. We have learned that the cornea is composed of 5 layers with specific microstructural and mechanical properties. Among them, the stroma is the most mechanically influential layer as it represents 90% of the total thickness of the tissue. Therefore, it is mainly the collagen network in the stroma that shapes the solid mechanics of the cornea.

Overall, the cornea displays a nonlinear elastic behavior characteristic of fiber-reinforced composites, namely, corneal stiffness rises when deformation increases and the collagen fibers become stretched.

We learned that the primary function of the corneal endothelium is to maintain corneal transparency by regulating corneal hydration and nutrition through a leaky barrier and a metabolic pump. Without its crucial action the cornea can become over hydrated and opaque, meaning that an equilibrium is needed between the amount of passive fluid flow into the cornea

and the active flux used to pump out excess fluid for maintenance of corneal transparency.

The bibliographic work showed that there are principally two modeling approaches that can fulfill the requirements of a micro structural description for our study. These approaches are either to use a multiscale model or a macroscopic but structure-motivated model. Based on the review and due to time and technical limitations, with an objective of addressing medical problematics, the macroscopic approach was chosen. The solid mechanics of our model will therefore be described by the HGO model, a structure-motivated model which includes contributions of an isotropic noncollagenous neo-Hookean matrix and two anisotropic 2D families collagen fibers with defined orientation and dispersion.

The Part(II) of the thesis will therefore investigate the biomechanics of corneal ectasia using the HGO fiber-reinforced structural model to reproduce a conical deformation similar as the one observed in Keratoconus disease. Since corneal shape mostly reflects the interplay between collagen fiber stiffness and IOP, no porous multiphasic features will be included in this part, and results will be compared to the medical knowledge existing on Keratoconus.

Secondly, because the collagen fiber lies within a matrix of polyelectrolytes and water, we will keep the same solid mechanics behavior and add a multiphasic aspect to the cornea using the continuum framework of mixture theory. In this framework, the tissue will be modeled as a mixture of a fluid and a solid, where the fluid itself will consist of a solvent and multiple solutes. This will incorporate a realistic contribution for the tissue volumetric behavior.

The Part(III) of the thesis will therefore focus on implementing and testing this multiphasic model of the cornea in order to describe the corneal hydration mechanism and how its impairment can lead to corneal edema. Because the tissue hydration depends on the endothelial layer, our numerical analysis will investigate how such a layer can prevent the cornea from swelling.

Part II
The cornea as a fiber-reinforced tissue

5 Objective

This part investigates the biomechanics of corneal ectasia and its more common manifestation in the disease called Keratoconus. Since corneal shape reflects the interplay between corneal mechanical stiffness and IOP, corneal ectasia can appear when the structure is compromised due to removal of corneal material (as occurs in refractive surgery) or collagen fiber disorganization (as occurs in keratoconus).

Keratoconus is a progressive, non-inflammatory, asymmetrical corneal disease that is most commonly diagnosed in the 20's [101] [102]. It arises when the biomechanical strength of the infero-central cornea weakens, causing the cornea to thin and soften. The cornea can no longer resist intraocular pressure and adopts a conical shape that blurs vision [1] [103] as shown in Fig(26).

Despite multiple histological, proteomic, genomic, and epidemiological studies, the exact pathogenesis of keratoconus remains unclear [5]. It is unrelated to an excessive IOP and is currently thought to be driven by genetics and environmental factors, including atopy, contact-lens use, and eye rubbing with the finger/knuckle[1] [2] [104] [105] . It should be noted that

while the link between keratoconus and eye rubbing is well-established by observational studies [1] [106] [107] and many ophthalmologists recommend their patients to stop rubbing their eyes to avoid progression of the ectasia [108], there is still debate about whether it can induce the disease.

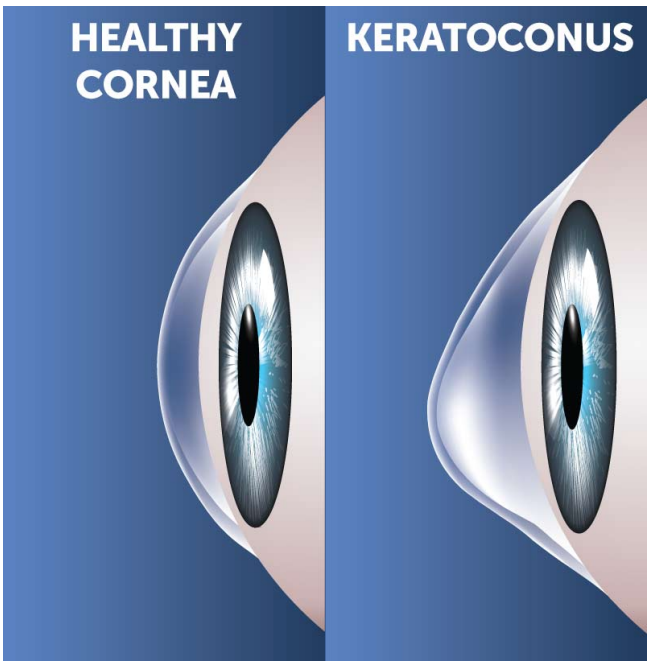

Figure 26: Curvature profile of a healthy cornea on the left and a keratoconic cornea on the right, showing the conic deformation and thinning specific of Keratoconus disease [109]

In keratoconic corneas, imaging studies show that the collagen architecture described in the introduction part (lamellae in the central cornea follows orthogonal directions) is disrupted within the keratoconic button, but not outside of it, and causes the stromal thickness in the button to drop markedly [18] [110] [111] [112] as shown in Fig(27d). This is apparently due to lamellar slippage out of the cone and structural changes to the lamellae. Specifically, the lamellae in the anterior stroma appear to lose some interlamellar adhesiveness which disturbs their interwoven pattern, whereas posterior lamellae exhibit thinning, splitting, and extensive distortion [22] [113].

Another clinical sign of keratoconus are Vogt's striae, which run from the deep posterior stroma to anterior layers. While normal corneas also have these striae, they are more numerous and longer in keratoconus [114]. Other marked changes are thinning and fragmentation of Bowman's layer [110] [115], thickening of the epithelial layer to fill the void left by the shrunken stroma, and in end-stage disease, rupture of Descemet's membrane and the onset of hydrops [116]. These changes are all largely concentrated in the region where the cone forms.

Mechanical theory on laminated composites [117] [118] suggests that keratoconus is due to repeated excessive stress that results in progressive biomechanical failure of the cornea. Specifically, stress on the cornea could provoke two of the predominant mechanisms by which fiber-reinforced composites fail, namely, fiber breakage and interfiber cross-link breakage. Fiber breakage in keratoconus is evident in Bowman's membrane and Descemet's membrane at later stages of the disease, i.e. stages 2 and 5 in the five-stage optical coherence tomography (OCT) classification of keratoconus progression, respectively [112].

By contrast, cross-link breakage (i.e. matrix cracking that leads to fiber/matrix interface debonding) is prevalent in the keratoconic stroma, as evidenced by the disorganization of the stromal lamellae, the localization of the damage, and Vogt's striae. This may reflect the weakness of the stromal cross-links relative to the stiff collagen lamellae in the stroma. Given the potent biomechanical role of the stroma, it seems possible that the accumulation of cross-link breaks in the stroma eventually fatally weakens the cornea and induces its conical IOP-induced elevation [119].

The imaging findings in subclinical keratoconus, the earliest known stage of the disease, suggest that this stromal cross-link breakage starts early in keratoconus. Indeed, the only clinical finding in subclinical keratoconus is posterior elevation on videokeratoscopy: there are no obvious signs of epithelial or Bowman's membrane degradation on slit-lamp/OCT, and the anterior curvature is normal on videokeratoscopy [120] as shown in Fig(42). Thus, the stroma may develop cross-link breakages that affect the biomechanical properties of the cornea well before significant anterior injuries are detected [121] [122] [123].

How these early microstructural changes develop is not known but it has been hypothesized that the shear stresses invoked by frequent eye rubbing break the interlamellar cross-links either directly [73] [124] and/or indirectly by inducing keratocyte apoptosis, matrix catabolic protein production, and/or impairing collagen/ground substance production [1] [125] [126] [127]. Of note, the stress that provokes stromal cross-link breakage in keratoconus is not from IOP.

We introduce here our hypothesis on the disease progression as pictured in the Fig(27), as we suspect that posterior stromal layers may play a key early role in keratoconus pathogenesis. The reasons that lead us to believe in this hypothesis are explained later in the results and discussion Chapters(7 & 8).

If validated by other experiments, this hypothesis suggests that characterizing the mechanical stability of the posterior stroma may help to diagnose keratoconus at a very early stage, thereby facilitating early interventions that prevent keratoconus progression. In order to test this hypothesis, a numerical model describing the fiber-reinforced biomechanics of the cornea is developed.

While models of keratoconus have been very useful for understanding the role of mechanics in corneal ectasia, none have to date successfully achieved the pronounced local bulging that characterizes keratoconus [7] [8] [119]. To further explore the biomechanical properties and corneal injuries that associate with keratoconus formation, we conducted two numerical studies as presented in Chapter(7). In the first, we weakened the corneal structure to determine which types of weaknesses and tissue zones contribute to the conical deformation in keratoconus. In the second study, we sought to identify the corneal layer that is most stressed by eye rubbing and thus is most likely to be damaged by this practice. These studies together suggested that posterior stromal weakening due to cross-link breakage (Fig. 27b–c) may play a key early role in keratoconus pathogenesis as discussed in Chapter(8).

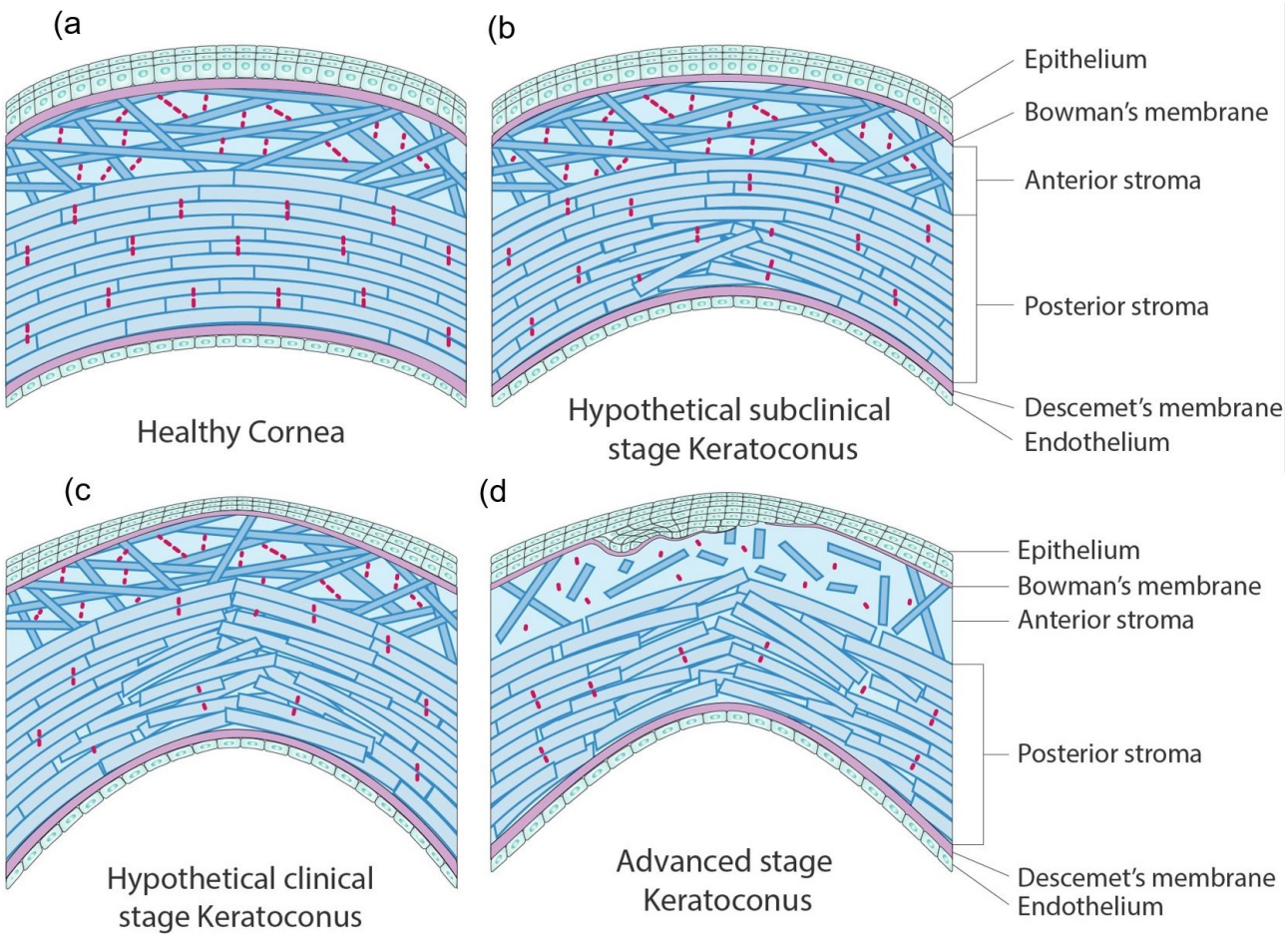

Figure 27: Schematic view of the cornea in cross-section that shows the hypothetical microstructural changes in the stroma that may lead to keratoconus onset and progression. (b) Our hypothesized very early stage keratoconus, which is characterized by a few cross-link breakages in the deep posterior stroma that disrupt the local lamellar organization and induce posterior elevation. (c) An hypothesized later stage in which cross-link breakages have accumulated. Posterior stromal lamellar disorganization has become more pronounced and epithelial thinning and deformation is now evident. (d) Advanced keratoconus exhibiting critical failure of the stromal microstructure and collagen fiber breaks in Bowman's layer that result in epithelial outgrowth. Blue bars/bricks=lamellae. Red dashes=interlamellar cross-links generated by ground substance

6 Modeling methods

The modeling of the cornea is a subject of study that has made great progress in the last two decades under the guidance of some major research groups as shown in the bibliographic Chapter(3). An important characteristic of the cornea is the presence of microstructural collagen reinforcements that call for the development of advanced material models.

In that regard, multiple studies have shown that the fiber-reinforced structural model of Holzapfel, Gasser, and Ogden (HGO) successfully describes how fibrous biological tissues like the cornea deform when a load (e.g. intra ocular pressure) is applied [128] and could replicate the in vivo corneal behavior in response to normal and high IOP, uniaxial tension, incisions for

astigmatism, and refractive surgery [57] [129] . Later, several groups adapted their models to reflect the fiber dispersion gradient in the stroma (i.e. changing from anisotropic posteriorly to isotropic anteriorly) and successfully modeled the corneal responses to high IOP [53] [54], air-puff tonometry [13][52], indentation with a probe [11], eye rubbing [12], and refractive surgery [130] [131] [132] [133].

With this knowledge, we will use the HGO model implemented in the Abaqus finite element analysis software in our study. In the HGO model, the deformation is composed of three independent contributions, such that the strain energy density function W is split into a volumetric contribution as shown in Eq(30), an isochoric isotropic contribution as shown in Eq(31) and an isochoric anisotropic contribution as shown in Eq(32). It gives us the ability to describe the complex fiber architecture of the corneal stroma resulting in its strain-hardening hyperelasticity and anisotropy.

6.1 Modeling the collagen fiber architecture in the stroma

We developed a geometrical model of the healthy cornea that describes the collagen distribution seen on ex-vivo X-ray imaging. The X-ray studies of the Meek group showed that the collagen fibers in the central and posterior stroma of the cornea follow a distinct orthogonal pattern and, as they approach the limbus, they start to curve, eventually forming a stiff reinforcing annular ring of fibers around the edge of the cornea in the posterior stroma [18] [40] . Several studies also showed that the anterior lamellae are randomly interwoven and isotropically dispersed whereas in the posterior two-thirds of the stroma, the lamellae start adopting a stacked plywood-like organization [31] [115] [134] .

To describe this complex lamellar architecture, we split the stroma into nine different regions that bear distinct lamellar architectures. These regions distinguish the anterior zone from the posterior one and the central area from the peripheral one, with transition zones in between as shown in Fig(28a). We then modeled the deep stroma with a planar distribution of perfectly aligned fibers (kappa=0, i.e. no dispersion) while the anterior stroma was modeled as fully isotropic (kappa=1/3, i.e. complete dispersion). The middle stroma was modeled with intermediate dispersion (kappa=1/6) as shown in Fig(28a), inset circle.

In addition, a family of circumferential fibers was added and the stroma was stiffened in its periphery to reflect the presence of reinforcing fibers coming from the sclera and the increasing fiber diameters as they move from the center to the periphery as shown in Fig(28b): this mimics the observations made by Boote et al. [40]. It should be noted that while other groups have achieved a similar gradient of material properties with various mathematical descriptions [20] [31] [54] [59], we chose to take our cutting approach so that we could later alter μ, k_1, and kappa in specific parts of the corneal stroma in our numerical study in Section(7.1) to see if that would reproduce a pathologically weakened structure.

In the end, our geometrical model describes the five corneal layers and splits the stroma into different regions that are characterized by distinct lamellar architectures. For that, the stroma was sectioned into nine parts to reflect the changes in lamellar interweaving and directions throughout corneal depth and at the four corneal meridians. This division meant that specific corneal areas could be assigned a pathologically weakened structure. The in vivo corneal dimensions used were those of the author (NF) as determined in the previous Section(2.4.3).

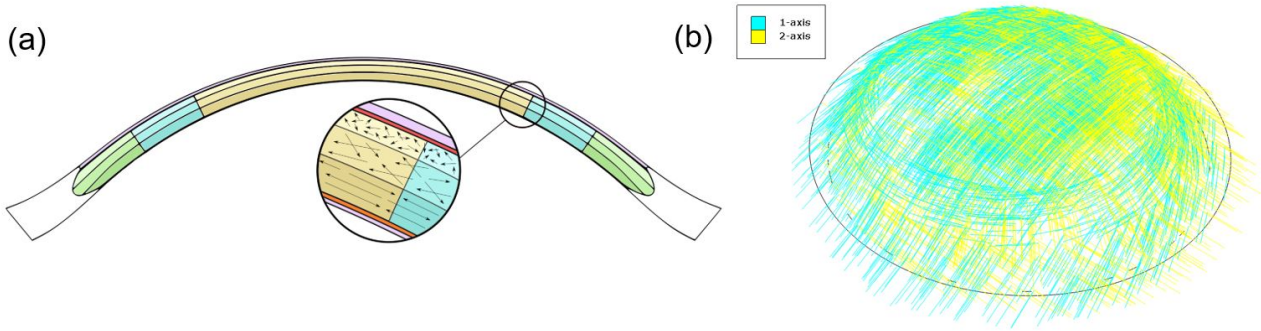

Figure 28: (a) Two-dimensional schematic showing the division of the stromal layer into three areas that bear specific collagen architecture, namely, the central corneal stroma (yellow), the peripheral corneal stroma (green), and the transitional middle area in between (blue). The arrows in the inset figure show the predominant orientations of the lamellae in the anterior stroma (fully dispersed), middle stroma (moderately dispersed), and posterior stroma (perfectly aligned without any dispersion). In the green zone, the collagen fibers arriving from the corneal center curve to provide annular reinforcement at the corneal edge (not depicted). (b) Three-dimensional view of the preferential organization of the collagen lamellae in the posterior stroma, namely, a predominant orthogonal fiber orientation that eventually curves to provide annular reinforcement at the limbus

6.1.1 Material parameters of the model

Regarding the attribution of material properties, two principles were respected: the stiffening of the cornea from the center towards the limbus and the decrease in fiber dispersion from the anterior stroma toward the posterior stroma. The anterior stroma was considered isotropic due to its random and highly interwoven fiber pattern. For the middle and posterior stroma, two fiber families were considered to follow a preferential orthogonal distribution in the center and an annular reinforcement at the limbus (Figure 28b). This accounts for the typical collagen architecture of the central stroma and its stiff peripheral areas [18].

Since the different dispersion, orientation, and fiber stiffness of the stromal parts impose different "absolute" stiffness, we proportionally tuned the matrix stiffness μ and fiber stiffness k_1 in each layer so that the stress distribution throughout the full thickness of the corneal stroma was homogeneous when the corneal model was submitted to normal IOP (this homogeneity is displayed in Fig(36b)).

To achieve this homogeneity, we conducted inflation tests on a monolayer corneal geometry onto which we imposed the HGO material properties found in the literature for a cornea with fully anisotropic properties which allows to calculate a reference value of apex vertical displacement [13] [52]. The aim was to ensure that a monolayer cornea with fully anisotropic properties such as that in the posterior stroma (no dispersion, kappa=0) generated the same apex vertical displacement as a cornea with fully isotropic properties such as that in the anterior stroma (full dispersion, kappa=1/3). We similarly tuned the stiffness parameters of the mildly dispersed layer (kappa=1/6). These tests together yielded the material parameters of the stroma.

Our review of the literature showed that the Yeoh hyperelastic model has been used to describe the sclera because it models the strain-hardening behavior of isotropic soft biological tissues like the sclera [51] [52]. Similar literature researches led us to adopt the Neo-Hookean hyperelastic model to describe the behavior of the epithelium, Descemet membrane, and en-

dothelium, while an isotropic formulation of the HGO law was used to describe the behavior of Bowman's membrane [12] [20]. Table(29) shows the parameters of the HGO, Neo-Hookean, and Yeoh models that were used to describe the indicated layers. Of particular interest are μ (ground substance stiffness), k_1 (collagen fiber stiffness), and kappa (fiber dispersion) in the stroma, which we altered in various analyses in the numerical study in Section(7.1). The Descemet's membrane and endothelium are merged into a single layer as the thickness of the endothelium is really small, and the stiffness of the two merged layers is assumed to be 0.01 MPa, a value averaging the Descemet's membrane stiffness reported in [17].

Parameters table	UNITS :	C10 = [MPa]	D = [1/MPa]	k1 = [MPa]	k2 = [Ø]	Kappa = [Ø]
Layer	Model	Parameters				
Epithelium	Neo Hookean	C10 = 0.002	D = 17			
Bowman	HGO	C10 = 0.09	D = 0.5	k1 = 0.9	k2 = 150	Kappa = 0.3333
Descemet - Endo	Neo Hookean	C10 = 0.01	D = 4.8			
Sclera	Yeoh	C10 = 0.085	C20 = 0.0056	C30 = 0.23	D1 = 1	D2 = D3 = 1
Stroma center anterior	HGO	C10 = 0.06	D = 0.5	k1 = 0.6	k2 = 150	Kappa = 0.333
Stroma center middle	HGO	C10 = 0.02	D = 0.5	k1 = 0.3	k2 = 150	Kappa = 0.16
Stroma center posterior	HGO	C10 = 0.01	D = 0.5	k1 = 0.1	k2 = 150	Kappa = 0.01
Stroma between anterior	HGO	C10 = 0.075	D = 0.5	k1 = 0.8	k2 = 150	Kappa = 0.333
Stroma between middle	HGO	C10 = 0.025	D = 0.5	k1 = 0.35	k2 = 150	Kappa = 0.16
Stroma between posterior	HGO	C10 = 0.0125	D = 0.5	k1 = 0.11	k2 = 150	Kappa = 0.01
Stroma peripheral anterior	HGO	C10 = 0.09	D = 0.5	k1 = 1	k2 = 150	Kappa = 0.333
Stroma peripheral middle	HGO	C10 = 0.03	D = 0.5	k1 = 0.4	k2 = 150	Kappa = 0.16
Stroma peripheral posterior	HGO	C10 = 0.015	D = 0.5	k1 = 0.12	k2 = 150	Kappa = 0.01

Figure 29: Material parameters used in the model with the specific tuning of stromal layers to describe the difference in fiber orientation and dispersion existing between the anterior and posterior part of the stroma and between the center and periphery

6.1.2 Geometry and boundary conditions

The corneal dimensions used to construct our geometrical model were those of the in vivo cornea of the healthy young author (NF), which corresponds to a cornea deformed by the IOP. They were measured as the Metz-Thionville hospital with pachymetry and tomography and are: central corneal thickness=500 µm, peripheral corneal thickness=620 µm, corneal height=3.4 mm, horizontal diameter=11.8 mm, and vertical diameter=10.7 mm as determined in the previous Section(2.4.3).

The reconstructed corneal geometry was inserted into a piece of sclera to define smooth boundary conditions and avoid an unphysical cut. Since the cornea was linked to the sclera, deformations were naturally transmitted in the 6 degrees of freedom. The sclera border was defined as fully blocked and the IOP loading was applied onto the internal surface of the cornea as shown in Fig(30). The IOP used was that of the author and was measured in vivo at 17.1 mmHg/2280 Pa.

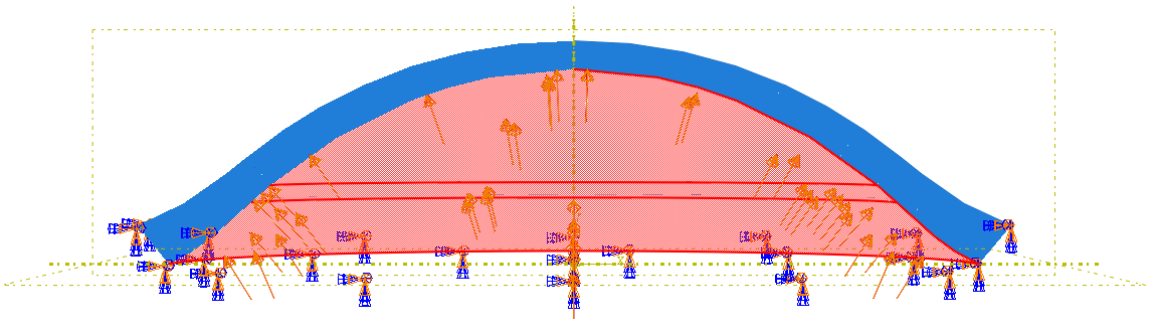

Figure 30: Visualisation of boundary conditions applied on the cornea. The orange arrows represents the Intra Ocular Pressure originating from the aqueous humor fluid that pushes on the cornea posterior surface. The scleral border are fully blocked as represented by the blue/orange symbols.

Then, we meshed the finite element model with 10-node quadratic tetrahedron elements (C3D10) and combined the material properties described above with the stroma-partitioned geometry (Fig(28)a). We applied boundary conditions of IOP and null displacements on the scleral border as shown in Fig(30). All these operations were conducted on the in vivo IOP-deformed geometry recreated from the ophthalmological measurements of the author.

6.2 Inverse procedure to recover the cornea initial/reference configuration

Since all the previous operations were conducted on the in vivo IOP-deformed geometry, an inverse procedure working on the corneal geometry (nodes coordinates) was run to determine the reference (initial) configuration corresponding to a cornea not deformed by the intra-ocular pressure. The model on which we ran the parametric analyses consisted of the multi-section geometry, material properties and boundary conditions defined before. During this process, the solution was always computed with an implicit scheme in static analysis.

For this procedure, we referred to the inverse method already applied on the cornea by Pandolfi [10]. The geometrical data derived from clinical measurements on the author's cornea were used to build the "target" finite element mesh. Therefore, the nodal coordinates X_0 in the procedure represent the physiological configuration of the author's cornea and correspond to the spatial coordinates x of the cornea in its deformed configuration. They equal the sum of the initially unknown material coordinates X and of the nodal displacements u after the IOP is applied:

$$X_0 = x = X + u \tag{45}$$

The procedure starts by setting the reference coordinates $X^1 = X_0$. At the iteration k, a static analysis is computed with the application of the IOP and gives the displacements u^k. The displacements are used to evaluate the new spatial coordinates $x^k = X^k + u^k$ and to calculate a stop criterion measure:

$$e^k = \|X_0 - x^k\| \tag{46}$$

where $\|a\|$ is the Eucledian norm of a. Then, the reference coordinates are updated as

$$X^{k+1} = X_0 - u^k \tag{47}$$

and a new analysis is performed. The new displacements u^{k+1} are used for a new error calculation and a new computation. The procedure ends when the stop criterion e^k becomes smaller than a predefined amount, e.g., $e^k \leq \epsilon\, D_{max}$, where D_{max} denotes the maximum diameter of the cornea.

The procedure was implemented as a fully automatized system of python scripts that worked on the nodes coordinates extracted from Abaqus FEA input files (.inp). Several scripts and files were executed and written step by step through the use of a batch file.

Reference geometry dimensions The reference (initial) dimensions of the author's cornea not submitted to intra-ocular pressure obtained with this method are presented in Table(2).

Central thickness	550 µm
Peripheral thickness	720 µm
Cornea height	2.9 mm
Horizontal diameter	11.8 mm
Vertical diameter	10.7 mm

Table 2: Corneal dimensions in reference configuration

The obtained reference thicknesses at the center of the epithelium, Bowman's layer, anterior, middle, and posterior stroma, and Descemet's membrane plus endothelium are presented in Table(3).

Corneal layer	Thickness
Epithelium	50 µm
Bowman's membrane	10 µm
Anterior stroma	115 µm
Middle stroma	166 µm
Posterior stroma	191 µm
Descemet and Endothelium	18 µm

Table 3: Corneal layers thickness at the central cornea after the inverse procedure. These dimensions corresponds to the cornea geometry in its reference configuration

And the obtained reference dimensions at the limbus are presented in Table(4). The increase in anterior stroma thickness tends to recover the fact that interweaving collagen lamellae goes deeper at the limbus.

Corneal layer	Thickness
Epithelium	70 µm
Bowman's membrane	18 µm
Anterior stroma	170 µm
Middle stroma	210 µm
Posterior stroma	230 µm
Descemet and Endothelium	22 µm

Table 4: Corneal layers thickness at the peripheral cornea after the inverse procedure

Using these dimensions, a reference multi-section geometry with scleral insertion of the author's cornea was reconstructed as shown in Fig(31) and Fig(32).

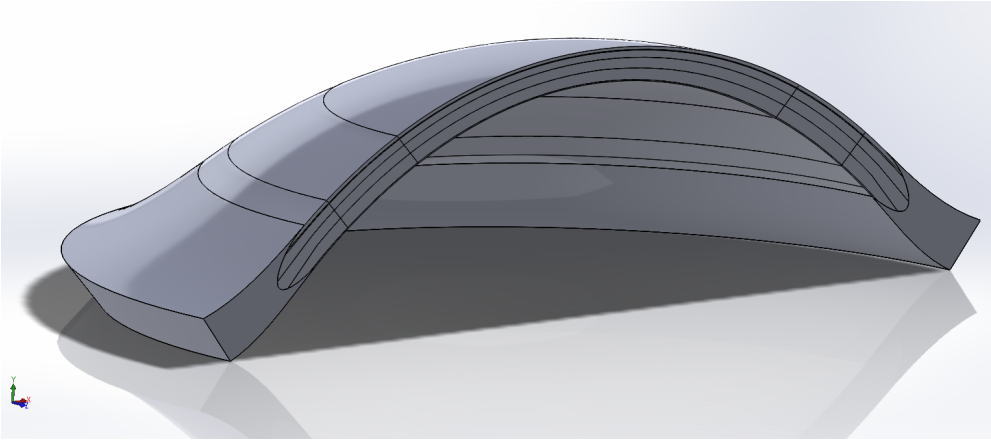

Figure 31: Three-dimensional view of the reference cornea geometry with its scleral border and multi-section stroma

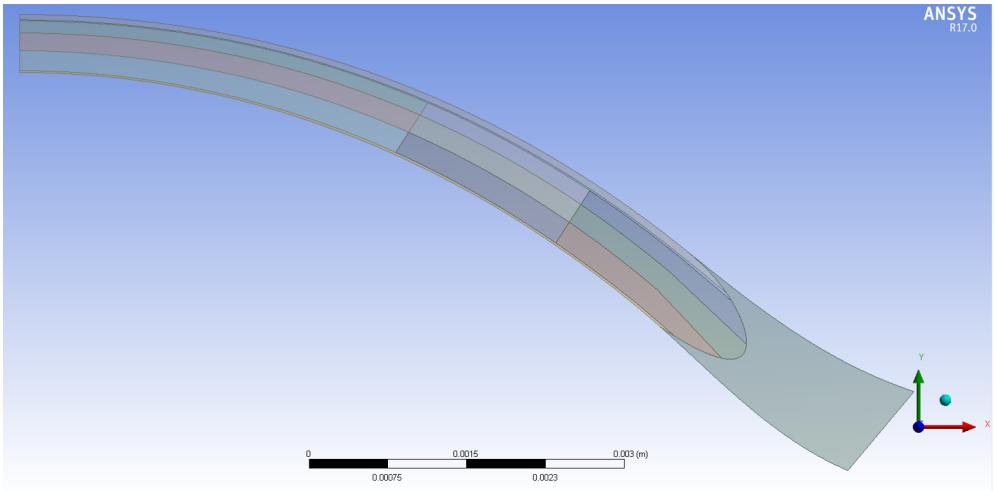

Figure 32: Two-dimensional section view of the cornea reference geometry

6.3 Mesh convergence study

On this model of the cornea with its specific material properties and boundary conditions, we conducted a mesh convergence study to ensure that the mesh was fine enough to obtain accurate solutions and was economic on computing resources as several parametric analysis were needed as presented in the results Chapter(7).

The convergence study was conducted by checking two variables that play key roles when the cornea is subjected to IOP, namely, the corneal vertical apex displacement and the stress in the central anterior stroma as shown in Fig(33). The number of 10-node quadratic tetrahedron elements (C3D10) elements was doubled at each iteration and the results reached convergence with a mesh of $\geq$ 40,000 elements. Given that we had to run a complete parametric analysis with numerous simulations, we therefore used 40,000 elements during the study, since it gave the best balance between precision and speed of calculation.

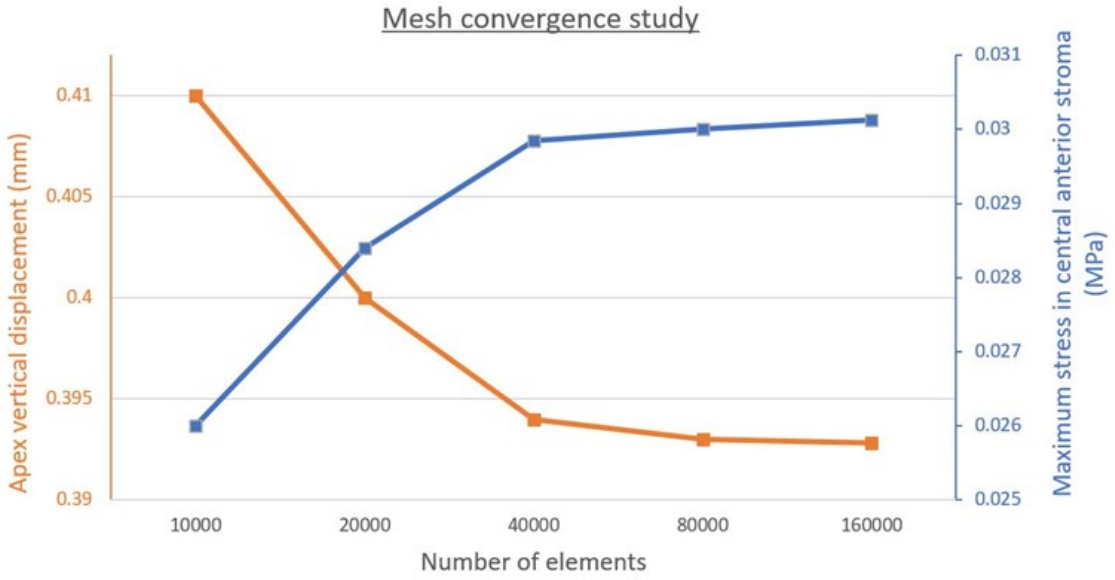

Figure 33: Mesh convergence study on the final corneal model checking results accuracy based on number of tetrahedral elements used. In orange is shown the apex vertical displacement in mm, in blue the maximum stress in the central cornea in MPa.

7 Results

To investigate the biomechanical injuries that associate with keratoconus formation, we conducted two numerical studies with the model developed in the previous Section(6). In the first, we weakened the corneal structure to determine which types of weaknesses and tissue zones contribute to the conical deformation in keratoconus. In the second study, we sought to identify the corneal layer that is most stressed by eye rubbing and thus is most likely to be damaged by this practice.

7.1 Identification of the corneal tissue zones whose softening yielded keratoconus

Studies showed that the corneal elevation in keratoconus most often occurs in an inferocentral corneal button [125], which is softer and exhibits lamellar disorganization [18] compared to the surrounding normal tissue [135]. We therefore first assessed whether gradually softening the collagen-based layers (i.e. Bowman's layer and stroma) in an inferocentral button in the corneal model would generate keratoconus.

For this, we added three concentric sections to the geometry, thus creating a button with a bullseye at the inferocentral cornea as shown in Fig(34 a–b). Bowman's membrane and all stromal layers in the center, middle, and periphery of the button were then softened by dividing both their μ (ground-substance stiffness) and k_1 (collagen-fiber stiffness) by 30, 20, and 10, respectively. This approach reduces stiffness in a linear pattern, as is typically seen in keratoconus [73]. Normal IOP was then imposed.

This effectively generated a keratoconus phenotype: the cornea bulged in an asymmetrical localized manner with a maximal vertical displacement of 846 µm (Figure 34d). By contrast, the normal cornea had a uniform curvature and maximal vertical displacement was 395 µm (Figure 34c). These changes were also accompanied by a reduction in the thickness of the cornea from 500 to 400 µm (Fig34c–d).

These findings were complemented by the distribution of the principal tensional stresses on Bowman's layer in the healthy and button corneas. In the healthy cornea, the tension spread evenly over the meridians and was regularly punctuated by concentric reinforcement stresses (Fig34e). By contrast, the keratoconic cornea exhibited a completely disrupted state of stress: tensional stress ran predominantly in latitudinal directions and was strong and highly disorganized at the inferocentral apex (Fig34f).

We then subjected this model to three analyses to determine the effect on corneal shape of (1) increasing the softening in the button or throughout the whole cornea, (2) softening specific corneal layers inside the button, and (3) simply dispersing the posterior stromal lamellae orientation in the button. To achieve this, either μ and k1 in the collagen-based layers in various corneal areas were reduced by the indicated divisors (Analyses 1–2) or kappa (fiber dispersion) in the posterior stroma was increased (Analysis 3).

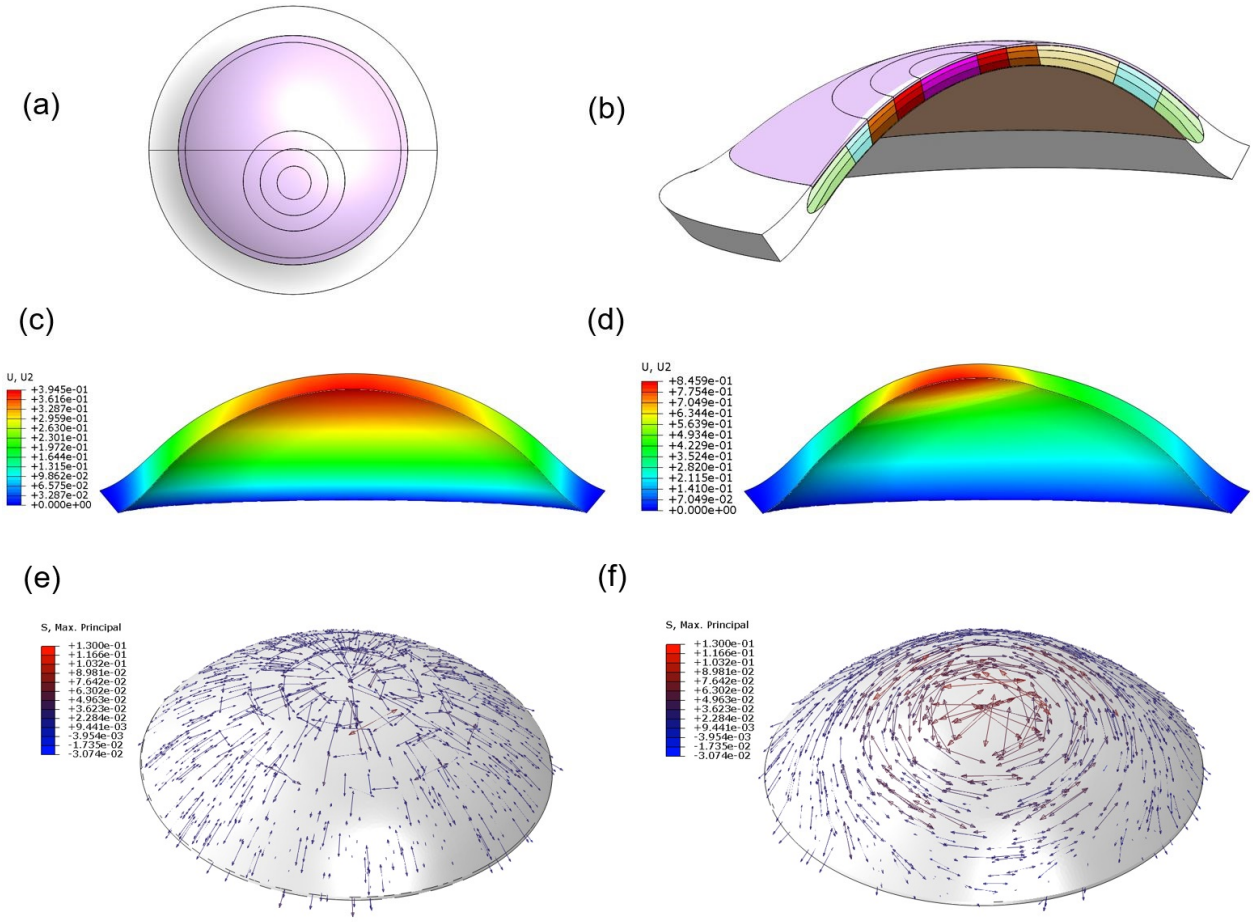

Figure 34: Generation of a button of tissue at the inferocentral cornea and the effect of gradually softening it on corneal displacement and directions of maximum principal tensional stress. (a, b) The button is shown from the anterior view (a) and in cross-section (b). It bears three concentric zones that describe the button center (dark-pink), middle (red), and periphery (brown). (c–f) Distribution of corneal displacement (c, d) and directions of maximum principal tensional stress (e, f) when Bowman's membrane and the stromal layers in the concentric zones of the button were increasingly softened with softest center. Softening was achieved by dividing the isotropic variable μ and the anisotropic variable k1 in Bowman's membrane and the stromal layers of the button center, middle, and periphery by 30, 20, and 10, respectively. Normal IOP was then applied. The healthy cornea without a softened button is shown in (c) and (e).

7.1.1 Analysis 1: Effect of local and global softening on corneal shape and thickness

Keratoconus has genetic links [136], including with congenital connective tissue disorders such as Ehlers-Danlos Syndrome (EDS). This condition is characterized by deranged synthesis/organization of collagen fibers and thin corneas [137]. It is thought that such collagen disorders may render individuals more prone to eye rubbing-induced keratoconus [5]. We used our model to test whether such a systemic condition, which would soften the entire corneal microstructure, spontaneously induced keratoconus.

Thus, the μ and k1 stiffness parameters of all collagen-based layers in our model were divided by 3. The resulting cornea-wide EDS-like softening did increase corneal deformability: the maximal displacement of the EDS-like cornea was 701 μm (Figure 35e) versus 395 μm for the healthy cornea (Figure 35a). The cornea-wide softening also induced corneal flattening and slight thinning (Case 5 in Figure 35), which is consistent with clinical observations of EDS

[137]. However, a conical shape was not achieved. A 10-fold increase in cornea-wide softening (achieved by dividing μ and k1 by 30) simply amplified the thinning and flattening: again, a bulge was not noted (data not shown). Moreover, strain distribution analyses showed that like the normal cornea, the EDS-like cornea exhibited homogeneous deformation (green/blue-green areas in Figure 35b, f).

In comparison, a mild softening in the inferocentral button generated keratoconus-like elevation and thinning. Indeed, when μ and k1 of the stromal and Bowman's layers in the center, middle, and periphery of the button were respectively divided by 10, 6.7, and 3.3 (mild softening; one-third of the softening in the heavily softened button in Figure 34d), a local conic deformation was observed. As shown by Fig(35), the maximal vertical displacement at the button apex rose from 395 μm in the healthy cornea Fig(35a) to 636 μm for the mildly softened case (Fig35c).

Analysis of the distribution of strain showed that while the normal cornea exhibited homogeneous deformation (green/blue-green areas in Figure 35b), the conic cornea displayed concentrated deformation in the inferocentral zone (red/orange areas in Figure 35d). Thus, cornea-wide thinning does not spontaneously induce keratoconus: local softening in a small area is needed to achieve this.

Finally, Fig(35) also shows the corneal thinning induced by softening as measured by black arrows. Imposing IOP on the healthy cornea caused it to deform and thin by a certain amount, but in the softened cornea, the thinning is much more important (up to 3-fold higher). This close relationship between vertical button displacement and corneal thinning can be attributed to Poisson's effect caused by the tissue deformation.

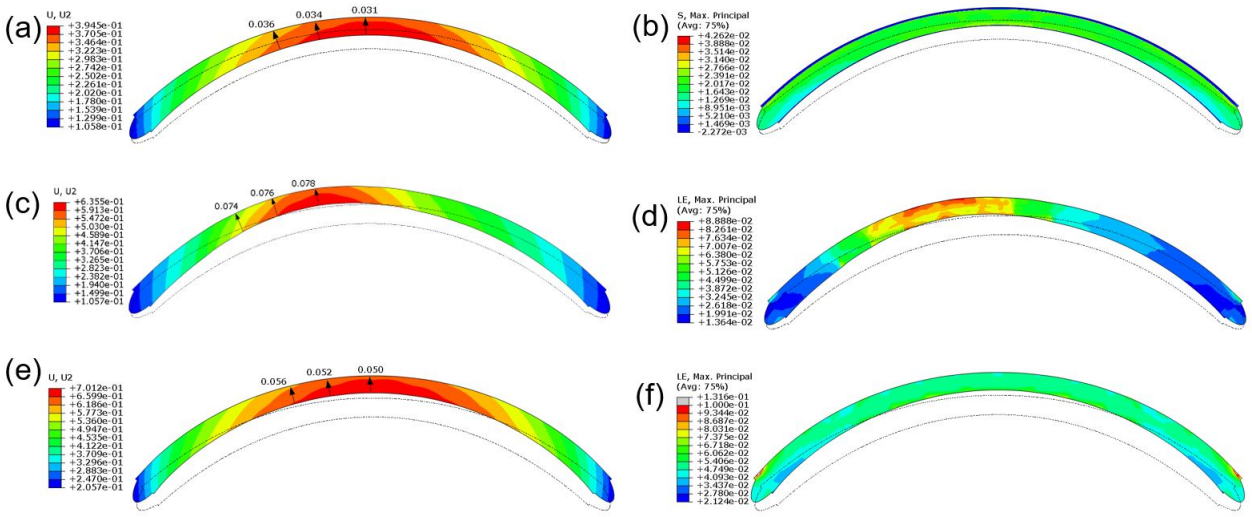

Figure 35: Effect of softening the cornea locally or globally on the vertical corneal displacement (U, U2) (a, c, e) and maximal principal strain (LE, Max. Principal) (b, d, f) when the cornea is exposed to normal IOP. (a, b) A healthy cornea. (c, d) The cornea in which a button of tissue was softened as shown in Fig(34a, b, d) but with a third of the softening (i.e. the isotrophic variable μ and the anisotrophic variable k1 in Bowman's layer and the stromal layers in the button center, middle, and periphery were divided by 10, 6.7, and 3.3, respectively). (e, f) An Ehlers-Danlos-like cornea where the whole cornea was softened by dividing μ and k1 in Bowman's layer and the stromal layers by 3. Red and blue in (a, c, e) indicate high and low displacement, respectively. Red and blue in (b, d, f) indicate high and low strain, respectively. The position of the cornea without IOP is depicted by the dotted-line shape

7.1.2 Analysis 2: effect of softening specific collagen-based layers on corneal shape and thickness

In this second analysis, we performed a sensitivity analysis in which we softened one or more of the collagenous corneal layers in the corneal button by dividing μ and k1 in the selected layer in the button center, intermediate zone, and periphery by 30, 20, and 10, respectively.

It showed that softening Bowman's layer plus the anterior stroma increased maximum displacement from 395 μm in the healthy cornea to 446 µm but did not thin the cornea (Fig(36a, c). It also reduced the stress on these layers while not significantly increasing it in other layers (Fig36b, d).

Softening Bowman's membrane, anterior stroma plus the middle stroma increased displacement to 527 μm, created very minor bulging and 1.7-fold more thinning compared to the effect of IOP on the healthy cornea. It also further reduced anterior layer stress while introducing stress in the posterior stroma (Figu36e, f). Softening only the middle stroma or only the posterior stroma had similar effects as anterior layer softening (Cases 8 and 10 in Figure 41).

Marked bulging was only observed when both the middle and posterior stromal layers were softened, leading to a displacement of 606 μm (Figure 36g). This associated with the most pronounced corneal thinning of 2.2-fold and increased anterior layer stress (Fig36h).

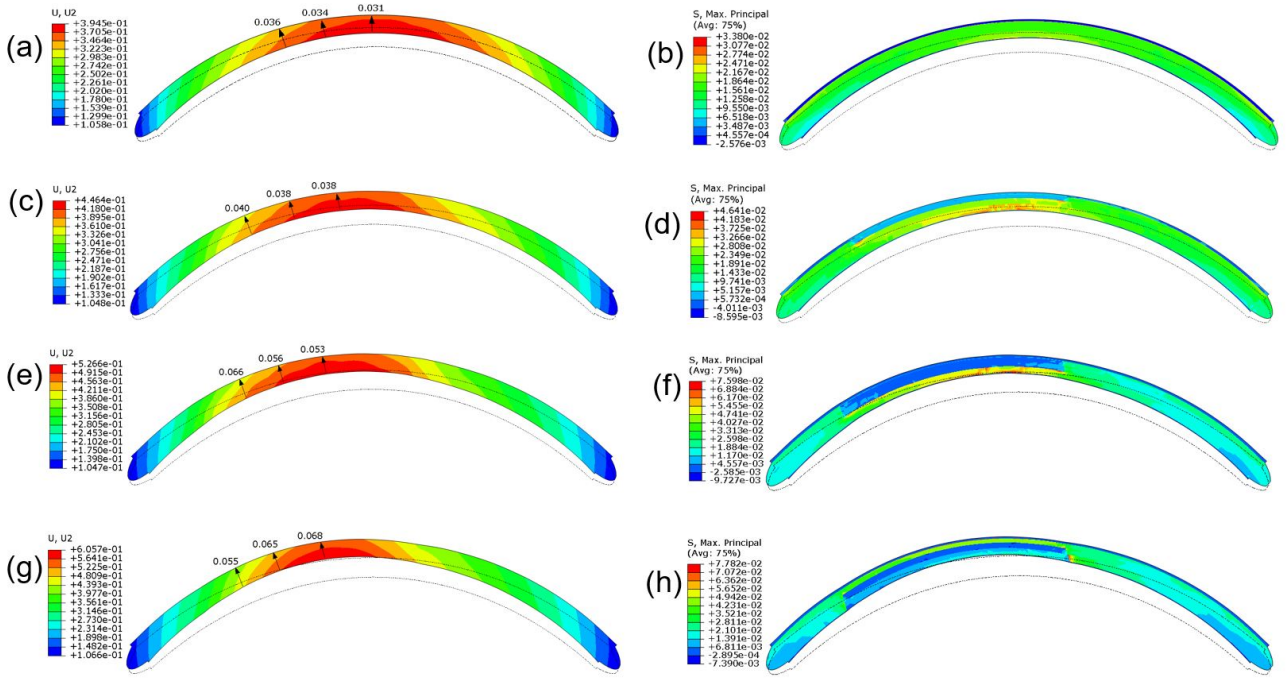

Figure 36: Effect of softening specific layers in a button of tissue on corneal displacement in the vertical axis (U, U2; mm) (c, e, g) and maximal principal strain (S. Max. Principal; MPa) (d, f, h). Gradual softening in the indicated button layer(s) was achieved by dividing the μ (isotropic variable) and k1 (anisotropic variable) of the button center, middle, and periphery by 30, 20, and 10, respectively. (a, b) The healthy cornea. (c, d) Bowman's layer and the anterior stroma were softened. (e, f) Bowman's layer and the anterior and middle stromal layers were softened. (g, h) The middle and posterior stromal layers were softened.

7.1.3 Analysis 3: effect of disrupting the anisotropic orientation of posterior lamellae on corneal shape

Since we observed that softening the middle-posterior stroma led to maximal displacement (Fig35 and 36), we investigated whether simply increasing lamellar disorganization in the posterior stroma of the button would induce corneal elevation. Thus, we increased kappa, which describes collagen fiber dispersion in our model, from 0.01 (no dispersion) to 0.33 (maximal dispersion) in the posterior stroma of the button. Stiffness variables (μ and k1) remained unchanged. Indeed, increasing fiber dispersion in the posterior stroma caused corneal displacement to rise to 461 μm. When we increased the dispersion in the posterior and in middle stroma simultaneously, the displacement was augmented to 581 μm (Figure 37).

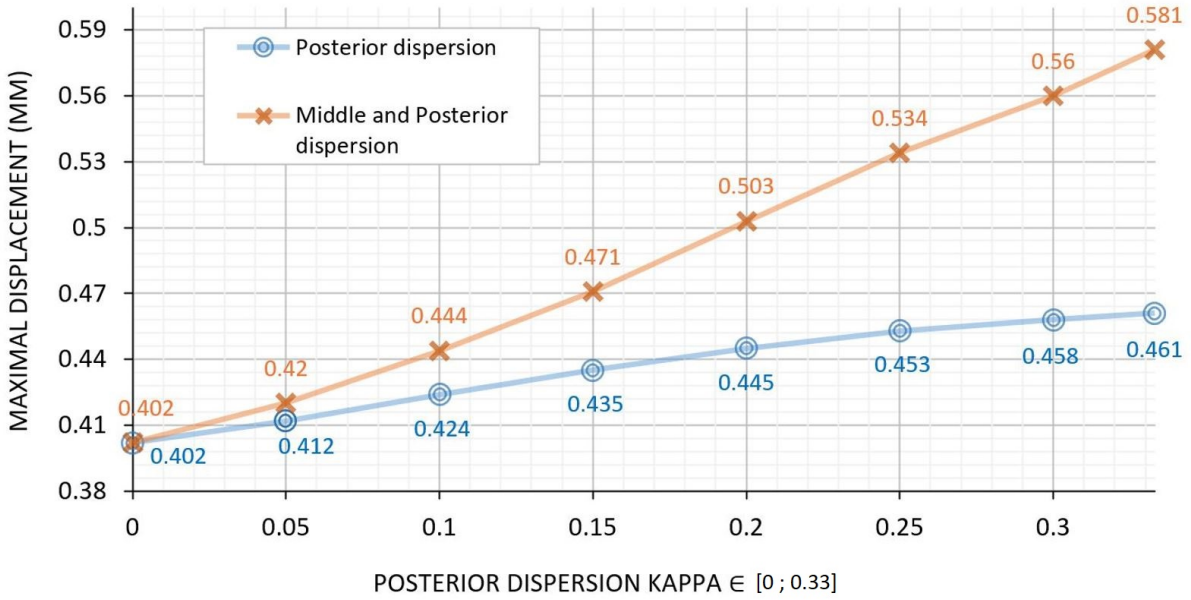

Figure 37: Effect of increasing the dispersion of the collagen fibers in the posterior stroma (blue plot) and the posterior and middle stroma (orange plot) of the button on corneal displacement in the vertical axis (mm). Only kappa (fiber dispersion) was changed in the selected layer(s). Note that while the x axis shows only the degree of posterior dispersion, the orange plot shows the effect of also dispersing the fibers in middle stroma. For this, kappa in the middle stroma was gradually increased from 0.16 to 0.33. Measurements are connected to show a trend line

7.2 Effect of eye rubbing on corneal layers

Eye rubbing has been proposed to be an important environmental etiological factor in keratoconus [1]. To determine how eye rubbing-induced stress is distributed throughout the cornea, we subjected the model of the healthy cornea (i.e. without any zones of weakening) to two common modes of eye rubbing in keratoconus [108], namely, horizontal rubbing of the cornea with either a rigid knuckle or a soft finger pad.

The same corneal model was used in Abaqus to simulate eye rubbing. For this, we defined a contact pair with the finger as the master surface and the cornea as the slave surface in a contact model. The tangential behavior between this contact pair was set to be frictionless, meaning that when nodes were in contact, they slid on each other without inducing shear forces. This is justified by the presence of the eyelid sliding between the finger and the cornea during

eye rubbing.

Since we did not want any penetration between this contact pair, we defined normal behavior as a "hard" contact pressure-overclosure formulation in Abaqus. As a constraint enforcement method for hard contact, we started with a direct method, which avoided approximations such as those in penalty or augmented Lagrangian constraint enforcement. Since our simulation converged with this method, we did not have to resort to other methods.

On the basis of a study modelling the biomechanical response to non-contact tonometry, [52] we anticipated that the indentation would compress the anterior stromal lamellae and relieve some of the IOP-induced tension on them. By contrast, the indentation would push the posterior stroma inward, thereby further stretching its lamellae. Thus, we hypothesized that the indentation tension would be transferred to the posterior cornea as shown in Fig(38).

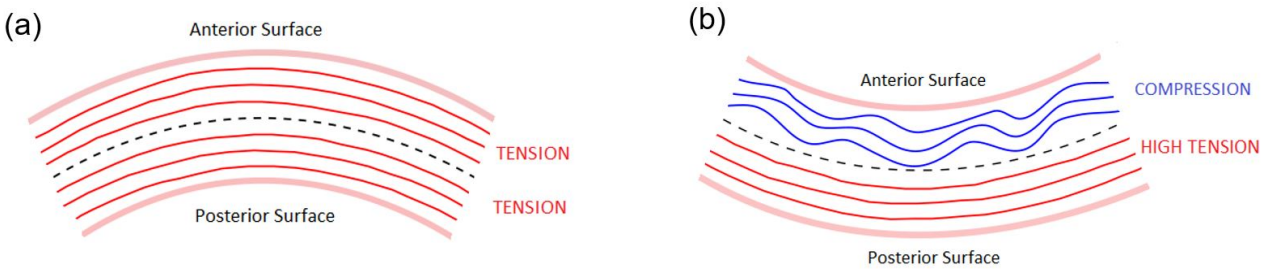

Figure 38: Depiction of the fibers in the cornea under normal IOP loading (a) or from abnormal loading due to eye rubbing or air puff test that bends the cornea inward (b)

The eye rubbing model showed that relative to a cornea in normal condition, eye rubbing with the knuckle tripled the maximal first principal stress from 338 kPa to 1230 kPa. Notably, the stress induced by knuckle rubbing manifested in the posterior stroma near Descemet's membrane (red/orange regions) while the anterior stroma experienced negative stress due to the lamellar compression (dark-blue regions) (Figure 39). Finger tip rubbing associated with less stress intensity (627 kPa) but the same distribution. These results confirmed that such indentation loading transfer the tension to the posterior stroma.

It has been proposed that the mechanical weakening that mediates keratoconus is due to failure of the cross-links between collagen fibers [18] [110] [135] [138], with Angelillo et al. showing that shear stress on the cornea loads the proteoglycan matrix that holds the collagen lamellae in place [139]. Since such stress could cause lamellar failure of the nature seen in keratoconus [22] [110] [113] [138], we asked whether finger rubbing would impose various types of stress on the cornea. For that, we displayed the distributions of Cauchy's stresses in the spherical coordinates σ_{rr} , $\sigma_{\theta\theta}$, and $\sigma_{r\theta}$ representing tensional-opening, shear-sliding, and shear-tearing stress, respectively.

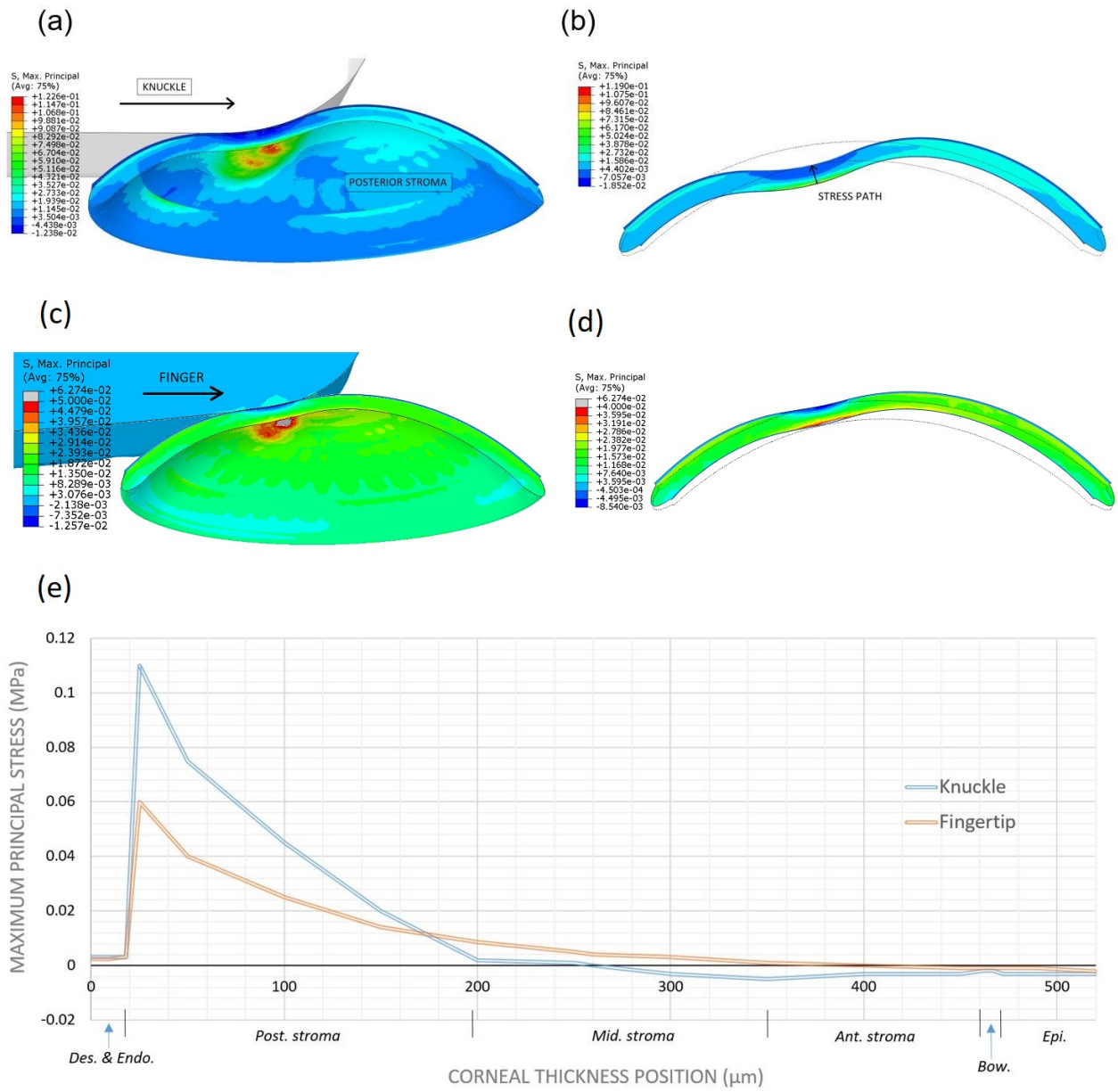

Figure 39: Effect of knuckle and fingertip rubbing on the maximal tensional stress (MPa) throughout the cornea. Effect of rubbing with a rigid knuckle (a–b) or fingertip (c–d) on stress throughout the cornea. In (a and c), the black arrow indicates the direction of knuckle/finger movement. Descemet's membrane and the endothelium are not displayed in these images. In (b and d), the unstressed cornea is indicated by the fine-line image. In (a–d), red indicates high stress areas. (e) Plot showing the distribution of maximal tensional stress on the various layers of the cornea during knuckle rubbing (blue) and fingertip rubbing (orange). Ant., anterior; Avg, average; Bow, Bowman's layer; Des. & Endo, Descemet's membrane and endothelium; Epi., epithelial layer; Mid., middle; Post., posterior; S, Max Principal, maximum principal strain

Numerical results showed that radial (tensional-opening) stress σ_{rr} was an order smaller than the others and mainly composed of compression areas on the anterior layers (Figure 40a). Hoop (shear-sliding) stress $\sigma_{\theta\theta}$ manifested high tensile posterior stress along with low compressive stress in the anterior layer (-30 kPa) (Figure 40b). This hoop-stress pattern under bending is consistent with findings from other studies [12] [52]. The distribution of shear-tearing stress $\sigma_{r\theta}$ showed shear bands that originated from the posterior stroma and ran to the anterior

layers (Figure 40c).

The position and orientation of these shear bands is similar to corneal Vogt's striae reported in the literature [111] [114], suggesting a mechanism of shearing strain damage resulting in the appearance of shear bands similar to the ones viewed in ductile materials.

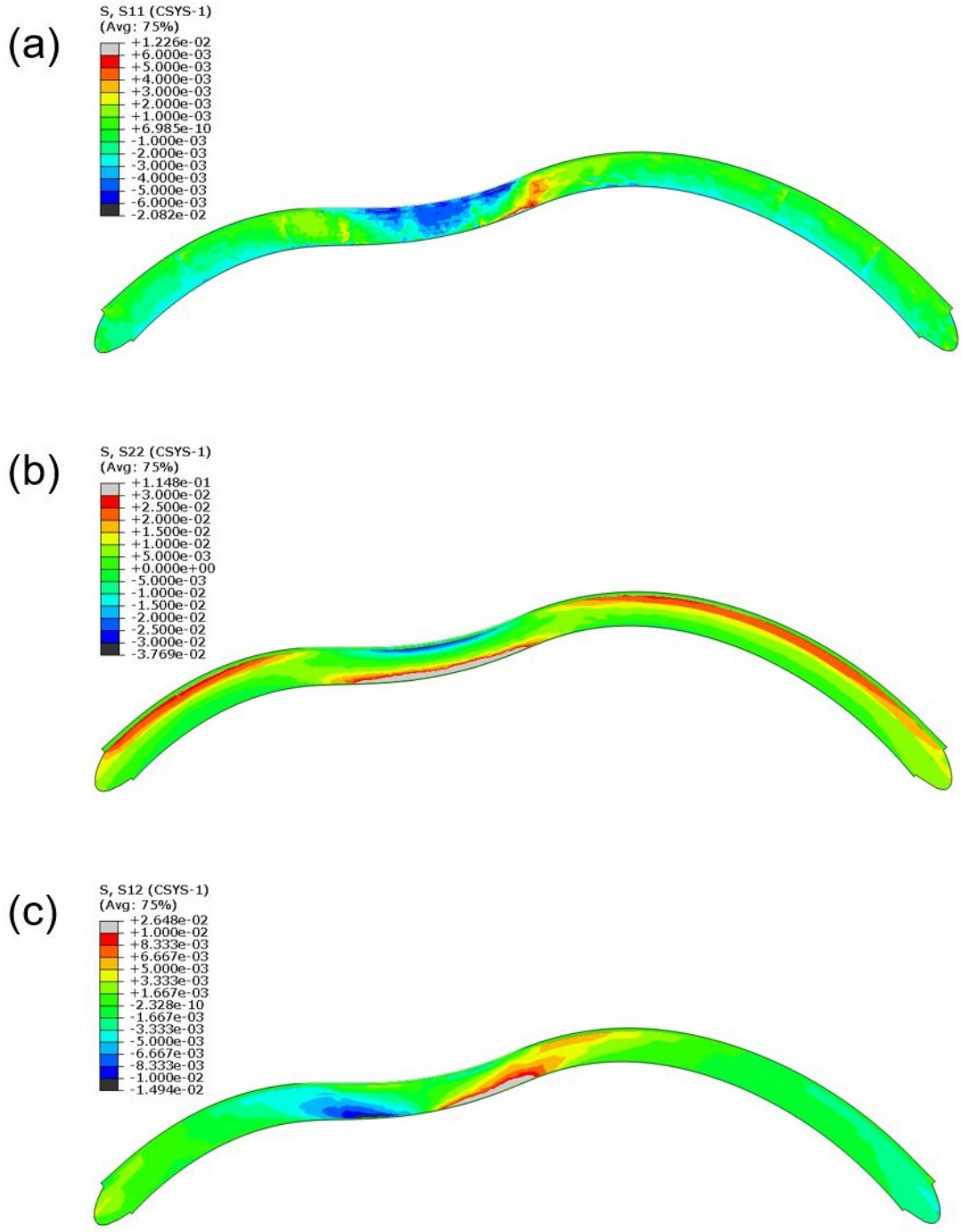

Figure 40: 2D cross-section of the cornea showing the effect of finger rubbing on different corneal stresses. (a) Radial stress (σ_{rr}). This indicates the radial tension towards or away from the central axis of the spherical coordinate system. (b) Hoop stress ($\sigma_{\theta\theta}$). This indicates the circumferential tension in the tangential direction along the cornea. The zone with negative stress (blue) is the compressed anterior zone. The greatest tension is on the most bent zone of the cornea. (c) Shear stress, pushing one part of the structure in one direction and the other in the opposite direction ($\sigma_{r\theta}$)

8 Discussion

Despite research over 1.5 centuries, keratoconus pathogenesis remains mysterious as numerous factors have been incriminated, indicating the existence of various degradation processes [1] [125]. The present study used finite element modeling to explore the potential contribution of mechanics to its pathogenesis.

Using finite element models of increasing complexity, several groups have showed that keratoconus-like bulging can be achieved by reducing fiber stiffness within part of the cornea [7] [8] [57], decreasing local corneal thickness [8], gradually reducing both corneal thickness and material properties [9], or weakening the transversal bonds between collagen fibrils [73].

Our simulation successfully reproduced the bulging shape of a keratoconic cornea and suggested that the progressive worsening of the disease (as indicated by its bulging and thinning) may be due to gradual loss of tissue stiffness that is localized in a concentric area. Two conditions for a conic deformation have been identified: the need for a gradual softening localized on a concentric area, and a loss of stiffness in the posterior stroma to get a significant steepening.

The study also demonstrated the importance of the orthogonal architecture of the posterior stroma: an increase in collagen fiber dispersion in the middle-posterior stroma of the corneal button induced subclinical keratoconus-like elevation. Thus, keratoconus may be initiated, at least in part, by localized damage to the deep stromal architecture [140].

These findings are consistent with the hypothesis in the field that keratoconus may be caused at least in part by mechanical stress that damages the microstructures in the stroma, especially the ground substance-mediated crosslinks (transverse bonds) between collagen lamellae that maintain an ordered collagen architecture [18] [126] [127] [141]. Indeed, Angelillo et al. [139] have shown that ectatic corneas exhibit abnormally high shear stress and disorganized principal stress lines that reflect deviant fiber organization, which was also confirmed by our plot of disrupted state of stress in the keratoconic cornea as shown in Fig(34e,f).

Together, these findings are suggestive of transmission of shear stress onto the stromal matrix in ectasia [139]. Since the plywood structure of the posterior stroma induces fewer of transversal bonds in this layer, it is possible that damage could occur easily in the posterior stroma. These microstructural changes together may eventually promote lamellar slippage and disorganization, thereby reducing the stiffness of the cornea and rendering it unable to resist IOP.

This mechanism would be facilitated in young and/or genetically predisposed individuals with a weakest stromal microstructure. In opposite, diabetics and older people with more rigid tissues due to more cross-links from glycosylation would develop significantly less the disease, as the vast majority of patients developing the disease are less than 30 years old [14] [142].

Additionally, the simulation showed that excessive pathological deformation is impossible as long as the middle and posterior layers of the stroma are not affected (Fig35c). These findings are consistent with the fact that in the vast majority of cases (99.97%), laser assisted in situ keratomileusis (LASIK) and photorefractive keratectomy (PRK) surgery do not induce corneal bulging [143]. These procedures, which are used to treat refractive errors, involve ablating part of the anterior stroma with or without the epithelium and Bowman's membrane. Thus, the mid-posterior stroma is generally strong enough on its own to resist the IOP and maintain the corneal curvature needed for good refraction after ablation of anterior layers.

A review of all the numerical experiments run on the conical deformation of the cornea is presented in the Fig(41). This figure summarizes the results presented before and shows that only the cases with a local loss of stiffness that also affects the posterior stroma give rise to a conical deformation, as identified by the asterisk symbol *.

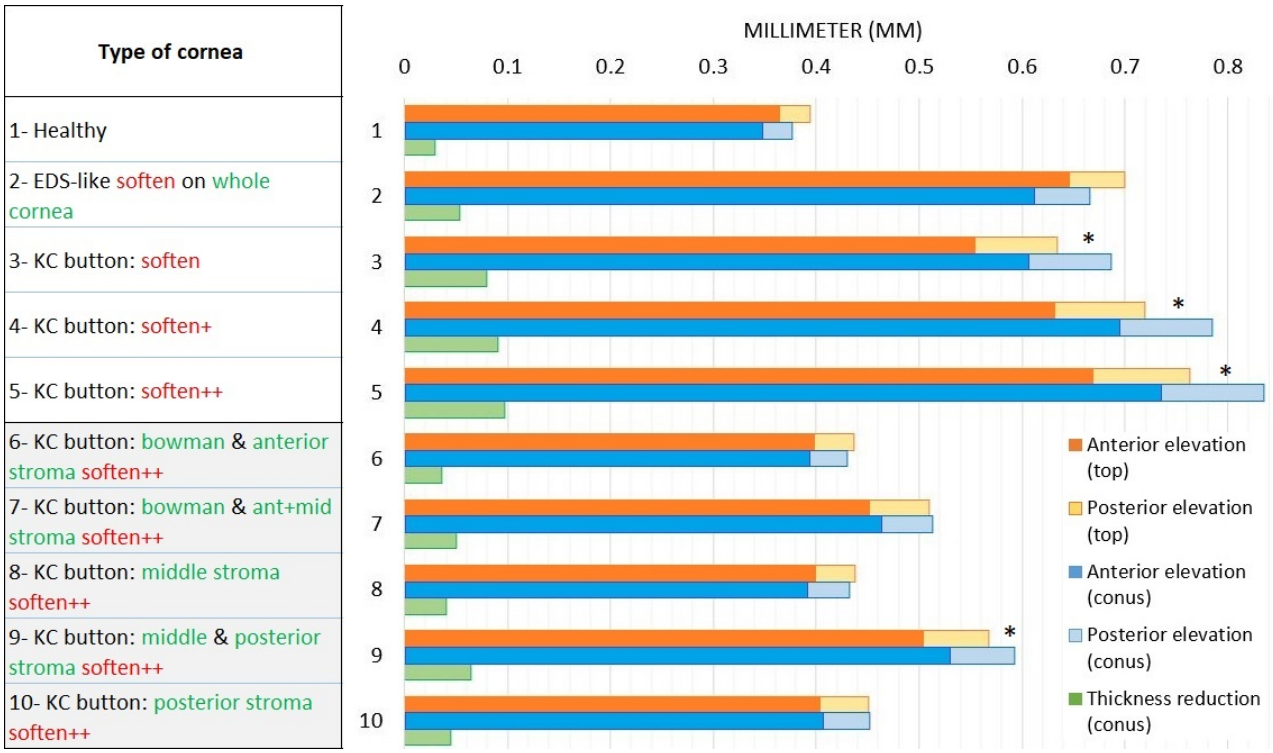

Figure 41: Summary of the effect of softening the whole cornea (Case 2), a button of corneal tissue (Cases 3–5), or specific corneal layers in the button (Cases 6–10) on the anterior and posterior elevation at the corneal apex (orange and yellow bars, respectively), the anterior and posterior elevation at the button apex (dark and light blue bars, respectively), and loss of corneal thickness (green bars). Cases where the blue bars are higher than the yellow/orange bars indicate keratoconus-like elevation (indicated by *). Note that button elevation is matched by corneal thinning (green bars). [In Case 2, the whole cornea was softened by dividing μ (isotropic variable) and k1 (anisotropic variable) throughout the cornea by 3. In Case 3, an inferocentral button of the cornea was gradually softened by dividing both μ and k1 in the center, intermediate zone, and periphery by 10, 6.7, and 3.3, respectively. In Cases 4 and 5, button softening was respectively doubled (to 20, 13.3, and 6.7, respectively) and tripled (to 30, 20, and 10, respectively). In Cases 6–10, the indicated button layer(s) were softened by dividing their μ and k1 values in the center, intermediate zone, and periphery by 30, 20, and 10, respectively. EDS, Ehlers-Danlos Syndrome-like; KC, keratoconus.]

So far, this research highlighted the importance of the posterior stroma in the biomechanics of the cornea and shows that the role of anterior layers may be less important than supposed for the development of Keratoconus. Of note, this result is not in agreement with the normally accepted physiopathology saying that Keratoconus starts with anterior layer degradation. The pathogenesis as perceived by ophthalmologists follows the order of appearance of observable clinical signs of corneal degradation. Indeed, because epithelial and Bowman's layer alteration have been among the most reported observations in Keratoconic cornea, the usual explanation for its pathogenesis advocates the involvement of epithelial cells. However, one element is questioning this hypothesis: the existence of subclinical keratoconus.

A subclinical Keratoconus is a form of the disease where the cornea presents topographic abnormalities but not pronounced enough to reach the threshold of KC suspicion with automated classification. This early stage of the disease is characterized by a normal anterior curvature but with the presence of an abnormal posterior elevation as shown in Fig(42) [144]. Because no clinical signs of epithelial thinning or Bowman's membrane degradation can be notified in tomography, it appears that anterior layers degradation are not early signs of the disease. Understanding the early mechanics of keratoconus may be particularly important to prevent the development of post-LASIK ectasia as this rare complication has been retrospectively linked to a subclinical keratoconus not diagnosed at the consultation [145]. Thus, early keratoconic corneas may have keratoconus-promoting microstructural weaknesses in their posterior stroma long before anterior layer degradation is observed.

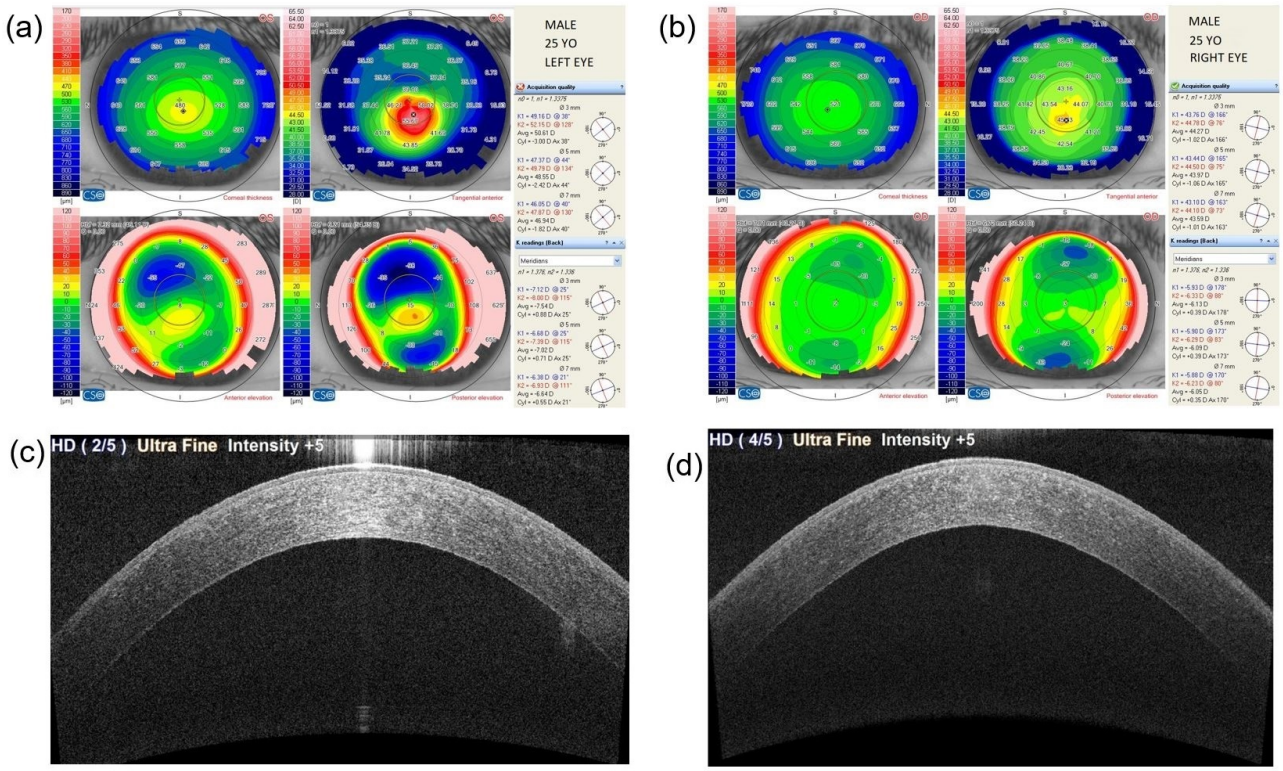

Figure 42: Videokeratoscopy (a, b) and OCT (c, d) in a patient with diagnosed keratoconus in the left eye (a, c) and suspicion of subclinical keratoconus in the right eye (b, d). Videokeratoscopy showed posterior corneal elevation as described by the red area in (a) but OCT showed no abnormal signs in (c). (Data of an anonimized 25 years old male patient from Metz-Thionville hospital)

This hypothesis is supported by ultrastructural studies by the Akhtar group [113] [138] as they showed that a corneal button from a patient with "mild" keratoconus who elected to undergo surgery due to contact lens-related discomfort did not show any epithelium, basement membrane, and Bowman's layer abnormality. In addition, this mild keratoconus had normal lamellae throughout the anterior stroma but undulating lamellae in the middle and posterior stroma. Significantly, more advanced keratoconus cases exhibited steeply undulating disorganized stromal lamellae that were much more prevalent in the posterior stroma near Descemet's membrane than in the anterior stroma. Thus, these ultrastructural studies suggest that changes to the lamellar architecture of the cornea start in the posterior stroma [113] [138]. Only later,

when keratoconus has progressed, do the lamellae in the anterior stroma show signs of disruption.

Thus, we hypothesize that mechanical instability in a small area of the mid-posterior stroma due to loss of cross-links between the collagen lamellae may play an important early role in keratoconus pathogenesis as shown in Fig(27: "hypothetical microstructural changes in the stroma that may lead to keratoconus onset and progression"). This hypothesis is of course deduced from the results of our numerical model and its specific parameters and therefore needs to be confirmed by further investigations.

We propose that in keratoconus, the conic deformation may be induced the loss of interlamellar cross-links and the consequent slipping of lamellae over each other and away from the keratoconic button. This possibility is supported by a growing number of studies and observations [126] [127] [134]. First, photooxidative corneal crosslinking, which introduces crosslinks between collagen fibers and increases corneal stiffness, is an effective treatment for keratoconus [146]. Second, the X-ray scattering study of Meek and Boote on advanced keratoconus buttons showed interlamellar slippage throughout the stroma [18][135]. Third, Pandolfi et al. showed with a different modeling approach that weakening the transverse bonds between the fibers, but not the fibers themselves, greatly increased corneal deformation [73].

Key clinical features of keratoconus are not only the bulging of the cornea but also its localized thinning. We observed in our simulation that keratoconus-like bulging always associated with proportional thinning of the cornea. Thus, tissue deformation by itself (i.e. without loss of material) can induce corneal thinning. This reflects Poisson's effect, namely, the phenomenon where materials that are expanding in one direction tend to contract in the transverse direction. Together, these observations suggest that instability in a small area of the middle-posterior stroma due to loss of cross-links between the collagen lamellae may play a crucial early role in keratoconus pathogenesis (Figure 27b).

We also observed that eye rubbing is often quite severe in patients with keratoconus [147] and considerable evidence suggests it may be an etiological factor of Keratoconus [107]. Indeed, many ophthalmologists currently recommend their patients to stop rubbing their eyes to avoid disease progression [6] [108].

We showed that eye rubbing tripled the stress on the posterior stroma and caused it to bend inward, therefore tensely stretching the posterior corneal layers. By contrast, the anterior layers, which were in direct/near contact with the knuckle/finger, were subjected to small compressive mechanical stress. This pattern was also replicated by a numerical study employing the Pandolfi model of the healthy cornea [10] [59] that showed the in vivo corneal responses to a probe pressed onto the corneal apex or air-puff tonometry [11].

Our simulation also displayed shear stresses starting from the posterior stroma and running obliquely towards the anterior layers. This orientation is evocative of Vogt's striae, a clinical sign often associated with keratoconus. These striae are more numerous in keratoconus than in healthy corneas [102] and may indicate an history of high mechanical stress on the stromal microstructure [114].

The possibility that keratoconus is initiated by external mechanical stress, potentially by eye rubbing, is also supported by the fact that: (1) the structural damage in keratoconus is limited to an inferocentral corneal button, which is also the thinnest and fragile area [18] [125] [135], and we showed that gradually softening such a button of tissue indeed generated keratoconic elevation; (2) the earliest sign of keratoconus is posterior corneal elevation, which is suggestive

of damage in this area; and (3) cornea-wide EDS-like softening [137] did not evoke keratoconus.

Thus, it seems possible that eye rubbing induces concentrated mechanical stress in the posterior stroma. The interlamellar links in this region may not be designed to deal with repeated bending stress and eventually break, causing posterior lamellar disorganization and eventually keratoconus [124] [126] [127] [134] [141]. It is likely that this mechanical effect works in conjunction with other likely etiological contributors, including those operating in the anterior layers [1].

Study strengths and limitations

The novelty of this study lies in the use of a different geometrical approach, namely, the splitting of the stroma into different parts, which allowed us to examine the relative contributions of each part to corneal mechanics and keratoconus pathogenesis. This approach led to a convincing shape of keratoconic deformation that associated with localized corneal thinning.

This study had also some limitations as it was limited to mechanical aspects and do not embrace the complexity of the cellular and biochemical mechanisms that participate in corneal physiology and keratoconus pathogenesis. Consequently, the study should only be seen as generating new hypotheses for subsequent experiments. Modeling studies that include key pathogenic matrix remodeling processes such as collagen turnover, enzymatic degradation, and mechanobiology are needed to determine the role(s) of these processes in keratoconus. Moreover, studies on subclinical keratoconus that examine the early changes in posterior stromal microstructure are warranted.

9 Fiber-reinforced cornea summary

We successfully developed a model of ectatic cornea which was able to recreate the pronounced local bulging characteristic of keratoconus disease. To further explore the biomechanical properties and corneal injuries that associate with keratoconus formation, we conducted two numerical experiments. In the first one, we weakened the corneal structure and determined that a conical deformation and corneal thinning emerged only when a local softening gradient was applied on a button of tissue in conjunction with a posterior stroma softening. Softening the anterior layers of the button or the whole cornea did not create conical deformation. In the second numerical experiment, we identified that eye rubbing profoundly stressed the deep posterior stroma while other layers were negligibly affected.

These studies together suggests that the posterior stroma plays an important early role in keratoconus pathogenesis as shown in Fig(27). Under the condition of additional validation, these findings would suggest that characterizing the posterior stroma may help to diagnose keratoconus at a very early stage, thereby facilitating early interventions that prevent disease progression.

The utility of the model could be further improved by smoothing the transition zone between material sections. For this purpose, an incorporation of an homogenization method from micromechanics could be used to average the mechanical properties between the layers. Another approach would be to analytically describes the parameters distribution throughout the whole geometry to improve the model accuracy, but it would make the modeling of pronounced local bulging much more difficult.

Another improvement would be to explicitly include the presence of cross-links between collagen fibers in order to directly assess the effect of their loss/breakage in the context of

diseases. A publication in this regard was recently made by Holzapfel in its 2020 paper "An arterial constitutive model accounting for collagen content and cross-linking" [24].

To continue the investigations on Keratoconus, a patient specific analysis could be conducted on several keratoconic corneas on which we have data over time to assess the disease evolution and see if it matches the model behavior.

This study could also be used as a basis for the development of a predictive model that would predict the evolution of keratoconus in each patient, based on previously collected topographical data that would be analyzed to create a statistical basis on the speed of disease progression according to the extent of the current deformation. Several axes of improvement are therefore conceivable following this part on the modeling of keratoconus.

Part III
The cornea as an hydrated tissue

10 Objective

Most biological tissues are highly hydrated, porous and permeable, such that their interstitial fluid flow and pressurization may contribute significantly to their mechanics. These porous tissues can be modeled as a mixture of a fluid and a solid, where the fluid itself may consist of a mixture of a solvent and multiple solutes [26] [74] [75]. The solutes in the interstitial fluid can be of several types such as nutrients, ionic species or waste products. The solid matrix of biological tissue can also be modeled as a heterogeneous mixture of solid constituents, such as collagen, elastin and charged proteoglycans.

As we saw with the modeling of fiber-reinforced tissue, current finite-element-based models for mechanical analysis of the cornea treat the interfibrillar fluid as an incompressible or nearly incompressible elastic solid [10] [11] [12] [13]. While this approach is convenient, it cannot describe the bulk compressibility and swelling behaviour of the tissue. Thus, a modeling capability for predicting tissue swelling pressure in the cornea would be of considerable clinical significance as excessive swelling modifies the curvatures of the cornea's bounding surfaces and defeats its focusing function [14].

A full biomechanical description of the tissue must describe how the solid collagen structure and its specific organization resists the fluid pressure. For example, in the human cornea, the collagen fibers are aligned with the surfaces and cannot resist swelling in the thickness direction, except near the anterior region where they become inclined and intertwined, possibly to stabilize the optical surface against abnormal hydration. As a result, the human cornea swells through its thickness mainly as a posterior bulge [89] [148].

Additionally, the cornea presents a particular and interesting case because the tissue depends on active transport processes to maintain its hydration level and prevent swelling. Indeed, the endothelial layer supports active molecular mechanisms that produce an outward flux of ions from the stroma into the aqueous humour [17] [35] [88] [149] as shown in Section(2.3). Our numerical analysis will investigate how such active pumping reduces the stromal ionic concentrations and contribute to lower the osmotic pressure and water swelling pressure of the cornea.

Because the complete molecular details of the regulatory system responsible for active ion transport are not yet fully understood, which could require Na^+, K^+, ATPase and carbonic anhydrase activity to transport HCO_3^-, Cl^- and possibly Na^+, a simplified active flux formulation based on bicarbonate only will be used in the model as suggested by Bonnano [35].

The goal of these chapters is to formulate a model of the in vivo cornea that includes active hydration control mechanisms and captures the features of charge effects and swelling missed by purely hyperelastic approaches. In that regard, a multiphasic mixture model is developed based on mixture theory to account for the presence of GAG fixed charges and mobile ions and to model their transport across the endothelium. The endothelium pump-leak balance mechanism is included in the model and applied to study Fuch's dystrophy.

In the Chapter(11), we present the mixture theory framework and all the others theoretical aspects needed to develop the multiphasic model. The Chapter(12) presents the model developments with its verification and validation steps. The Chapter(13) presents the application of the model to recreate a cornea with impaired hydration control such as in Fuch's dystrophy. This part ends with a preliminary modeling work to describe membrane reactions into a multiphasic mixture in Chapter(14).

11 Mixture theory for biological tissue

This chapter is a presentation of the theory required to develop the multiphasic corneal model. It is composed of 3 sections: a first one introducing the mixture theory (with its complete description given in appendix A), a second section on the physical phenomena related to the presence of solute, and a third section on the modeling of solute fluxes in the cornea. The development of the model itself starts in the next chapter.

Mixture theory is used to model multiphase systems using the principles of continuum mechanics generalised to several interpenetrable continua. It requires the formulation of mass, momentum, and energy balance equations for each of the mixture constituents, which may then be summed together to produce equivalent formulations for the mixture as a whole as shown in appendix A. It allows to model various phenomena such as problems of permeation, diffusion and barophoresis, as well as electrokinetic phenomena such as electrophoresis, electro-osmosis, and streaming potentials and currents [26].

Initially developed for materials made of single solid and liquid phases, the first extension of mixture theory to include solutes was presented by Lai et al. (1991) [150], who modeled cartilage as a triphasic material consisting of a charged porous solid matrix, an interstitial fluid composed of a neutral solvent (water) and two monovalent counterions such as Na^+ and Cl^-. This formulation was used to reproduce Donnan's law that predicts the osmotic swelling pressure arising from soluble charge isolation between the triphasic mixture and its surrounding fluid environment.

Before mixture theory, most models of solute transport within porous media employed Fick's phenomenological law, neglecting the friction between solutes and the solid matrix. However, experiments had showed that solute diffusivity within a free fluid versus the diffusivity within the mixture could be different, depending on the molecular size of the solute relative to the pore of the solid [151]. Consequently, when phenomenological relations emerge from the mixture equations, such as Darcy's law and Fick's law, terms neglected in these earlier phenomenological formulations were rediscovered [26]. Indeed, in mixture theory, frictional drag tensors $f^{\alpha\beta}$

between every pair of constituents are defined, resulting in interaction not described by the phenomenological relations [34] [94].

11.1 Linear Momentum balance expressed in nodal variables

The complete development of the mixture theory framework is presented in appendix A. Here are presented only information essential for the model development.

The three constituents of a mixture are the porous-permeable solid matrix (α=s), the solvent (α=w), and solutes (α=u). The motion of constituent α in a mixture is given by $\boldsymbol{\chi}^\alpha(\boldsymbol{X}^\alpha,\mathrm{t})$, where t is time and $\boldsymbol{X}^\alpha$ is the position of a material point of constituent α in the reference configuration of that constituent. In the current configuration at time t, an elemental region whose center of mass is $\boldsymbol{x} = \boldsymbol{\chi}^\alpha(\boldsymbol{X}^\alpha,\mathrm{t})$ contains material from all constituents α. The velocity of α is given by $\boldsymbol{v}^\alpha = \partial\boldsymbol{\chi}^\alpha/\partial t$.

Functions of state in a multiphasic material are the stresses $\boldsymbol{\sigma}^\alpha$, the internal momentum supplies $\hat{\boldsymbol{p}}^\alpha$, and the mixture free-energy density Ψ_r. When solutes are included, the list of state variables must be extended to include the solute apparent density $\rho_r^\alpha = J\rho^\alpha$ (mass of solute α per volume of the mixture in the reference configuration). The dependence of the mixture free energy Ψ_r on solute density is then embodied in the chemical potential $\mu^\alpha = \partial\Psi_r/\partial\rho_r^\alpha$. All developments are shown in appendix A.

In a finite element modeling framework, nodal variables (degrees of freedom) are defined continuous across elements boundaries. In this mixture framework, variables that satisfy continuity requirements are the solid displacement $\boldsymbol{u}$ and the mechano-electro-chemical potentials $\tilde{\mu}^\alpha$ of the solvent and solutes. However, since $\tilde{\mu}^\alpha$'s are less practical to use as nodal variables, an alternative form of the solvent mechano-chemical potential $\tilde{\mu}^w$ is introduced as the the effective fluid pressure $\tilde{p}$ by subtracting the referential chemical potential:

$$\tilde{p} \equiv \rho_T^w(\tilde{\mu}^w - \mu_0^w) = p - p_0 - R\theta \sum_{\alpha\neq s,w} c^\alpha \tag{48}$$

Note that $p - p_0$ represents a gauge pressure relative to some ambient pressure p_0; thus, it is common to let $p_0 = 0$ so that p represents that gauge pressure.

Physically, since $R\theta\sum_{\alpha\neq s,w} c^\alpha$ is the osmotic contribution to the fluid pressure, $\tilde{p}$ may be interpreted as the mechanical contribution of the total fluid pressure which does not result from osmotic effects. Similarly, the effective solute concentration $\tilde{c}^\alpha$ is an alternative form of the solute electro-chemical potential $\tilde{\mu}^\alpha$ that subtracts out the referential chemical potential of the solute,

$$\tilde{c}^\alpha \equiv c_0^\alpha exp[\frac{M^\alpha}{R\theta}(\tilde{\mu}^\alpha - \mu_0^\alpha)] = \frac{c^\alpha}{\tilde{\kappa}^\alpha} \tag{49}$$

with the partition coefficient previously defined as $\tilde{\kappa}^\alpha = \hat{\kappa}^\alpha exp[-z^\alpha\frac{F_c}{R\theta}(\psi-\psi_0)]$. Here again, $\psi - \psi_0$ represents the electric potential relative to some reference potential ψ_0; it is common to assume that $\psi_0 = 0$. Because $\tilde{p}$ and $\tilde{c}^\alpha$ are formulated by subtracting the arbitrary referential chemical potentials, they are more convenient to use than $\tilde{\mu}^w$ and $\tilde{\mu}^\alpha$ as nodal degrees of freedom [100].

When using $\tilde{p}$ and $\tilde{c}^\alpha$ as potentials, the mass fluxes given in Eqs.(A.14), (A.15) may be reordered to express the equivalent fluid volume flux,

$$\boldsymbol{w} = -\tilde{\boldsymbol{k}}.(grad\tilde{p} + R\theta \sum_{\alpha \neq s,w} \frac{\tilde{k}^\alpha}{d_0^\alpha} \boldsymbol{d}^\alpha.grad\tilde{c}^\alpha) \tag{50}$$

and solute molar fluxes,

$$\boldsymbol{j}^\alpha = \tilde{k}^\alpha \boldsymbol{d}^\alpha.(-\varphi^w grad\tilde{c}^\alpha + \frac{\tilde{c}^\alpha}{d_0^\alpha}\boldsymbol{w}), \quad \alpha \neq s, w \tag{51}$$

These two expressions are relatively compact but describe a broad set of phenomena. In the generalized Darcy's law (50), the first term (gradient of effective fluid pressure $grad(\tilde{p})$) includes both permeation (fluid flux in response to a pressure gradient: $grad(p)$) and osmosis (fluid flux in response to a concentration gradient: $grad(R\theta \sum_\alpha c^\alpha)$). The second term includes the partition coefficient and ratio of diffusivities in the mixture and in free solution $\frac{\tilde{k}^\beta}{d_0^\beta}\boldsymbol{d}^\beta.grad(\tilde{c}^\alpha) = \frac{\tilde{k}^\beta}{d_0^\beta}\boldsymbol{d}^\beta.grad(c^\alpha \hat{k}^\alpha exp(\frac{z^\alpha F_c \psi}{R\theta}))$ and accounts for the increased resistance to solvent flux due to the friction between solute and solid matrix. It also includes gradients in electric potential and therefore equally describes electro-osmosis.

If the solid matrix does not slow down the diffusivity of the solute (an idealized situation), then d and d_0 are the same; if the solute is not charged, or if the electric potential is uniform, then the effect of the electric potential is eliminated; if additionally we assume that the solute solubility is 1 (the solute can occupy all of the pore space in the solid matrix), then all these terms in the second part of the equation combine to cancel out the osmosis mechanism in the first term, so that only the permeation mechanism remains (Darcy's law). In summary, the second term describes interactions between the solute and the charged solid matrix, which influence the solvent flux.

The second expression is the generalized Fick's law (51) which incorporates diffusive term from the concentration gradient of solute ($-\varphi^w grad\tilde{c}^\alpha$) and a convective term related to the volumetric flux of fluid described with the generalized Darcy's law ($\frac{\tilde{c}^\alpha}{d_0^\alpha}\boldsymbol{w}$). These two terms are related to the hindrance of solid matrix in the current configuration described by the diffusivity tensor $\boldsymbol{d}^\alpha$.

11.2 Physics of solutes in mixture

In addition to permeation, diffusion and barophoresis, including solutes and charged particles in the theory allows to describe electrokinetic phenomena such as electrophoresis, electro-osmosis, and streaming potentials and currents [150] [152].

Therefore, the various transport phenomena that can be described in a multiphasic model are hereby listed:

1. Permeation: solvent transport in response to a pressure gradient
2. Barophoresis: solute transport in response to a pressure gradient
3. Diffusion: solute transport in response to its concentration gradient
4. Electrophoresis: solute transport in response to an externally applied electric potential gradient

5. Osmosis: solvent transport in response to solute concentration gradient

6. Electro-osmosis: solvent transport in response to an electric potential gradient

Electro-osmosis is a transport phenomenon in which water molecules are dragged as solvation shell by ionic species along electric field lines, which are conducted from anode to cathode. Solvation is the process of reorganizing solvent and solute molecules into solvation complexes (ions surrounded by solvent). Solvation involves bond formation, hydrogen bonding, and van der Waals forces. The solvation of a solute by water is called hydration as illustrated in Figure 43.

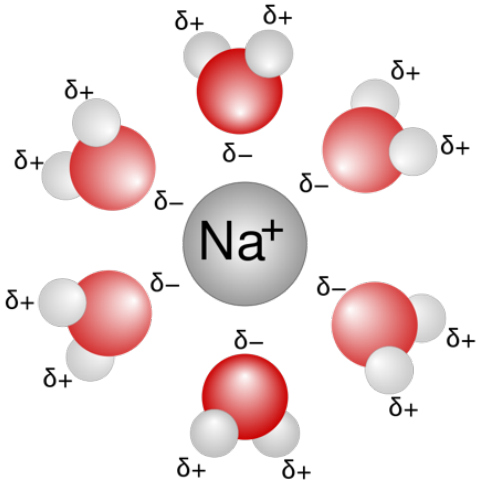

Figure 43: Schematic showing a sodium ion solvated by water molecules. This complex drags water by electro-osmosis when an electric gradient is present [74]

11.2.1 Osmotic pressure definition

From the introduction of chemical potential, the development leading to the osmotic pressure equation shows how the pressure is governed by the presence of electric charges in an electrolytic solution. The entire development can be found in the book "Mechanics and physics of porous solids" from Olivier Coussy [74] and a synthesis is presented in this section.

In the case where a single solute is present, with $x = \bar{N}_{solute}$ its molar fraction so that the molar fraction relative to the solvent is $1 - x$, a mathematical development exists to find an expression of the osmotic pressure. We assume the solution to be ideal so that the chemical potential of the solvent noted μ_0 can be expressed in the form:

$$\mu_0 = \mu_0^*(p, T) + RTln(1 - x) \tag{52}$$

If the solution is dilute so that $x << 1$, we have $ln(1 - x) \approx -x$. From the previous expression we then obtain

$$\mu_0 = \mu_0^*(p, T) - RTx \tag{53}$$

On the right-hand side, the first term $\mu_0^*(p, T)$ represents the chemical potential related to the solvent of the solution at pressure p and temperature T as if it was pure, while the second term $-RTx$ accounts for the decrease of its chemical potential resulting from the entropy of

mixing induced by the presence of the solute.

Considering a pure solvent separated from the solution by a semipermeable membrane that allows the transfer of solvent but not the solute molecules, the composition equilibrium equation $\mu_j = \mu_j^{'}$ applies to the solvent in the solution since it is in contact with the pure solvent through the membrane as illustrated in Fig(44).

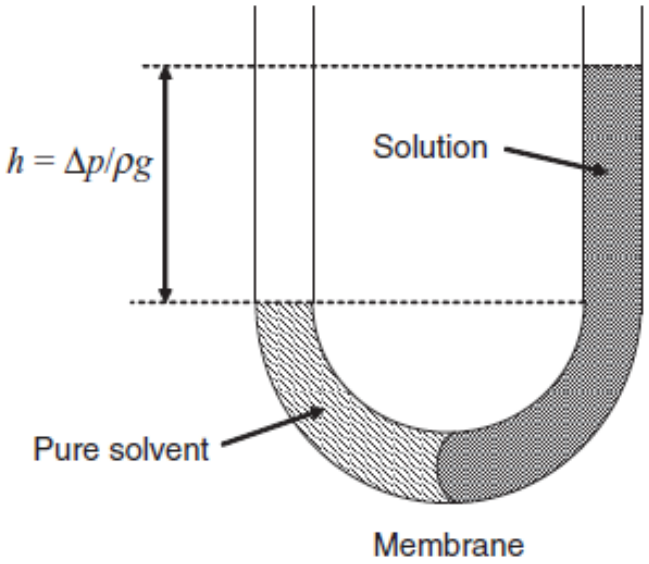

Figure 44: Illustration showing that osmotic pressure can be measured by the difference in heights observed when thermodynamic equilibrium is achieved between two compartments separated by a semipermeable membrane [74]

The chemical potential of the solvent in both compartments must therefore be equal, allowing us to write

$$\mu_0^*(p - \Delta p, T) = \mu_0^*(p, T) - RTx \tag{54}$$

where Δp is the difference in pressure that the membrane has to sustain. The dilute assumption $x << 1$ induces $\Delta p/RT << 1$ so that previous equation can be rewritten in the form

$$\frac{\partial \mu_0^*}{\partial p}\Delta p \approx RTx \tag{55}$$

The first part of the state equation $\bar{V} = \frac{\partial \mu}{\partial p}$ from [74] applied to the pure solvent and combined with Equation (55) provides

$$\Delta p \approx RTx/\bar{V}_0 \tag{56}$$

The solution being dilute, we have $N_{solute} << N_{solvent}$ so that $x/\bar{V}_0 \approx N_{solute}/V = c$, where c is the solute concentration, thus we can rewrite the previous equation in the form of Van't Hoff's law

$$\Delta p \approx RTc \tag{57}$$

The excess pressure Δp undergone by the solution with respect to the pure solvent is called the osmotic pressure. The osmotic pressure is the extra pressure that is required to establish the thermodynamic equilibrium between the solvent in the solution and the pure solvent. This extra pressure offsets the loss in free energy of the solvent induced by the mixing with the solute.

11.2.2 Electroneutrality condition in mixture

If the solid matrix and solutes are electrically charged, an electric potential ψ may arise if it is assumed that the mixture must satisfy the electroneutrality condition. This is similar to the pressure p arising from the assumption that the mixture constituents are incompressible.

A charge number z^α may be associated with each mixture constituents, representing the number of charges per mole of that constituent. In most biological mixtures, the solvent is water and thus neutral ($z^w = 0$).

For solids, a parameter c^F may be used in lieu of a molar concentration and associated charge number, which describes a net fixed charge density $c^F = z^s c^s$. The fixed charge density in the deformed configuration is then obtained from the dilation J as:

$$c^F(J) = J^{-1} c_0^F \tag{58}$$

With $\boldsymbol{E}$ the electric field, ϵ_w the dielectric permittivity of the electrolyte solvent and c^α and c^F the mobile ions and fixed charge density. Gauss's law for the mixture is then expressed as:

$$\nabla.(\epsilon_w \boldsymbol{E}) = c^F + \sum_{i=+,-} z^\alpha c^\alpha \tag{59}$$

Because it is assumed that there can be no charge accumulation in the mixture, the electroneutrality condition must therefore be enforced with the following constraint:

$$c^F + \sum_\alpha z^\alpha c^\alpha = 0 \tag{60}$$

Multiplying the mass balance with z^α / M^α, taking the sum over all constituents and making use of the above electroneutrality constraint (60) produces $div \sum_\alpha z^\alpha \boldsymbol{j}^\alpha = 0$, or equivalently,

$$div \boldsymbol{I_e} = 0 \tag{61}$$

where $\boldsymbol{I}_e = F_c \sum_\alpha z^\alpha \boldsymbol{j}^\alpha$ is the electric current density (the net rate of flow of electric charge per unit area of the mixture) and F_c is Faraday's constant. Thus, the electro-neutrality condition produces a constraint on the current density vector field in the mixture.

Poisson-Boltzmann equation for electric potential To calculate the electrostatic potential ψ, the non linear Poisson–Boltzmann equation is derived from two components: the Poisson equation, which relates the variation in electrostatic potential in a medium of constant dielectric to the charge density, and the Boltzmann distribution, which governs the ion distribution in the system.

With the electric field E related to the electric potential ψ by:

$$E = -\nabla \psi \tag{62}$$

If we assume that the ionic species in the mixture follows a Boltzmaan distribution with $c_0 = c(\psi(0))$ the bulk concentration, the local ion concentration is calculated as:

$$c^\alpha = c_0^\alpha exp(\frac{-z^\alpha F_c \psi}{RT}) \tag{63}$$

Employing previous Eq.(62) into Eq.(59), we obtain the Poisson-Boltzmann equation for a uniform fixed charge concentration.

$$-\nabla^2 \psi(\boldsymbol{X}) = \frac{F_c}{\epsilon_w}[c^F(\boldsymbol{X}, J) + \sum_{i=+,-} z^\alpha c^\alpha(\psi(\boldsymbol{X}))] \tag{64}$$

Application to triphasic material Because of the electroneutrality of the whole system, the bulk concentrations of anions and cations c_0 are identical. With the concentrations following a Boltzmaan distribution as in Eq.(63), we calculate the net space charge as:

$$\rho_v(\psi) = c^F + c_0 F_c(exp(-\frac{F_c\psi}{RT}) - exp(\frac{F_c\psi}{RT})) = c^F - 2c_0 F_c sinh(\frac{F_c\psi}{RT}) \tag{65}$$

And then from the Poisson's equation:

$$\nabla^2\psi = -\frac{\rho_v}{\epsilon_w} \tag{66}$$

Substituting Eqs. (65) and (63) into Eq. (66) yields the Poisson–Boltzmann equation for a triphasic material:

$$\nabla^2 \psi(\boldsymbol{X}) = \frac{F_c}{\epsilon_w}[c^F(\boldsymbol{X}, J) + 2c_0 sinh(\frac{F_c}{RT}\psi(\boldsymbol{X}))] \tag{67}$$

11.2.3 Donnan equilibrium of a polyelectrolyte in salt solution

When a multiphasic material with a charged solid matrix is immersed in a solution with ions that may transport into or out of its boundaries, the electroneutrality condition enforces an imbalance in the quantity of ionic species of the solid interstitial fluid and external bathing solution. This fixed charge-induced imbalance produces an osmotic pressure difference known as the Donnan osmotic pressure.

Donnan theory is used to model the osmotic pressure of materials at equilibrium and is therefore a special case of the more general Poisson-Boltzmaan theory [153]. Because it provides an analytical solution, it is very useful for verification purposes of a mixture model. It can include spatially invariant fixed charges or it can be extended to model complex charge distributions [89].

A Donnan equilibrium model is computationally more efficient than a multiphasic model because it only describes the volumetric contribution of a solid material instead of modeling the different phases in a multiphasic framework. It also requires much less effort in setting up initial and boundary conditions since solute concentrations and fluid pressure are implicitly incorporated in the analysis. The downside of a Donnan equilibrium model is that variables such as solute concentrations, fixed charge density, osmotic pressure and electric potential are not outputted through time and only a steady solution exists.

In a triphasic model under traction-free conditions on its boundaries, a state known as free swelling, an equilibrium is achieved when solvent and solute fluxes have stopped [88]. If we

consider a sample of isolated corneal stromal tissue placed in a NaCl bath, for an ideal Donnan equilibrium model the distribution of mobile ions at equilibrium should satisfy

$$c_{Na^+} * c_{Cl^-} = c_0^2 \tag{68}$$

where c_{Na^+} and c_{Cl^-} are the mobile ion concentrations in the tissue and c_0 the ionic concentration in the bath. The GAG disaccharide units provide a fixed (non mobile) negative charge density c_0^F in the reference configuration and can be calculated in the deformed state from the dilation J as $c^F(J) = c_0^F/J$. The electroneutrality condition within the polyelectrolyte phase then requires

$$c_{Na^+} - c_{Cl^-} + c^F = 0 \tag{69}$$

Equations (68) and (69) can be solved for the concentrations of mobile ions at equilibrium (details in [154]), giving

$$c_{Na^+/Cl^-} = \pm\frac{c^F}{2} + \sqrt{\frac{(c^F)^2}{4} + c_0^2} \tag{70}$$

The osmotic pressure in the tissue and in the bath (with $c_{Na^+} > 0$ and $c_{Cl^-} < 0$) are given respectively by

$$P_{tissue} = RT(c_{Na^+} - c_{Cl^-}), \qquad P_{bath} = 2RTc_0 \tag{71}$$

where R is the gas constant and T is the absolute temperature. The analytical expression of osmotic pressure difference P_{os} between the two phases is then expressed as

$$P_{os} = P_{tissue} - P_{bath} = 2RTc_0\left(\sqrt{\left(\frac{c_0^F}{2Jc_0}\right)^2 + 1} - 1\right) \tag{72}$$

and yields to the osmotic compressibility of the material [89].

$$K_{os}(J) = \frac{RTc_0^F}{J^2\sqrt{1 + \left(\frac{2Jc_0}{c_0^F}\right)^2}} \tag{73}$$

This simple model shows swelling behavior. For example, if the electrolyte fixed charge c_0^F is increased or the bath ionic concentration c_0 is decreased, the osmotic pressure increases by virtue of Eq.(72), which in turn increases the interstitial fluid pressure and the swelling tendency of the tissue. In the corneal stroma, the internal elastic fiber system will engage and resist the swelling pressure.

Finally, the Donnan electrostatic potential denoted $\tilde{\psi}$ can be calculated by substituting $c^F(J) = \frac{c_0^F}{J}$ into the Poisson-Boltzmann Eq.(67) which allows it to be solved analytically as:

$$\tilde{\psi}(J) = -\frac{RT}{F_c} sinh^{-1}\left(\frac{c^F(J)}{2c_0}\right) = -\frac{RT}{F_c} sinh^{-1}\left(\frac{c_0^F}{2Jc_0}\right) \tag{74}$$

The higher the electric potential, the greater the concentration of the counterions in the tissue. These counterions form a diffuse layer around the solid fixed charges where the intensity of the electric potential is the highest. This concentration decreases away from the fixed charges.

Since the electric potential has the same sign as the electric charges from which it originates, its contribution to the chemical potential is negative in our case. A greater positive contribution

to the chemical potential has to offset the negative contribution of the fixed charges so that when the equilibrium is achieved, the chemical potential within the tissue is equal to the chemical potential of the bulk solution of the bath.

Since the bath is not subjected to any electrostatic interactions ans has a constant potential, an excess of osmotic pressure develops within the tissue by dragging water molecules trapped into solvation complexes, which eventually provokes its swelling.

11.3 Modelling flux of solutes

In a multiphasic framework, transports of fluid results from a combination of passive (non-reactive) and active (reactive) processes involving solvent and solutes. We previously introduced several passive transport phenomena such as permeation, diffusion, barophoresis, electrophoresis and electro-osmosis, that depend on fluid pressure and concentration gradient of charged or neutral species [74].

Active processes on the other hand depend on chemical reactions that occur on cell membranes to trigger the transport of solutes and molecules across it by means of energy consumption. This type of transport across membranes enables solute movement against their concentration gradient and is one of the major factors for keeping homeostasis of biological tissues. In the cornea, the movement of fluid and solutes across endothelial membranes allows the transport of nutrients and the maintenance of a balanced osmotic pressure.

To understand the concept of active momentum supply, we can consider an analogous concept to that of a membrane pump: an exhaust fan that pulls air across it. If the fan is not turning, air can flow across it in the presence of a pressure difference across the wall: this would be considered passive transport, and the air flowing past the fan blades encounters some frictional resistance caused by the drag force against the blades. This would be represented by a dissipative momentum supply in mixture theory $\hat{\boldsymbol{P}}_{\boldsymbol{d}}$.

Now considering the fan motor turned on, it imparts momentum to the air, driving it across the wall. This would represent the active momentum supply, and an external source of energy is required to produce this active momentum supply. Both passive and active momentum supplies may co-exist. The fan may try to push air down the pressure gradient or against it, implying that these momentum supplies may add or subtract.

For a biological membrane, the ideal way of modeling active membrane transport is via chemical kinetics, whereby one models the binding of a molecule to the molecular motor, the translocation of the complex across the membrane, and the dissociation of the complex to release the molecule on the other side of the membrane.

Alternatively, in order to keep it simple and still recover the cornea physiology, active mechanisms can be incorporated through an active ionic flux treated as an independent term that is additive to the passive solute flux. Prescribing a solute molar flux as a boundary condition to model active flux can be compared to chemical kinetics as we impose a desired flux of solute no matter what other forces might be acting on it.

In this objective of modeling a simplified active flux, we may model the membrane as a volumetric domain (albeit a thin one), whose mechanisms of momentum dissipation are taken into account by $\hat{\boldsymbol{p}}_d^{\alpha}$, as represented in Eqs.(A.8,A.9) and the resulting flux equations (50) & (51). Then, we define non-dissipative interfaces Γ_i and Γ_e on the internal and external surfaces of the membrane.

These interfaces are immaterial analytical representations of the internal and external membrane boundaries and do not produce frictional exchanges with the solvent and solutes transporting across them. The friction is taken into account by the diffusive drag coefficients defined in the volumetric domain between the two interfaces, which arises from the difference of diffusivity between species in relation with their free diffusivity, as showed in the Section(11.3.2).

11.3.1 Non-equilibrium thermodynamics prerequisite

Non-equilibrium thermodynamics is concerned with transport processes and with the rates of chemical reactions. Understanding the basic concepts of non-equilibrium thermodynamics is essential as most phenomenological coefficients measured experimentally find their meaning in this theory, from which equivalences can be made with mixture theory.

In the article "The balance of fluid and osmotic pressures across active biological membranes with application to the corneal endothelium" by Cheng and Pinsky [88], a set of fluxes and conjugate forces equations based on non-equilibrium thermodynamics is presented. It describes fluxes of water and solutes across the endothelial membrane, and is applied to analyze the relationship between fluid pressure and active transport mechanisms in the cornea.

In their paper they provided the mathematical development showing that the liquid volume flux J_V and solute flux J_i across the membrane can be described by a linear combination of ΔP, ΔC_i and $\Delta\psi$:

$$J_V = L_p(\Delta P - \sum_k(\sigma_k RT\Delta C_k - (1-\sigma_k)z_k F\bar{C}_k\Delta\psi)) \tag{75}$$

$$J_i = (1-\sigma_i)J_V\bar{C}_i + w_i(RT\Delta C_i + z_i\bar{C}_i F\Delta\psi) \tag{76}$$

where L_p in $cm^3.(dyn.s)^{-1}$ is the hydraulic conductivity coefficient, ΔP in $dyn.cm^{-2}$ is the hydrostatic pressure difference on the two sides of the membrane, σ_k is the reflection coefficient of species k, ΔC_j in $mole.cm^{-3}$ is the concentration difference of species j on the two sides of the membrane, $\Delta\psi$ in V is the electrostatic potential difference on the two sides of the membrane, and ω_i in $mole.(dyn.s)^{-1}$ is the permeability coefficient of species i.

They treated the active ionic flux as an independent term that is additive to the passive solute flux without considering the underlying molecular mechanisms. In that regard, they incorporated an active pump rate of species i called J_{ai} expressed in $mole.(s.cm^2)^{-1}$ and rewrote the net solute flux equation as:

$$J_i = (1-\sigma_i)J_V\bar{C}_i + w_i(RT\Delta C_i + z_i\bar{C}_i F\Delta\psi) + J_{ai} \tag{77}$$

11.3.2 Link with Mixture Theory

In order to describe transport processes in a mixture framework, the general equations of mixture theory may be reduced to the case of a thin membrane and compared to the classical equations of non-equilibrium thermodynamics.

Like developed in previous Section(11.1) introducing Eqs.(50 & 51), the expression for the solvent flux takes the form:

$$\boldsymbol{w} = -\tilde{\boldsymbol{k}}.(grad\tilde{p} + R\theta \sum_{\alpha \neq s,w} \frac{\tilde{k}^{\alpha}}{d_0^{\alpha}} \boldsymbol{d}^{\alpha}.grad\tilde{c}^{\alpha}) \tag{78}$$

and for the solute flux

$$\boldsymbol{j}^{\alpha} = \tilde{k}^{\alpha}\boldsymbol{d}^{\alpha}.(-\varphi^{w} grad\tilde{c}^{\alpha} + \frac{\tilde{c}^{\alpha}}{d_0^{\alpha}}\boldsymbol{w}), \quad \alpha \neq s, w \tag{79}$$

where

$$\tilde{\boldsymbol{k}} = [\boldsymbol{k}^{-1} + \frac{R\theta}{\varphi^{w}} \sum_{\alpha \neq s,w} \frac{c^{\alpha}}{d_0^{\alpha}} (\boldsymbol{I} - \frac{\boldsymbol{d}^{\alpha}}{d_0^{\alpha}})]^{-1} \tag{80}$$

is the effective permeability of the interstitial fluid within the charged porous solid and

$$\tilde{\kappa}^{\beta} = \hat{\kappa}^{\beta} exp(-\frac{z^{\beta} F_c \psi}{R\theta}) \tag{81}$$

is the partition coefficient of solute β in the multiphasic mixture. This partition coefficient depends on the electric potential ψ. The effective fluid pressure $\tilde{p}$ is given by

$$\tilde{p} = p - R\theta\Phi \sum_{\beta} c^{\beta} \tag{82}$$

where p is the actual pressure and c^{β} is the actual concentration of solute β. We can adapt these flux relations for membrane transport by projecting them along the unit normal $\boldsymbol{n}$ to the membrane. We also assume that the hydraulic permeability $\tilde{\boldsymbol{k}}$ of the interstitial fluid and the diffusivities $\boldsymbol{d}^{\beta}$ of the solutes are directed along $\boldsymbol{n}$ such that

$$\begin{aligned} \tilde{\boldsymbol{k}} &= \tilde{k}\boldsymbol{n} \otimes \boldsymbol{n} \\ \boldsymbol{d}^{\beta} &= d^{\beta}\boldsymbol{n} \otimes \boldsymbol{n} \end{aligned} \tag{83}$$

Substituting Eqs.(83) into the projected fluxes $w_n = \boldsymbol{w} \cdot \boldsymbol{n}$ and $j_n^{\beta} = \boldsymbol{j}^{\beta} \cdot \boldsymbol{n}$ produces

$$\begin{aligned} w &= -\tilde{k}(\boldsymbol{n} \cdot grad\tilde{p} + R\theta \sum_{\beta \neq s,w} \frac{\tilde{k}^{\beta} d^{\beta}}{d_0^{\beta}} \boldsymbol{n}.grad\tilde{c}^{\beta}) \\ j_n^{\beta} &= \tilde{k}^{\beta} d^{\beta}(-\varphi^{w}\boldsymbol{n} \cdot grad\tilde{c}^{\beta} + \frac{\tilde{c}^{\beta}}{d_0^{\beta}} w_n), \quad \beta \neq s, w \end{aligned} \tag{84}$$

Now we assume that the membrane is very thin, with thickness h, such that we can approximate the projected gradients appearing in Eqs.(84) as

$$\begin{aligned} -\boldsymbol{n} \cdot grad(\tilde{p}) &\approx \frac{\Delta\tilde{p}}{h} \\ -\boldsymbol{n} \cdot grad(\tilde{c}^{\beta}) &\approx \frac{\Delta\tilde{c}^{\beta}}{h} \end{aligned} \tag{85}$$

where $\Delta f \equiv f_i - f_e$, with f_i the value of f on the internal side and f_e the value of f on external side, with $\boldsymbol{n}$ pointing from the internal side to the external side. Substituting (85) into Eqs.(84) produces the final membrane flux equations,

$$w_n = L_p(\Delta\tilde{p} + R\theta\sum_{\beta}(1-\sigma^{\beta})\Delta\tilde{c}^{\beta})$$
$$j_n^{\beta} = P^{\beta}\Delta\tilde{c}^{\beta} + (1-\sigma^{\beta})\tilde{c}^{\beta}w_n \tag{86}$$

where

$$L_p = \frac{\tilde{k}}{h} \tag{87}$$

is the membrane hydraulic conductance,

$$P^{\beta} = \frac{\tilde{\kappa}^{\beta}d^{\beta}\varphi^{w}}{h} \tag{88}$$

is the membrane permeability of solute β, and

$$\sigma^{\beta} = 1 - \frac{\tilde{\kappa}^{\beta}d^{\beta}}{d_0^{\beta}} \tag{89}$$

is Staverman's reflection coefficient for the solute across the membrane. These expressions account for the effect of charges and the electrical field they produce by incorporating the solute partition coefficient $\tilde{\kappa}$. This permeability expression is consistent with the one formulated early by Klyce [155] in 1979.

12 Hydrated corneal model development

This chapter introduces the multiphasic corneal model which also incorporates the endothelial active regulation. The mechanical properties needed to develop the multiphasic model are detailed in the Section(12.1). The Section(12.2) presents an introductory numerical test on biphasic material and the notion of pore pressure and consolidation. The Section(12.3) presents a model verification against the analytical solutions known on the triphasic case. The Section(12.4) presents the inverse procedure updated to incorporate additional parameters needed for multiphasic material. The Section(12.5) presents a validation that compares the model results to the clinical data available to assess its consistency.

12.1 Material properties for the multiphasic cornea

The amount of material parameters required in developing a multiphasic model is significant due to the need of describing each constituent and their interactions with each other. This is especially true for biological tissues that are composed of several layers with different properties.

In our case, the cornea is a multiphasic electrolyte gel with reinforcing fibers, consisting of a mixture of solid, fluid and ionic phases, immersed in an ionic bath at constant electrostatic potential ψ_0, hydrostatic pressure p_0, and ionic concentration c_0^{α}. The pressure acting on the internal surface of the cornea is taken to be 2266 Pa, or equivalently 17mmHg, a physiological value of the intra ocular pressure (IOP) of the cornea in vivo. The model temperature is set to 311K as summarized in Table(5).

Parameter	Symbol	Value	SI Unit
Temperature	T	311	K
Faraday constant	F_c	96485	A.s/mole
Gas constant	R	8.314	kg.m^2/(K.mol.s^2)
Intra Ocular Pressure	IOP	2266.17	Pa

Table 5: Global parameters used in the multiphasic model. The temperature corresponds to the one of the human body

As shown in Part(II) on Keratoconus , the fibrous aspects of biological tissues may be modeled using a continuous fiber distribution (CFD) to capture tension-compression nonlinearity, anisotropic fiber distributions, and load-induced anisotropy. The generalized structure tensor of Gasser et al. (2006) [49] is used in the HGO model to describe the dispersion of collagen fibers around a mean direction and is an adequate way of incorporating collagen fibers contribution in a soft tissue.

The stromal mechanical behavior of the solid phase in our multiphasic model will therefore be described with the same HGO model as previously. The main difference will be that the geometry of the stroma will not be cut in 9 parts but simplified in 2 parts: one for the anterior stroma and one for the posterior stroma. This is because this part focuses on multiphasic and transport aspects and doesn't need to describe in detail the distribution of fibers in the stroma.

In the HGO model, the strain energy density $\Psi(E_n)$ is designed with an exponential and power-law relations commonly used in soft tissue mechanics to describe strain hardening properties [49] :

$$\Psi_n(I_n) = \frac{\xi}{\alpha\beta}(exp[\alpha(I_n-1)^\beta]-1)\ , \quad \beta \geq 2,\ \xi, \alpha \geq 0 \tag{90}$$

where α, β, ξ are the material parameters. When $\alpha = k2$, $\beta = 2$, and $\xi = k1$, Eq.(90) reduces to the exponential function described by Holzapfel et al. (2000) [49]. The posterior stroma parameters used in this multiphasic model are shown in Table(6).

Parameter	Symbol	Value	SI Unit
Matrix stiffness	C_{10}	0.01	MPa
Poisson ratio	ν	0.3	-
Fiber stiffness	ξ	0.1	MPa
Coef. exponential term	α	150	-
Power exponential term	β	2	-

Table 6: Mechanical properties for the fiber reinforced solid phase of the posterior stroma: the isotropic ground substance of the corneal stroma is described with a Neo-Hookean model of elastic modulus C_{10} and the anisotropic fibers are described with an exponential power law with fiber stiffness ξ. The combination of these two contributions is known as the HGO model.

In this part on the multiphasic cornea, we use a simplified geometry and fiber organization as shown in Fig(45). To describe the two-third posterior stroma we use an elastic modulus $C_{10} = 0.01$ MPa and fiber stiffness ξ=0.1 MPa corresponding to the "Stroma center posterior" properties of the Abaqus model in Part(II), with fibers following an orthogonal distribution. For the anterior one-third of the stroma, we use an elastic modulus $C_{10} = 0.06$ MPa and fiber stiffness ξ=0.6 MPa corresponding to the "Stroma center anterior" properties in the Abaqus model in Part(II), with an isotropic fiber distribution.

Similarly, the epithelium and endothelium solid behavior were described with the same material models and properties as previously, which are a Neo-Hookean model with a stiffness coefficient $C_{10} = 0.002$ MPa for the epithelium and a Neo Hookean model with a stiffness $C_{10} = 0.001$ MPa for the endothelium. The Bowman's and Descemet's membrane were not included in the geometry as their function are purely mechanical and can be neglected in this multiphasic model, mainly because the stroma accounts for the most part of the solid mechanical behavior of the cornea [10].

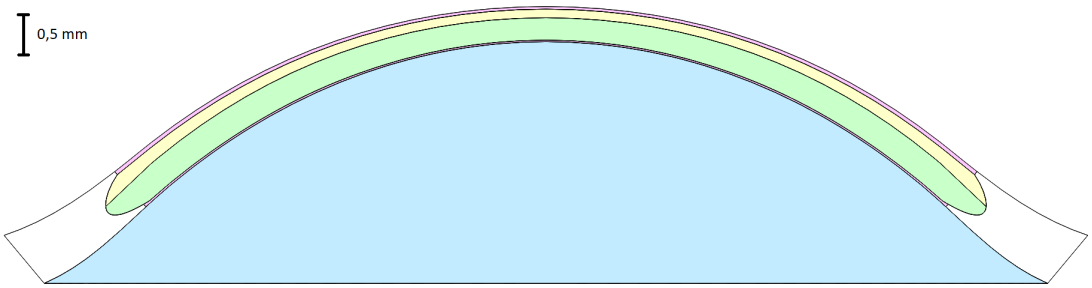

Figure 45: Model geometry: in Blue the intra ocular liquid, in White the sclera, in Pink the epithelium membrane, in Yellow the anterior stroma, in Green the posterior stroma, in Orange the endothelium. Both Bowman's and Descemet's membrane were not incorporated because their contribution to the overall mechanics is estimated to be minor

The limitation of the HGO model is that the material is assumed incompressible. Within the mixture theory, the volumetric behavior can be accounted for by including a fluid phase to describe the porous nature of the tissue. To model water flow in the corneal stroma, the value of hydraulic conductivity is taken from [156] as $K = 5 * 10^{-14} cm^2$. The dynamic viscosity of water being $\mu = 8.90 * 10^{-4} Pa.s$, the stroma permeability to water is calculated as $k = K/\mu \approx 0.6 * 10^{-14} m^4/(N.s) = 6 * 10^{-3} mm^4/(N.s)$.

In the stroma, collagen fibrils, proteoglycans and keratocyte cells occupy volume that is excluded from the electrolyte fluid. Denoting the volume fraction of collagen fibrils φ_{col}, fibril PG coating φ_{coat} and keratocyte φ_{ker}, the volume fraction of the remaining water is expressed as $\varphi_{electrolyte} = 1 - \varphi_{col} - \varphi_{coat} - \varphi_{ker}$. Pinsky and Cheng [89] have estimated $\phi_{col} = 24.9\%$, $\varphi_{coat} = 13.3\%$, $\phi_{ker} = 11.2\%$ for a resulting $\phi_{electrolyte} = 49.4\%$. However, most of cells content is actually water and their direct contribution to tissue mechanics is low. As most biological tissue (artereries, cartilage ...) seems to converge around 70% of water content, this value will be used instead in our cornea model. In addition, Meek et al. [135] estimated the water volume fraction of cornea to be around 78%.

Regarding the fixed charge density in corneal stroma, in [157] they measured a charge concentration of $C_F = -48\ nEq/mm^3$. In [19], Cheng and Pinsky estimated mathematically the average stromal fixed charge density as $C_F = Q/V^0_{stroma} = -38mMol$, with the total GAG fixed charge Q calculated from the average ionization fraction and protein geometry, and divided it by a chosen representative volume $V^0_{stroma} = 1mm^3$. Problematically, they referred to this value as calibrated so in our model we chose to use the experimental value of $C_F = -48\ nEq/mm^3$.

To find the endothelium water permeability $\tilde{k}$, we used the equation $L_p = \frac{\tilde{k}}{h}$ which relates the permeability value to the hydraulic conductivity coefficient $L_p = 53 * 10^{-4}\ mm^3/(N.s)$ [33] and the membrane thickness. For the membrane thickness we chose to do not include the thickness of the cytoplasm in its calculation as it is mainly composed of water and does not participate in the regulatory mechanism of water transport. The thickness h was consequently defined as the sum of the basal and apical cell membrane, both having approximately 10 nm walls. It leaded to $h = 10 + 10 = 20\ nm$.

From these values we found an endothelial water permeability of $k = 1.06 * 10^{-7}\ mm^4/(N.s)$, a value 50000 times lower than the stromal one. This difference in magnitude seems intuitively right as the endothelium act as a barrier to restrict the passive water flow and maintain the right stromal hydration.

Now looking at solutes, the dominant ionic species found in the cornea are Na^+, K^+, Cl^- and HCO_3^-. The initial concentrations of these species in the corneal stroma are assumed of uniform distribution. The same species are present in the aqueous humor and from Li et al. [33] we defined the following external ionic concentrations: $c_*^{Na^+} = 135mM$, $c_*^{Cl^-} = 115mM$, $c_*^{K^+} = 15mM$ and $c_*^{HCO_3^-} = 35mM$. It is probably reasonable to assume these external concentrations in the aqueous humor as being constant because the volume of the eye anterior chamber is much greater than the stromal volume and the exchanges taking place do not alter the concentration in this external larger volume.

All materials are considered to be ideal chemical mixture where the only interactions occurring between molecules are those resulting from the shocks they undergo when they meet. In mixture theory, this ideal physico-chemical behavior is set by defining constant solubility $\kappa = 1$ (which induces a constant solute activity coefficient γ from the effective solubility ratio $\hat{\kappa} = \frac{\kappa}{\gamma}$) and an osmotic coefficient $\phi = 1$ for all species. Additionally, for all species we assume a constant isotropic permeability through the tissue and constant isotropic diffusivity as shown in Table(7).

Parameter	Symbol	Value	SI Unit
Stroma fluid volume fraction	Φ_f	0.7	-
Stroma fixed charge density	C_f	48	mol/m^3
Stroma hydraulic conductivity	K	$5*10^{-18}$	m^2
Water dynamic viscosity	μ	$8.9*10^{-4}$	Pa.s
Stroma water permeability	k	$0.6*10^{-14}$	$m^4/(N.s)$
Endo. hydraulic conductivity	L_p	$53*10^{-13}$	$m^3/(N.s)$
Endo. membranes thickness	h	$20*10^{-9}$	m
Endo. water permeability	k	$1.06*10^{-19}$	$m^4/(N.s)$
A.H. electrostatic potential	Ψ_0	0	V
A.H. Na^+ concentration	C_{Na^+}	135	mol/m^3
A.H. Cl^- concentration	C_{Cl^-}	115	mol/m^3
A.H. K^+ concentration	C_{K^+}	15	mol/m^3
A.H. HCO_3^- concentration	$C_{HCO_3^-}$	35	mol/m^3
Osmotic coefficient	Φ	1	-
Solubility	κ	1	-

Table 7: First set of parameters used in the multiphasic model in SI units. Parameters must be defined for each layer of the cornea and for each component of the mixture (solid, solvent, solutes). A.H. = aqueous humor ; Endo. = endothelium

Diffusivity and free diffusivity material properties Finally, diffusivities and free diffusivities of each solute species should be defined. For macromolecules, standard relations between solute molecular weight and diffusivity can be determined using the Stokes-Einstein relation which gives a good approximation of diffusivity over a very wide range of molecular weights. However, when it comes to small salt ions, the most reliable results are experimental measurements, sometimes providing a wide range of values.

Li et al. [33] provided their experimental values of ionic diffusivities in the corneal stroma: $D_{Na^+} = 0.591 * 10^-5\ cm^2/s$, $D_{Cl^-} = 0.900 * 10^-5\ cm^2/s$, $D_{K^+} = 0.867 * 10^-5\ cm^2/s$, $D_{HCO_3^-} = 0.489 * 10^-5\ cm^2/s$.

In papers published by Maurice in 1961 [158] and Maroudas in 1968 [159] experiments provided a value for NaCl diffusivity in articular cartilage and cornea which was two times less than that for its free solution diffusion. From these results, we defined values of ionic free diffusivities as twice the value of their diffusivities, giving values consistent with those found in the literature of ionic free diffusivity being of the order $d_0^\beta \approx 1 * 10^{-3} mm^2/s$.

For the endothelial and epithelial membranes, fundamental equations describing the transport of solutes across membranes, such as the Nernst and Nernst-Planck equations, have been

classically formulated in the framework of non-equilibrium thermodynamics [74]. In this framework, ionic permeabilities and reflection coefficients were measured experimentally on cellular membranes assuming Fickian diffusion as the only transport mechanism. It has been shown that these equations may be reproduced using the framework of mixture theory (previous Section(11.3.2) : "Link with mixture theory"). From these coefficients, diffusivity parameters d and d_0 needed in the mixture framework can be calculated from the equations 91 and 92. Therefore, the diffusivity of solute d^β is calculated from its permeability with:

$$P^\beta = \frac{\tilde{\kappa}^\beta d^\beta \varphi^w}{h} \tag{91}$$

and the free diffusivity of solute d_0^β is calculated from Staverman's reflection coefficient with:

$$\sigma^\beta = 1 - \frac{\tilde{\kappa}^\beta d^\beta}{d_0^\beta} \tag{92}$$

Few litterature exists that reference permeability and reflection coefficients applied to the cornea. Two main papers can be found [33] [160] that are based on the same early work of [155] but gives opposite values for bicarbonate HCO_3^- permeability and reflection coefficient through the endothelium. Because values in [160] are referred as "adjusted", we will refer to data in the second paper from Li et al. [33]. In this paper, using osmotic shocks experiments, they found greatest change in stromal thickness associates with a solution of $NaHCO_3$, for which bicarbonate permeability coefficient is the smallest and reflection coefficient is the largest, leading to smaller diffusivities. This seems intuitively correct because in vivo, the endothelium consumes energy to actively transport bicarbonate ions out of the stroma and this effect should not be directly counterbalanced from passive flux due to a large endothelial permeability to bicarbonate.

The final step to calculate endothelial solute diffusivity would be to determine the membrane porosity φ^w. However, because we considered water permeability and ionic diffusivities constant, porosity does not influence the governing equations of the multiphasic framework, unless we choose to model body forces (not relevant in our analysis) or we choose porosity-dependent constitutive models for hydraulic permeability and/or solute diffusivities (not needed for a cell membrane, as we use an uncoupled formulation for the solid matrix, with a high bulk modulus that enforces isochoric deformations).

In other words, if we ignore body forces and employ constitutive models with constant hydraulic permeability and solute diffusivities, we can pick any desired value for the porosity of our multiphasic medium, it won't have any effect on the solution because the ratio between diffusivities value will still be the same. In the end we chose an approximative value of $\varphi^w = 0.2$.

From equation (91), we calculated the following values of endothelial ionic diffusivities: $D_{Na^+} = 0.464 * 10^-6\ cm^2/s$, $D_{Cl^-} = 0.905 * 10^-6\ cm^2/s$, $D_{K^+} = 0.682 * 10^-6\ cm^2/s$, $D_{HCO_3^-} = 0.492 * 10^-6\ cm^2/s$

To represent the active metabolic pump, we used the reported values of bicarbonate endothelium flux in [33] which was $-4 * 10^{-10}\ mole/(cm^2.s)$.

In the end, the diffusivity parameters assigned in the model are shown in Table(8).

Parameter	Symbol	Value	SI Unit
Stroma Na^+ diffusivity	$D^s_{Na^+}$	$0.591*10^{-9}$	m^2/s
Stroma Cl^- diffusivity	$D^s_{Cl^-}$	$0.900*10^{-9}$	m^2/s
Stroma K^+ diffusivity	$D^s_{K^+}$	$0.867*10^{-9}$	m^2/s
Stroma HCO_3^- diffusivity	$D^s_{HCO_3^-}$	$0.489*10^{-9}$	m^2/s
Endo. Na^+ diffusivity	$D^e_{Na^+}$	$0.464*10^{-10}$	m^2/s
Endo. Cl^- diffusivity	$D^e_{Cl^-}$	$0.905*10^{-10}$	m^2/s
Endo. K^+ diffusivity	$D^e_{K^+}$	$0.682*10^{-10}$	m^2/s
Endo. HCO_3^- diffusivity	$D^e_{HCO_3^-}$	$0.492*10^{-10}$	m^2/s
Na^+ free diffusivity	$D^0_{Na^+}$	$1.18*10^{-9}$	m^2/s
Cl^- free diffusivity	$D^0_{Cl^-}$	$1.8*10^{-9}$	m^2/s
K^+ free diffusivity	$D^0_{K^+}$	$1.73*10^{-9}$	m^2/s
HCO_3^- free diffusivity	$D^0_{HCO_3^-}$	$0.978*10^{-9}$	m^2/s
Endo. porosity	φ_w	0.2	-
Endo. HCO_3^- active flux	$j_{HCO_3^-}$	$-4*10^{-6}$	mol/(m^2.s)

Table 8: Second set of parameters displaying the various diffusivities coefficient used in the multiphasic model and the value of endothelial active flux. Endo. = endothelium

12.2 Introduction to biphasic material: consolidated undrained triaxial test

As an introduction to porous material, we perform a so called numerical consolidated undrained triaxial test. This test is thought to determine the mechanical properties of porous material by subjecting the sample to different stress levels and drainage conditions. This simulation will be used to provide an insight on biphasic material and introduce the notion of pore pressure and consolidation. In this test, the specimen is confined into a chamber where various stress can be applied on the material while controlling its hydration level through drainage valve.

A consolidated undrained triaxial test is performed in several stages, involving the successive saturation, consolidation and shearing of each specimens.

- First, saturation is carried out in order to ensure that the porous specimen is completely filled with fluid [161].
- Then, the specimen is subjected to a constant confining stress, σ_3, and allowed to consolidate by opening the drainage valves. Consolidation refers to the mechanical process by which biphasic material changes volume gradually in response to an external pressure. When a tissue saturated with water is subjected to an increase in pressure, the water initially absorbs all the change in pressure without changing volume, creating excess pore water pressure. This excess pore pressure dissipates from the boundaries as water flows out, resulting in consolidation settlement and change in volume.

- Finally begin the shear stage. Once consolidation is complete, the drainage valves are closed and the specimen is subjected to a monotonically increasing deviator stress, $\sigma_1 - \sigma_3$. These undrained conditions mean that there will be no volumetric change in the specimen (i.e., volume remains constant). It also means that excess pore water pressure will be developed inside the specimen throughout the test.

During the shear stage the vertical stress is increased, and measurements are made at regular intervals to analyse deformation, effective stress and pore pressure. These measurements are converted to graphs of principal stress difference ($\sigma 1$ - $\sigma 3$) and pore pressure as a function of strain. In experiments, failure corresponds to the point of maximum principal stress difference. In practice, triaxial tests are often used to determine the strength envelope of materials.

12.2.1 Undrained triaxial test model description

We perform the test in the finite element analysis software Abaqus. The geometry is a cylinder with a 500 µm diameter and 250 µm height. The bottom of the cylinder is defined as fully blocked, with or without permeable boundary conditions applied.

A biphasic material is considered with an hyperelastic solid matrix described by a Neo-Hookean constitutive model with a stiffness parameter of C_{10}=0.01 MPa. The value of stroma permeability to water is $k = K/\mu \approx 0.5 * 10^{-14} m^4/N.s$. The volume fraction of fluid is taken to be 70%, representing the volume fraction of electrolyte fluid in the cornea. The lateral consolidation pressure is taken to be 2266 Pa = 17mmHg, the value of the internal eye pressure.

The total stress on the specimen is defined as the sum of effective stress on the solid phase plus the fluid pore pressure: $\sigma_{tot} = \sigma_{eff} + pI$ with σ_{eff} the effective stress carried by the solid phase and p the hydrostatic pore pressure, with I the identity tensor.

12.2.2 Results

In the initial step the sample gets saturated in water. The sample is then consolidated by applying a lateral surface load of 2266 Pa representing the fluid cell pressure in a triaxial test apparatus. This confining stress is applied from 0 to 20 seconds with drainage allowed until the specimen is consolidated and all pore pressure are dissipated. The load is applied slowly to allow for the dissipation of the excess pore pressure due to the low hydraulic conductivity of the corneal stroma. From this numerical experimentation, we can observe a drop in the water volume fraction in the tissue during the consolidation as shown in Fig(46).

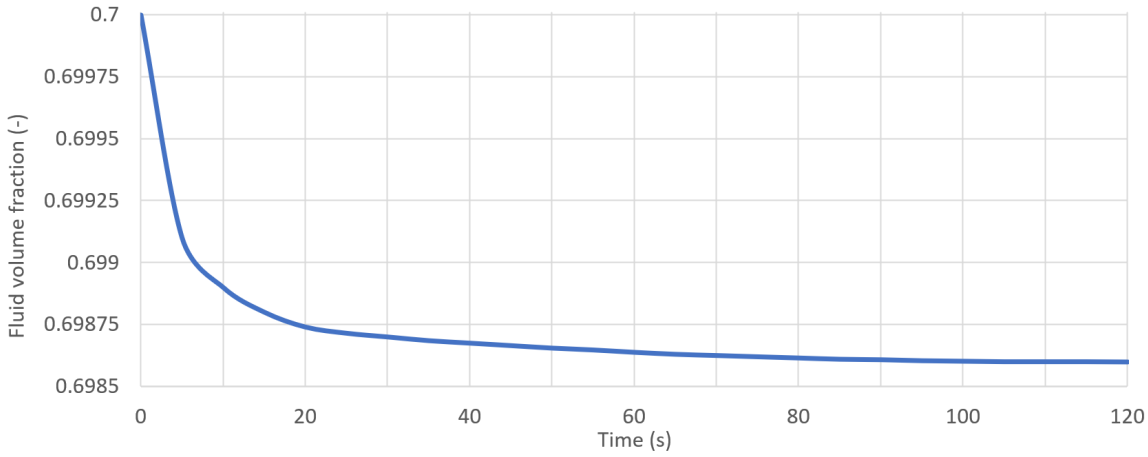

Figure 46: Decrease in fluid volume fraction in the tissue during consolidation from 0 to 20 s

The drainage is then stopped, creating undrained condition for the shearing phase of the test. The shearing is increased starting at 20 to 120 seconds and the effective stress in the solid along with excess of pore pressure are measured as shown in Fig(47 & 48). In this final shear step, minor volume change will occur as all walls are impermeable. A vertical stress σ_1 is applied to the specimen corresponding to the major principal stress $\sigma_1 = \sigma_3 + \sigma_d$ with σ_d the deviatoric stress.

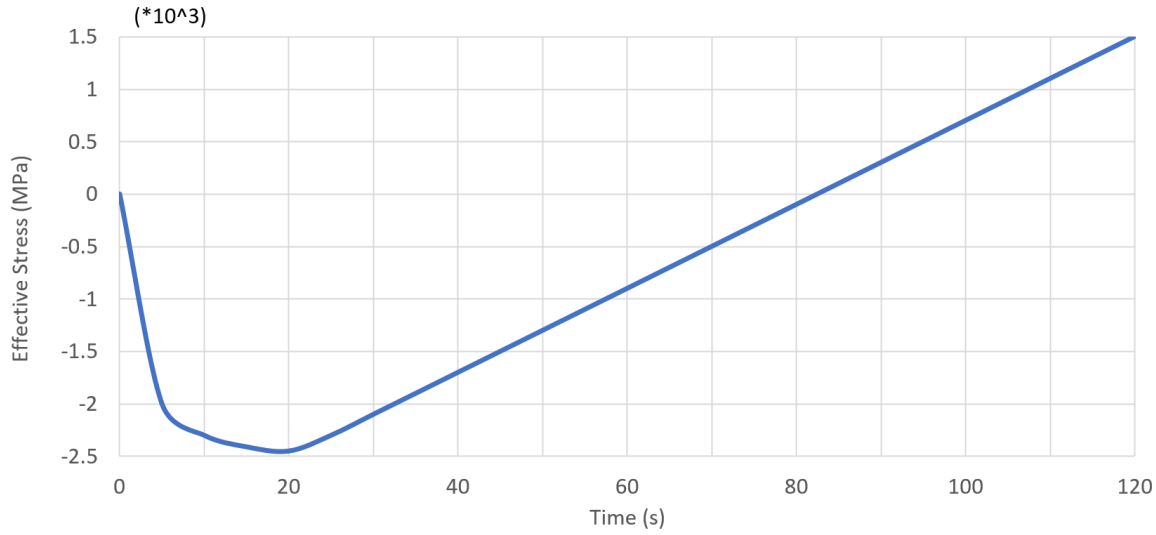

Figure 47: Effective stress evolution during the consolidation from 0 to 20 seconds and then in the shearing phase from 20 to 120

We can see that the consolidation procedure (0-20 seconds) provides the tissue with a pre-stress strengthening with the effective solid stress turning negative (Fig47), whereas the pore pressure is null at the end of this step due to the drained condition as shown in (Fig48). As expected, during the shear phase the tissue is compressed by the vertical stress σ_1 and the fluid pore pressure consequently increases due to the undrained condition.

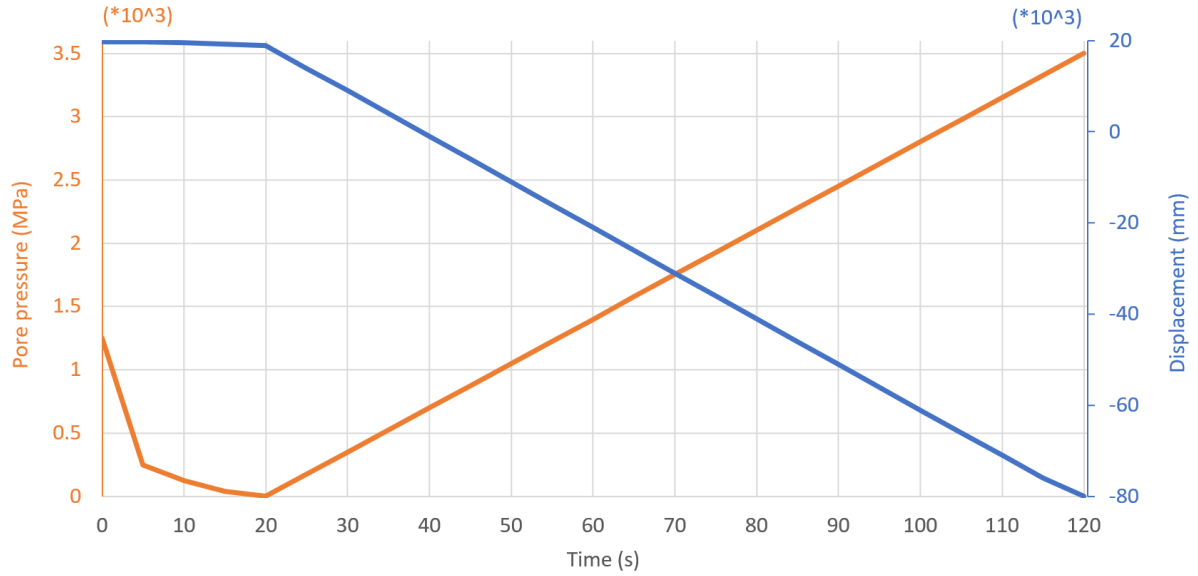

Figure 48: Superposition of displacement in blue and fluid pore pressure evolution in orange. It shows that during the shearing phase, the pore pressure in orange increases wgile the solid is being compressed as depicted by the blue top displacement curve

Assuming that the value of major principal stress σ_1 corresponds to failure of the specimen, the effective-stress Mohr–Coulomb failure criterion can be drawn from the associated value of confining stress σ_3. If we test a second specimen consolidated to a higher confining stress, the specimen will gain more strength during the consolidation process and will have a larger Mohr circle at failure. Repeating the process for a third value of confining stress, we can plot the failure envelope as the line tangential to the circles and compute the failure envelope equation as shown in Fig(49).

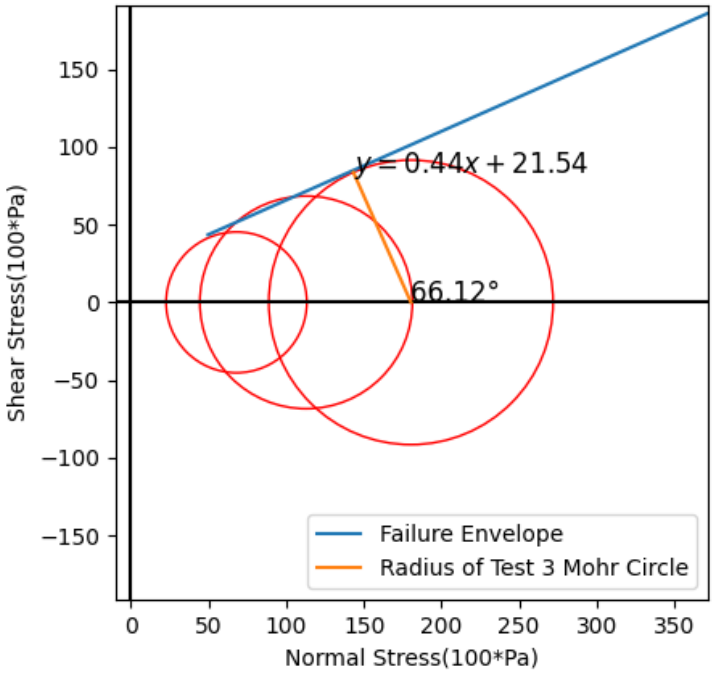

Figure 49: Mohr circles showing the failure envelope of the specimen tested in our model

The slope of the envelope represent the effective friction angle ϕ of the specimen (non applicable to soft tissue). The effective stress Mohr circle are similar to total stress but shifted to the right by adding the pore pressure at failure $\sigma_{eff} = pI + \sigma_{tot}$.

12.2.3 Interpretation

This process of consolidation is time dependent and is a function of the tissue water permeability, the length of the drainage path and the compressibility of the material. When the cornea is submitted to external loads like eye rubbing, a punctual excess of pore pressure will occur, increasing the total fluid pressure in the tissue. Permeation of water through the corneal membranes may then happen because of this punctual gradient in pressure, possibly disturbing the tissue homeostasis by transporting several solutes or inducing mechanobiological stress signals on keratocytes. This was a preliminary exercise on porous material.

12.3 Model verification: analytical calculation and comparison

In this section we will perform a model verification against the analytical solutions we have determined in the Chapter(11). It will provide us with valuable insight on the model reliability,

still on a testing geometry. The behavior of the model will also be compared to the results of an equivalent approach used by Pinsky et al [89].

The following material characteristics will be used in our model:

- Multiphasic
- NeoHookean solid
- Constant Isotropic Permeability (water hydraulic conductivity is constant and independent of strain)
- Constant Osmotic Coefficient
- Constant Isotropic Diffusivity
- Constant Solubility

We used a triphasic material which consists of a mixture of a porous solid, an interstitial solvent, and two monovalent counter-ions (solutes whose electrical charges are +1 and -1). The solid matrix may or may not be electrically charged with either positive or negative fixed charge, depending on the needs to describe the GAG fixed charge. The solvent is assumed to be neutral.

The stress tensor σ for the mixture includes a contribution from the fluid pressure p and the effective stress in the solid such as:

$$\boldsymbol{\sigma} = -p_s \boldsymbol{I} + \frac{\partial \Psi_r}{\partial \boldsymbol{F}}.(\boldsymbol{F})^T \tag{93}$$

with p_s representing the swelling pressure of the tissue defined as $p_s = p_{hyd} + p_{os}$. This relation tells us that the fluid swelling pressure is composed of the hydraulic pressure p_{hyd} representing the "mechanical pressure" exerted by the fluid free of solutes (pure solvent), and the osmotic pressure $p_{os} = R\theta\phi \sum_\alpha c^\alpha$. In the cornea the hydraulic pressure is dictated by the intra ocular pressure of the eye.

The sign convention is defined as positive for net fluxes of solution and solutes from outside to inside. The difference in solute concentration across the membrane is calculated by the outside concentration minus the inside one. Differences of hydrostatic and osmotic pressures are defined in a similar manner.

12.3.1 Model description

The geometry considered is a cube of 500 µm edges with mesh refinement on the top and bottom surface to ease convergence under the various boundary conditions applied. Depending on the case, several cubic parts can be joined to describe the presence of solution and membrane domain in addition to the stromal domain.

To ensure continuity of electrochemical potential across boundaries, we need to use the effective pressure and concentration as nodal degrees of freedom. The expression for effective pressure is defined as $\tilde{p} \equiv \rho_T^w(\tilde{\mu}^w - \mu_0^w) = p - p_0 - RT\Phi \sum_{\alpha \neq s,w} c^\alpha$ with the actual fluid pressure denoted by p and the actual solute concentration c (or c^+ and c^- for the two ions), with p and c the fluid pressure and solute concentration and $p_0 = 0$ and $\psi_0 = 0$ as reference values.

For an ideal mixture with osmotic coefficient Φ equal to 1, the effective fluid pressure is then given by:

$$\tilde{p} = p - RT \sum_{\alpha \neq s,w} c^{\alpha}$$

where R is the universal gas constant (8.314e-6 mJ/nmol.K) and T is the body temperature temperature (311 K). In a triphasic material, the osmolarity is calculated as $c_{osm} = \sum_{\alpha \neq s,w} c^{\alpha} = c^{+} + c^{-}$. From this expression, it becomes apparent that $\tilde{p}$ represents only the mechanical contribution to the fluid pressure (total pressure − osmotic pressure). Then, in a charged triphasic mixture, p includes the contribution of both osmotic effects and hydraulic effects.

For an ideal mixture with solute solubility and activity coefficient equals to 1, the effective solute concentration is given by:

$$\tilde{c} = c * exp(\frac{zF_c\psi}{RT})$$

where z is the solute charge number (e.g., +1 and -1 for cation and anion, respectively), ψ is the electric potential, and F_c is Faraday's constant (96500e-9 C/nmol). This expression shows that the effective solute concentration accounts for the effects of electrical charge (+/-) and electric potential. For a neutral solute (z=0), or in the absence of electric potential ($\psi = 0$ mV), we find that $\tilde{c} = c$.

Thus, in a triphasic analysis, the nodal degrees of freedom are the solid displacement components (u_x, u_y, u_z), the effective fluid pressure ($\tilde{p}$), and the effective solute concentrations $\tilde{c}$ ($\tilde{c}_+$ for the positive cation and $\tilde{c}_-$ for the negative anion).

In our triphasic analysis with the following environmental conditions $c_0^{Na^+} = c_0^{Cl^-} \equiv c_0$, the effective fluid pressure in the external environment is therefore $\tilde{p}_0 = -R\theta\Phi_0 \sum_\alpha c_0^\alpha$ and the effective concentrations are $\tilde{c}_0^\alpha = c_0^\alpha / \tilde{\kappa}_0^\alpha$. Whenever the external environment contains solutes with non-zero concentrations c_0^α, it must be prescribed non-zero boundary conditions for the effective solute concentrations and the effective fluid pressure.

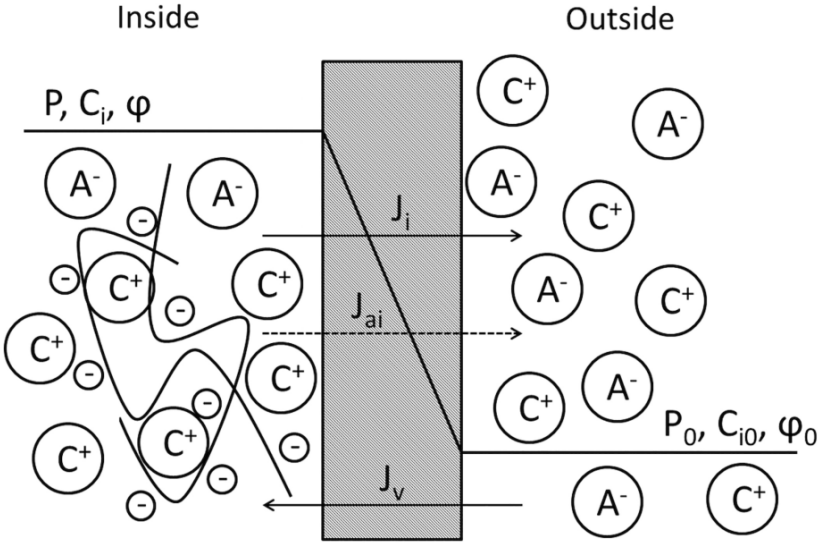

Figure 50: Illustration of a biological membrane that separates two electrolyte solutions, with the inside corresponding to the corneal stroma and containing negative fixed charges, and the outside corresponding the the aqueos humor of the eye [89]

12.3.2 Analytical verification

Under traction-free conditions, a multiphasic material is usually in a state of swelling due to the osmotic pressure difference between the interstitial fluid and the external environment. This difference in pressure results in an influx of solvent into the porous solid matrix and mechanical stress since it has to expand until it resists the swelling pressure as shown in Fig(51).

If the osmotic pressure arises from the presence of fixed charges on the solid matrix that induces a difference in interstitial versus external concentrations of cations and anions, the resulting osmotic pressure at equilibrium is known as Donnan osmotic pressure and an analytical solution exists for its triphasic formulation. The increase in osmotic pressure induces an increase in water content and the consequent swelling of the tissue.

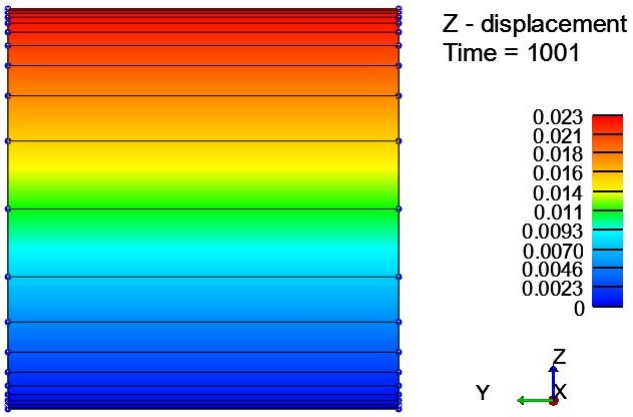

Figure 51: One-dimensional free swelling of the testing geometry with $C_f = -48mM$ and $C_0 = C_{Na^+} = C_{Cl^-} = 150mM$. A vertical expansion is observed

Verification against electric potential An electric potential gradient is produced from the presence of fixed charge attached to the solid matrix. In the cornea, the stroma fixed charge is almost entirely due to GAGs which carry negative charges that contributes to the electroneutrality condition (60) and induce a variation in tissue ionic concentration. In the triphasic free swelling case, the Donnan electrostatic potential denoted $\tilde{\psi}$ can be calculated from the Jacobian (i.e the ratio of final volume to initial volume) by injecting $c^F(J) = \frac{c_0^F}{J}$ into the Poisson-Boltzmann Eq.(67) which allows it to be solved analytically as:

$$\psi(J) = -\frac{RT}{F_c} sinh^{-1}(\frac{c^F(J)}{2c_0}) = -\frac{RT}{F_c} sinh^{-1}(\frac{c_0^F}{2Jc_0}) \tag{94}$$

Following the swelling of the tissue, the simulation gives a Jacobian value of $J = 1.023371$. Plugging this value into the analytical expression we obtain an electric potential of $-4.157mV$. By comparison the numerical value of electric potential obtained with the simulation is $-4.117mV$, showing an agreement of more than 99% between the analytical and numerical values.

Verification against ionic concentration From the electric potential obtained by the simulation, we can calculate the actual ionic concentration at equilibrium with the analytical expression:

$$c^\alpha = \tilde{c}^\alpha e^{\frac{-z^\alpha F_c \psi}{R\theta}} \tag{95}$$

We use the numerical electric potential $\psi = -4.117mV$ to calculate the analytical actual ionic concentration at equilibrium. The calculated change in ionic concentrations result from

electro-osmosis, a transport phenomenon in which water molecules are dragged by ionic species along electric field lines until electroneutrality is reached.

From the analytical expression we calculate $c_{Na^+} = 175mM$ and $c_{Cl^-} = 128mM$. These values are the exact same as the one obtained numerically, demonstrating the reliability of our multiphasic model based on mixture theory.

Verification against osmotic pressure The electric potential gradient produced from the presence of fixed charge gives the tissue a tendency to swell for all positive values of osmotic pressure P_{os}. At equilibrium, the resulting osmotic pressure for a triphasic material is known as Donnan osmotic pressure and its analytical expression is:

$$P_{os} = P_{tissue} - P_{bath} = 2RTc_0(\sqrt{(\frac{c_0^F}{2Jc_0})^2 + 1} - 1) \tag{96}$$

The analytical osmotic pressure calculated with $c_0 = 150mM$, $c_0^F = -48\ nEq/mm^3$ and $J = 1.023371$ is: $P_{os}^{analytical} = 9.423 * 10^{-3} MPa$. In comparison, the numerical value of osmotic pressure obtained from the simulation is $P_{os}^{numerical} = 9.239 * 10^{-3} MPa$. The agreement between the analytical and numerical solutions is therefore about 98%.

12.3.3 Further testing and comparison

To further assess the soundness of the mixture theory approach against others approach, we will reproduce a series of numerical tests made by Pinsky and Cheng [89] and compare with the results of their thermodynamic approach.

Osmotic pressure evolution against compression First we reproduced a compression test and plotted the profile of the tissue osmotic pressure submitted to an increasing compression from $J = 1$ to $J = 0.35$ as shown in Fig(52). The non linear curve's shape obtained is in accordance with the one described by Pinsky in [89] and describes how the tissue fluid pressure rises abruptly above a 50% compression.

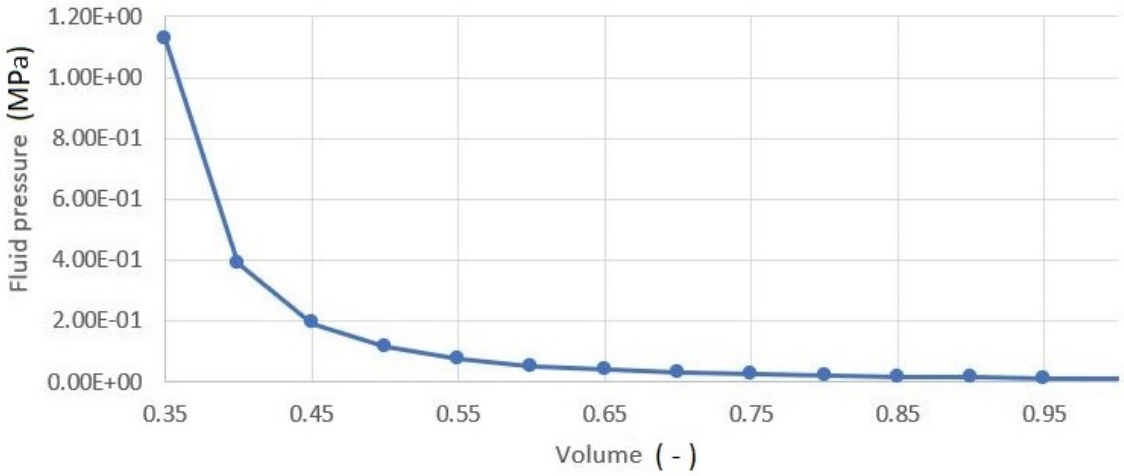

Figure 52: One-dimensional compression of the testing geometry with $C_f = -48mM$ and $C_0 = N_{Na^+} = C_{Cl^-} = 150mM$. The model shown an exponential increase in fluid pressure above a treshold of 50% compression

At $J = 0.35$, the corneal osmotic pressure is approximately $1.127MPa$, which exceeds the equilibrium electrolyte osmotic pressure by a factor of more than 110. This can be explained by the volume exclusion effect: as the tissue shrinks, the volume of solution reduces, forcing the mobiles ions into a smaller volume and greatly increasing the fixed charge density and osmotic pressure. Above a certain level of compression, the local charge density is too high for the model to converge.

Osmotic pressure evolution against fixed charge density Another test was reproduced showing the effects of the concentration of fixed charges on the fluid pressure. We used the same geometry and plotted a curve showing the evolution of tissue volume and fluid pressure against the fixed charge density in Fig(53) in the range of $C_f \in [0; 200]$, with $C_f^0 = -48mM$ the physiologic fixed charge concentration in corneal stroma.

It shows that the fluid pressure P increases monotonically with the fixed charge concentration C_f, increasing from 0 to 0.0863 MPa as the fixed charge concentration varies from 0 to 200 mM. The geometry dilatation follows the same pattern, confirming that the tissue has a tendency to swell for all positive values of fluid pressure and that the cornea can easily swell by absorbing water if no membranes are regulating its ionic transport. In vivo, the intraocular pressure applied on the cornea internal surface plays a role not considered in this free-swelling set up.

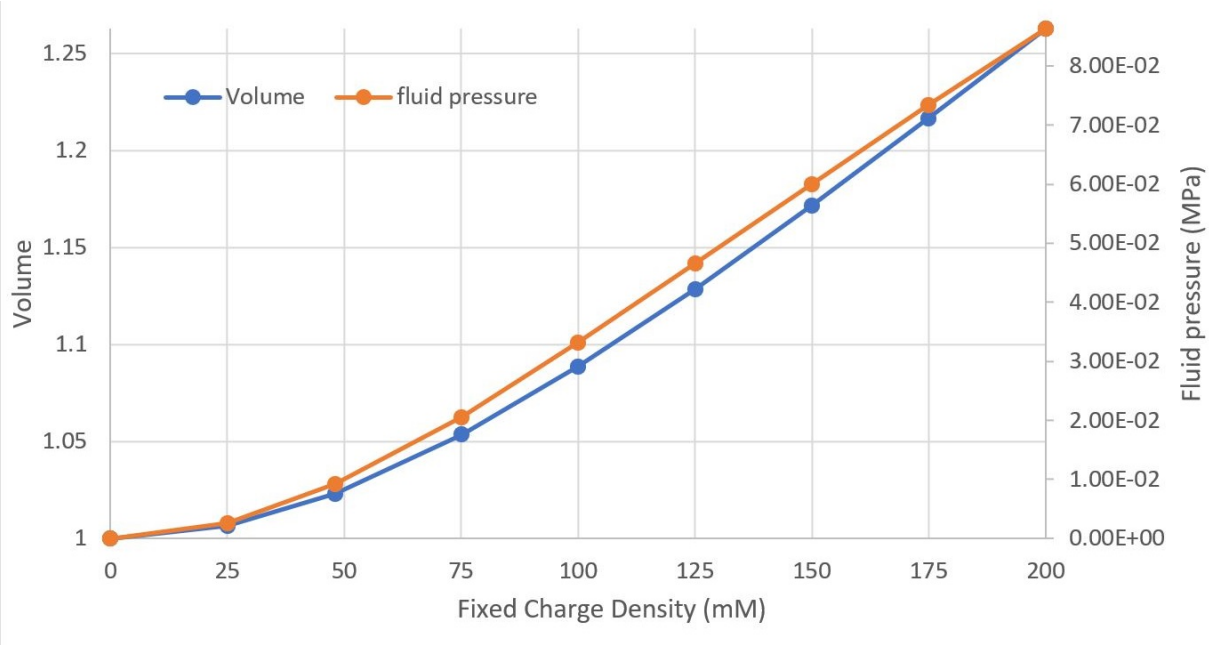

Figure 53: One-dimensional free-swelling of the testing geometry with $C_f \in [0; 200]$ mM and $C_0 = N_{Na^+} = C_{Cl^-} = 150mM$. The volume expands proportionally to the concentration of fixed charge

In this range of fixed charge density, the simulation shows that the sodium concentration difference ΔC_{Na^+} displays the highest sensitivity to C_f among the two solutes, varying from 0 to +89.4 mM as C_f increases from 0 to 200 mM as shown in Fig(54). On the other hand, the predicted chloride concentration displays an opposite trend by decreasing with C_f with a ΔC_{Cl^-} of -56mM. The contrast between the curves of cation and anion is attributed to the electroneutrality condition, which requires accumulation of cations to compensate for the concentration of negative fixed charges C_f.

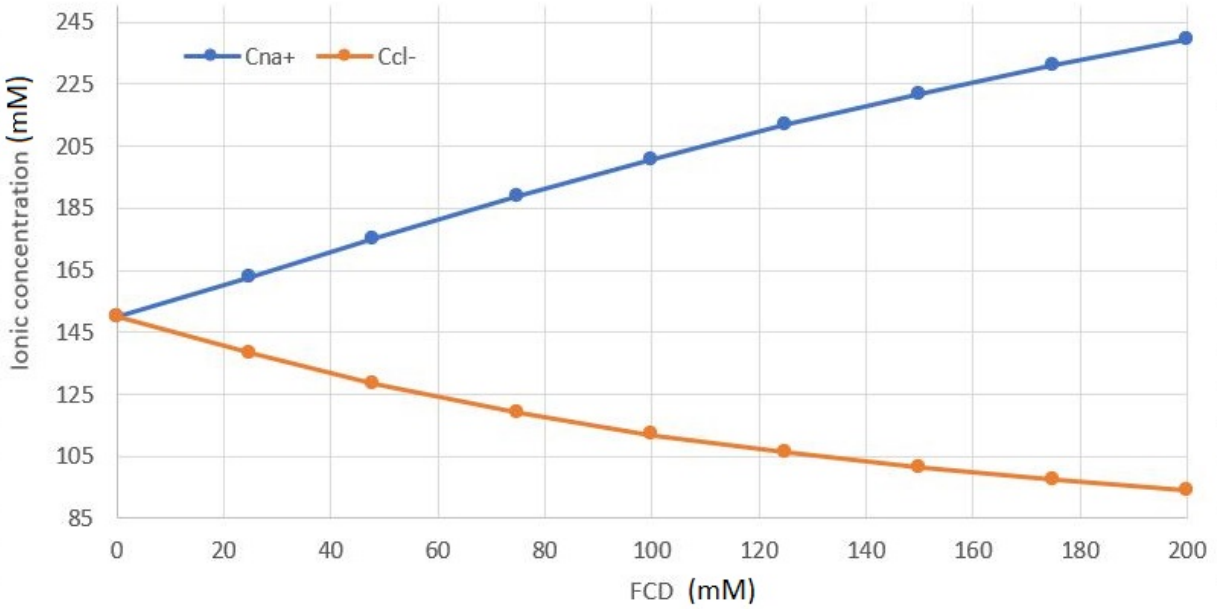

Figure 54: Variation of ionic concentration against concentration of negative fixed charge density $C_f \in [0; 200]$. Due to electroneutrality requirement, an increase in negative fixed charge density corresponds to an increase in positive ions and a decrease in negative ions

Osmotic pressure evolution against bath ionic concentration The swelling behavior predicted by the model can also be illustrated by varying the external bath ion concentration c_0. The Fig(55) shows the osmotic pressure variation due to changes of bath concentration by plotting the fluid pressure $P_{swelling}$ against the values of $c_0 \in [50; 550]$ mM.

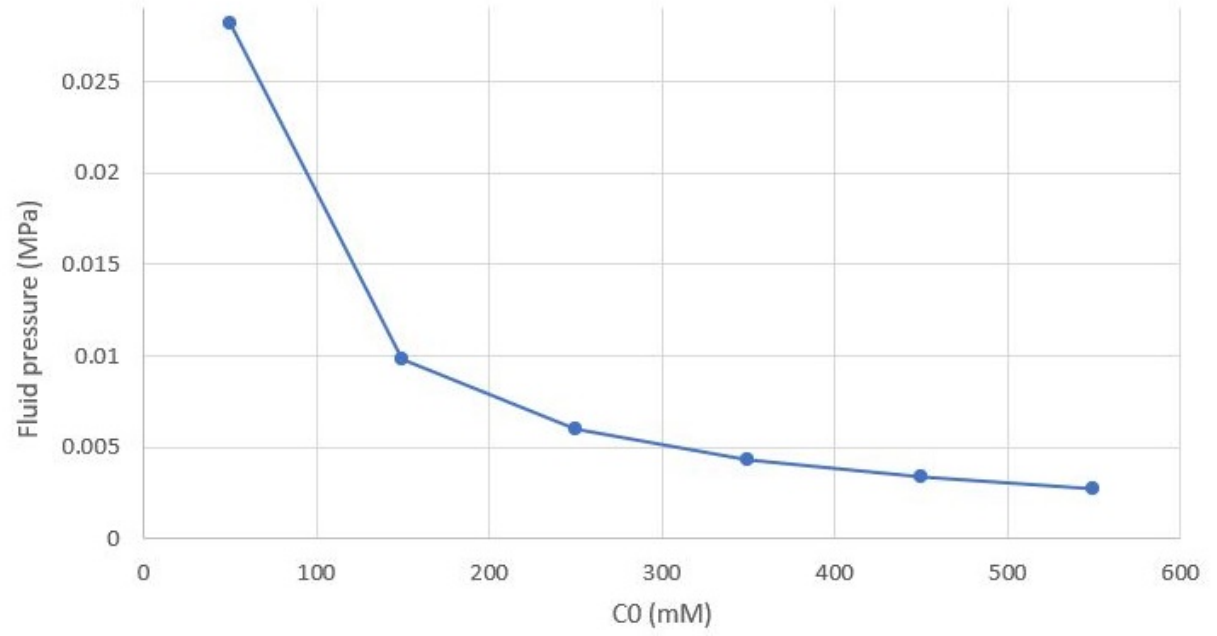

Figure 55: One-dimensional free-swelling of the testing geometry with $c_0 \in [50; 550]$ mM. When the ionic concentration increases in the external bath, the tissue internal fluid pressure decreases due to the ion shielding effect

The predicted osmotic pressure decreases monotonically with the increasing bath concentration, which is attributed to the ion-shielding effect from the abundance of mobile ions. This

effect means that the higher the ionic concentrations in the bath, the closer to 1 the ratio of total negative charge upon total positive charge. Indeed, a much larger quantity of ions present in the external fluid can flow into the strom through the permeable endothelial membrane, diminishing the difference between the cornea and the external fluid charge ratio. This effect is also in agreement with the Pinsky et al. study [89].

12.4 Inverse procedure for multiphasic material

Similarly as for the fiber-reinforced model, the current configuration Ω from which multiphasic material parameters are measured corresponds to the cornea in vivo configuration. Therefore, to find the reference configuration of our model, we will extend the inverse procedure presented in Section(6.2) to the case of multiphasic material, which includes more parameters.

As a reminder, the hospital measurements of the author's cornea were: central corneal thickness=500 µm, peripheral corneal thickness=620 µm, corneal height=3.4 mm, horizontal diameter=11.8 mm, and vertical diameter=10.7 mm. We reconstructed the geometry based on these dimensions, in which the corneal geometry was inserted into a piece of sclera to define smooth boundary conditions. Additionally, a part corresponding to the external fluid bath inside the eye was incorporated as shown earlier in Fig(45).

On this geometry, we applied a surfacic pressure of 2266 Pa corresponding to the intra ocular pressure of the eye using the mixture normal traction $t_n = -p + t_{ne}$, where p is the fluid pressure and t_{ne} is the elastic normal traction. We then defined the several ionic concentrations, ionic diffusivities in the stroma and endothelium, solid fixed charge density, membrane active flux, and all others parameters necessary and previously defined in the material section.

12.4.1 Procedure description

In general, three configurations can be distinguished when it comes to biological tissue:

1. the current configuration Ω corresponding to the in vivo deformed configuration when the tissue is observed in its physiological state.

2. the reference (initial) configuration Ω_0 corresponding to the configuration ex vivo when the tissue is not deformed from environmental loading (like intra-ocular pressure) but still has residual stresses due to its microstructure.

3. the stress-free configuration $\Omega_0^{'}$ corresponding to a theoretical configuration where the tissue is free of all stresses whether they arise from environmental or microstructural contributions.

To predict the corneal swelling behavior under normal and pathological conditions, the model equilibrium has to match the in vivo physiological state of the cornea, hence the need for this procedure. Because all experimentally measured parameters describes the in vivo physiological configuration Ω of the cornea, we need to perform an inverse procedure to find the reference configuration Ω_0 (geometry and material properties) related to the cornea not submitted to the intra ocular pressure. This reference configuration still incorporates osmotic pressure and is not stress-free.

Among the parameters defined in the model, we distinguished those depending exclusively on external conditions, those assumed constant to simplify the problem and those that should undergo the inverse procedure:

External parameters: As ionic concentrations inside the cornea depends on bath concentrations and membrane properties, they are not incorporated in the procedure. Indeed, the final concentrations in the tissue depend on the solid fixed charge density value through the requirements of mixture electro-neutrality.

Assumed constant parameters: For experimentally measured quantity such as elastic modulus, membrane ionic permeabilities, stroma water permeability... Due to experimental variability and the high inter-connectivity between parameters, it seems hardly possible to incorporate them in the actual linear inverse procedure.

It may require to develop a specific approach to deal with them in the form of a system of non linear coupled PDEs (example: coupled equations 3.1 and 3.2 associated with flux source described by Nernst-Planck equation [33], used to model 1D osmotic shock experiments). For now we assume these parameters equivalent in the in vivo and reference configurations to simplify the problem. Additionally, the corneal endothelium and its active ionic flux is considered constant to simplify the problem.

Incorporated parameters: Ultimately, the parameters incorporated into the procedure are the one related to the geometry and volume of the cornea, namely the nodal coordinates, the solid volume fraction and the fixed charge density. The procedure will therefore operate in parallel on these three parameters, updating them simultaneously at each iteration.

To ensure that the deformed configuration matches the physiological value of fixed charge density, we used a check criterion based on the reference fixed charge density c_0^F from its relation with dilation J expressed as: $c^F(J) = J^{-1}c_0^F$, updating its value at each iteration and checking it against the physiological value of $-48mM$. A similar process is done on the solid volume fraction to ensure that the deformed configuration porosity matches the physiological value when the procedure stops.

The inverse calculation is then run to determine the reference corneal dimensions when not submitted to IOP loading. For this, we used the same method as in Section(6.2) and incorporated the loop on parameters specific to the multiphasic model as described in Fig(56):

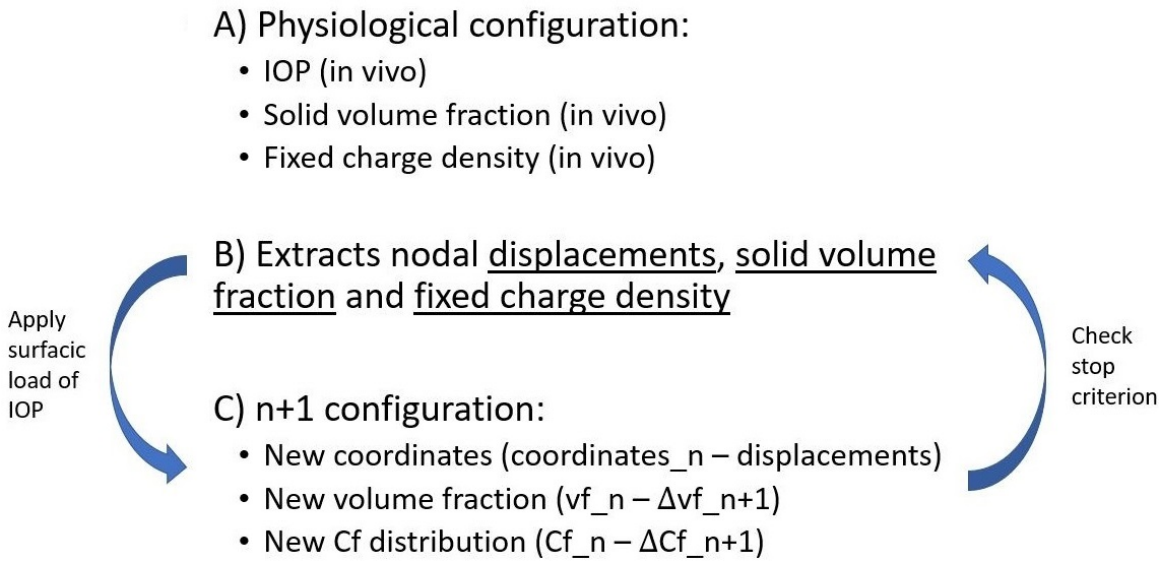

Figure 56: Schematic illustrating the 3 steps involved in the inverse procedure. (A) Reconstruction of the in vivo corneal geometry with its specific IOP, water content and fixed charge density. (B) Use of python scripts to extract nodal datas corresponding to the n configuration on which IOP is applied. (C) Extraction of nodal data corresponding the n+1 configuration deformed by IOP from which is calculated the difference from the precedent configuration to construct an updated reference configuration $n_new = n - n + 1$. A check criterion is defined to stop when the reference n configuration deform into a n+1 configuration corresponding to the in vivo corneal data defined in (A)

After performing this new inverse procedure from the author in vivo corneal dimensions, the reference dimensions obtained are shown in Table(9).

Central thickness	550 µm
Peripheral thickness	715 µm
Cornea height	2.92 mm
Corneal diameter	11.8 mm

Table 9: Corneal reference dimensions after the inverse procedure is performed on the multiphasic cornea

The obtained reference configuration fixed charge density is -43 nEq/mm^3 for the targeted deformed configuration value of -48 nEq/mm^3 and the reference configuration solid volume fraction is 0.27 for a targeted deformed configuration value of 0.3, demonstrating a reference configuration with a bigger volume due to the lack of compression normally induced by the intra-ocular pressure and the smaller fixed charge density.

12.4.2 Fixed charge density and residual stresses in the cornea

Residual stresses are those stresses that remain in a solid material even in the absence of external loading or thermal gradients. They are known to be essential in biological tissue to maintain a uniform stress distribution in their structure in physiological condition [87] [162].

Residual stresses in biological tissue can arise from a variety of mechanical and microstructural properties. Their origin are from several factors that coexist such as growth, remodeling, plastic deformation, inhomogeneous repartition of proteoglycans, etc.

Here we focus on a simple microstructural origin of residual stresses in the cornea: the inhomogeneous repartition of proteglycans in the stroma leading to an inhomogeneous distribution of solid fixed charges. Indeed, when the distribution of negative fixed charge density is inhomogeneous throughout the tissue, residual stresses induced by the resulting difference in osmotic pressure may manifest themselves in the form of tissue curling in response to cuts.

Because some flexibility exists in how long or how sulfated a proteoglycan can become, depending on the function of the connective tissue producing them, inhomogeneities can arise from the difference in PG repartitions through the stroma. Indeed, a comparative study of corneas from 12 mammalian species suggests that dermatan sulfate is the preferred proteoglycan in oxygen-rich environments, such as in the anterior portion of the cornea of mammals, such as humans or rabbits. In contrast, keratan sulfate is more abundant in the posterior corneal stroma. [14]

Because Keratan sulfate is a larger and more sulfated molecule than Dermatan sulfate, this dual distribution induces an imbalance of fixed charge density throughout the cornea with the presence of more negative fixed charges in the posterior stroma than in the anterior stroma, as shown in Fig(57).

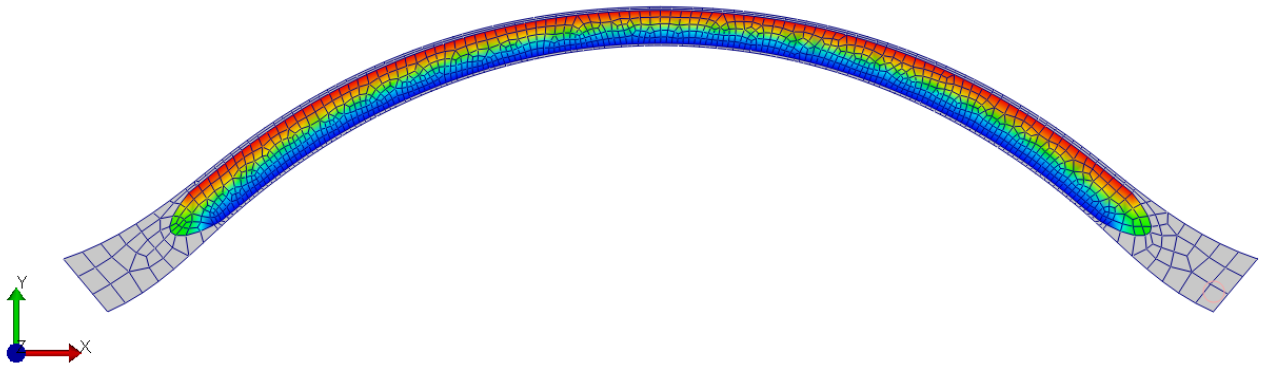

Figure 57: Supposed inhomogeneous distribution of negative fixed charges in the cornea, minimum of -43 nEq/mm^3 in red in the anterior stroma, maximum -48 nEq/mm^3 in blue in the posterior stroma with a linear interpolation in between

This distribution produces inhomogeneous compressive properties throughout the tissue and residual stresses appears. These residual stresses can be depicted using the opening angle test where the tissue is cut on its periphery and deforms consequently from the action of residual stresses without applying any external loads as shown in Fig(58).

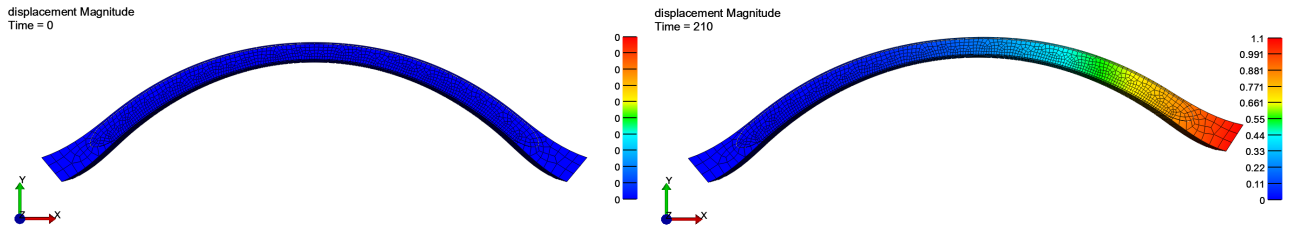

(a) t_0 displacement (b) t_f displacement

Figure 58: Numerical opening angle test showing displacements due to residual stresses arising from the imbalance in fixed charge distribution in the cornea when the right side of the sclera is free to move

This numerical opening angle test showed that a deformation can originates from the presence of an inhomogeneous fixed charge distribution in the corneal tissue, which induces mechanical stress. The stress distribution is displayed in (Fig59).

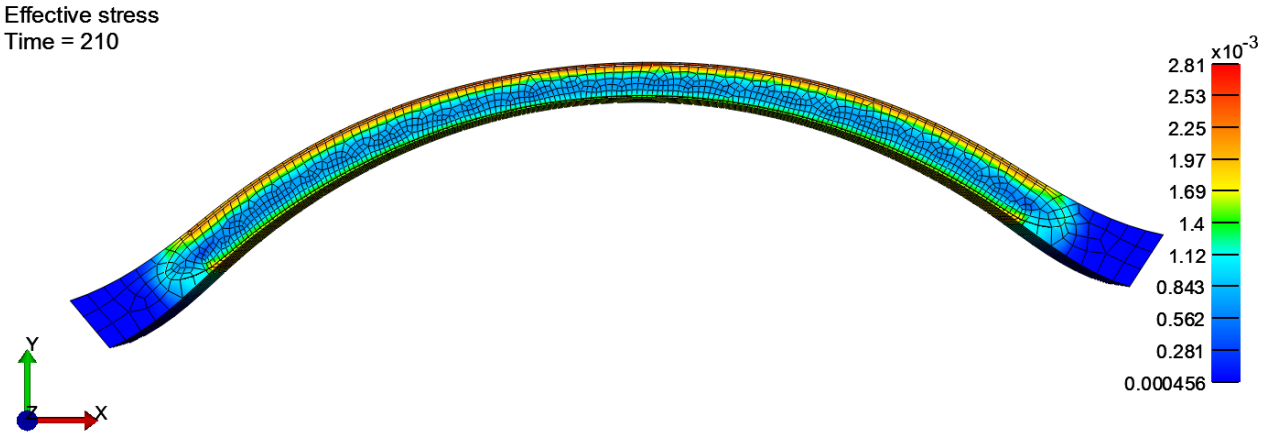

Figure 59: Stress arising from the imbalance in fixed charge distribution in the cornea highlighted by the numerical opening angle test

12.5 Model validation from in vivo corneal data

This section presents a corneal model validation by comparing its outputted results to the clinical data available on corneal biomechanics. Firstly, to assess the consistency between the model equilibrium and cornea physiological condition, we refer to the cornea in vivo swelling pressure measured at 60 mmHg [14] [89]. The swelling pressure corresponds to the total fluid pressure summing both hydraulic and osmotic pressure and defined as $P_s = P_{hyd} + P_{osm}$. Secondly, the model outputs are also compared to results from the study of Pinsky et al. [89] obtained on their own model. The intra ocular pressure and the active endothelial bicarbonate flux will be applied for the first time in this corneal model.

12.5.1 Swelling pressure and intra ocular pressure in a multiphasic framework

The intra ocular pressure is the total pressure one would measure with a pressure transducer, which includes both hydraulic and osmotic effects. There is no standard way to measure each pressure contribution separately; one can calculate each contribution from measurements of the actual fluid pressure and actual solute concentrations, and use a suitable constitutive model that relates the osmotic pressure to the solute concentrations (ex: Eq(57)). Alternatively,

the osmotic contribution in a fluid solution could be estimated experimentally under static conditions by equilibrating the solution against distilled water across a membrane which is impermeable to all solutes (which may be difficult to do for salt ions).

This means that the swelling pressure in the cornea is the combination of hydraulic and osmotic effects. At equilibrium, the diffusive ionic fluxes are balanced by the active ionic fluxes of endothelial cells, resulting in a vanishing water flux. In this state the cornea has an internal swelling pressure of 60 mmHg [89] as shown in Fig(60). This fluid swelling pressure is resisted by the swollen collagen matrix.

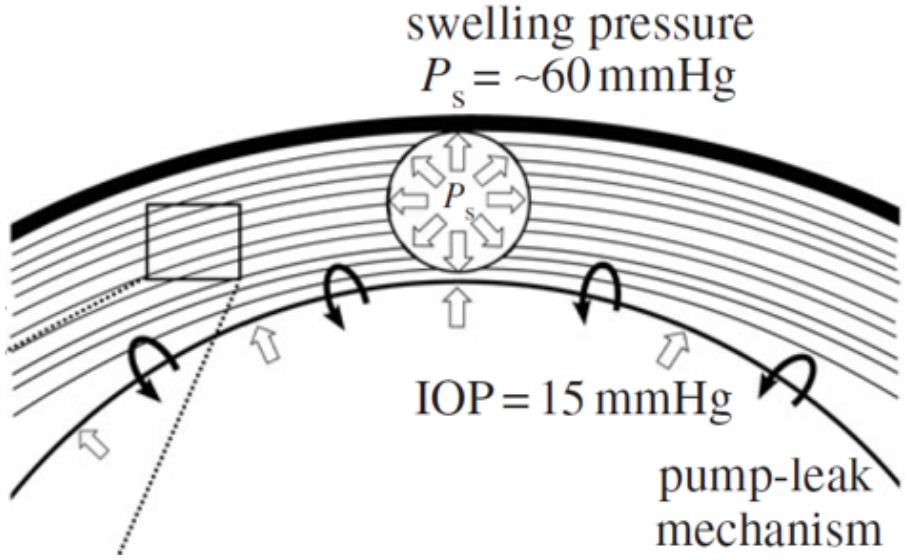

Figure 60: The swelling pressure is the fluid pressure inside the stromal tissue which depends on both the IOP and the tissue osmotic pressure [89]

If we want to model the intra ocular pressure p applied on the inner surface of a multiphasic material, two things has to be done:

- Prescribe the effective fluid pressure as $\tilde{p} = p - R \times T \times osm$, with osm = osmolarity of the fluid present in the external bath, and p the intra ocular pressure.
- Prescribe a mixture normal traction such that traction=p with p the actual fluid pressure, here 2266 Pa.

The mixture normal traction t_n is evaluated internally as $t_n = -p + t_{ne}$, where p is the actual fluid pressure and t_{ne} is the elastic normal traction. In the tissue, the actual fluid pressure p is evaluated from the effective fluid pressure $\tilde{p}$ as $p = \tilde{p} + RT \sum_\alpha c^\alpha$, where c is the actual solute concentrations, and $c = \kappa * \tilde{c}$, where $\tilde{c}$ is the effective solute concentration and $\tilde{\kappa}$ is the partition coefficient (accounts for electrical potential and solubility).

12.5.2 The active ionic flux in a multiphasic framework

A multiphasic material can swell or shrink simply from the active pumping of ionic species inside or outside of its boundaries, increasing or reducing its ionic concentration and osmotic pressure. To account for the metabolic reactions taking place in the corneal endothelium that induce fluxes of metabolic species such as bicarbonate and lactate ions [89], our model will incorporate an active flow of bicarbonate ions from the stroma into the external bath.

Because the regulatory system and details of the molecular mechanisms responsible for active ion transport, which requires Na^+, K^+, ATPase and carbonic anhydrase activity to transport HCO_3^-, Cl^- and possibly Na^+, are not yet fully understood, we relied on a simplified model based only on bicarbonate transport. Doing osmotic experiments in [33], they showed that when the bicarbonate pump is turned off during an osmotic shock, the stromal thickness is about double in magnitude as when the pump is on, displaying the soundness of the bicarbonate model.

12.5.3 Numerical experiments for model validation

In this section we model the in vivo cornea geometry, material properties and boundary conditions to assess the accuracy of the model against clinical data and to compare its results against a corneal model previously developed by Pinsky et al. [89]. We consider four ionic species, namely sodium (Na^+), chloride (Cl^-), bicarbonate (HCO_3^-) and potassium (K^+) distributed on both sides of the endothelium. The reported hydraulic permeability, ionic diffusivities and free diffusivities of corneal endothelium and stroma are given in the material properties section. Additionally, the model input includes the active bicarbonate flux J_a, which was estimated by Li et al. [33] at -0.004 $nm/(mm^2.s)$.

Validation against thickness and fluid pressure In physiological conditions, the environment of the cornea is hypotonic with an osmolarity of $\sum_\alpha c^\alpha = 300$ mM, and the imbalance in charges concentration from to the presence of fixed charges in the stroma induces a swelling of the tissue until a steady state is reached. In the model, this osmotic equilibrium is reached after 1 second as shown in Fig(61).

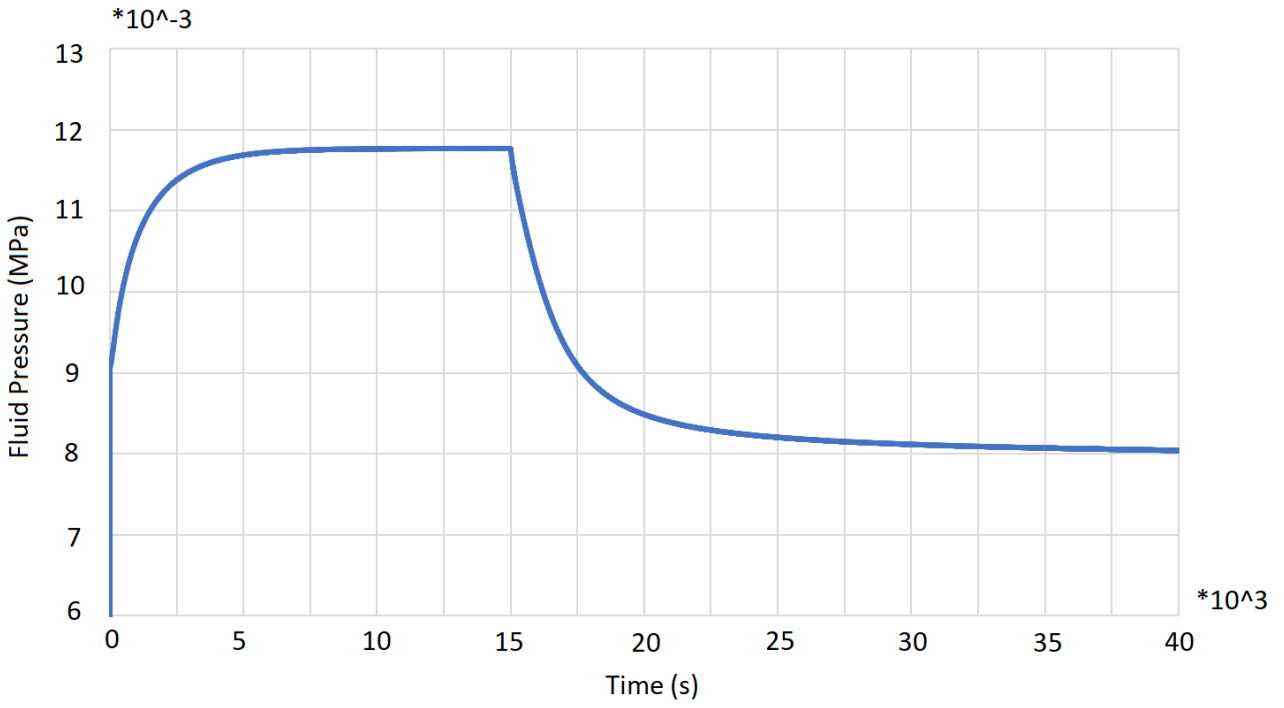

Figure 61: Evolution of the tissue fluid swelling pressure measured at a node in the central posterior stroma as a function of the boundary conditions: at 1s the osmotic equilibrium is reached, the second step from 1 to $15 * 10^3$s corresponds to the application of IOP, the third step corresponds to the application of active bicarbonate flux J_a

In a second stage, the application of IOP from 1 to 15000 seconds increases the stromal fluid pressure above its osmotic free-swelling level. In the last stage, the active ionic flux starts from 15000 to the end of the simulation and pumps the excess of ions out the stroma until an equilibrium is reached when the osmotic passive leak going in compensates the active flux going out. In this step the fluid pressure reduces to a lower value expected close to the fluid pressure measured in vivo in the corneal stroma.

The increase in fluid pressure from 1 to $15 * 10^3$s corresponds to the settlement of the hydrostatic pressure from the IOP, a phenomenon called drained consolidation. From $15 * 10^3$s to the end, the decrease in fluid pressure is associated with the application of active bicarbonate flux J_a and the consequent reduction of tissue negative charge imbalance.

Fig(61) showed that without the active ionic flux, the stromal pressure rises up to a value close to 0.0118 MPa, that converts into 88.5 mmHg, a nonphysiological fluid pressure that will cause the tissue to swell severely and damage the stroma and endothelial membrane. When the active flux is on, the fluid pressure decreases to an equilibrium value of 0.0081 MPa, that converts into 61 mmHg, a value close to the physiological 60 mmHg measured in the in vivo corneal stroma.

In this model, the increase in fluid pressure is associated with an increase in tissue thickness as measured by the distance between anterior and posterior surfaces of the central cornea as shown in Fig(62). This behaviour is also observed in the ex vivo cornea, where the cornea swells due to loss of active flux like in osmotic shocks experiments as performed by Li et al. [33], or in the case of conservation of a corneal graft in solution before its transplantation.

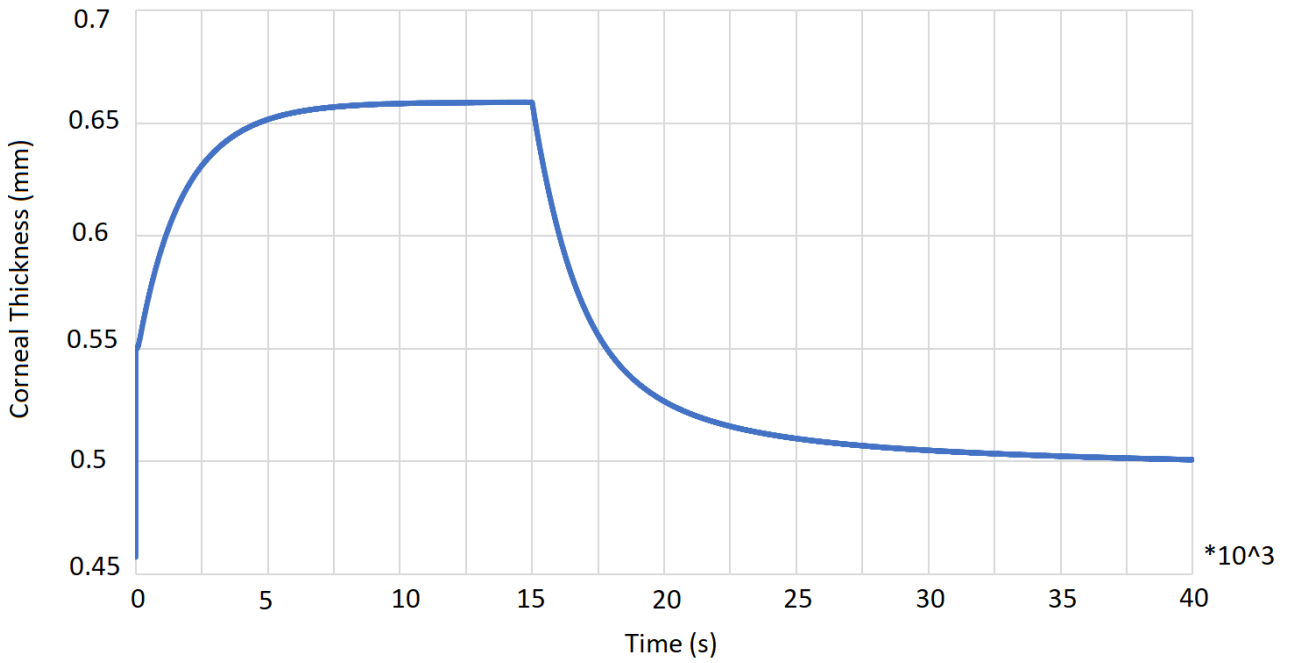

Figure 62: Evolution of the corneal thickness, measured as the difference between a top and a bottom node in the central cornea, through the application of osmotic equilibrium (0 to $1s$), IOP (1 to $15 \times 10^3 s$) and active flux (15×10^3 to $40 \times 10^3 s$)

These two graphs (61 & 62) illustrate the hydration control mechanism from the active endothelial ionic transport, using a simplified bicarbonate model. The active mechanism is essential to maintain an adequate corneal thickness and consequently the adequate refractive

properties for the cornea, and its impairment can be critical for the biomechanical properties of the cornea.

Observation in 3 dimension The tissue swelling can also be evaluated through a 3D visualization of the relative volume, which is the ratio of tissue actual volume upon initial volume. This relative volume depends on the quantity of water present and thus on the swelling pressure in the tissue at the observed time. This swelling pressure P_s is dictated by the tissue microstructure (fixed charge density) and boundary conditions (IOP + active flux).

The Fig(63) shows the evolution of the corneal relative volume during the four stages of the simulation. We can see that the volume, mainly related to the quantity of water in the tissue, is maximized after the phase of intraocular pressure application and before the start of the endothelial active pump. Under the action of the endothelial pump, it reduces to a seemingly more adequate level.

It is also observed that tissue dilation is concentrated in the posterior stroma because of its specific architecture of collagen fibers distributed parallel to the surface of the cornea. On the contrary, the anterior stroma is composed of a quantity of transverse fibers that gives this area isotropic mechanical properties and provides tissue stiffness in the radial direction to resist swelling.

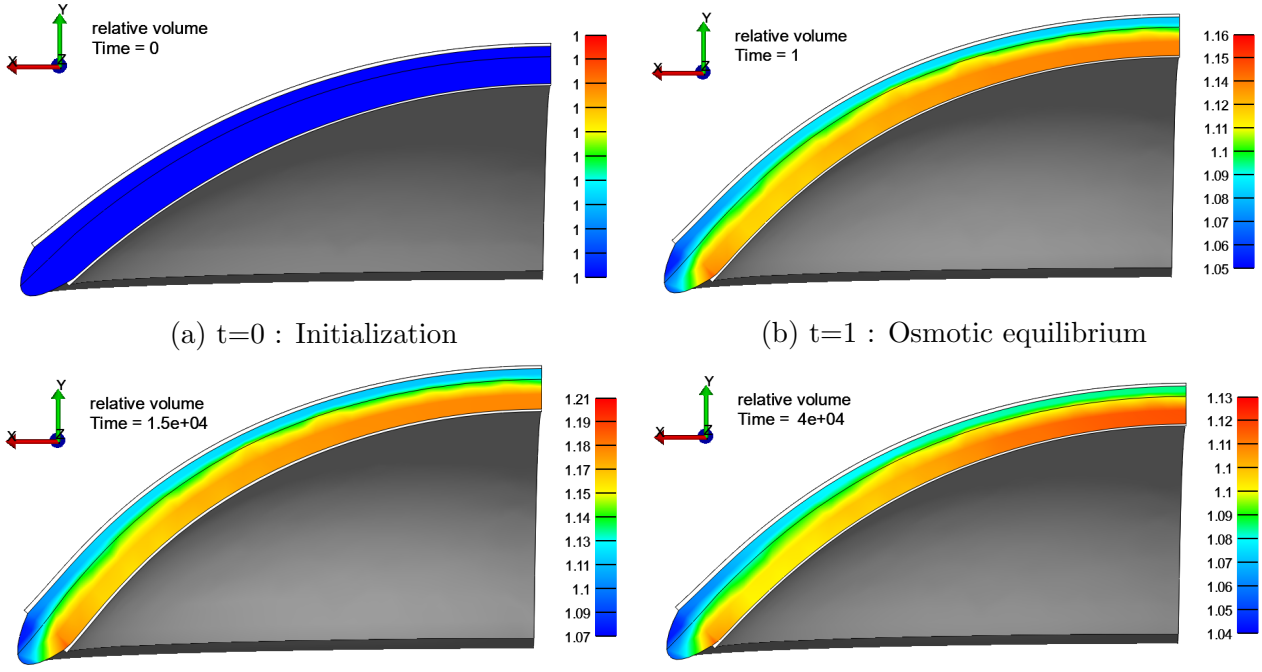

(a) t=0 : Initialization

(b) t=1 : Osmotic equilibrium

(c) t=15 $\times$ 10^3 : Pressurization

(d) t=40 $\times$ 10^3 : with Active flux

Figure 63: The four steps to model the in vivo cornea in a multiphasic framework as shown in 3D sectional view. Each step is associated with a different tissue volume due to changes in fluid pressure. The pressure drops to physiological level after activation of the endothelial active pump as depicted in the last step (d)

To obtain a first confirmation of the model's accuracy in its equilibrium state, we refer to a previous value of vertical displacements of the tissue when submitted to the intra-ocular pressure. This value of apex displacement was estimated to be between 390 and 400 µm in the

model of Pandolfi et al. [10], which is consistent with the vertical displacement obtained in this multiphasic model as shown in Fig(64).

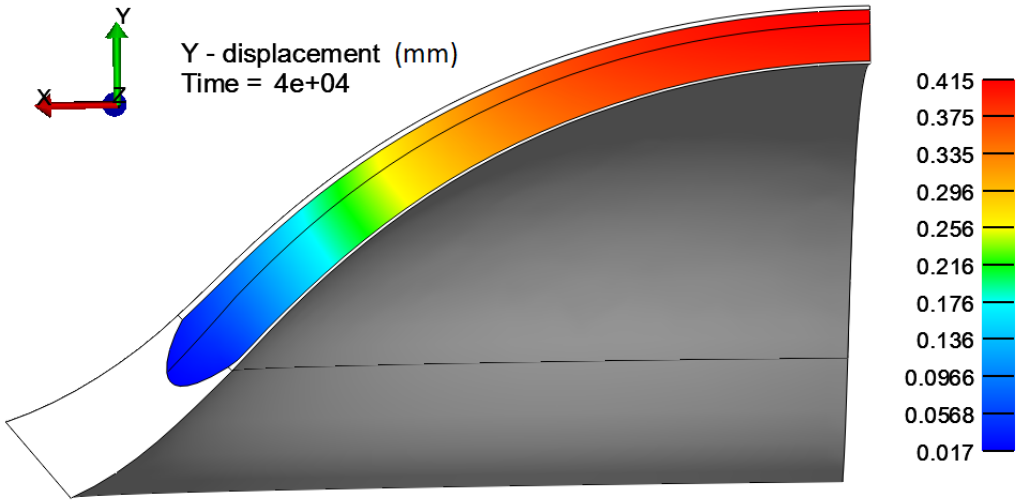

Figure 64: Final vertical displacement of the corneal model after all the steps are applied corresponding to the tissue physiological state. A displacement of 415 µm is depicted, a value close to the one found in the previous part of 400 µm

More importantly, to validate the model, we compare its fluid pressure value to the cornea swelling pressure measured experimentally at $P_s = 60$ mmHg $= 0.008$ MPa found in the litterature [14] [89]. A good agreement of our model with this value was previously found in Fig(61) which reassured us on the predictive capacity of this in vivo corneal model. This time we display the 3D distribution of fluid pressure through the corneal stroma as shown in Fig(65).

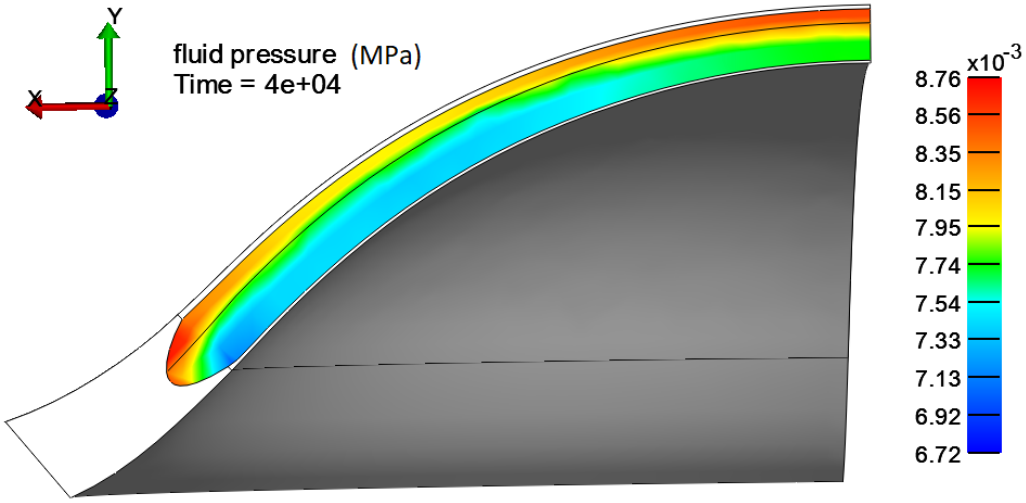

Figure 65: Fluid pressure distribution in the cornea at equilibrium (physiological condition), showing values close to the swelling pressure of 0.008 MPa measured in vivo. A higher pressure is depicted in the anterior stroma as its isotropic fiber architecture is resisting the swelling

As a result of the simulation we observe an average fluid pressure value of 0.008 MPa = 60 mmHg in the equilibrium state of the cornea, i.e. with the intraocular pressure and the active ionic flux of the endothelium. We observe a gradient of pressure between the anterior

and posterior stroma due to difference in microstructure, but the values of fluid pressure remain in overall adequacy with the one measured experimentally.

The higher fluid pressure in the anterior part is explained by its greater stiffness in the radial direction due to its isotropic fiber dispersion, therefore resisting the deformation induced by the fluid pressure. In contrast, the ply-wood structure of the posterior stroma deforms more easily in the radial direction thereby lowering the fluid pressure when increasing in volume.

Evaluation against ionic concentration and fixed charge density To go further on the model evaluation, we compare its results to the one obtained by Pinsky and Cheng [88] on the effect of fixed charge density on solute concentrations. They plotted the evolution of ionic concentrations through the evolution of negative fixed charge from 0 to C_f^0 as shown in Fig(66). Of note the ionic concentrations are representative of a model at equilibrium, i.e. with a working endothelial active flux.

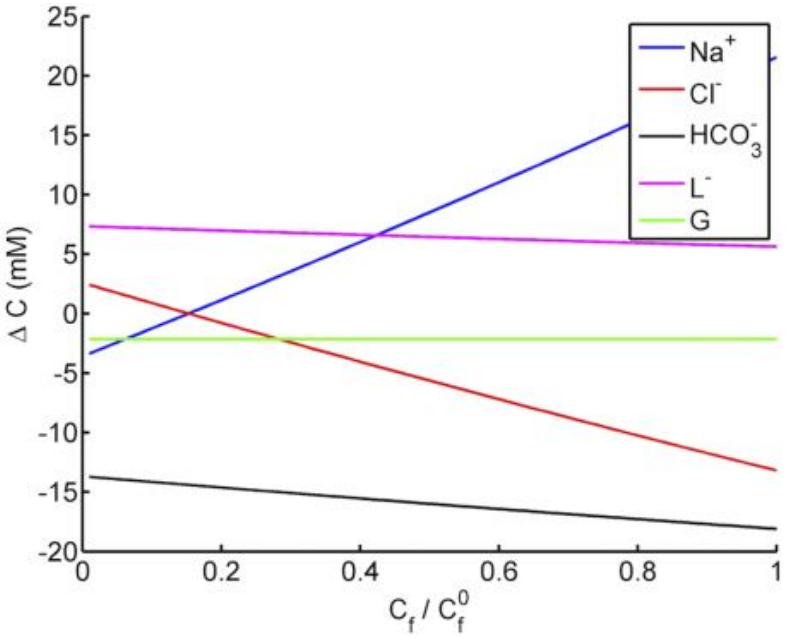

Figure 66: Solute concentration varying with fixed charge density predicted by the irreversible thermodynamics model from Pinsky et al. An increase in positive species and a decrease in negative species are depicted as imposed by the electroneutrality condition [88]

In the range of $C_f \in [0, C_f^0]$, where C_f^0 denotes the reported value of fixed charge density in the cornea of -48 nEq/mm^3, different trends in ionic species concentrations are observed depending on the fixed charge density. As expected, all charged solutes shows sensitivity to C_f and adjusts their concentration to achieve electro-neutrality. In that regard, concentrations of negative species tend to decrease and concentrations of positive species tend to increase. Of note, the osmolarity, which is the total of all ionic concentrations, stay the same for any value of fixed charge density.

Now let's compare these results with our model as shown in Fig(67) to see if it predicts the same trends and magnitudes in ionic concentrations through the variation in negative fixed charge. Because we did not include the same ionic species, the results are expected to be quantitatively different, but the same trend should be observed: a decrease in negative species and an increase in positive species.

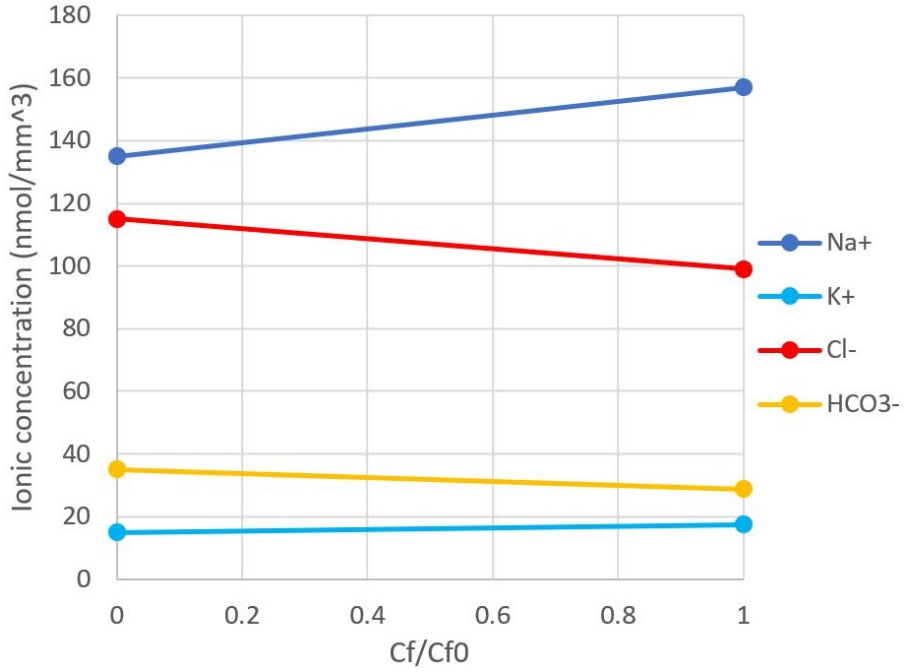

Figure 67: Solute concentration varying with fixed charge density predicted by our multiphasic model. Solute concentrations are changing with the presence of a different fixed charge density in the range of $C_f \in [0, C_f^0]$. An increase in positive species and a decrease in negative species are depicted

First, we can see that the same trend in concentration is respected, with increasing concentration of cations and decreasing concentration of anions. Going from $C^f = 0$ to $C^f = -48\ nEq/mm^3$, we observe a sodium concentration ΔC_{Na^+} highly dependent on the fixed charge density and rising about 22 mM to recover electroneutrality. Deltas of $\Delta C_{Cl^-} = -18mM$ and $\Delta C_{HCO_3^-} = -5mM$ are also decreasing to recover electroneutrality. The osmolarity is observed constant.

Overall the trends and magnitude of concentration changes appear to be consistent with the results of Pinsky et al, a hint that our material properties, and especially ionic diffusivities and ratio of free diffusivities/diffusivities defined in our model, are corrects.

12.5.4 Validation interpretation

These experiments have shown that our model can successfully reproduce the multiphasic behavior of the in vivo cornea, accounting for its hydration control mechanisms in a transient analysis. At equilibrium, the model achieves volumetric stability by a pump-leak mechanism from the endothelium accounting for the passive leak of water through a set of membrane ionic diffusivities and an active control through a constant flux of bicarbonate.

Our analysis herein confirmed that the active pumping reduces the stromal ionic concentrations and hence lowers the osmotic pressure. The incorporation of the bicarbonate active flux J_a was necessary both to match physical observations as well as to continuously counter the passive diffusion of solutes in the stroma. Indeed, at steady state, only the water flux is zero, while the solute fluxes are nonzero.

This corneal model can be applied to study the hydration homeostasis of the cornea and its dysregulation in case of diseases. Because the pump-leak mechanism of the endothelium is dependent on several coupled phenomena, we could further investigates how the tissue can maintain hydration and determine above which threshold the homeostasis is no longer maintained and the tissue start to swell/shrink abnormally as shown in Chapter(13).

13 Model application: study of Fuch's dystrophy and Glaucoma

In this chapter we apply the model developed previously to study a pathological condition characterized by an excessive corneal hydration called Fuch's Endothelial Corneal Dystrophy (FECD). This disease is characterized by a dysfunction of the barrier and pump functions of the corneal endothelium, which results in an abnormally high corneal fluid pressure and subsequent corneal edema.

Because of the osmotic pressure arising from the charged imbalance between the corneal stroma and the aqueous humor, the stroma can swell to many times its normal thickness in free swelling experiments, i.e. without the presence of any boundary conditions. As a consequence, the spacing between fibers would become non-uniform, light scatter would increase, and the cornea would lost its transparency. In vivo, this tendency to swell is counteracted by the endothelial layer barrier and pump functions as shown in previous Chapter(12).

The function of the corneal endothelium is dependent upon a sufficient number of endothelial cells to cover the posterior surface of the cornea as explained in Section(2.3). Endothelial cells are selective barriers that allow leakage of solutes and nutrients from the aqueous humor to the cornea and also possess metabolic pumps inducing flux of specific species. Dysfunction of the barrier function of the endothelium from loss of endothelial cells results in corneal edema, as seen in Fuch's Endothelial Corneal Dystrophy (FECD).

Additionally, several studies demonstrated that active transporters, located primarily in the basolateral cell membrane, transport ions, principally bicarbonate (HCO_3^-), out of the stroma and into the aqueous humor [35] [163]. An osmotic gradient is thus created by the endothelium and water is osmotically drawn from the stroma into the aqueous humor. Steady-state hydration occurs when the endothelial pump rate equals the leak [164]. In this chapter we will study the necessary conditions for the maintenance of a proper hydration of the cornea.

13.1 Description of Fuch's endothelial dystrophy

Fuchs endothelial corneal dystrophy (FECD) is characterized by an accelerated loss of corneal endothelial cells and a simultaneous thickening of the Descemet's membrane from an increase in the cellular deposition. Because the endothelial cells exhibit minimal ability to divide in vivo, endothelial cell loss seen in FECD is permanent.

When the number of cells becomes critically low, the endothelial layer becomes unable to support corneal deturgescence, leading to stromal and epithelial over hydration, and thus causing corneal edema and decrease in visual acuity [149]. The FECD corneas examined present an increased corneal thickness ranging from 580 µm in the early stage [165] to 690 µm in the late stage [166], compared to a normal thickness of 530 µm.

Ultrastructural studies of FECD suggest that the primary disease is in the corneal endothelium and that the accompanying changes in Descemet's membrane, stroma and epithelium are

secondary to that pathology [4]. The accumulation of endothelial cellular excrescences results in the apparition of a characteristic sign of Fuch dystrophy: corneal guttae. The guttae usually start in the central cornea and spread toward the periphery as the disease progresses [166] [167] [168]. The number of cells is inversely proportional to the number of guttae [3].

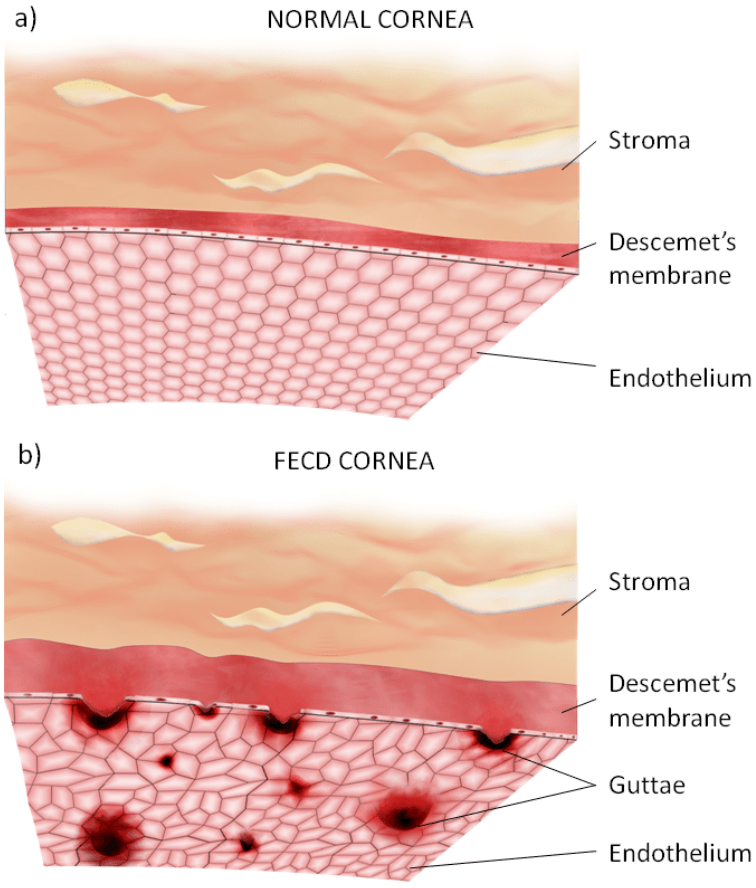

Figure 68: Schematic of an healthy cornea (a) with an intact endothelium and a cornea affected by Fuch's dystrophy in a late stage (b) where guttae that can be observed associated to a thicker Descemet's membrane [4]

Clinically, two forms of FECD have to be differentiated. A rare early form of FECD that starts in the first decade of life and progresses fast [169], characterized by a massively thickened DM at birth, causing corneal over hydration at a very early age [170] [171]. And a more typical late form of FECD that progresses slowly during 10-20 years before becoming clinically evident, on average in the sixth decade of life. This late form have female predominance at a ratio of 2.5-3 for 1 male [3] [172].

Molecular pathology of Fuch's dystrophy regroups a lot of factors but apoptosis, oxidative damage and oxidant-antioxidant imbalance are often cited in its pathogenesis [37]. However, since the pathological mechanisms remain largely unknown, corneal transplantation is currently the only modality used to restore vision [4].

Barrier or pump dysfunction as the cause of Fuch's dystrophy ?

In this disease, the two main functions of the endothelium, barrier and pump, follow different courses of decline. The barrier function depends on the ability of endothelial cells to fully cover

the stromal surface and to maintain cell to cell tight junctions. Both appear to be intact until end stage disease as a proper integrity of the cell-cell tight junctions was found even at low cell density, showing that endothelial cells can expand to cover a larger surface area to maintain barrier integrity [173].

However, when central ECDs are between 2000 and 750 cells/mm^2, endothelial permeability does gradually increase. Interestingly, as pointed at by medical research, compensatory metabolic pump mechanisms can still prevent corneal edema from occurring at this cellular density level. It seems that the active flux can be over activated to compensate for the loss of barrier function [165] by either increasing the metabolic activity of pump sites, or by increasing the total number and density of pump sites on the lateral membranes of endothelial cells [14].

When the central ECD reaches approximately 500 cells/mm^2 or less, compensatory mechanisms fail and cornea over-hydration occur. At this point, the permeability has increased to a point where the metabolic pump fails to balance the leak and FECD symptoms gradually appears. In this late stage, endothelial cells are spread so thin that they do not have enough room on their cell membranes for more pump sites, with all the existing pump sites maximally active. It also seems that the cellular pump function is compromised in this late stage [4] [14].

In summary, the endothelium is able to maintain a sufficient hydration control function until late FECD thanks to the ability of endothelial cells to extend and cover the stromal posterior surface, and to their ability to increase their metabolic pump activity. However, the loss of endothelial cells continue due to pathological condition, and in late stage of the disease, the permeability has increased to a point where compensatory mechanisms ultimately fail to balance the leak and corneal edema results.

13.2 Modeling of Fuch's dystrophy disease

With this knowledge on Fuch's dystrophy, the model developed in the previous Chapter(12) can now be used to investigate the mechanisms of the disease and to study the influence of the endothelial barrier and active pump functions on the maintenance of an healthy fluid pressure and corneal thickness.

Knowing that the model was able to predict the swelling pressure of the cornea measured in physiological condition, a parametric study can be done on the influence of several parameters on the two biomarkers that we know: the fluid pressure and the corneal thickness.

With the objective of studying the role of the endothelium in the corneal hydration homeostasis, the two parameters included in the analysis will be the bicarbonate diffusivity representing the barrier function of the endothelium, and the bicarbonate active flux representing the pump function of the endothelium.

That way the simulation could be used to better understand the physical mechanisms of the disease and eventually propose an hypothesis on how to counter the over pressurization and corneal swelling observed in FECD.

13.2.1 Link between endothelial permeability and corneal swelling pressure

This section presents a parametric study showing the influence of the bicarbonate endothelial diffusivity $d^e_{HCO_3^-}$ on the stromal fluid swelling pressure P_s. The ratio of bicarbonate diffusivity / healthy bicarbonate diffusivity is used as horizontal axis to better appreciate the change in membrane permeability. A normal active flux $J^{a0}_{HCO_3-}$ is considered throughout the experiment.

As shown in Fig(69), at the condition of a completely non-functional barrier properties represented by a high diffusivity coefficient ($d^e_{HCO_3^-} = 100 \times d^e_{healthy}$), the fluid pressure in the central cornea is predicted to be approximately 0.0118 MPa = 88.5 mmHg, a nonphysiological value 50% higher than the healthy one.

When $d^e_{HCO_3^-} = d^e_{healthy}$, P_s is predicted to be 0.0081 MPa which is an acceptable physiological value of swelling pressure. This result confirms the necessity of the endothelial barrier function to maintain the hydration of the tissue at good levels and to ensure the right cornea mechanical and optical properties.

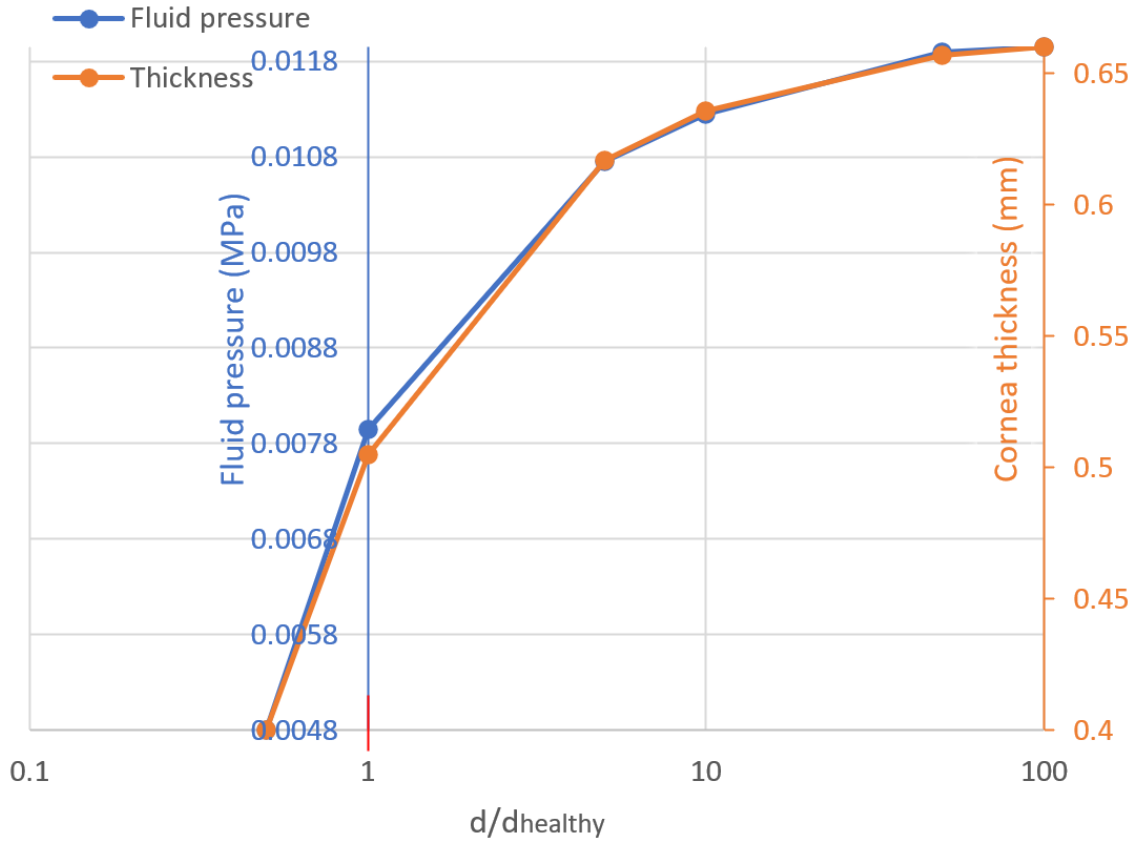

Figure 69: Figure showing the effect of bicarbonate diffusivity on P_s and cornea thickness. The horizontal axis represents the ratio of actual bicarbonate diffusivity / healthy bicarbonate diffusivity in the range of $d/d_{healthy} \in [0.5;100]$ in log scale

When $d^e_{HCO_3^-} = 100 \times d^e_{healthy}$, the model predicted a maximum swollen central corneal thickness (CCT) of approximately 660 µm, which lies in the range of Fuch's dystrophy clinical observation (580-690 µm) for patients in late stage disease. The maximum pressure and thickness are reached when the endothelial barrier is no longer enforcing any permeability limitation on the passage of ions through the membrane. We can observe a curve flattening when the diffusivity ratio reaches a value 50 to 100 times higher than the diffusivity in the normal cornea, showing the threshold at which the permeability becomes too high to be compensated by the active flux.

In contrast, when the membrane diffusivity is decreased as described by the ratio $d/d_{healthy} < 1$, the fluid swelling pressure P_s and corneal thickness are reduced under their physiological values. Going into really small bicarbonate diffusivities, calculations were not able to converge as the active flux without passive leak induced an important shrinkage of the cornea under 440 µm.

These results are consistent with the fact the GAGs negative fixed charges in the stroma are just over one-quarter saturated or bound with Na^+. The remaining unbound proportion are therefore still available to bind more Na^+ and absorb more water if given the opportunity, such as when the endothelial barrier function is impaired. The maximum swelling state of a cornea with impaired endothelium would therefore correspond to a state where all negative fixed charges are saturated.

13.2.2 Link between endothelial active flux and corneal swelling pressure

Another parametric study is performed in this section to show the influence of the bicarbonate active flux $J^a_{HCO_3^-}$ on the stromal fluid swelling pressure P_s. The ratio of bicarbonate flux / healthy bicarbonate flux is used as horizontal axis to better appreciate the change in membrane active pump. An healthy bicarbonate diffusivity $d_{healthy}$ is considered throughout the experiment.

As shown in Fig(70), at the condition of no active bicarbonate transport ($J^a_{HCO_3^-} = 0$), the fluid pressure in the central cornea is predicted to be approximately 0.0118 MPa = 88.5 mmHg, a nonphysiological value that will cause the tissue to swell. It shows that even with an intact barrier function, a slow diffusion still operates, and without the endothelial pump action, there is no maintenance of the right fluid swelling pressure and hydration. The value of 88.5 mmHg represents the maximal fluid swelling pressure of a cornea at osmotic equilibrium subjected to the intraocular pressure and without any endothelial pump function. This result confirms the necessity of the active transport mechanism to maintain the hydration of the tissue. When $J^a_{HCO_3^-} = J^{a0}_{HCO_3^-} = -0.004 nm/(mm^2.s)$, P_s is predicted to be 61 mmHg which is an acceptable physiological value of swelling pressure.

The plot also shows that the tissue swelling pressure P_s is reduced when the active ionic flux increase, with an essentially linear relationship between the two. However, a curve flattening is depicted at $J^a/J^{a0} > 1.5$ when the specimen starts to be too much compressed and electrostatic repulsion takes place due to volume exclusion effect, showing the limit dictated by the tissue contraction capability.

The effect of active ionic flux on P_s are summarized in Fig(70) over a range of $J^a_{HCO_3^-}/J^{a0}_{HCO_3^-}$ $\in$ [-2;3] :

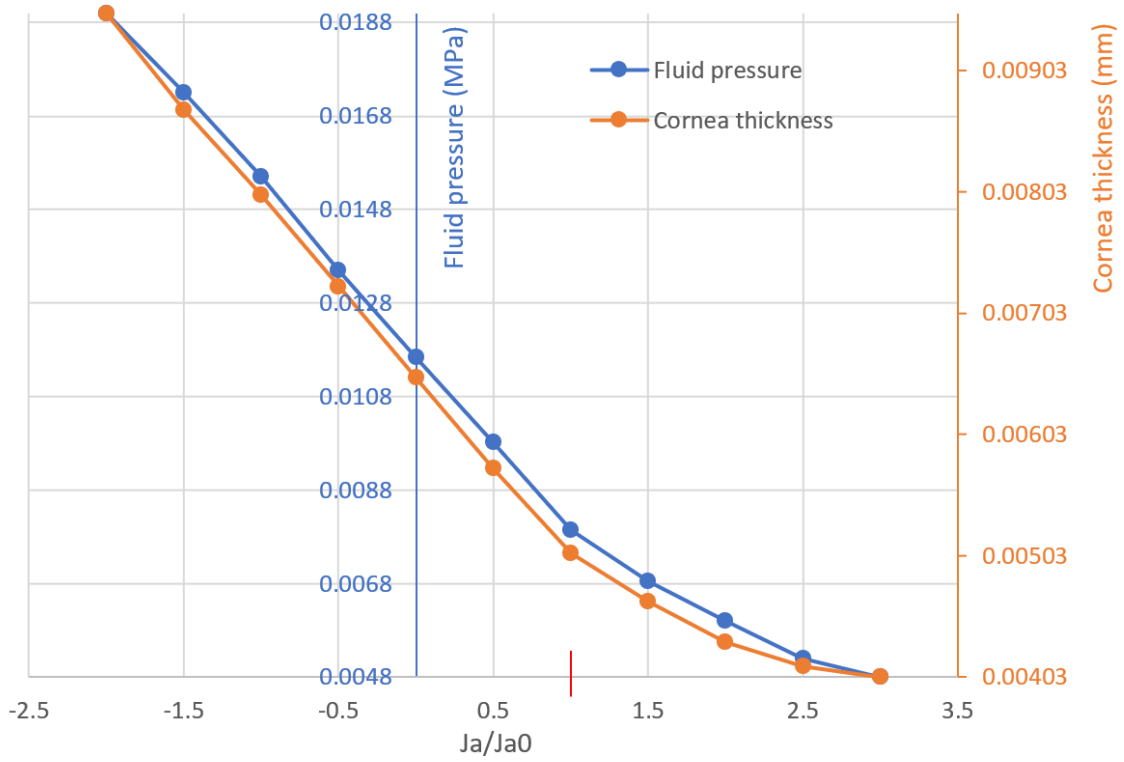

Figure 70: Figure showing the predicted fluid swelling pressure P_s and the cornea thickness against ratio of actual/healthy active bicarbonate flux of the corneal endothelium. A positive J^a/J^{a0} means a flux of bicarbonate directed from inside the cornea to outside, and negative J^a/J^{a0} from outside to inside.

In summary, both diffusivity barrier and active pump mechanisms are needed to maintain the adequate fluid pressure inside the stroma. The maximum swelling state of a cornea with impaired endothelium would therefore correspond to a state where all negative fixed charges are saturated, which in our model associates with a fluid pressure of approximately 0.0118 MPa = 88.5 mmHg and a maximum swollen corneal central thickness (CCT) of approximately 660 µm.

However, before reaching that critical state, it seems that several combinations of diffusivity and active flux could maintain a good hydration level in the cornea, as long as the diffusivity does not become excessively high or the active flux excessively low. The next section explores how this compensatory mechanism translates into the in vivo cornea and influence the disease progression.

Active flux compensatory mechanism As pointed at by medical research, it seems that up to a certain point, the endothelial active flux may be over activated to compensate for the loss of barrier function due to cell loss happening in FECD. This section investigates if different combinations of diffusivity and active flux can give a similar fluid pressure at equilibrium, thereby trying to confirm the compensatory hypothesis.

In that objective, we developed a model with a membrane 10 times more permeable, i.e. with a bicarbonate diffusivity 10 times higher, but coupled with a 10 times higher active bicarbonate flux $J^a_{HCO_3^-}$. The resulting curves of fluid pressure and corneal thickness are then plotted and compared with the healthy case as shown in Fig(71) and Fig(72).

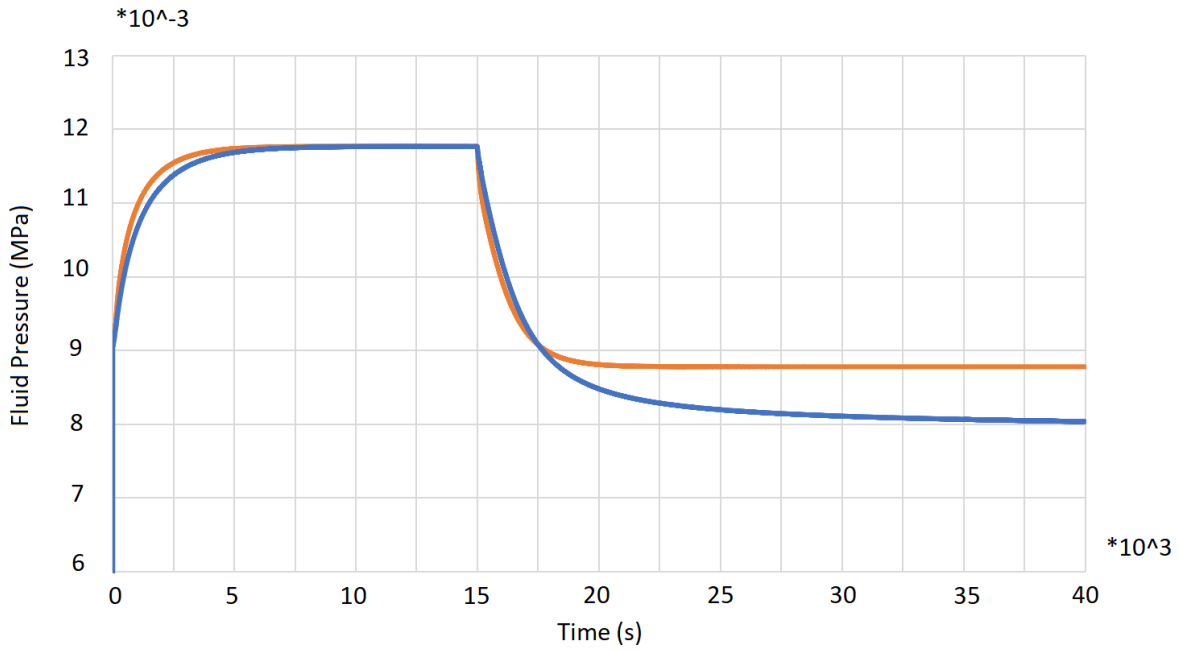

Figure 71: Evolution of the fluid pressure in the healthy case (blue curve) and comparison with a pathological compensated case (orange curve) modeled with a 10 times higher bicarbonate endothelial permeability and a 10 times higher bicarbonate active flux. It shows that the loss in barrier function is mostly compensated by the higher pump rate, but an incompensated increase in fluid pressure is already noticed

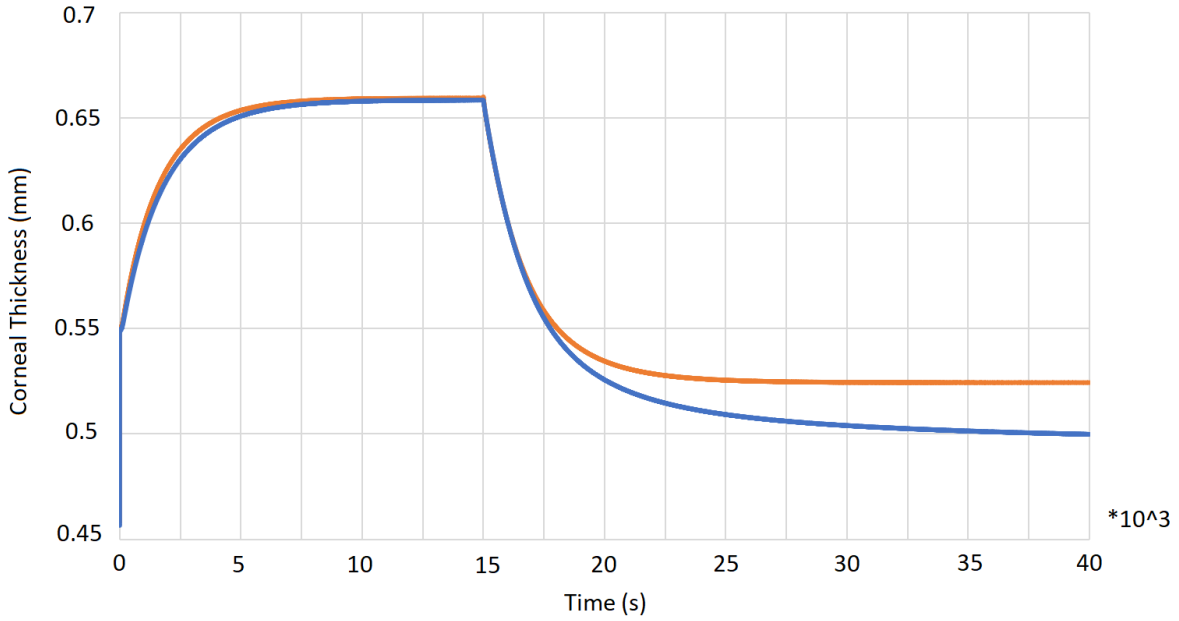

Figure 72: Evolution of the corneal thickness in the healthy case (blue curve) and comparison with a pathological compensated case (orange curve) modeled with a 10 times higher bicarbonate endothelial permeability and a 10 times higher bicarbonate active flux. The loss in barrier function is mostly compensated by the higher pump rate, but an incompensated increase in corneal thickness is noticed

The simulation showed that a 10 times increase in membrane bicarbonate diffusivity can be compensated by a 10 times increase in active flux, demonstrating that up to a certain point, the loss of barrier function can be compensated by an increase in active flux. However, the

compensation effect is not perfect, and the equilibrium point of the compensated model is different from that of the healthy case. Indeed, an "irreversible" increase in fluid pressure of 0.0008 MPa and an increase in corneal thickness of 25 µm are observed in Fig(71) and Fig(72) despite the over-activation of the endothelial pump.

Looking in more detail, the simulation also showed that the model with a higher diffusivity reaches equilibrium faster, as materialized by steeper slopes of pressure and thickness evolution when boundary conditions are applied at t=1s and t=$15 * 10^3$s.

Further experimenting showed that when diffusivity and flux are further increased, although a compensation is observed, the cornea does not return to a healthy value of stromal fluid pressure and thickness. This shows that, even with a perfectly working endothelial active flux, when the barrier function is impaired and permeability is too high like in an advanced state of Fuch's dystrophy, the tissue will swell inevitably.

13.3 Fuch's dystrophy edema presentation in the 3D cornea

This second section on Fuch's dystrophy presents the collagen-swelling interaction of a 3D cornea in a swelling state typical of edematous disease and highlights the interaction of the local collagen network with the fluid.

It has been shown that when a sample of corneal stroma is immersed in deionized water, the tissue swells beyond its original thickness by absorbing water from the bath and corneal edema can be observed [157]. This edema is not homogeneous and occurs mainly in the posterior stromal in the thickness direction [89]. In contrast, the anterior stroma swells less readily and maintain an adequate corneal anterior curvature due to its higher cohesive strength.

If we simulate a cornea in advanced Fuch's dystrophy state where the endothelium barrier is completely compromised, the distribution of the volume change under tissue over-hydration can be analyze. It shows that, as the barrier function is weakened and the fluid pressure increases, the posterior surface moves inwardly towards the inner eye as shown in Fig(73).

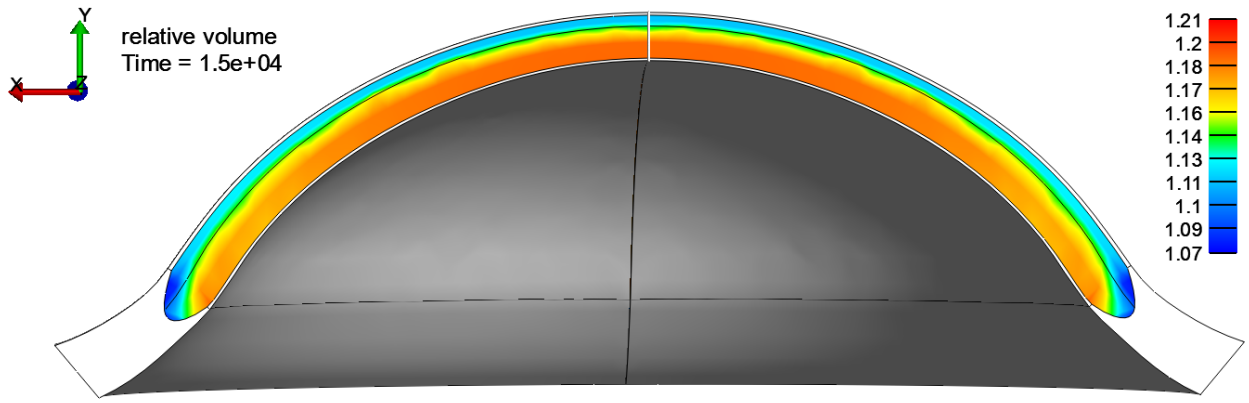

Figure 73: Posterior swelling of a stroma in over-hydration states depicted by relative volume change from initial volume. The swollen cornea represents an advanced state of Fuch's dystrophy where the endothelium barrier is completely compromised leading to a 20% increase in posterior stromal volume

Although depth-related differences in the concentration of charged proteoglycans may account for the higher hydration levels in the posterior stroma in healthy conditions as seen in the

residual stress Section(12.4.2), in disease state it appears that the collagen fibers orientation and the degree of lamellar interweaving have the greatest influence on the amount of regional stromal thickening from edema-related swelling. Indeed in our model, the anterior isotropic lamellar interweaving induced only a mildly swells and actually maintained the anterior corneal curvature when the remaining posterior two-thirds swells up 20% above its normal thickness. Therefore when edematous condition applies, corneal thickness and interfibrillar spacing increase with stromal depth.

The increase in tissue volume is due to the influx of water in the tissue and can be depicted by the volume fraction of water, which rises from 70% to 80% in swelling condition, thereby greatly increasing interfibrillar spacing as shown in Fig(74).

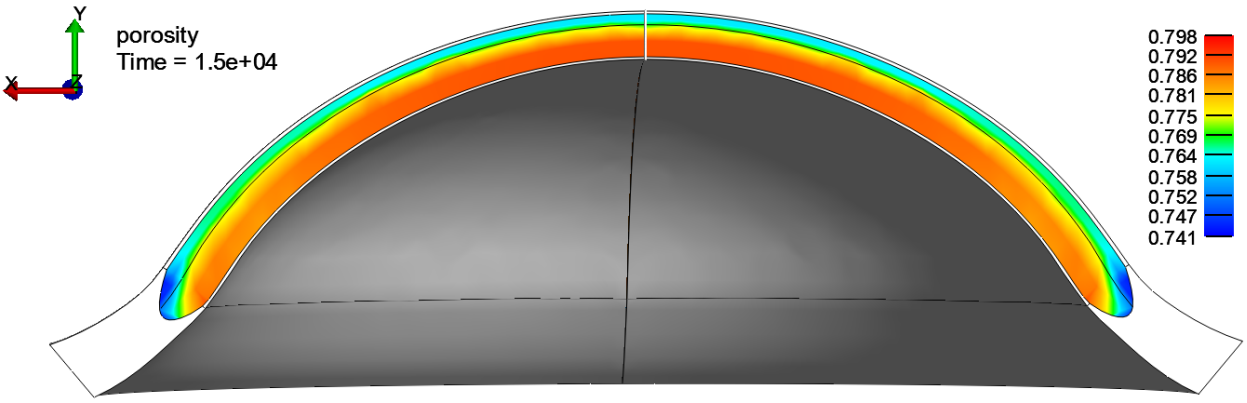

Figure 74: Expected higher volume fraction of water in the posterior stroma than in the anterior stroma in advanced state of Fuch's dystrophy as depicted by the red area. Porosity = volume fraction of water

This influx of water is responsible for an increase in fluid pressure in the tissue, rising from the physiological value of 60 mmHg to a level around 0.012 MPa = 90 mmHg, way over its healthy value. This increase in pressure can damage the stroma microstructure and endothelium from mechanical and mechanobiological stresses. The posterior stroma can swell most readily and absorb the deformation due to its lower cohesive strength, thus showing a lower fluid pressure as shown in Fig(75).

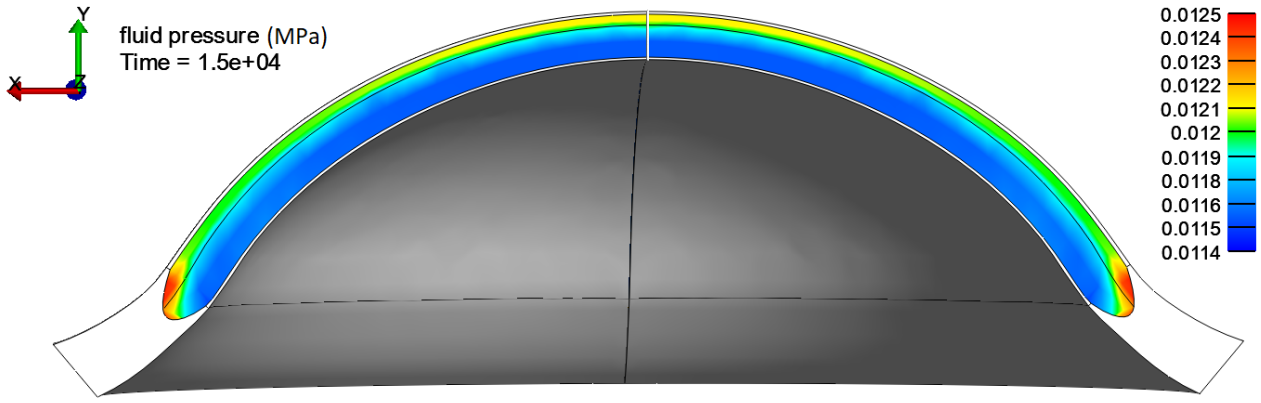

Figure 75: Posterior stroma presenting a lower fluid pressure value than the anterior stroma due to its lower radial stiffness. The cornea is in an advanced state of Fuch's dystrophy where the endothelium barrier is completely compromised, leading to a 50% increase in fluid pressure

Thanks to this corneal multiphasic model, we were able to describe the 3D poro hyper elastic behavior of the cornea, which included a fluid phase whose pressure was the sum of an hydraulic and an osmotic contribution. With the incorporation of charged solutes, the model recovered the osmotic pressure induced by the osmotic flow of water from the aqueous humor into the stroma. The endothelial pump-leak hydration control was also described, which turned to be an essential feature for the hydration homeostasis of the cornea that also greatly affected its mechanical behavior.

We were able to recreate a pathological condition of the cornea called Fuch's dystrophy by altering the endothelial barrier and pump functions, which resulted in an increased fluid pressure and consequent swelling of the tissue. This simulation showed that the loss of barrier function can be compensated by an increase in the active flux up to a certain point, after which symptoms of the disease start to appear. The 3D model showed that the increase in thickness mostly happens in the posterior two third of the stroma in the radial direction.

13.4 Glaucoma presentation in the 3D cornea

Using the same model, it is also possible to simulate pathological conditions not necessarily linked to endothelial malfunction but to abnormal hydrostatic fluid pressure, such as glaucoma. Glaucoma is a disease in which abnormally high intra ocular pressure builds up, which can damage the optic nerve and also lead to corneal edema. Many forms of glaucoma have no warning signs because the effect is so gradual that patients may not notice a change in vision until the condition is at an advanced stage [14].

The thinner corneas are associated with an increased severity of visual loss and a more rapid progression of the disease because the tonometry examinations tends to underestimate the intra-ocular pressure on softer corneas and medical treatments are started later [174].

The internal fluid pressure boundary condition in the simulation can be increased to look at the fluid pressure distribution in a cornea with an acute glaucoma, which is represented by an intraocular pressure of 50 mmHg, i.e. almost 4 times higher than the healthy one. The result of such an elevated intraocular pressure is a higher than normal fluid pressure in the stroma as shown in Fig(76).

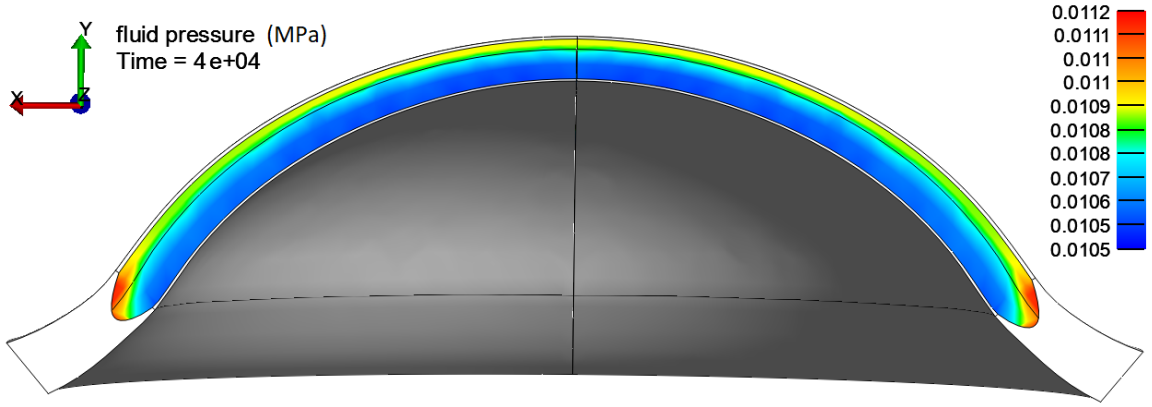

Figure 76: Cornea in glaucomatous condition associated with a higher tissue fluid pressure in physiological equilibrium, even with a healthy endothelium function. The mean fluid pressure in this cornea is 0.0108 MPa = 80 mmHg, whereas the normal pressure is 0.008 MPa = 60 mmHg

From the application of this abnormally high hydraulic pressure, the simulation showed a consequent higher tissue swelling pressure. Whether the corneal endothelium can counteract this effect and reduce the pressure on the stroma is not known, however corneal edema from glaucomatous condition has been observed for values of intra ocular pressure above 50 mmHg [14].

Such an elevation of pressure is a diagnostic feature of acute angle-closure glaucoma, an extreme condition with almost a complete outflow obstruction of aqueous humor. The simulation could help predict the evolution of fluid pressure and corneal thickness in such a case.

14 What's next ?: molecular mechanisms underlying the corneal endothelial pump

To conclude this part on hydrated tissue, a preliminary modeling work considering the biological complexity of the endothelial chemical exchanger is presented in this section.

In order to describe the endothelium without using a simplified bicarbonate model, modeling membrane reactions in a reactive mixture framework could provide the capability to reproduce membrane physiology and expand the toolbox needed to describe how membranes adapts to their evolving environment. It allows for the distinction between passive transport across the membrane channels, as well as active transport mediated by carriers and pumps.

Chemical reactions can be incorportated into a multiphasic mixture by adding a mass supply term $\hat{\rho}^\alpha$ to the equation of mass balance

$$\frac{\partial \rho^\alpha}{\partial t} + div(\rho^\alpha \boldsymbol{v}^\alpha) = \hat{\rho}^\alpha \tag{97}$$

All the development for balance equations and constitutive relations needed to describe reactive mixtures can be found in [175]. The formulation allows a full coupling of mechanical and chemical effects, providing a framework where material properties and response functions may depend on solid matrix strain as well as solute concentration.

14.1 Description of the corneal molecular endothelial pump-leak exchanger

How all the molecular exchangers combine to give the complex regulatory system of the corneal endothelium is a subject in ongoing research. It has been suggested that the endothelial pump leak involves complicated ionic exchanges (such as Na^+/H^+ and Cl^-/HCO_3^-) and ion cotransport (such as Na^+/HCO_3^- and K^+/HCO_3^-, $Na^+/K^+/2Cl^-$) [35].

Although molecular detail of the endothelial transporters is not complete, the net result is an active component of bicarbonate-ion flux directed from the stroma toward the anterior chamber. The resulting efflux of bicarbonate ions across the endothelium lowers the osmolarity at the stromal interface relative to that in the aqueous humor. As a consequence of this active ion transport, water is osmotically driven across the endothelium toward the anterior chamber.

One of the driving force for the endothelial-osmotic water outflow comes from the energy released when converting ATP to ADP in the Na^+/K^+ active ionic pump [164]. It is stated in [35] that if either the Na^+/K^+ - ATPase ionic pump is blocked or all sources of bicarbonate ion (including carbon dioxide) are replaced, the fluid pump ceases. Others contribution, including

bicarbonate ionic exchanger contributes to this mechanism.

Fig(77) shows a possible bicarbonate transport model for the corneal endothelium, displaying the complexity of exchanges happening in a biological membrane.

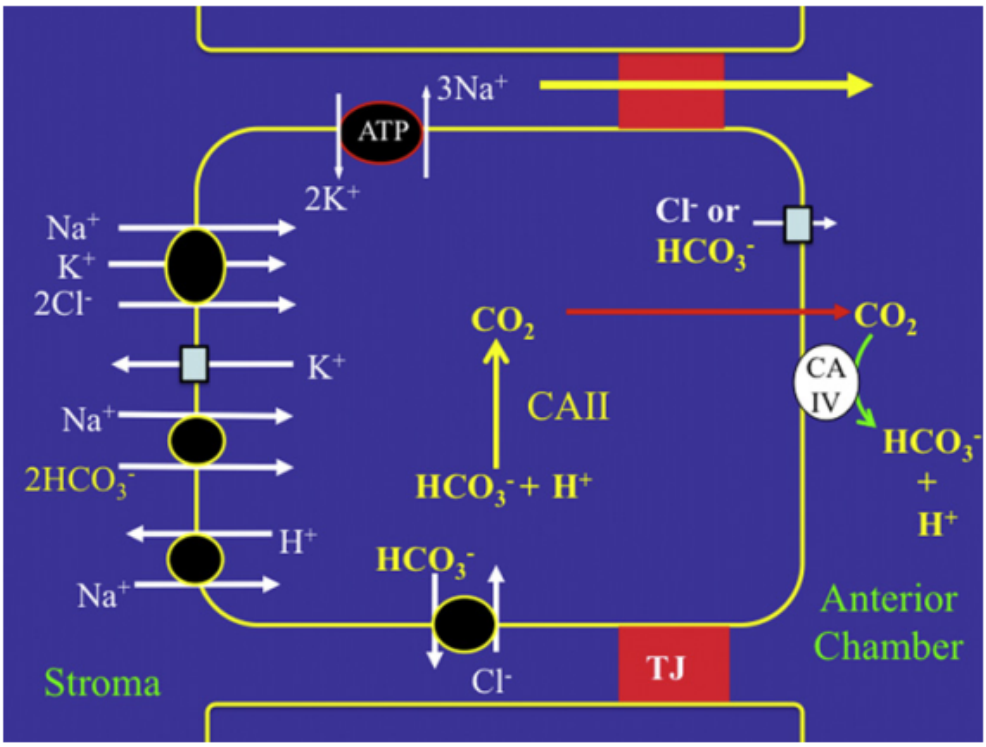

Figure 77: Hypothetical bicarbonate secretion model for the corneal endothelial pump as proposed by Bonanno et al. [35], showing the complexity of the endothelial regulation function

14.2 Numerical application with a simple model of reactive membrane

As a preliminary work, the model is applied to describe an irreversible chemical reaction involving a neutral solute delivered from one side of the cytoplasmic region of the endothelium to the extracellular environment. This simple reactive model is therefore limited to a net exchange of solute between the stroma and the aqueous humour.

The stoichiometric coefficients ν_R^α of the reactants and ν_P^α for the products are specified, with equal initial reactants concentration of $c^\alpha = 1$ and a forward reaction rate $k = 1$. For this type of forward reaction, the constitutive relation for the molar production rate $\hat{\xi}$ is given in Eq(98), with $\hat{\xi}$ in $[n/L^3.t]$ and c^α in $[n/L^3]$.

$$\hat{\xi} = k \prod_\alpha (c^\alpha)^{\nu_R^\alpha} \tag{98}$$

An application of this simple forward reaction could be to model the production of solid copper sulfide from solid copper and solid sulfur,

$$Cu + S \rightarrow CuS$$

All three species could be modeled in the mixture as solid-bound molecules, with the stoichiometric coefficients of the reactants $v_R^{Cu} = 1$, $v_R^S = 1$ and those of the products are $v_P^{CuS} = 1$.

The geometry of our model is made of a cytoplasmic region, a membrane, and an extracellular region to describe the exchange between a single cell and its environment. Each solid domain is a cube of 1 µm edges and the 2D endothelial membrane has a thickness of 10 nm.

For simplicity we model a neutral generic reaction $A + A \rightarrow 2A$. Neutral solute A is initially presents in all three domains, with an initial concentration of 10 mM. The extracellular solution has boundary conditions prescribed on five faces, to force the extracellular domain to remain at 10 mM and prescribe the concentration on the extracellular side of the membrane.

The membrane reaction is a forward reaction with a constant reaction rate. The reactant is the intracellular solute and the product is the extracellular solute. The model does nothing for the first 10 s to make sure that initial conditions are at steady state, then the active flux is turned on at time 10 s until the end of the analysis at time 20 s. Once the active transport starts, the solute concentration in the cytoplasm gets depleted.

The membrane reaction consumes the intracellular solute as reactant and deliver the extracellular solute as product in the solution. This reaction simulates a facilitated diffusion channel where a carrier (an enzyme for example) transports a neutral molecule across a membrane. This reaction induces a change in solute concentration and creates a flux of water from the cytoplasmic region into the external solution as shown in Fig(78).

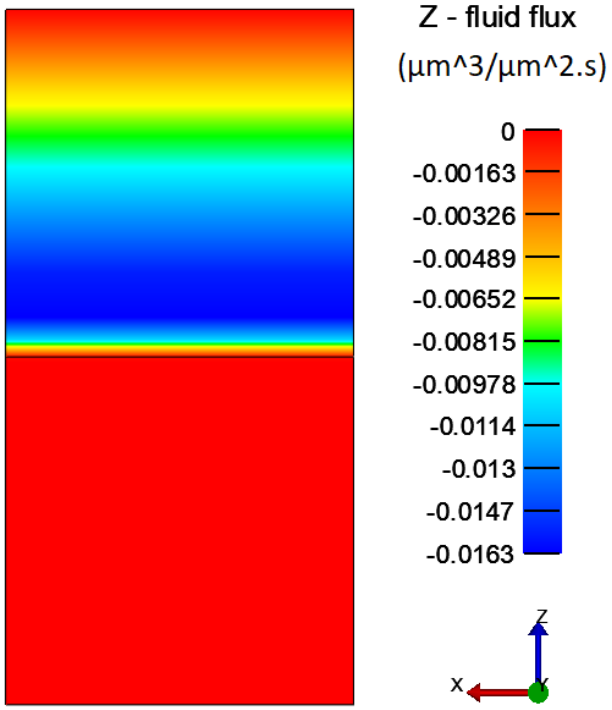

Figure 78: Vertical fluid flux in the model displaying fluid leaving the upper cellular part and going into the external environment while the membrane reaction is taking place

By adjusting the stochiometry of the reaction, it is possible to visualize a greater or lesser effect of the ionic pump on the various model outputs. The 100% activation corresponds to a complete reaction where every ion pumped into the cell is delivered into the outside. The 10% corresponds to the lowest reaction rate as shown in Fig(79).

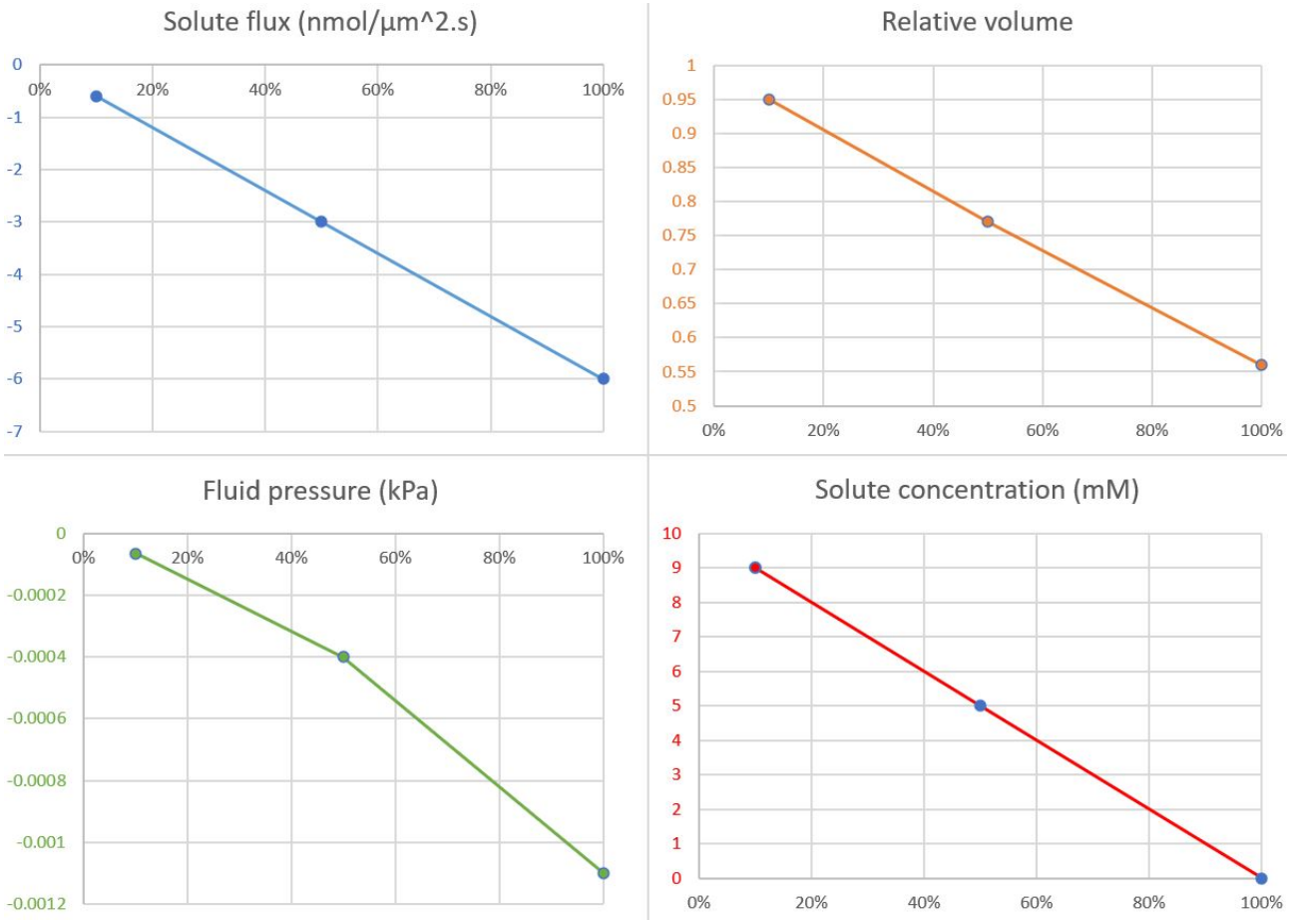

Figure 79: Outputs of the membrane reactive model describing a forward reaction from the cell into its external environment. 4 quantities evolution are displayed based on the reaction stochiometry varying from 10% to 100% of products to be delivered in the external environment. Solute flux in the membrane in blue, relative volume of the cell in orange, fluid pressure in the cell in green, solute concentration in the cell in red

Linear correlations can be observed between the reaction stochiometry and outputs in this simple model. The more the pump is operating, the more the solute concentration in the cytoplasm decreases, with others quantities varying accordingly. As the solute flux intensify and transports more solute through the membrane, the solute concentration gets lower in the cytoplasmic region, the fluid pressure decreases due to less osmotic effects from the lower concentration of solute in the cell and consequently induces a shrink in volume.

This simple model recover the basic effects of the cellular active pump function and its importance in maintaining an equilibrium in tissue hydration to counter its osmotic swelling tendency. However, in a multi-solutes environment, biological membranes are finely tuned to regulate solutes concentrations with specific ion channels, facilitated diffusion channels and active pumps working simultaneously. It is beyond the scope of this thesis to develop such a complex model but this preliminary work may serve as a basis for its future development. A straightforward continuation would be to model the Na^+/K^+ - ATPase ionic pump as described in Fig(80).

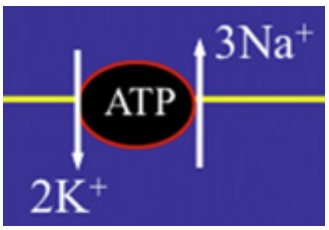

Figure 80: Na^+/K^+ - ATPase ionic pump as described in [35]

15 Hydrated cornea summary

Thanks to this multiphasic model, we were able to recreate the complex mechanism of corneal hydration and fluid pressure homeostasis of an in vivo cornea. With the incorporation of charged solutes we modeled the evolution of ionic concentration and volume fraction of water that maintain the corneal stroma in electroneutral condition and defines the its osmotic pressure. The pump-leak action of the endothelial membrane was also incorporated and proved to be essential in the control of tissue hydration.

Based on a simplified bicarbonate model of the endothelial membrane exchanger, we recreated a condition called bullous keratopathy in which the endothelial outward flux of water is diminished in comparison to the healthy cornea. This condition is notably associated with Fuch's endothelial corneal dystrophy (FECD), a disease characterized by an accelerated loss of corneal endothelial cells. This allows us to study the impairments leading to this pathological state.

In FECD the two main functions of the endothelium, barrier and pump, follow different courses of decline. We modeled pathological conditions by altering separately the endothelial barrier function represented by the bicarbonate diffusivity and the endothelial pump function represented by the bicarbonate active flux, which resulted both in an increase in fluid pressure. We found that even with an intact barrier, a slow diffusion still operates and without the endothelial pump action, there is no maintenance of the right fluid pressure. In summary, both barrier and pump functions were needed to maintain the adequate fluid pressure inside the stroma and to keep the cornea at normal hydration level and thickness.

We showed that in the case of Fuch's dystrophy, the initial loss of barrier function can be compensated by an increase in the active flux, but when diffusivity and flux are further increased, although a compensation is observed, the cornea does not return to a healthy value of stromal fluid pressure. This situation was observed before in medical research [165] and corresponds to a cornea in an advanced state of Fuch's dystrophy.

The model predicted a maximum swollen corneal central thickness (CCT) of approximately 660 µm, which lies in the range of Fuch's dystrophy clinical observation going from 580 µm in the early stage [165] to 690 µm in the late stage [166], compared to a normal thickness of 530 µm. This swelling has been observed to occur mainly in the posterior stromal region and in the thickness direction, like observed clinically [89].

To go further, this multiphasic model could be used to study any diseases related to an imbalance between IOP, stromal swelling pressure and the endothelium function. For example, diseases related to excessive intra ocular pressure like glaucoma, or simultaneous IOP and

endothelium dysfunctions like in phthisis bulbi. A focus could also be made on epithelial cell edema.

Finally, an opening was provided on the modeling of molecular mechanisms underlying the corneal endothelial pump using reactive mixture theory. This preliminary work could be further advanced to detail the exact membrane reactions taking place in endothelial cells that controls the nutrient supply and the level of hydration of the tissue, which also affects its mechanical behavior.

Part IV
Conclusion

This thesis work focused on modeling the biomechanical behavior of the human cornea and its impairment in pathological cases. Two models were developed: a first one describing the detail of the collagen architecture in the corneal stroma to study the mechanisms leading to a conical deformation as in keratoconus. A second model describing the corneal multiphasic properties, tissue swelling pressure and hydration control mechanism through the endothelial action, to study the physical mechanisms involved in the swelling and opacification of the cornea in Fuch's dystrophy.

The use of numerical simulation:

1. involved the need to detail the microstructure and the physico-chemical phenomena of the corneal tissue in order to model them,

2. allowed to perform flexible parametric and sensitivity analyses on the role of each corneal layers and microstructural parameters to assess their influence on corneal biomechanics.

First, the geometry of the human cornea was numerized from OCT and videokeratoscope data taken at the Metz-Thioville hospital. From these data, we reconstructed a geometry of the cornea in vivo conditions, i.e. already deformed by the intraocular pressure. An inverse procedure was therefore developed to obtain a reference geometry on which application of boundary conditions recovered the in vivo configuration. This inverse procedure was then extended to the multiphasic material model where geometry-dependent parameters only known in vivo (fixed charge density, fluid volume fraction ...) were included in the inverse iterative calculation.

The first numerical analysis focused on the fibrous aspects of the corneal stroma with the objective of identifying the necessary conditions for a conical deformation of the cornea as observed in keratoconus disease. The corneal stroma was described with a material model accounting for the presence of collagen fibers: the HGO model. This structure-motivated model includes contributions of an isotropic noncollagenous neo-Hookean matrix and two anisotropic families of collagen fibers with defined orientation and dispersion, describing the anisotropic strain-hardening hyperelastic behavior of fiber reinforced materials.

It was shown that as long as the posterior layers of the stroma were stiff, the cornea would not deform conically and keep an adequate anterior spherical shape needed for the refraction of light. If because of disease, the collagen fibers in the posterior stroma were damaged or disorganized, the mechanical support of the tissue at this site would weaken, resulting in a conical deformation transmitted to the above layers.

To obtain a conical deformation of the cornea, it was shown that the loss of stiffness had to be located on a small part of the tissue and to move concentrically away from this point, creating a very soft center and a linear stiffening pattern towards the healthy tissue at the border. A loss of stiffness over the entire cornea did not result in a conical deformation. These two points may indicate an origin of corneal ectasia due to localized damage in the posterior stroma which then spreads to the rest of the tissue.

In the second numerical analysis, the cornea was modeled as a multiphasic material using mixture theory to describe its volumetric behavior dictated by the stromal fluid pressure and the endothelial hydration control. The multiphasic cornea was composed of solid, fluid and electrically charged solutes, and transport phenomena such as osmosis and electro-osmotis were recovered. The fluid swelling pressure of the model at equilibrium was consistent with the fluid pressure measured experimentally in the in vivo cornea, thus acting as a validation. This model represented an improvement over the incompressible material used in the first numerical analysis and produced a volumetric behaviour that allowed us to study edematous diseases related to impairment of hydration and fluid pressure in the cornea.

Additionally, a simplified description of a membrane ionic exchanger was incorporated in the model to describe the endothelial hydration regulation happening in the cornea and to study a disease resulting from its dysfunction called Fuch's dystrophy. The description of the barrier and active pump function of the membrane allowed to model the incoming and outgoing ionic fluxes in the cornea and the resulting osmotic flux of water that controls the tissue hydration.

The simulation showed that two essential phenomena are involved in the endothelial membrane regulation:

1. a barrier function against some negatively charged ions, such as bicarbonate, that compensates for the presence of fixed negative charges in the stroma. This barrier function is characterized by a lower diffusivity of negatively charged ions through the endothelial membrane compared to other ions to help in the maintenance of tissue electroneutrality,

2. an active pumping of some ions from the stroma into the aqueous humour that actively lowers the negative charges in the stroma and pumps water out of the cornea by electro-osmosis. This cellular membrane pumping function results in an outward flux of negative charges, such as bicarbonate ions, delivered from the stroma into the external fluid.

Parametric analyses on bicarbonate diffusivity and active flux showed that even with an intact barrier function, a slow diffusion still operates and an active flux is needed to counter the passive leak of ions in the cornea and maintain the correct hydration level. In the same logic, even with a perfectly functioning pump function, when the barrier function is too impaired and ionic permeability is too high, it is no longer possible to compensate the leak and the cornea eventually becomes over-hydrated and swells. A balance between the two regulating mechanisms is therefore needed.

Indeed, the simulation showed that the loss of barrier function can be compensated by an increase in active flux. This observation is in agreement with one of the current medical hypothesis on Fuch's dystrophy progression stating that, in its pre-clinical phases, the pump mechanism may be over activated to compensate for cell loss, up to a degree where the endothelium cannot adjust and disease symptoms gradually appears.

The results obtained in this thesis were considered interesting by the clinical partners as numerical analysis provided new perspectives on the two studied diseases.

For Keratoconus disease, the numerical simulation highlighted some inconsistencies in the traditional view stating that anterior layers of the cornea are first affected and are therefore the roots of the disease. As a result, an article combining mechanical results and clinical observations was published, proposing a modified hypothesis on the etiology of the disease and indicating that a conic deformation is not possible if the posterior layers of the cornea are not affected.

In the case of Fuch's dystrophy, numerical simulations were in agreement with the medical knowledge saying that the loss of endothelial barrier function is due to cell loss and is initially compensated by an over activation of the pump mechanism of the remaining cells. This over activation is effective until a point where the compensation is no longer sufficient and the tissue swells, resulting in an increased fluid pressure and a swollen cornea.

In the end, this doctoral research was able to show the interest of applying modeling techniques from mechanics of materials to medical problematic. The combination of different expertise was prolific for the study of these two corneal diseases and demonstrated the benefits of a multidisciplinary approach. The results brought by this research were useful for the medical community, which was the principal objective.

Appendix

A Mixture theory

This appendix is a presentation of the mixture theory framework to model multiphasic materials. The complete theory for biphasic material with an example of linear isotropic poro-elasticity can be found in the chapter written by Pr. Gerard Atashian [26].

Mixture theory requires the formulation of mass, momentum, and energy balance equations for each of the mixture constituents, which may then be summed together to produce equivalent formulations for the mixture as a whole. The mixture as a whole should behave as a pure substance as it places a constraint on the mass, momentum, and energy exchanges between constituents and simplifies the formulation.

The three constituents of a mixture are the porous-permeable solid matrix (α=s), the solvent (α=w), and solutes (α=u). The motion of constituent α in the mixture is given by $\boldsymbol{\chi}^\alpha(\boldsymbol{X}^\alpha,\mathrm{t})$, where t is time and $\boldsymbol{X}^\alpha$ is the position of a material point of constituent α in the reference configuration of that constituent. In the current configuration at time t, an elemental region whose center of mass is $\boldsymbol{x} = \boldsymbol{\chi}^\alpha(\boldsymbol{X}^\alpha,\mathrm{t})$ contains material from all constituents α. The velocity of α is given by $\boldsymbol{v}^\alpha = \partial\boldsymbol{\chi}^\alpha/\partial t$.

Functions of state in a multiphasic material are the stresses $\boldsymbol{\sigma}^\alpha$, the internal momentum supplies $\hat{\boldsymbol{p}}^\alpha$, and the mixture free-energy density Ψ_r (free energy of solid and fluid in the current configuration, per volume of the mixture in the reference configuration). When solutes are included, the list of state variables must be extended to include the solute apparent density $\rho_r^\alpha = J\rho^\alpha$ (mass of solute α per volume of the mixture in the reference configuration). The dependence of the mixture free energy Ψ_r on solute density is then embodied in the chemical potential $\mu^\alpha = \partial\Psi_r/\partial\rho_r^\alpha$.

A.1 Mass balance

The axiom of mass balance for each constituent α of a mixture is given by:

$$\frac{D^\alpha\rho^\alpha}{Dt} + \rho^\alpha div\boldsymbol{v}^\alpha = \hat{\rho}^\alpha \tag{A.1}$$

where ρ^α is the apparent mass density of constituent α, $\boldsymbol{v}^\alpha$ is the velocity of that constituent, and $\hat{\rho}^\alpha$ is the apparent mass density supply to constituent α from all other constituents. The apparent density ρ^α represents the mass of constituent α per mixture volume taken in the current configuration. Similarly, $\hat{\rho}^\alpha$ represents the mass supply to constituent α per mixture volume. The operator $D^\alpha(.)/Dt = \partial(.)/\partial t + grad(.)\cdot\boldsymbol{v}^\alpha$ is the material time derivative in the spatial frame, following constituent α.

When a constituent is intrinsically incompressible, its true density ρ_T^α (mass of constituent α per volume of that constituent) is invariant in space and time. The apparent and true densities are related by the volume fraction φ^α of the constituent (volume of constituent α per mixture volume) according to $\rho^\alpha = \varphi^\alpha\rho_T^\alpha$. In a saturated mixture (a mixture with no voids), volume fractions satisfy the saturation condition

$$\sum_{\alpha} \varphi^{\alpha} = 1 \tag{A.2}$$

If the volume fraction of solutes is negligible, this relation reduces to $\varphi^s + \varphi^w \approx 1$, where $\alpha = s$ represents the porous solid matrix and $\alpha = w$ represents the solvent. In the case of the solvent, the apparent density ρ^w is related to the true solvent density according to $\rho^w = \varphi^w \rho_T^w$. Another measure of relative content used for solutes is the molar concentration c^α, defined as the number of moles dn^α in the elemental region, per volume of the solution; thus, $c^\alpha = dn^\alpha/(dV - dV^s)$. Since the molar mass of α is defined as $M^\alpha = dm^\alpha/dn^\alpha$ (an invariant property), it follows that $\rho^\alpha = (1 - \varphi^s) M^\alpha c^\alpha \approx \varphi^w M^\alpha c^\alpha$.

In the absence of chemical reactions, the differential statement of the axiom of mass balance for constituent α may be given by:

$$\frac{\partial \rho^\alpha}{\partial t} + div(\rho^\alpha \boldsymbol{v}^\alpha) = 0 \tag{A.3}$$

When the mixture constituents are incompressible, the relation $\rho^\alpha = \varphi^\alpha \rho_T^\alpha$ can be substituted into Eq.(A.3) and the invariant ρ_T^α can be canceled out from the resulting expression. Taking the sum over all constituents and using the mixture saturation condition, $\sum_\alpha \varphi^\alpha = 1$, produces a mass balance relation for the mixture

$$div(\boldsymbol{v}^s + \sum_{\alpha} \boldsymbol{w}^\alpha) = 0 \tag{A.4}$$

When the solute volume fraction is negligible, the volume flux of solutes is negligible in comparison to that of the solvent, therefore the net volume flux of interstitial fluid (solvent+solutes) relative to the solid, $\boldsymbol{w} = \sum_\alpha \boldsymbol{w}^\alpha$, reduces to the flux of the solvent, $\boldsymbol{w} \approx \boldsymbol{w}^w$. Thus, the incompressibility constraint eliminates the need to explicitly enforce the balance of mass for the solvent.

A.2 Linear Momentum balance

The axiom of linear momentum balance for each constituent α is given by

$$\rho^\alpha \boldsymbol{a}^\alpha = div\boldsymbol{\sigma}^\alpha + \rho^\alpha \boldsymbol{b}^\alpha + \hat{\boldsymbol{p}}^\alpha \tag{A.5}$$

where $\boldsymbol{a}^\alpha = D^\alpha \boldsymbol{v}^\alpha / Dt$ is the acceleration of constituent α, $\boldsymbol{b}^\alpha$ represents external body forces per mixture volume acting on constituent α, $\boldsymbol{\sigma}^\alpha$ is the apparent stress in constituent α, and $\hat{\boldsymbol{p}}^\alpha$ is the momentum supply to constituent α due to internal momentum exchanges with other constituents in the mixture. The momentum supply $\hat{\boldsymbol{p}}^\alpha$ is an internal body force accounting for momentum exchanges among constituents.

With the mixture area as a common denominator, it is possible to sum traction vectors and stresses over multiple constituents [26]. Summing Eq.(A.5) over all constituents, the momentum balance for the mixture takes the familiar form with $\boldsymbol{a} = D\boldsymbol{v}/Dt$ the mixture acceleration and $\boldsymbol{b}$ the mixture body force:

$$\rho \boldsymbol{a} = div\boldsymbol{\sigma} + \rho \boldsymbol{b} \tag{A.6}$$

The two simplifying assumptions adopted are quasi-static conditions (negligible effects of inertia) and negligible effects of solute and solvent viscosities. The validity of neglecting the effects of viscosity was experimentally justified in Hou et al. [176].

With negligible viscosity, the Cauchy stress tensor $\boldsymbol{\sigma}$ in a mixture of incompressible constituents only includes two contributions: the hydrostatic pressure p of the interstitial fluid (solvent+ solute), and the Cauchy stress $\boldsymbol{\sigma}^s$ in the solid, thus $\boldsymbol{\sigma} = -p\boldsymbol{I} + \boldsymbol{\sigma}^s$, where $\boldsymbol{I}$ is the identity tensor and $\boldsymbol{\sigma}^s$ is the stress arising from the strain in the porous solid matrix.

A constitutive relation is needed to relate $\boldsymbol{\sigma}^s$ to the state variables adopted for a particular analysis, such as solid matrix strain. Because it is porous, the solid matrix is compressible since the volume of pores changes as interstitial fluid enters or leaves the matrix. Under these conditions, the balance of linear momentum Eq.(A.6) for the mixture reduces to:

$$div\boldsymbol{\sigma} = -grad(p) + div(\boldsymbol{\sigma}^s) = 0 \tag{A.7}$$

Under quasi-static conditions, in the absence of external body forces and without momentum supply from active transport, the balance of linear momentum equation (A.5) for solvent and solute can be rewritten with the gradient in the mechano-electro-chemical potential (in units of energy per mass) balanced by the frictional interactions between constituents:

$$\rho^w grad(\tilde{\mu}^w) + \hat{\boldsymbol{p}}_{\boldsymbol{d}}^{\boldsymbol{w}} = 0 \tag{A.8}$$

$$-\rho^u grad(\tilde{\mu}^u) + \hat{\boldsymbol{p}}_{\boldsymbol{d}}^{\boldsymbol{u}} = 0 \tag{A.9}$$

where $\tilde{\mu}^\alpha$ is the mechano-electro-chemical potential of solvent and solute constituents $\alpha = w, u$ and $\hat{\boldsymbol{p}}_{\boldsymbol{d}}^{\boldsymbol{\alpha}}$ is the dissipative momentum supply to constituent α due to interactions with other mixture constituents. Without chemical reactions between constituents, the entropy inequality induces a constraint on $\hat{\boldsymbol{p}}_{\boldsymbol{d}}^{\boldsymbol{\alpha}}$, which is satisfied by adopting a linear constitutive relation on the relative velocities between constituent α and other constituents in the mixture:

$$\hat{\boldsymbol{p}}_{\boldsymbol{d}}^{\boldsymbol{\alpha}} = \sum_{\alpha \neq \gamma} \boldsymbol{f}^{\alpha\gamma}.(\boldsymbol{v}^\gamma - \boldsymbol{v}^\alpha) \tag{A.10}$$

where $\boldsymbol{f}^{\alpha\gamma}$ a tensor called the diffusive drag coefficient, with γ spanning all mixture constituents. In a multiphasic mixture model, the transport of solute may be hindered by frictional interactions with the solid matrix and the solvent, but, with negligible volume fraction of solutes, solute-solute frictional interactions are neglected. In the end, the non-negligible diffusive drag coefficients are $\boldsymbol{f}^{uw}$ (solute-solvent), $\boldsymbol{f}^{us}$ (solute-solid), and $\boldsymbol{f}^{ws}$ (solvent-solid).

For the fluid constituents of a mixture, according to the momentum equations Eqs.(A.8,A.9), solvent and solute fluxes are driven by gradients in $\tilde{\mu}^\alpha$, and resisted by dissipative momentum exchanges $\hat{\boldsymbol{p}}_d^\alpha$. The fluid pressure p, electrical potential ψ, and chemical potential μ^α may then be combined into a single scalar variable $\tilde{\mu}^\alpha$ called the mechano-electro-chemical potential, which for the neutral solvent is given by:

$$\tilde{\mu}^w = \mu_0^w(\theta) + \frac{1}{\rho_T^w}(p - p_0 - R\theta\phi \sum_\alpha c^\alpha) \tag{A.11}$$

where $\mu_0^w(\theta)$ is the solvent chemical potential in the solvent standard state, θ is the absolute temperature and ρ_T^w is the true density of the solvent, which is invariant because the solvent is assumed incompressible.

Here the mechanical contribution is proportional to the fluid pressure p minus p_0, the corresponding pressure in the standard state, and subtracted to the osmotic pressure according to Van't Hoff theory Eq.(57). Like cover in the Section(11.2.1), the Van't Hoff theory says that substances in dilute solution obey the ideal gas laws, resulting in the osmotic pressure formula $R\theta\phi\sum_\alpha c^\alpha$ summed over all solutes in the mixture, with R the universal gas constant, ϕ the non-dimensional osmotic coefficient (equal to 1 for ideal mixtures), and c^α the solution volume-based concentration of solute α.

In our approach, we assume that solutes occupy a negligible volume fraction in the solution, so that their mechanical potential is negligible. Thus, their mechano-electro-chemical potential reduces to the electro-chemical potential:

$$\tilde{\mu}^\alpha = \mu_0^\alpha(\theta) + \frac{R\theta}{M^\alpha}(\frac{z^\alpha F_c}{R\theta}(\psi-\psi_0) + ln(\frac{\gamma^\alpha c^\alpha}{\kappa^\alpha c_0^\alpha})) \tag{A.12}$$

where $ln(\frac{\gamma^\alpha c^\alpha}{\kappa^\alpha c_0^\alpha})$ represents the chemical contribution with γ^α the solute activity coefficient and κ^α its solubility, representing the fraction of the interstitial pore volume which is accessible to the solute α. The electrical contribution is proportional to the electrical potential ψ minus ψ_0, the corresponding potential in the standard state, but reduces to zero for a neutral constituent ($z^\alpha = 0$). M^α is the molar mass of the solute, F_c is Faraday's constant, z^α its charge number, and c_0^α its concentration in the solute standard state.

Since κ^α and γ^α appear together as a ratio, they may be combined into a single material function, $\hat{\kappa}^\alpha = \kappa^\alpha/\gamma^\alpha$, called the effective solubility of solute α [175], which is equal to 1 for ideal mixtures in the context of physical chemistry. From this ratio we introduce $\tilde{\kappa}^\alpha$, the partition coefficient of solute α relative to an ideal solution:

$$\tilde{\kappa}^\alpha = \frac{\kappa^\alpha}{\gamma^\alpha} exp(-\frac{z^\alpha F_c \psi}{R\theta}) = \hat{\kappa}^\alpha exp(-\frac{z^\alpha F_c \psi}{R\theta}) \tag{A.13}$$

In relations (A.11,A.12), ϕ and γ^α are functions of state that describe the deviation of the mixture from ideal physico-chemical behavior. Therefore, the values of $\mu_0^w(\theta)$, p_0, ψ_0, $\mu_0^\alpha(\theta)$, and c_0^α represent reference conditions for the physico-chemical state of each constituent and remain invariant over the entire domain.

After defining the expressions for solvent and solutes potentials, we go back to the momentum equations. Without active transport mechanisms, the linear momentum balance equations (A.8,A.9) may be inverted to produce the following expressions for the fluxes of water and solutes:

$$\boldsymbol{m}^w = -\tilde{\boldsymbol{k}}.[(\rho_T^w)^2 grad\tilde{\mu}^w + \frac{(\rho_T^w)^2}{\rho^w}\sum_{\alpha\neq s,w}\frac{\boldsymbol{d}^\alpha}{d_0^\alpha}.\rho^\alpha grad\tilde{\mu}^\alpha] \tag{A.14}$$

$$\boldsymbol{m}^\alpha = -\rho^\alpha\frac{M^\alpha}{R\theta}\boldsymbol{d}^\alpha.grad\tilde{\mu}^\alpha + \frac{\rho^\alpha}{\rho_w}\frac{\boldsymbol{d}^\alpha}{d_0^\alpha}.\boldsymbol{m}^w, \quad a\neq s,w \tag{A.15}$$

where $\boldsymbol{d}^\alpha$ is the diffusivity tensor of solute α in the mixture (solid and fluid), with $d_0^\alpha\boldsymbol{I}$ the corresponding diffusivity in free solution (solvent). $\tilde{\boldsymbol{k}}$ is the hydraulic permeability tensor of the interstitial fluid (solvent and solutes) through the porous solid given by

$$\tilde{\boldsymbol{k}} = [\boldsymbol{k}^{-1} + \frac{R\theta}{\varphi^w}\sum_{\alpha\neq s,w}\frac{c^\alpha}{d_0^\alpha}(\boldsymbol{I} - \frac{\boldsymbol{d}^\alpha}{d_0^\alpha})]^{-1} \tag{A.16}$$

with $\boldsymbol{k}$ the corresponding hydraulic permeability tensor of the porous solid to the solvent alone. Constitutive relations must be provided for $\boldsymbol{k}$, $\boldsymbol{d}^\alpha$, and d_0^α to relate them to state variables such as solid matrix strain and suitable measures of solute concentrations. In the end the transport properties are related to the diffusive drag coefficients according to

$$\boldsymbol{k} = (\varphi^w)^2(\boldsymbol{f}^{ws})^{-1} \tag{A.17}$$
$$\boldsymbol{d_0^\alpha} = R\theta\varphi^w c^\alpha(\boldsymbol{f}^{\alpha w})^{-1} \equiv d_0^\alpha \boldsymbol{I} \tag{A.18}$$
$$\boldsymbol{d^\alpha} = R\theta\varphi^w c^\alpha(\boldsymbol{f}^{\alpha s} + \boldsymbol{f}^{\alpha w})^{-1} \tag{A.19}$$

Linear Momentum balance expressed in nodal variables

This section is a repetition of the Section(11.1) already present in the main text.

In a finite element modeling framework, we define nodal variables (degrees of freedom) that are continuous across elements boundaries. In this mixture framework, variables that satisfy continuity requirements are the solid displacement $\boldsymbol{u}$ and the mechano-electro-chemical potentials $\tilde{\mu}^\alpha$ of the solvent and solutes. However, since $\tilde{\mu}^\alpha$'s are less practical to use as nodal variables, an alternative form of the solvent mechano-chemical potential $\tilde{\mu}^w$ is introduced as the the effective fluid pressure $\tilde{p}$ by subtracting the referential chemical potential:

$$\tilde{p} \equiv \rho_T^w(\tilde{\mu}^w - \mu_0^w) = p - p_0 - R\theta \sum_{\alpha\neq s,w} c^\alpha \tag{A.20}$$

Note that $p - p_0$ represents a gauge pressure relative to some ambient pressure p_0; thus, it is common to let $p_0 = 0$ so that p represents that gauge pressure.

Physically, since $R\theta\Phi\sum_{\alpha\neq s,w} c^\alpha$ is the osmotic contribution to the fluid pressure, $\tilde{p}$ may be interpreted as the mechanical contribution of the total fluid pressure which does not result from osmotic effects. Similarly, the effective solute concentration $\tilde{c}^\alpha$ is an alternative form of the solute electro-chemical potential $\tilde{\mu}^\alpha$ that subtracts out the referential chemical potential of the solute,

$$\tilde{c}^\alpha \equiv c_0^\alpha exp[\frac{M^\alpha}{R\theta}(\tilde{\mu}^\alpha - \mu_0^\alpha)] = \frac{c^\alpha}{\tilde{\kappa}^\alpha} \tag{A.21}$$

with the partition coefficient previously defined as $\tilde{\kappa}^\alpha = \hat{\kappa}^\alpha exp[-z^\alpha \frac{F_c}{R\theta}(\psi - \psi_0)]$. Here again, $\psi - \psi_0$ represents the electric potential relative to some reference potential ψ_0; it is common to assume that $\psi_0 = 0$. Because $\tilde{p}$ and $\tilde{c}^\alpha$ are formulated by subtracting the arbitrary referential chemical potentials, they are more convenient to use than $\tilde{\mu}^w$ and $\tilde{\mu}^\alpha$ as nodal degrees of freedom [100].

When using $\tilde{p}$ and $\tilde{c}^\alpha$ as potentials, the mass fluxes given in Eqs.(A.14), (A.15) may be reordered to express the equivalent fluid volume flux,

$$\boldsymbol{w} = -\tilde{\boldsymbol{k}}.(grad\tilde{p} + R\theta \sum_{\alpha\neq s,w} \frac{\tilde{k}^\alpha}{d_0^\alpha}\boldsymbol{d}^\alpha.grad\tilde{c}^\alpha) \tag{A.22}$$

and solute molar fluxes,

$$\boldsymbol{j}^\alpha = \tilde{k}^\alpha \boldsymbol{d}^\alpha.(-\varphi^w grad\tilde{c}^\alpha + \frac{\tilde{c}^\alpha}{d_0^\alpha}\boldsymbol{w}), \quad \alpha \neq s, w \tag{A.23}$$

These two expressions are relatively compact but describe a broad set of phenomena. In the generalized Darcy's law (50), the first term (gradient of effective fluid pressure $grad(\tilde{p})$) includes both permeation (fluid flux in response to a pressure gradient: $grad(p)$) and osmosis (fluid flux in response to a concentration gradient: $grad(R\theta \sum_\alpha c^\alpha)$). The second term includes the partition coefficient and ratio of diffusivities in the mixture and in free solution $\frac{\tilde{k}^\beta}{d_0^\beta}\boldsymbol{d}^\beta.grad(\tilde{c}^\alpha) = \frac{\tilde{k}^\beta}{d_0^\beta}\boldsymbol{d}^\beta.grad(c^\alpha \hat{k}^\alpha exp(\frac{z^\alpha F_c \psi}{R\theta}))$ and accounts for the increased resistance to solvent flux due to the friction between solute and solid matrix. It also includes gradients in electric potential and therefore equally describes electro-osmosis.

If the solid matrix does not slow down the diffusivity of the solute (an idealized situation), then d and d_0 are the same; if the solute is not charged, or if the electric potential is uniform, then the effect of the electric potential is eliminated; if additionally we assume that the solute solubility is 1 (the solute can occupy all of the pore space in the solid matrix), then all these terms in the second part of the equation combine to cancel out the osmosis mechanism in the first term, so that only the permeation mechanism remains (Darcy's law). In summary, the second term describes interactions between the solute and the charged solid matrix, which influence the solvent flux.

The second expression is the generalized Fick's law (51) which incorporates diffusive term from the concentration gradient of solute ($-\varphi^w grad\tilde{c}^\alpha$) and a convective term related to the volumetric flux of fluid described with the generalized Darcy's law ($\frac{\tilde{c}^\alpha}{d_0^\alpha}\boldsymbol{w}$). These two terms are related to the hindrance of solid matrix in the current configuration described by the diffusivity tensor $\boldsymbol{d}^\alpha$.

A.3 Angular Momentum balance

The axiom of angular momentum balance reduces to $\boldsymbol{\sigma}^\alpha - (\boldsymbol{\sigma}^\alpha)^T = \hat{\boldsymbol{M}}^\alpha$, where $\hat{\boldsymbol{M}}^\alpha$ is the tensor that represents the internal angular momentum supply to constituent α due to interactions with other mixture constituents.

In applications of mixture theory to biological tissues, it is most commonly assumed that $\hat{\boldsymbol{M}}^\alpha = 0$, $\forall\alpha$, as there is no strong physical argument for assuming that individual constituents behave as polar materials. Thus, assuming that the mixture as a whole models a nonpolar material, the constraint on this angular momentum exchange reduces to $\sum_\alpha \hat{\boldsymbol{M}}^\alpha = 0$.

A.4 Balance of internal energy

The equations of mass and momentum balance are sufficient to address a broad range of analyses in biological tissue mechanics. The energy balance equations are not reviewed here but can be found in [177]. They are only needed for more specialized analyses, such as those arising in bioheat transfer.

A.5 Entropy inequality

The entropy inequality is needed to place constraints on constitutive relations for functions of state, such as the stress, mass supply, and dissipative momentum exchange for each mixture constituent. Since the formulation of these constraints is particularly involved, its full mathematical development for multiphasic material is not described here and can be found in [177].

References

[1] G Ferrari and P Rama. "The keratoconus enigma: A review with emphasis on pathogenesis". In: *The Ocular Surface* (2020). DOI: 10.1016/j.jtos.2020.03.006.

[2] U Soiberman, JW Foster, AS Jun, and S Chakravarti. "Pathophysiology of Keratoconus: What Do We Know Today". In: *The Open Ophthalmology Journal* (2017). DOI: 10.2174/1874364101711010252.

[3] GO Waring, WM Bourne, HF Edelhauser, and KR Kenyon. "The corneal endothelium. Normal and pathologic structure and function". In: *Ophtalmology* 89(6) (1982), pp. 531–590.

[4] H Elhalis, B Azizi, and UV Jurkunas. "Fuchs Endothelial Corneal Dystrophy". In: *The Ocular Surface* (2010). DOI: 10.1016/s1542-0124(12)70232-x.

[5] J Sugar and MS Macsai. "What Causes Keratoconus?" In: *Cornea* (2012). DOI: 10.1097/ICO.0b013e31823f8c72.

[6] JAP Gomes, D Tan, CJ Rapuano, MW Belin, R Ambrósio, and JL Guell. "Global consensus on keratoconus and ectatic diseases". In: *Cornea* (2015). DOI: 10.1097/ICO.0000000000000408.

[7] LA Carvalho, M Prado, RH Cunha, AC Neto, A Paranhos, P Schor, and W Chamon. "Keratoconus Prediction Using a Finite Element Model of the Cornea with Local Biomechanical Properties". In: *Arquivos brasileiros de oftalmologia* (2009). DOI: 10.1590/s0004-27492009000200002.

[8] A Gefen, R Shalom, D Elad, and Y Mandel. "Biomechanical analysis of the keratoconic cornea". In: *J Mech Behav Biomed Mater.* (2009). DOI: 10.1016/j.jmbbm.2008.07.002.

[9] AS Roy and WJ Dupps. "Patient-specific computational modeling of keratoconus progression and differential responses to collagen cross-linking". In: *Invest Ophthalmol Vis Sci* (2011). DOI: 10.1167/iovs.11-7395.

[10] A Pandolfi. "Computational Biomechanics of the Human Cornea". In: *Computational Modeling in Biomechanics* (2009). DOI: 10.1007/978-90-481-3575-215.

[11] A Montanino, A Gizzi, M Vasta, M Angelillo, and A Pandolfi. "Modeling the biomechanics of the human cornea accounting for local variations of the collagen fibril architecture". In: *Z Angew Math Mech.* (2018). DOI: 10.1002/zamm.201700293.

[12] PJ Shih, IJ Wang, WF Cai, and JY Yen. "Biomechanical Simulation of Stress Concentration and Intraocular Pressure in Corneas Subjected to Myopic Refractive Surgical Procedures". In: *Scientific Reports* (2017). DOI: 10.1038/s41598-017-14293-0.

[13] MA Ariza-Gracia, JF Zurita, DP Piñero, JF Rodriguez-Matas, and B Calvo. "Coupled Biomechanical Response of the Cornea Assessed by Non-Contact Tonometry. A Simulation Study". In: *PLoS ONE* (2015). DOI: 10.1371/journal.pone.0121486.

[14] Daniel G. Dawson, John L. Ubels, and Henry F. Edelhauser. *Adler's physiology of the eye, 11th edition.* ELSEVIER, 2011. ISBN: 9780323057141.

[15] A Elsheikh. "Finite Element Modeling of Corneal Biomechanical Behavior". In: *J Refract Surg.* (2010). DOI: 10.3928/1081597X-20090710-01.

[16] A Elsheikh, D Alhasso, and P Rama. "Assessment of the epithelium's contribution to corneal biomechanics". In: *Experimental Eye Research* (2008). DOI: 10.1016/j.exer.2007.12.002.

[17] M Ali, V Raghunathan, JY Li, CJ Murphy, and SM Thomasy. "Biomechanical relationships between the corneal endothelium and Descemet's membrane". In: *Experiemental eye research* (2016). DOI: 10.1016/j.exer.2016.09.004.

[18] KM Meek and C Boote. "The use of X-ray scattering techniques to quantify the orientation and distribution of collagen in the corneal stroma". In: *Progress in Retinal and Eye Research* (2009). DOI: 10.1016/j.preteyeres.2009.06.005.

[19] X Cheng and PM Pinsky. "Mechanisms of self-organization for the collagen fibril lattice in the human cornea". In: *Journal of the Royal Society* (2013). DOI: 10.1098/rsif.2013.0512.

[20] X Cheng, SJ Petsche, and PM Pinsky. "A structural model for the in vivo human cornea including collagen-swelling interaction". In: *J. R. Soc. Interface* (2015). DOI: 10.1098/rsif.2015.0241.

[21] N Morishige, Y Takagi, T Chikama, A Takahara, and T Nishida. "Three-Dimensional Analysis of Collagen Lamellae in the Anterior Stroma of the Human Cornea Visualized by Second Harmonic Generation Imaging Microscopy". In: *Investigative Ophthalmology and Visual Science* (2011). DOI: 10.1167/iovs.10-5657.

[22] KM Meek and C Knupp. "Corneal structure and transparency". In: *Progress in Retinal and Eye Research* (2015). DOI: 10.1016/j.preteyeres.2015.07.001.

[23] N Morishige, Y Takagi, T Chikama, A Takahara, and T Nishida. "Three-dimensional analysis of collagen lamellae in the anterior stroma of the human cornea visualized by second harmonic generation imaging microscopy". In: *Investigative Ophthalmology and Visual Science* (2011). DOI: 10.1167/iovs.10-5657.

[24] GA Holzapfel and RW Ogden. "An arterial constitutive model accounting for collagen content and cross-linking". In: *Journal of the Mechanics and Physics of Solids* (2020). DOI: 10.1016/j.jmps.2019.103682.

[25] GA Holzapfel and RW Ogden. "On the tension–compression switch in soft fibrous solids". In: *European Journal of Mechanics A-solids* (2015). DOI: 10.1016/j.euromechsol.2014.09.005.

[26] GA Ateshian. "Mixture Theory for Modeling Biological Tissues: Illustrations from Articular Cartilage". In: *Biomechanics: Trends in Modeling and Simulation* (2017). DOI: 10.1007/978-3-319-41475-1_1.

[27] A Elsheikh, D Wang, and D Pye. "Determination of the Modulus of Elasticity of the Human Cornea". In: *Journal of refractive surgery* (2007). DOI: 10.3928/1081-597X-20071001-11.

[28] JA Last, SM Thomasy, CR Croasdale, P Russell, and CJ Murphy. "Compliance profile of the human cornea as measured by atomic force microscopy". In: *Micron* (2012). DOI: 10.1016/j.micron.2012.02.014.

[29] Baldit Adrien. "Biomechanical characterization and modeling of biological tissues". In: *ENIM Biomechanical course* (2018).

[30] YC Fung, K Fronek, and P Patitucci. "Pseudoelasticity of Arteries and the Choice of its Mathematical Expression". In: *Am. J. Physiol. Heart Circ.* (1979). DOI: 10.1152/ajpheart.1979.237.5.H620.

[31] SJ Petsche and PM Pinsky. "The role of 3-D collagen organization in stromal elasticity: a model based on X-ray diffraction data and second harmonic-generated images". In: *Biomech Model Mechanobiol* (2013). DOI: 10.1007/s10237-012-0466-8.

[32] M Winkler. "(Re-)Discovering A Blueprint Of The Cornea: Structural, Biomechanical, Evolutionary and Developmental Perspectives". PhD dissertation. University of California, 2014.

[33] L Li and B Tighe. "Numerical simulation of corneal transport processes". In: *J. R. Soc. Interface* (2006). DOI: 10.1098/rsif.2005.0085.

[34] GA Ateshian, M Likhitpanichkul, and CT Hung. "A mixture theory analysis for passive transport in osmotic loading of cells". In: *Journal of Biomechanics* (2006). DOI: 10.1016/j.jbiomech.2004.12.013.

[35] JA Bonanno. "Molecular mechanisms underlying the corneal endothelial pump". In: *Experimental eye research* (2011). DOI: 10.1016/j.exer.2011.06.004.

[36] P Mlyniuk, E Maczynska-Walkowiak, J Rzeszewska-Zamiara, I Grulkowski, and B Kaluzny. "Probing biomechanical properties of the cornea with air-puff-based techniques - an overview". In: *Advanced Optical Technologies* (2021). DOI: 10.1515/aot-2021-0042.

[37] A Adamis, V Filatov, B Tripathi, and R Tripathi. "Fuchs' endothelial dystrophy of the cornea". In: *Surv Ophthalmol.* (1993). DOI: 10.1016/0039-6257(93)90099-s.

[38] KP Mashige. "A review of corneal diameter, curvature and thickness values and influencing factors". In: *The south african optometrist* (2011). DOI: 10.4102/aveh.v72i4.58.

[39] M Dubbelman, VA Sicam, and GL Van der Heijde. "The shape of the anterior and posterior surface of the aging human cornea". In: *Vision research* (2006). DOI: 10.1016/j.visres.2005.09.021.

[40] C Boote, CS Kamma-Lorger, S Hayes, J Harris, M Burghammer, J Hiller, NJ Terrill, and KM Meek. "Quantification of Collagen Organization in the Peripheral Human Cornea at Micron-Scale Resolution". In: *Biophysical journal* (2011). DOI: 10.1016/j.bpj.2011.05.029.

[41] GI Barenblatt and DD Joseph. *Collected Papers of R.S. Rivlin*. Springer-Verlag, 1997. ISBN: 978-1-4612-2416-7.

[42] Gerhard A Holzapfel. *Nonlinear Solid Mechanics: A Continuum Approach for Engineering*. Wiley, 2000. ISBN: 978-0-471-82319-3.

[43] AJM Spencer. *Continuum Mechanics*. Dover Publications Inc, 2004. ISBN: 978-0486435947.

[44] LA Taber. *Nonlinear Theory of Elasticity-Applications in Biomechanics*. World Scientific Publishing, 2008. ISBN: 978-981-4483-39-1.

[45] G Saccomandi and RW Ogden. *Mechanics and Thermomechanics of Rubberlike Solids*. Springer, 2004. ISBN: 978-3-7091-2540-3.

[46] K Takamizawa and K Hayashi. "Strain Energy Density Function and Uniform Strain Hypothesis for Arterial Mechanics". In: *J. Biomech.* (1987). DOI: 10.1016/0021-9290(87)90262-4.

[47] JD Humphrey. "Mechanics of the Arterial Wall: Review and Directions". In: *Crit. Rev. Biomed. Eng.* (1995). DOI: 10.1615/critrevbiomedeng.v23.i1-2.10.

[48] SL Woo, AS Kobayashi, WA Schlegel, and C Lawrence. "Nonlinear material properties of intact cornea and sclera". In: *Exp Eye Res.* (1972). DOI: 10.1016/0014-4835(72)90139-x.

[49] GA Holzapfel, TC Gasser, and RW Ogden. "A New Constitutive Framework for Arterial Wall Mechanics and a Comparative Study of Material Models". In: *Journal of elasticity and the physical science of solids* (2000). DOI: 10.1023/A:1010835316564.

[50] TC Gasser, RW Ogden, and GA Holzapfel. "Hyperelastic modelling of arterial layers with distributed collagen fibre orientations". In: *J R Soc Interface* (2006). DOI: 10.1098/rsif.2005.0073.

[51] Y Xiang, M Shen, C Xue, D Wu, and Y Wang. "Tensile biomechanical properties and constitutive parameters of human corneal stroma extracted by SMILE procedure". In: *Journal of the mechanical behavior of biomedical materials* (2018). DOI: 10.1016/j.jmbbm.2018.05.042.

[52] MA Ariza-Gracia, J Zurita, DP Piñero, B Calvo, and JF Rodríguez-Matas. "Automatized Patient-Specific Methodology for Numerical Determination of Biomechanical Corneal Response". In: *Biomedical Engineering Society* (2015). DOI: 10.1007/s10439-015-1426-0.

[53] I Simonini and A Pandolfi. "Customized Finite Element Modelling of the Human Cornea". In: *PLoS ONE* (2015). DOI: 10.1371/journal.pone.0130426.

[54] H Studer, X Larrea, H Riedwyl, and P Büchler. "Biomechanical model of human cornea based on stromal microstructure". In: *Journal of Biomechanics* (2010). DOI: 10.1016/j.jbiomech.2009.11.021.

[55] GA Holzapfel, TC Gasser, and RW Ogden. "Comparison of a multi-layer structural model for arterial walls with a Fung-type model, and issues of material stability". In: *J. Biomech. Eng.* (2004). DOI: 10.1115/1.1695572.

[56] G Chagnon, J Ohayon, JL Martiel, and D Favier. "Hyperelasticity modeling for incompressible passive biological tissues". In: *Biomechanics of Living Organs* (2017). DOI: 10.1016/B978-0-12-804009-6.00001-8.

[57] A Pandolfi and F Manganiello. "A model for the human cornea: constitutive formulation and numerical analysis". In: *Biomechan Model Mechanobiol* (2006). DOI: 10.1007/s10237-005-0014-x.

[58] GA Holzapfel, RW Ogden, and S Sherifova. "On fibre dispersion modelling of soft biological tissues: a review". In: *Proc. R. Soc* (2019). DOI: 10.1098/rspa.2018.0736.

[59] A Pandolfi and GA Holzapfel. "Three-Dimensional Modeling and Computational Analysis of the Human Cornea Considering Distributed Collagen Fibril Orientations". In: *Journal of Biomechanical Engineering* (2008). DOI: 10.1115/1.2982251.

[60] PM Pinsky and DV Datye. "A microstructurally-based finite element model of the incised human cornea". In: *J Biomech* (1991). DOI: 10.1016/0021-9290(91)90169-n.

[61] PM Pinsky, D van der Heide, and D Chernyak. "Computational modeling of mechanical anisotropy in the cornea and sclera". In: *J Cataract Refract Surg* (2005). DOI: 10.1016/j.jcrs.2004.10.048.

[62] R Grytz and G Meschke. "A computational remodeling approach to predict the physiological architecture of the collagen fibril network in corneo-scleral shells". In: *Biomech Model Mechanobiol* (2010). DOI: 10.1007/s10237-009-0173-2.

[63] C Whitford, H Studer, C Boote, KM Meek, and A Elsheikh. "Biomechanical model of the human cornea: Considering shear stiffness and regional variation of collagen anisotropy and density". In: *Journal of the mechanical behavior of biomedical materials* (2014). DOI: 10.1016/j.jmbbm.2014.11.006.

[64] A Barkaoui and R Hambli. "Nanomechanical properties of mineralised collagen microfibrils based on finite elements method: biomechanical role of cross-links". In: *Comput Methods Biomech Biomed Engin.* (2013). DOI: 10.1080/10255842.2012.758255.

[65] A Gautieri, S Vesentini, A Redaelli, and MJ Buehler. "Hierarchical structure and nanomechanics of collagen microfibrils from the atomistic scale up". In: *Nano letters* (2011). DOI: 10.1021/nl103943u.

[66] H Tang, MJ Buehler, and B Moran. "A constitutive model of soft tissue: from nanoscale collagen to tissue continuum". In: *Ann Biomed Eng.* (2009). DOI: 10.1007/s10439-009-9679-0.

[67] MJ Buehler. "Nanomechanics of collagen fibrils under varying cross-link densities: atomistic and continuum studies". In: *J Mech Behav Biomed Mater.* (2008). DOI: 10.1016/j.jmbbm.2007.04.001.

[68] F Maceri, M Marino, and G Vairo. "A unified multiscale mechanical model for soft collagenous tissues with regular fiber arrangement". In: *Journal of biomechanics* (2010). DOI: 10.1016/j.jbiomech.2009.07.040.

[69] SJ Petsche. "Multiscale mechanics and experimental investigation of the human cornea". PhD dissertation. Stanford University, 2014.

[70] M Marino and G Vairo. "Multiscale elastic models of collagen bio-structures: from cross-linked molecules to soft tissues". In: *Stud Mechanobiol Tissue Eng Biomater* (2013). DOI: 10.1007/8415_2012_154.

[71] M Marino and G Vairo. "Stress and strain localization in stretched collagenous tissues via a multiscale modelling approach". In: *Comput Methods Biomech Biomed Engin.* (2012). DOI: 10.1080/10255842.2012.658043.

[72] B Raju, SR Hiremath, and D Roy. "A review of micromechanics based models for effective elastic properties of reinforced polymer matrix composites". In: *Composite structures* (2018). DOI: 10.1016/j.compstruct.2018.07.125.

[73] A Pandolfi, A Gizzi, and M Vasta. "A microstructural model of cross-link interaction between collagen fibrils in the human cornea". In: *Philosophical transactions Royal Society A* (2019). DOI: 10.1098/rsta.2018.0079.

[74] Olivier Coussy. *Mechanics and physics of porous solids.* Wiley, 2010. ISBN: 978-0-47072135-3.

[75] Michelacci. "Collagens and proteoglycans of the corneal extracellular matrix". In: *Brazilian Journal of Medical and Biological Research* (2003). DOI: ISSN0100-879X.

[76] MA Biot. "General theory of three-dimensional consolidation". In: *J. Appl. Phys.* (1941). DOI: 10.1063/1.1712886.

[77] APS Selvadurai. *Thermo-hydro-mechanical behaviour of porous media.* Taylor and Francis, 2015. ISBN: 978-0486435947.

[78] AH Cheng. *Poroelasticity.* Springer-Verlag, 2015. ISBN: 978-3-319-25200-1.

[79] BR Simon, MV Kaufman, MA McAfee, and AL Baldwin. "Poroelastic theory and finite element models for soft tissues with applications to arterial mechanics". In: *Solid Mechanics and its Applications* (1996). DOI: 10.1007/978-94-015-8698-6_14.

[80] APS Selvadurai and AP Suvorov. "Coupled hydro-mechanical effects in a poro-hyperelastic material". In: *Journal of the Mechanics and Physics of Solids* (2016). DOI: 10.1016/j.jmps.2016.03.005.

[81] APS Selvadurai. *Partial Differential Equations in Mechanics. I Fundamentals, Laplace's Equation, Diffusion Equation, Wave Equation*. Springer-Verlag, 2000. ISBN: 978-3-662-04006-5.

[82] X Du and M Ostoja-Starzewski. "On the size of representative volume element for Darcy law in random media". In: *Proc. Roy Soc. Mathe Phys. Sci. Ser.* (2006). DOI: 10.1098/rspa.2006.1704.

[83] APS Selvadurai and AP Suvorov. "Thermo-poromechanics of a fluid-filled cavity in a fluid-saturated porous geomaterial". In: *Proc. Roy Soc. Mathe Phys. Sci. Ser.* (2014). DOI: 10.1098/rspa.2013.0634.

[84] APS Selvadurai and A Glowacki. "Evolution of permeability hysteresis of Indiana Limestone during isotropic compression". In: *Ground Water* (2008). DOI: 10.1111/j.1745-6584.2007.00390.x.

[85] APS Selvadurai, A Letendre, and B Hekimi. "Axial flow hydraulic pulse testing of an argillaceous limestone". In: *Env. Earth Sci.* (2011). DOI: 10.1007/s12665-011-1027-7.

[86] S Federico and A Grillo. "Elasticity and permeability of porous fibre-reinforced materials under large deformations". In: *Mech. Mater.* (2012). DOI: 10.1016/j.mechmat.2011.07.010.

[87] Yoram Lanir. "Osmotic swelling and residual stress in cardiovascular tissues". In: *Journal of Biomechanics* (2012). DOI: 10.1016/j.jbiomech.2011.11.018.

[88] X Cheng and PM Pinsky. "The Balance of Fluid and Osmotic Pressures across Active Biological Membranes with Application to the Corneal Endothelium". In: *PLoS ONE* (2015). DOI: 10.1371/journal.pone.0145422.

[89] PM Pinsky and X Cheng. "A Constitutive Model for Swelling Pressure and Volumetric Behavior of Highly-Hydrated Connective Tissue". In: *Journal of Elasticity: The Physical and Mathematical Science of Solids* (2017). DOI: 10.1007/s10659-016-9616-z.

[90] O Kedem and A Katchalsky. "Thermodynamic analysis of the permeability of biological membranes to non-electrolytes". In: *Biochimica and biophysica acta* (1958). DOI: 10.1016/0006-3002(58)90330-5.

[91] O Coussy. *Mechanics of Porous Continua*. John Wiley and Sons, 1995. ISBN: 9780471952671.

[92] DS Drumheller. "On theories of reacting immiscible mixtures". In: *Int. J. Eng. Sci.* (2000). DOI: 10.1016/S0020-7225(99)00047-6.

[93] JM Huyghe. *General theory of mixtures. Physical chemistry of mixtures and swelling*. Schrefler Sanavia Collin, 2015.

[94] RL Mauck, CT Hung, and GA Ateshian. "Modeling of Neutral Solute Transport in a Dynamically Loaded Porous Permeable Gel: Implications for Articular Cartilage Biosynthesis and Tissue Engineering". In: *J Biomech Eng.* (2003). DOI: 10.1115/1.1611512.

[95] D Munaf, AS Wineman, KR Rajagopal, and DW Lee. "A boundary value problem in groundwater motion analysis - comparison of predictions based on Darcy law and the continuum theory of mixtures". In: *Math. Model. Meth. Appl. Sci.* (1993). DOI: 10.1142/S0218202593000138.

[96] TJ Pence. "On the formulation of boundary value problems with incompressible constituent constraints in finite deformation poroelasticity". In: *Math. Model. Meth. Appl. Sci.* (2012). DOI: 10.1002/mma.2541.

[97] FP Duda, A Souza, and E Fried. "A theory for species migration in a finitely strained solid with application to polymer network swelling". In: *J. Mech. Phys. Solids* (2010). DOI: 10.1016/j.jmps.2010.01.009.

[98] SA Chester and L Anand. "A coupled theory of fluid permeation and large deformations for elastomeric materials". In: *J. Mech. Phys. Solids* (2010). DOI: 10.1016/j.jmps.2010.07.020.

[99] S Baek and TJ Pence. "Inhomogeneous deformation of elastomer gels in equilibrium under saturated and unsaturated conditions". In: *J. Mech. Phys. Solids* (2011). DOI: 10.1016/j.jmps.2010.12.013.

[100] GA Ateshian, S Maas, and JA Weiss. "Multiphasic Finite Element Framework for Modeling Hydrated Mixtures With Multiple Neutral and Charged Solutes". In: *Journal of Biomechanical engineering* (2013). DOI: 10.1115/1.4024823.

[101] M Naderan, S Shoar, F Rezagholizadeh, and M Zolfaghari. "Characteristics and associations of keratoconus patients". In: *Contact lens and anterior eye* (2015). DOI: 10.1016/j.clae.2015.01.008.

[102] K Zadnik, K Steger-May, BA Fink, and CE Joslin. "Between-Eye Asymmetry in Keratoconus". In: *Cornea* (2002). DOI: 10.1097/00003226-200210000-00008.

[103] A Gordon-Shaag, M Millodot, and E Shneor. "The Epidemiology and Etiology of Keratoconus". In: *International Journal of Keratoconus and Ectatic Corneal Diseases* (2012). DOI: 10.5005/jp-journals-10025-1002.

[104] A Mazharian, C Panthier, R Courtin, C Jung, R Rampat, A Saad, and D Gatinel. "Incorrect Sleeping Position and Eye Rubbing in Patients with Unilateral or Highly Asymmetric Keratoconus: A Case-Control Study". In: *Graefe's archive for clinical and experimental ophthalmology* (2020). DOI: 10.1007/s00417-020-04771-z.

[105] CNJ McGhee, BZ Kim, and PJ Wilson. "Contemporary Treatment Paradigms in Keratoconus". In: *Cornea* (2015). DOI: 10.1097/ICO.0000000000000504.

[106] H Najmi, Y Mobarki, K Mania, B Altowairqi, M Basehi, MS Mahfouz, and M Elmahdy. "The Correlation between Keratoconus and Eye Rubbing: A Review". In: *International Journal of Ophthalmology* (2019). DOI: 10.18240/ijo.2019.11.17.

[107] H Hashemi, M Khabazkhoob, N Yazdani, H Ostadimoghaddam, R Norouzirad, K Amanzadeh, M Miraftab, A Derakhshan, and A Yekta. "The Prevalence of Keratoconus in a Young Population in Mashhad, Iran". In: *Ophthalmic and physiological optics: the journal of the British College of Ophthalmic Opticians* (2014). DOI: 10.1111/opo.12147.

[108] R Ambrósio. "Violet June: The Global Keratoconus Awareness Campaign". In: *Ophthalmology and Therapy* (2020). DOI: 10.1007/s40123-020-00283-5.

[109] Wolfe Eye Clinic. "Keratoconus causes and treatment" (2020). DOI: www.wolfeeyeclinic.com/medical-services/corneal-disease/keratoconus.

[110] JH Mathew, JD Goosey, PG Söderberg, and JPG Bergmanson. "Lamellar Changes in the Keratoconic Cornea". In: *Acta ophthalmologica* (2015). DOI: 10.1111/aos.12811.

[111] MC Mocan, PT Yilmaz, M Irkec, and M Orhan. "The Significance of Vogt's Striae in Keratoconus as Evaluated by in Vivo Confocal Microscopy". In: *Clinical and Experimental Ophthalmology* (2008). DOI: 10.1111/j.1442-9071.2008.01737.x.

[112] O Sandali, M Sanharawi, C Temstet, T Hamiche, and A Galan. "Fourier-Domain Optical Coherence Tomography Imaging in Keratoconus: A Corneal Structural Classification". In: *Ophthalmology* (2013). DOI: 10.1016/j.ophtha.2013.05.027.

[113] A Alkanaan, R Barsotti, O Kirat, T Almubrad, A Khan, and S Akhtar. "Ultrastructural Study of Peripheral and Central Stroma of Keratoconus Cornea". In: *British Journal of Ophthalmology* (2017). DOI: 10.1136/bjophthalmol-2016-309834.

[114] K Grieve, D Ghoubay, C Georgeon, G Latour, and A Nahas. "Stromal striae: a new insight into corneal physiology and mechanics". In: *Nature scientific report* (2017). DOI: 10.1038/s41598-017-13194-6.

[115] M Winkler, G Shoa, Y Xie, SJ Petsche, PM Pinsky, T Juhasz, DJ Brown, and JV Jester. "Three-Dimensional Distribution of Transverse Collagen Fibers in the Anterior Human Corneal Stroma". In: *Investigative ophthalmology and visual science* (2013). DOI: 10.1167/iovs.13-13150.

[116] JCF Gaskin, WR Good, CA Jordan, DV Patel, and CN McGhee. "Identifying Predictors of Acute Corneal Hydrops in Keratoconus". In: *Clinical and experimental optometry* (2013). DOI: 10.1111/cxo.12048.

[117] D Hull and TN Clyne. *An introduction to composite materials. 2nd ed.* Cambridge University Press, 1996. ISBN: 9781139170130.

[118] M Knops. *Analysis of Failure in Fiber Polymer Laminates: the theory of Alfred Puck.* Springer-Verlag, 2008. ISBN: 978-3-540-75765-8.

[119] AS Roy, KM Rocha, JB Randleman, RD Stulting, and WJ Dupps. "Inverse computational analysis of in vivo corneal elastic modulus change after collagen crosslinking for keratoconus". In: *Experimental eye research* (2013). DOI: 10.1016/j.exer.2013.04.010.

[120] MA Henriquez, M Hadid, and L Izquierdo. "A Systematic Review of Subclinical Keratoconus and Forme Fruste Keratoconus". In: *Journal of refractive surgery* (2020). DOI: 10.3928/1081597X-20200212-03.

[121] R Vinciguerra, R Ambrósio, CJ Roberts, C Azzolini, and P Vinciguerra. "Biomechanical Characterization of Subclinical Keratoconus Without Topographic or Tomographic Abnormalities". In: *Journal of refractive surgery* (2017). DOI: 10.3928/1081597X-20170213-01.

[122] MA Wolle, JB Randleman, and M Woodward. "Complications of Refractive Surgery: Ectasia After Refractive Surgery". In: *International ophthalmology clinics* (2016). DOI: 10.1097/IIO.0000000000000102.

[123] NM Yenerel, RB Kucumen, and E Gorgun. "Changes in Corneal Biomechanics in Patients with Keratoconus after Penetrating Keratoplasty". In: *Cornea* (2010). DOI: 10.1097/ICO.0b013e3181ca6383.

[124] D Zhou, A Abass, B Lopes, A Eliasy, Hayes, C Boote, KM Meek, A Movchan, N Movchan, and A Elsheikh. "Fibril Density Reduction in Keratoconic Corneas". In: *J R Soc Interface* (2021). DOI: 10.1098/rsif.2020.0900.

[125] J Baum. "On the Location of the Cone and the Etiology of Keratoconus". In: *Cornea* 14.2 (1995), pp. 142–143.

[126] BJ Blackburn, MW Jenkins, AM Rollins, and WJ Dupps. "A Review of Structural and Biomechanical Changes in the Cornea in Aging, Disease, and Photochemical Crosslinking". In: *Front. Bioeng. Biotechnol* (2019). DOI: 10.3389/fbioe.2019.00066.

[127] AS Roy, R Shetty, and MK Kummelil. "Keratoconus: A Biomechanical Perspective on Loss of Corneal Stiffness". In: *Indian journal of ophthalmology* (2013). DOI: 10.4103/0301-4738.116057.

[128] TC Gasser, RW Ogden, and GA Holzapfel. "Hyperelastic modelling of arterial layers with distributed collagen fibre orientations". In: *J. R. Soc. Interface* (2006). DOI: 10.1098/rsif.2005.0073.

[129] V Alastrué, B Calvo, E Peña, and Doblaré. "Biomechanical modeling of refractive corneal surgery". In: *J Biomech Eng.* (2006). DOI: 10.1115/1.2132368.

[130] AS Roy, M Kurian, H Matalia, and R Shetty. "Air-puff associated quantification of non-linear biomechanical properties of the human cornea in vivo". In: *Journal of the Mechanical Behavior of Biomedical Materials* (2015). DOI: 10.1016/j.jmbbm.2015.04.0101751-6161.

[131] M Francis, P Khamar, R Shetty, K Sainani, R Nuijts, and B Haex. "In Vivo Prediction of Air-Puff Induced Corneal Deformation Using LASIK, SMILE, and PRK Finite Element Simulations". In: *IOVS* (2018). DOI: 10.1167/iovs.18-2470.

[132] P Sánchez, K Moutsouris, and A Pandolfi. "Biomechanical and optical behavior of human corneas before and after photorefractive keratectomy". In: *J Cataract Refract Surg* (2014). DOI: 10.1016/j.jcrs.2014.03.020.

[133] A Vahdati, I Seven, N Mysore, JB Randleman, and WJ Dupps. "Computational Biomechanical Analysis of Asymmetric Ectasia Risk in Unilateral Post-LASIK Ectasia". In: *J Refract Surg* (2016). DOI: 10.3928/1081597X-20160929-01.

[134] F Bao, B Geraghty, Q Wang, and A Elsheikh. "Consideration of corneal biomechanics in the diagnosis and management of keratoconus: is it important?" In: *Eye Vis.* (2016). DOI: 10.1186/s40662-016-0048-4.

[135] KM Meek, S Dennis, and S Khan. "Changes in the Refractive Index of the Stroma and Its Extrafibrillar Matrix When the Cornea Swells". In: *Biophysical Journal* (2003). DOI: 10.1016/S0006-3495(03)74646-3.

[136] DM Nowak and M Gajecka. "The Genetics of Keratoconus". In: *Middle East African journal of ophthalmology* (2011). DOI: 10.4103/0974-9233.75876.

[137] A Walkden, E Burkitt-Wright, and L Au. "Brittle Cornea Syndrome: Current Perspectives". In: *Clinical ophthalmology* (2019). DOI: 10.2147/OPTH.S185287.

[138] S Akhtar, AJ Bron, SM Salvi, NR Hawksworth, SJ Tuft, and KM Meek. "Ultrastructural Analysis of Collagen Fibrils and Proteoglycans in Keratoconus". In: *Acta ophthalmologica* (2008). DOI: 10.1111/j.1755-3768.2007.01142.x.

[139] M Angelillo, A Montanino, and A Pandolfi. "On the Connection Between Geometry and Statically Determined Membrane Stresses in the Human Cornea". In: *J Biomech Eng.* (2020). DOI: 10.1115/1.4044742.

[140] N Falgayrettes, E Patoor, F Cleymand, Y Zevering, and JM Perone. "Biomechanics of keratoconus: Two numerical studies". In: *PLOS ONE* (2023). DOI: 10.1371/journal.pone.0278455.

[141] S Chen, MJ Mienaltowski, and DE Birk. "Regulation of Corneal Stroma Extracellular Matrix Assembly". In: *Experimental eye research* (2015). DOI: 10.1016/j.exer.2014.08.001.

[142] R Mahadevan, AO Arumugam, V Arunachalam, and B Kumaresan. "Keratoconus - a Review from a Tertiary Eye-Care Center". In: *J Optom* (2009). DOI: 10.3921/joptom.2009.166.

[143] M Bohac, M Koncarevic, A Pasalic, A Biscevic, M Merlak, and N Gabric. "Incidence and Clinical Characteristics of Post LASIK Ectasia: A Review of over 30,000 LASIK Cases". In: *Semin Ophthalmol.* (2018). DOI: 10.1080/08820538.2018.1539183.

[144] Shi Yue. "Strategies for Improving the Early Diagnosis of Keratoconus". In: *Clinical Optometry* (2016). DOI: 10.2147/OPTO.S63486.

[145] R Ambrósio. "Post-LASIK Ectasia: Twenty Years of a Conundrum". In: *Seminars in ophthalmology* (2019). DOI: 10.1080/08820538.2019.1569075.

[146] TB McKay, S Priyadarsini, and D Karamichos. "Mechanisms of Collagen Crosslinking in Diabetes and Keratoconus". In: *Cells* (2019). DOI: 10.3390/cells8101239.

[147] AN Carlson. "Keratoconus". In: *Ophthalmology* (2009). DOI: 10.1016/j.ophtha.2009.08.026.

[148] H Munakata, K Takagaki, M Majima, and M Endo. "Interaction between collagens and glycosaminoglycans investigated using a surface plasmon resonance biosensor". In: *Glycobiology* (1999).

[149] T Schmedt, MM Silva, A Ziaei, and U Jurkunasa. "Molecular bases of corneal endothelial dystrophies". In: *Experimental Eye Research* (2012). DOI: 10.1016/j.exer.2011.08.002.

[150] WM Lai, JS Hou, and VC Mow. "A Triphasic Theory for the Swelling and Deformation Behaviors of Articular Cartilage". In: *J Biomech Eng.* (1991). DOI: 10.1115/1.2894880.

[151] WM Deen. "Hindered transport of large molecules in liquid-filled pores". In: *AICHE Journal* (1987). DOI: 10.1002/aic.690330902.

[152] WY Gu, WM Lai, and VC Mow. "A Mixture Theory for Charged-Hydrated Soft Tissues Containing Multi-electrolytes: Passive Transport and Swelling Behaviors". In: *J Biomech Eng.* (1998). DOI: 10.1115/1.2798299.

[153] K Dahnert and D Huster. "Comparison of the Poisson-Boltzmann model and the Donnan Equilibrium of a Polyelectrolyte in salt solution". In: *Journal of Colloid and interface science* (1999). DOI: 10.1006/jcis.1999.6238.

[154] MD Buschmann and AJ Grodzinsky. "A molecular model of proteoglycan-associated electrostatic forces in cartilage mechanics". In: *J Biomech Eng* (1995). DOI: 10.1115/1.2796000.

[155] SD Klyce and SR Russell. “Numerical solution of coupled transport equations applied to corneal hydration dynamics”. In: *J Physiol* (1979). DOI: 10.1113/jphysiol.1979.sp012841.

[156] D Overby, J Ruberti, H Gong, TF Freddo, and M Johnson. “Specific Hydraulic Conductivity of Corneal Stroma as Seen by Quick-Freeze/Deep-Etch”. In: *Journal of Biomechanical Engineering* (2001). DOI: 10.1115/1.1351888.

[157] Stuart Hodson. “Why the cornea swells”. In: *J. Theor. Biol.* (1971). DOI: 10.1016/0022-5193(71)90090-7.

[158] David Maurice. “The use of permeability studies in the investigation of submicroscopic structure”. In: *The Structure of the Eye* (1961).

[159] Alice Maroudas. “Physicochemical properties of cartilage in the light of ion exchange theory”. In: *Biophysical Journal* (1968). DOI: 10.1016/S0006-3495(68)86509-9.

[160] BK Leung, JA Bonanno, and CJ Radke. “Oxygen-deficient metabolism and corneal edema”. In: *Progress in retinal and eye research* (2011). DOI: 10.1016/j.preteyeres.2011.07.001.

[161] Sam Helwany. *APPLIED SOIL MECHANICS with ABAQUS Applications*. John Wiley and Sons, Inc., 2007. ISBN: 978-0-471-79107-2.

[162] T Sigaeva, G Sommer, GA Holzapfel, and ES Di Martino. “Anisotropic residual stresses in arteries”. In: *J. R. Soc. Interface* (2019). DOI: 10.1098/rsif.2019.0029.

[163] GA Ateshian, B Morrison, and CT Hung. “Modeling of active transmembrane transport in a mixture theory framework”. In: *Ann Biomed Eng* (2010). DOI: 10.1007/s10439-010-9980-y.

[164] DM Maurice. “The location of the fluid pump in the cornea”. In: *The journal of physiology* (1972). DOI: 10.1113/jphysiol.1972.sp009737.

[165] RR Rums, WM Rourne, and RF Rrubaker. “Endothelial function in patients with cornea guttata”. In: *Invest Ophthalmol Vis Sci* 20 (1981), pp. 77–85.

[166] TS Alomar, M Al-Aqaba, T Gray, J Lowe, and HS Dua. “Histological and Confocal Microscopy Changes in Chronic Corneal Edema: Implications for Endothelial Transplantation”. In: *Cornea* (2011). DOI: 10.1167/iovs.11-8047.

[167] AA Hidayat and GCC Cockerham. “Epithelial Metaplasia of the Corneal Endothelium in Fuchs Endothelial Dystrophy”. In: *Cornea* (2006). DOI: 10.1097/01.ico.0000228786.84581.ee.

[168] Y Davies, NJ Fullwood, B Marcyniuk, R Bonshek, A Tullo, and A Ian. “Keratan sulphate in the trabecular meshwork and cornea”. In: *Current Eye Research* (1997). DOI: 10.1076/ceyr.16.7.677.5053.

[169] M Magovern, GR Beauchamp, JW McTigue, BS Fine, and RC Baumiller. “Inheritance of Fuchs’ Combined Dystrophy”. In: *Ophtalmology* (1979). DOI: 10.1016/s0161-6420(79)35340-4.

[170] JD Gottsch, OH Sundin, SH Liu, AS Jun, KW Broman, WJ Stark, ECL Vito, AK Narang, JM Thompson, and M Magovern. “Inheritance of a Novel COL8A2 Mutation Defines a Distinct Early Onset Subtype of Fuchs Corneal Dystrophy”. In: *Cornea* (2005). DOI: 10.1167/iovs.04-0937.

[171] C Zhang, WR Bell, OH Sundin, Z De La Cruz, WJ Stark, WR Green, and JD Gottsch. "Immunohistochemistry and electron microscopy of early onset fuchs corneal dystrophy". In: *Trans Am Ophthalmol Soc.* 104 (2006), pp. 85–97.

[172] SE Wilson and WM Bourne. "Fuchs' dystrophy". In: *Cornea* 7(1) (1988), pp. 2–18.

[173] JS Singh, TA Haroldson, and SP Patel. "Characteristics of the low density corneal endothelial monolayer". In: *Exp Eye Res.* (2013). DOI: 10.1016/j.exer.2013.06.024.

[174] A Montanino, M Angelillo, and A Pandolfi. "Modelling with a meshfree approach the cornea-aqueous humor interaction during the air puff test". In: *Journal of the Mechanical Behavior of Biomedical Materials* (2018). DOI: 10.1016/j.jmbbm.2017.05.042.

[175] GA Ateshian, MB Albro, SA Maas, and JA Weiss. "Finite element implementation of mechanochemical phenomena in neutral deformable porous media under finite deformation". In: *Journal of Biomechanical Engineering* (2011). DOI: 10.1115/1.4004810.

[176] Chieh Hou. "Implementation and Validation of Finite Element Framework for Passive and Active Membrane Transport in Deformable Multiphasic Models of Biological Tissues and Cells". PhD dissertation. Columbia University, 2018.

[177] D Ambrosi, L Preziosi, and G Vitale. "The insight of mixtures theory for growth and remodeling". In: *Z. Angew. Math. Phys.* (2009). DOI: 10.1007/s00033-009-0037-8.